MULTIPLE JET INTERACTIONS WITH SPECIAL RELEVANCE TO RECOVERY BOILERS

By

Daniel C.M. Tse

B. Sc. (Mathematics and Physics) University of British Columbia, 1987

M. Math. (Applied Mathematics) University of Waterloo, 1989

A THESIS SUBMITTED IN PARTIAL FULFILLMENT OF

THE REQUIREMENTS FOR THE DEGREE OF

DOCTOR OF PHILOSOPHY

in

THE FACULTY OF GRADUATE STUDIES

DEPARTMENT OF MECHANICAL ENGINEERING

We accept this thesis as conforming

to the required standard

THE UNIVERSITY OF BRITISH COLUMBIA

February 1994

In presenting this thesis in partial fulfilment of the requirements for an advanced degree at the University of British Columbia, I agree that the Library shall make it freely available for reference and study. I further agree that permission for extensive copying of this thesis for scholarly purposes may be granted by the head of my department or by his or her representatives. It is understood that copying or publication of this thesis for financial gain shall not be allowed without my written permission.

(Signature)

Department of Mechanical Engineering

The University of British Columbia
Vancouver, Canada

Date March 22nd, 1994.

DE-6 (2/88)

Abstract

The problem of multiple turbulent jet interactions is investigated with special attention to applications in kraft recovery boilers. The phenomena due to turbulence are simulated with the $k - \epsilon$ turbulence model, and a multigrid numerical technique is applied to solve the time-averaged Navier-Stokes equations governing the flows. Investigations carried out include a study on the simulation of primary level jets and on the characteristics of a row of jets discharging into a confined crossflow. For the primary level jets, the interaction and merging of the jets are investigated. The jets merge rapidly and a suitable open slot representation gives an adequate description of the velocity field. For jets in a row interacting with a confined crossflow, the effects of varying the jet spacing on flow characteristics are investigated. At moderate spacing, the penetration decreases as the spacing is reduced. It is also observed that the vorticity structures of a jet within the row can be substantially different from those of an isolated jet. The penetration of rectangular jets from orifices having different aspect ratios is then studied. A quantitative analysis is carried out to examine the extent of mixing between the jets and the crossflow. The applicability of a correlation by Holdeman and his co-workers is extended to rectangular jets. The correlation yields information on the penetration at various values of jet spacing, confinement size, and jet-to-crossflow momentum ratio. Holdeman's correlation is also found to be applicable to a crossflow having a peaked non-uniformity in the velocity profile. The use of Holdeman's correlation indicates that, for a given mass flow from the jets, large jets at a low momentum can penetrate as far as smaller jets at a higher momentum. Furthermore, because of their low momentum, these large jets introduce a lower degree of flow non-uniformity in the mainstream.

Table of Contents

List of Tables

List of Figures

Nomenclature

SI units for all physical quantities

a_i	coefficients of finite difference equations
AR	aspect ratio of jet orifice ($= L/W$)
C_1,C_2,C_μ	turbulence model constants
C_e	convective flux through the east cell face
$\overline{d}$	defect or residual quantity
D	diameter of circular jet orifice
D_e	diffusive flux through the east cell face
$\hat{D}$,$\mathbf{D}(\mathbf{\Omega})$	diffusion term in the vorticity equation
$f(\xi)$	probability density function of ξ
$f_x(\xi)$	$f(\xi)$ computed at the streamwise location x
G	generation term of turbulent kinetic energy
$\tilde{G}$	grid used in the discretization of domain
H	dimension of the confinement facing a jet
I_H^h	prolongation operator for $\hat{s}$
I_h^H	restriction operator for $\overline{d}$
$\hat{I}_h^H$	restriction operator for $\overline{q}$
J	jet-to-crossflow momentum ratio
k	turbulent kinetic energy
L	length of jet orifice
L_x,L_y,L_z	dimensions of the domain in the single jet in crossflow simulation
$\mathcal{L}$	non-linear differential operator
L_h,L_H	discrete approximations to $\mathcal{L}$ on grids $\tilde{G}_h$ and $\tilde{G}_H$, respectively

L_{diss}	dissipation length scale
M	jet-to-crossflow mass flow ratio
p	pressure
P	modified pressure ($= p + \frac{2}{3}\rho k$)
$\hat{P}$	production term in the vorticity equation
Q_1	volume flow rate of the cross-stream
Q_2	volume flow rate of the jet
Q	solution vector
Q_h	discrete approximation to Q
q	approximation to Q_h
$\overline{q}$	smoothed version of q
$\hat{s}$	correction to $\overline{q}$
S	spacing between neighboring jet orifices
S_Ψ	source term in the transport equation for Ψ
S_P^Ψ,S_C^Ψ	coefficients of linearized source term
t	time
$\mathbf{U}$	velocity vector
U_1,U_2,U_3	Cartesian velocity components, also written as U,V,W in Eq.(3.1)
u_i	fluctuating velocity components
U_C	crossflow velocity far upstream of a jet
V_{jet}	jet velocity
W	width of jet orifice
x,y,z	Cartesian coordinates
y_{2d}	distance along y at which discrete jets have been merged to become effectively two-dimensional

Greek Symbols

δ_x	normalized standard deviation measuring the degree of mixing
δx_i	grid spacing
ϵ	dissipation rate of turbulent kinetic energy
Γ_Ψ	diffusion coefficient for Ψ
κ	von Karman constant
λ	dynamic mass diffusivity for Φ
	(= product of density [$\mathrm{kg\,m^{-3}}$] and kinematic mass diffusivity [$\mathrm{m^2\,s^{-1}}$])
μ	dynamic viscosity
μ_t	turbulent viscosity
μ_{eff}	effective viscosity ($= \mu + \mu_t$)
ν	kinematic viscosity
$\mathbf{\Omega}$	vorticity vector
Ω_x	x-component of the vorticity vector
Ψ	general variable
$\overline{\Psi}$	time-averaged component of Ψ
ψ	fluctuating component of Ψ
Φ	passive scalar, also denotes its fractional concentration value
ϕ	fluctuating component of Φ
Φ_{av}	fully mixed concentration value of Φ
ρ	density
$\sigma_k, \sigma_\epsilon, \sigma_\phi$	parameters in k, ϵ, and Φ equations

σ_x^2	variance of $f_x(\xi)$
σ_o^2	maximum variance computed before mixing
ξ	deviation of Φ from Φ_{av} $(= \Phi - \Phi_{av})$
ζ	porosity factor

Superscripts

c	coarse grid
j	generic index representing the stage of iteration
f	fine grid

Subscripts

C	value associated with the crossflow
cr	for critical spacing ratio
h	value associated with the fine grid
H	value associated with the coarse grid
jet	value associated with the jet
n,s,e,	
w,b,t	cell faces
P,N,S,E,	
W,B,T	grid points

Acknowledgement

I would like to express my sincere gratitude to the many individuals who have helped me in different ways during the course of my research. This study was carried out under the supervision and guidance of Professors Martha Salcudean and Ian Gartshore whose patience, sensitivity, encouragement, and contributions have been most helpful during the many trying moments. I would also like to acknowledge Dr. Paul Nowak and Dr. Zia Abdullah for teaching and sharing their insights on problems with numerical simulations. The code MGFD employed in this study was developed by Dr. Paul Nowak. The assistance of Mr. Mike Savage with the experiments and graphics, together with his sincere friendship, are whole-heartedly appreciated. The many stimulating conversations with Dr. Yacov Barnea have been enjoyable and often brought brightness into an otherwise monotonous day. The communications with Dr. Peri Sabhapathy, Mr. Paul Matys, Ms. Fariba Aghdasi, Mr. Steve Ketler, and Mr. Jeff Quick have been valuable in the understanding of flow phenomena in recovery furnaces. Finally, I wish to remember the fellowship I have been deeply enjoying with many friends at *CCC* whose support and care have helped me to journey through this period of my life.

The financial support for this study has been provided partly by NSERC, BC Science Council, and Weyerhaeuser Company Limited.

Chapter 1

Introduction : Simulation of Kraft Recovery Boilers

The objective of the present study is to investigate characteristics of jet interactions relevant to the design and operation of kraft recovery boilers. This type of boiler is central to a pulp mill because of its role in the kraft pulping process. Spent cooking fluid left after the pulping process is called black liquor; it contains inorganic chemicals such as phosphates and sulphates, as well as organic lignin. The purpose of a recovery boiler is to provide a medium both for the combustion of organic matter to produce heat energy and for reduction reactions to take place to recover valuable chemicals such as sulphides.

Most of the energy consumed by a pulp mill is generated by the recovery boiler. This, together with its role in recovering useful chemicals, makes it a very critical component in the kraft pulp mill. The operational efficiency of the mill is very dependent on the proper functioning and efficiency of the boiler. Thus, it is necessary to ensure that the combustion process within the boiler is efficiently carried out, with due regard to environmental requirements.

1.1 A Kraft Recovery Boiler

A detailed description of the physical and chemical processes that take place in a kraft recovery boiler can be found in the monograph by Adams and Frederick (1988). Additional design considerations can be found in Barsin (1989). The recovery boiler is a very large piece of equipment. The furnace section alone can have dimensions of 10 m width by 10 m length by 40 m height. A schematic representation of a typical boiler is

shown in Figure 1.1. The current design is the result of numerous modifications based on operational experience over the past several decades.

Two main sections constitute a kraft recovery boiler: a furnace and a convective heat transfer section. At the base of the furnace is the char bed which is formed by the accumulation of partially burned black liquor deposits. It is a design goal to maintain the bed at a high temperature for chemical reduction to take place. Another design goal is that, higher up in the furnace, mixing of black liquor with air and subsequent combustion should be completed. In addition, a substantial amount (about 40%) of the heat transfer from the combustion gas should also be completed in the furnace. Heat transfer to the boiler water which forms high pressure steam is then completed in the convective heat transfer section. The bullnose shown in Figure 1.1 shields the heat transfer surface from extreme conditions in the furnace, and its location is the general demarcation between the two main sections.

The furnace walls consist of numerous vertical tubes set in columns. Water is used as the heat absorbing agent. It is made to run in the tubes and receives heat from radiation due to the char bed and from gases in the furnace. Ports must be provided for introduction of air and liquor guns. These ports are formed by bending one or several wall tubes to the side. It is common practice to use ports in the shape of vertical slots so that a given port area can be obtained with the minimum number of bends in the tubes.

1.2 Recovery Boiler Air System

The requirement that a recovery boiler has both high chemical and thermal recovery efficiency leads to difficulties in designing a good air delivery system. The reason is that these two tasks can only be optimized in diametrically opposing environments. To maximize the recovery of inorganic chemicals, the smelting area of the furnace must be

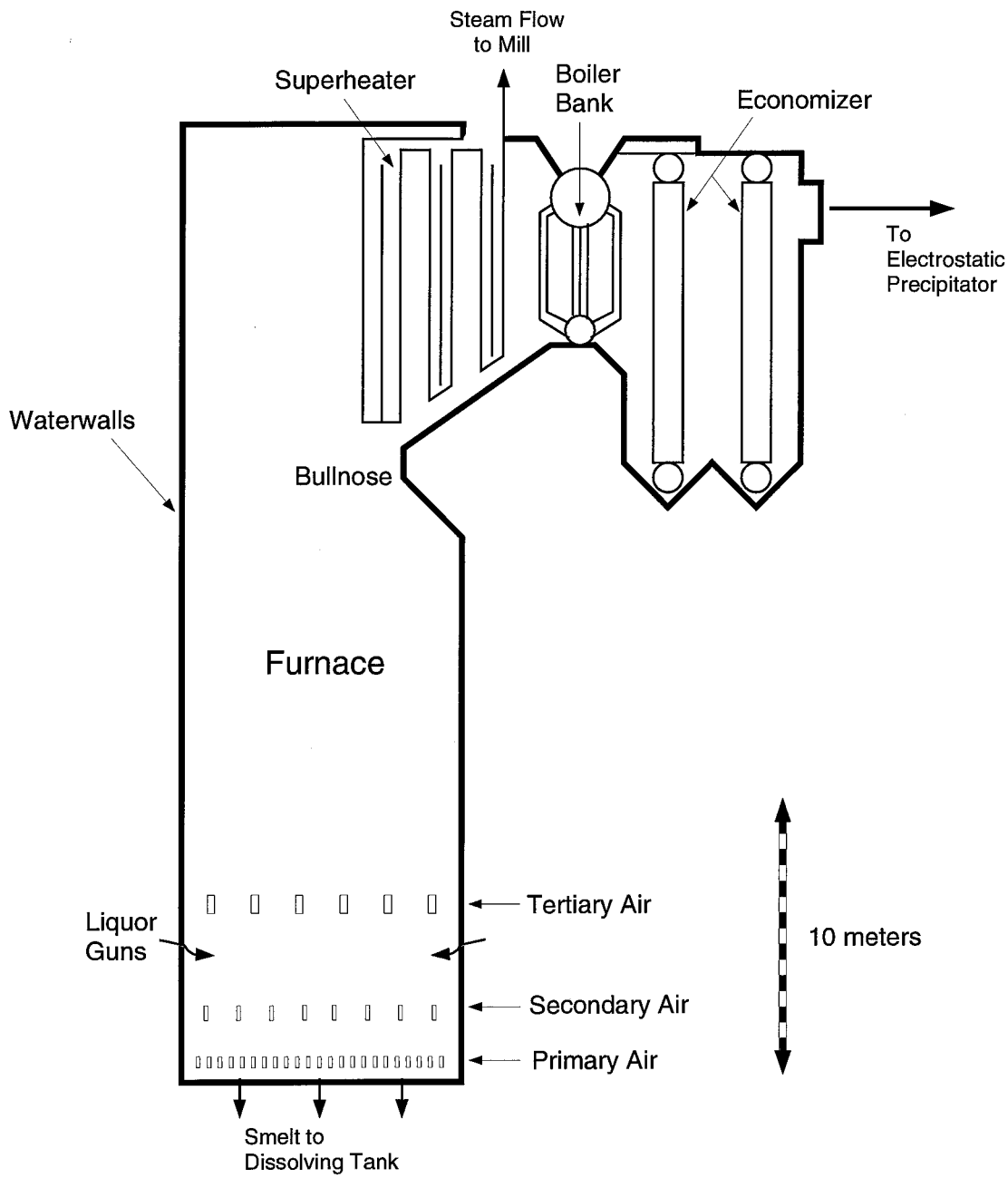

Figure 1.1: A schematic representation of a kraft recovery boiler.

in an oxygen deficient *reducing* atmosphere so that the inorganic chemicals recovered will be in a useful form for the pulping process – in the form of sodium sulphide instead of sodium sulphate. In contrast, to optimize the thermal efficiency of the unit, the organic material must be exposed to an oxygen rich *oxidizing* atmosphere where the combustible material can be burnt to completion and thereby liberates the required heat to produce steam.

As a result of these divergent process demands, the recovery boiler is divided into distinct zones and the introduction of air usually takes place at three different levels, as outlined in the following sections.

1.2.1 Primary Air

The primary air ports provide 30% to 50% of all air supplied. This maintains the reducing condition in the bed. Their sizes and locations are important to obtain a high reduction efficiency. Generally, these air ports are located on four walls approximately 1 m above the furnace floor. They supply air to maintain sufficient distribution of oxygen around the full furnace periphery. The air contributes oxygen for the carbon burnout which produces the heat for the reduction reaction to proceed.

1.2.2 Secondary Air

The secondary air ports are located above the char bed, which has a maximum height of about 1 m to 3 m above the primary air level. They provide up to 50% of the total air required and their role is to control the top of the char bed, since their momentum is sufficient to provide scouring across the top. The full penetration of these secondary air jets into the bulk furnace gas is critical for completing burnout low in the furnace, for breaking up the combustion gas cone, and for assuring mixing and combustion of the air with the volatile gases rising from the char bed.

1.2.3 Tertiary Air

The tertiary air ports are located 1.5 m to 5 m above the black liquor spray nozzles, which themselves are located 3 m to 7.5 m above the furnace floor. These air ports supply up to 30% of the total air required. They are usually located on only two walls. The momentum of jets developed at this level is critical: to complete combustion of the partially burned fuel components flowing up from the lower furnace; to complete the break up of the flame cone, and to insure oxygen availability throughout the upper furnace which eliminates unwanted sulphide gases. It is also the role of the tertiary air jets to aid in the establishment of a uniform flow profile and uniform heat distribution in the upper furnace tube banks.

1.2.4 Issues Related to the Air System

Concerns for the design of the air distribution system stem from the multitude of tasks the system is required to fulfill. In a recovery boiler, unlike many other combustion devices, the fuel, in the form of black liquor, and air are introduced separately. Good jet mixing is mandatory in these types of designs to obtain complete combustion. The size and number of nozzles at each level are mainly dictated by the amount of combustion air required. Other considerations do apply; for instance, the practical range of the quantity of air below the liquor gun is from 80% to 95% of the stoichiometric requirement for the liquor. This amount of air is used to ensure bed stability and to maximize bed temperature in order to improve reduction efficiency and SO_2 control. However, increased air in the lower furnace also increases the potential for entrainment of the char, which contributes to unwanted 'carryover' of char particles.

Considerations such as those mentioned above have created a need to predict the flow characteristics in a boiler unit. Although numerous studies have been carried out

to investigate the physics of fluid jets issuing into quiescent, co-flowing, or cross-flowing surroundings, most of the established observations for single jet and related correlations are not directly applicable to recovery boiler applications. In the monograph by Adams and Frederick (1988, p.158), the authors remarked that the use of single jet relationships leads to over-prediction of jet penetration due to the neglect of multiple jet interactions. Moreover, the non-uniformity of the crossflow could create additional complications in the prediction process. Thus, there is this need to investigate the flow field using experimental and numerical methods.

1.3 Simulation of the Recovery Boiler Air System

Many investigators have carried out experimental and numerical simulations to predict the effects of design changes on the aerodynamic characteristics inside a boiler. Experimental studies in scaled models running air or water have been carried out by Lefebvre and Burelle (1988), Chapman and Jones (1990), and Ketler et al. (1992,1993). These experimental investigations reveal valuable information regarding the flow patterns observed in boilers. For example, the results of the water model experiment by Ketler et al. (1993) show that the flow is often asymmetric and contains large regions of low frequency unsteadiness. However, measurement problems do cause difficulties in assessing the validity of the observation and complicated thermal-chemical processes are difficult or impossible to simulate in an experimental facility. Thus, in view of the rapid development of computational fluid dynamics (CFD), a numerical technique is an essential tool for predicting flows in recovery boilers.

It is necessary to apply numerical methods to compute the flow in a furnace because there is a lack of analytical techniques available for the prediction of complex jet interactions. A number of investigators have attempted to perform parametric studies using full

scale numerical models for the flow fields in kraft recovery boilers. The simulations by Uppstu et al. (1989), Grace et al. (1990), and Chapman and Jones (1990) used commercially available codes. In these simulations, certain simplifying assumptions were made in the representation of an actual boiler. For the purpose of fluid flow calculation, the shape of the domain may be simplified to that shown in Figure 1.2, where many complicated structures in the top exit portion of the boiler have been ignored. Much valuable insight has been gained through those simulations. For example, the results of Grace et al. and Chapman and Jones show that a simple isothermal model is adequate to capture the essential flow characteristics of a boiler.

Many difficulties have been experienced with these numerical simulations. It was found that even when all complex thermal and chemical processes were neglected, the full scale calculations for boilers were difficult to converge. A reason for this difficulty was the need to use a very large number of grid cells to represent the domain of the interior of the boiler. This problem arises due to large variations in dimensions that are found in a typical boiler. Recall that the furnace portion of a typical boiler has the dimensions of 10 m wide by 10 m long by 40 m high, while a secondary air port has dimensions of 5 cm by 25 cm in size. Thus, to resolve each of these ports within such a large domain, a very fine grid relative to the domain is needed. This requirement causes problems in both computational time and memory allocation. Moreover, the use of a fine grid also strains the performance of most common numerical solution techniques: slow convergence is to be expected and very often stalling in error reduction occurs.

Because of this lack of efficiency in standard numerical techniques for the study of large flow simulations of this type, our research group at UBC has been developing an algorithm that will deal with this type of problem more effectively. The algorithm uses a multigrid solution acceleration procedure together with segmentation capability to partition the domain for efficient calculation. Some details of the algorithm will be

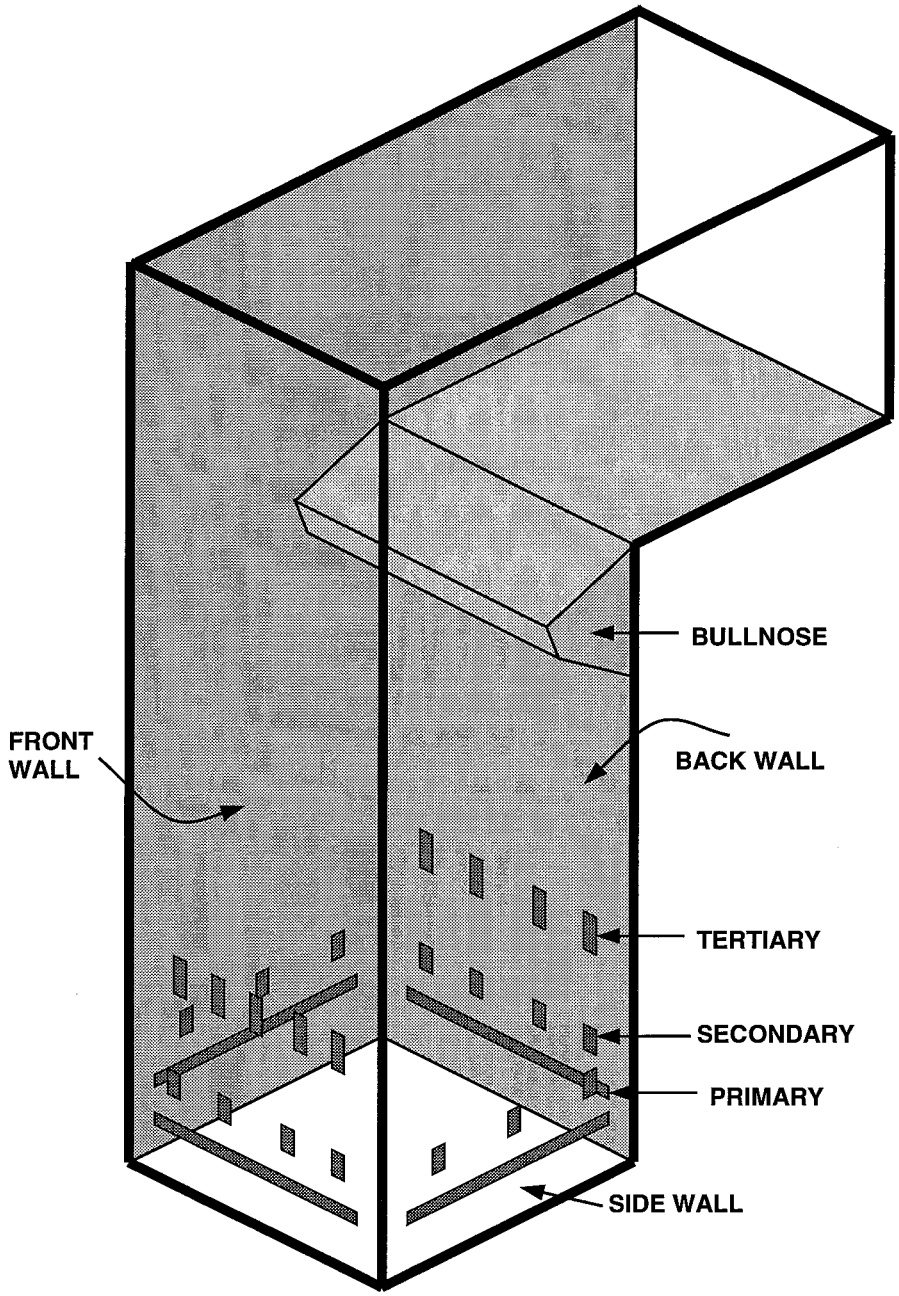

Figure 1.2: Domain of a recovery boiler used in numerical simulations.

described in Chapter 3. Preliminary results have been reported in Salcudean et al. (1992) and show fast convergence and promising robustness. Presently, the code has been used for isothermal flow simulations. A modified version that takes into account heat transfer and chemical reactions is under development.

Even with this improvement in numerical methodology, comprehensive full scale numerical simulation is still plagued with problems. At this stage of the development of the algorithm, a complete simulation of multiple jet interactions in a boiler still requires substantial computer memory and CPU time. This problem can certainly be improved in the future with better computer technology. However, a major short-coming with full scale simulation is that it can be difficult to decipher the effects of different flow parameters when they are subjected to variations. This difficulty is compounded by the long computation time involved for each simulation such that systematic parametric studies could become prohibitive. In view of this limitation of full scale numerical modelling, it is of great value to perform simplified flow simulations to study the basic flow characteristics of multiple jet interactions.

1.4 Merits of Simplified Studies

An obvious advantage with performing simplified jet flow studies is the large saving in computing resources so that more parametric cases can be investigated in a given amount of time. This advantage is utilized in the study of simulations for primary jets and in the systematic parametric investigation into the details and phenomena of multiple jet interactions in the presence of a crossflow. The results obtained can be related to the full scale problem if those simplifying assumptions made do not deviate too far from the phenomena in the full scale model. For example, in the study of multiple jets in a crossflow, parameters such as the jet spacing, jet size, jet momentum, and jet shape are

designed to vary systematically for the investigation of the effect on those parameters of jet penetration and mixing. These studies are carried out to identify trends that can be useful both for the understanding of observed phenomena and for future design considerations. With proper verification using the full scale simulation, such trends will be useful in providing guidelines for design. In addition, this parametric study can reveal aspects of jet dynamics such as the vorticity characteristics that often have been overlooked without such a detailed investigation.

Another important by-product from these simplified studies is that these comparatively small calculations provide good examples for the testing and debugging of our algorithm. This is particularly necessary since the application of the multigrid technique to equations representing turbulent flows has rarely been tested. The simulations involving jets in a crossflow provide flow situations with small enough domains so that only a moderate number of grid points is needed and yet the flow characteristics are complex enough to test the efficiency and robustness of the numerical algorithm. It has been found that the results of these computations provide experience that is necessary for the development of the algorithm and the calculation of more complex cases of full boiler simulations.

1.5 Objectives and Contributions of the Present Study

Most systematic studies on multiple jet interactions have been carried out on circular jets with application to the design of small combustion chambers. The specific needs of kraft recovery boilers, such as the use of rectangular jets and the presence of non-uniformity of the ambient flow, have seldom been addressed. In the present investigation, studies are carried out on the interaction of turbulent jets from rectangular orifices in simple geometrical domains. These lead to a better understanding of the complexities in

numerical modelling and in physical phenomena for kraft recovery boilers. The objectives of the present study are as follows: to investigate the interaction of multiple jets in the presence and in the absence of a crossflow using numerical methods; to investigate the interaction of jets similar to those found in a recovery boiler; to make recommendations for full boiler modelling; to carry out parametric studies on multiple jet interactions, and to identify trends for design considerations. The following results are obtained:

1. The application of the multigrid algorithm to obtain solutions of turbulent flow problems has been extensively tested. The performance of the algorithm has been examined for a variety of flows with turbulent jets. Some difficult cases have been identified and experience has been gained to improve the robustness of the algorithm. When the algorithm is implemented with precaution, it can return a fast convergence performance for the type of problems under study.

2. With the aid of the multigrid solution technique, the simulation of primary level jets is successful. Because these jets are closely spaced, they merge rapidly, which allows for their effective representation by using slot equivalences. The use of open slots and porous slots has been examined and it is observed that both representations yield good approximations to the velocity distribution.

3. The high efficiency of this solution technique has also allowed for a detailed parametric investigation on the characteristics of multiple jets placed in a row injecting into a crossflow. The variation of jet penetration with orifice spacing has been examined. Our mathematical model predicts that the vorticity characteristics of each jet in this row configuration will undergo unexpected changes as the jet momentum increases. This finding is of interest in clarifying and contrasting the dynamics of multiple jets versus a single jet in a crossflow.

4. A quantitative study of jet mixing has been carried out to clarify the effectiveness of jet mixing according to the extent of jet penetration into the cross-stream. It is also found that as the geometric parameters are varied, the changes in the jet mixing effectiveness are consistent with the corresponding decay rate of the stream-wise vorticity of the jet. This observation confirms the important role of vorticity dynamics on jet mixing.

5. The parametric study of a row of rectangular jets in a crossflow has confirmed the use of a semi-empirical relationship relating geometric and operational parameters for effective jet penetration and mixing between the jet fluid and the cross-stream fluid.

6. An application of this semi-empirical relationship has led to the realization that at a given mass flow rate, larger, slower jets can penetrate as deep into the cross-stream as smaller, faster jets. In addition, it is found that for interlaced jets interacting with a non-uniform crossflow having a peaked velocity profile, these larger jets operating at a lower momentum can satisfy the mass flow requirement and will create less flow non-uniformity downstream.

In the following chapters, attention will be focussed on a series of studies of multiple jet interactions, both with and without the presence of a cross-stream. First, a literature review on the dynamics of turbulent jets that are relevant to problems in kraft recovery boilers is presented. Secondly, the numerical solution algorithm employed in this study is described. Results and discussion of the simulations, together with the difficulties encountered, will be addressed in subsequent chapters.

Chapter 2

Dynamics of Turbulent Jets : A Literature Review

There have been many studies on the properties of jets in quiescent environments and in crossflows. The monographs by Rajaratnam (1976) and by Schetz (1980) provide a detailed description of the characteristics of many types of jet mixing phenomena. This chapter presents an overview of those aspects of jet dynamics that are relevant to the operation of kraft recovery boilers. Attention is limited to incompressible turbulent jets. For jets in quiescent environments, also known as free jets, the focus is on the flow characteristics which are affected by the orifice aspect ratio, the merging of multiple free jets, and flow stability. For jets in crossflows, the focus is on the flow properties that are characterized by jet penetration, the extent of mixing, and the extent of interaction between neighboring jets. These two common types of jets are found in kraft recovery boilers. Their respective physical characteristics are described in the sections to follow.

2.1 Mathematical Description of Jet Flows

The equations describing the flow of incompressible turbulent jets are the Navier-Stokes equations, which have the following vector form:

$$\nabla \cdot \mathbf{U} = 0 \tag{2.1}$$

$$\rho \left[\frac{\partial \mathbf{U}}{\partial t} + (\mathbf{U} \cdot \nabla)\mathbf{U} \right] = -\nabla p + \nabla \cdot (\mu \nabla \mathbf{U}) \tag{2.2}$$

In Cartesian tensor notation, the above equations become

$$\frac{\partial U_i}{\partial x_i} = 0 \tag{2.3}$$

and

$$\rho\left[\frac{\partial U_i}{\partial t}+\frac{\partial}{\partial x_j}(U_iU_j)\right]=-\frac{\partial p}{\partial x_i}+\frac{\partial}{\partial x_j}\left\{\mu\left(\frac{\partial U_i}{\partial x_j}+\frac{\partial U_j}{\partial x_i}\right)\right\} \tag{2.4}$$

These equations represent the conservation of mass and momentum within the fluid. In the above mathematical model, it is assumed that the fluid is Newtonian, has constant density ρ and molecular dynamic viscosity μ. Also, the effects of body forces have been neglected. These are valid assumptions for gas flow.

The equation governing the transport of a passive inert quantity by the fluid is

$$\rho\frac{\partial \Phi}{\partial t}+\rho\frac{\partial}{\partial x_j}(\Phi U_j)=\frac{\partial}{\partial x_j}\left\{\lambda\left(\frac{\partial \Phi}{\partial x_j}\right)\right\} \tag{2.5}$$

where Φ is the scalar concentration value and λ is the molecular diffusivity of the inert quantity. Examples of such quantities are propane and ethylene gases, which serve as markers in many flow experiments using air. In the above equation, it is assumed that the flux of the scalar is related to its spatial gradient through a Fourier-type law. Additional equations describing the energy balance may also be coupled with the above equations, although they are not considered in the present study.

To complete the description of fluid motion, we state the principle of conservation of angular momentum. This principle is expressed through the vorticity vector $\mathbf{\Omega}$, defined by

$$\mathbf{\Omega}=\nabla\times\mathbf{U} \tag{2.6}$$

The vorticity vector is transported by, and evolved in, the flow field according to the vorticity equation, which is obtained by taking the curl of the momentum equation (2.2). The result is

$$\frac{\partial \mathbf{\Omega}}{\partial t}+(\mathbf{U}\cdot\nabla)\mathbf{\Omega}=(\mathbf{\Omega}\cdot\nabla)\mathbf{U}+\nu\nabla^2\mathbf{\Omega} \tag{2.7}$$

where ν is the molecular kinematic viscosity. The left hand side of the above equation describes the convective transport of the vorticity vector. The first term on the right

hand side is customarily labelled the 'production' term for the vorticity, even though it only refers to the strengthening or weakening of the vorticity in a fluid element through the respective action of stretching or compressing that element. The last term in the equation refers to the diffusion of vorticity through the action of viscosity.

Time-Averaging

At high Reynolds numbers, a flow can be said to be steady only on an average basis, since small scale high frequency fluctuations are always present. In the precise numerical simulation of this type of flow, it is necessary to solve the full three-dimensional time-dependent form of the equations of motion with a very fine scale of resolution in order to capture small turbulent eddies. This is still beyond the capability of present technology for most practical problems.

A standard method of by-passing this stringent computational requirement is to introduce time-averaging to obtain equations for average quantities. The time-averaging process consists of decomposing a general variable Ψ into its mean component $\overline{\Psi}$ and its fluctuating component ψ as

$$\Psi = \overline{\Psi} + \psi \tag{2.8}$$

The time-averaged value, $\overline{\Psi}$, is defined as

$$\overline{\Psi} = \frac{1}{\Delta t} \int_{t_o}^{t_o+\Delta t} \Psi \, dt \tag{2.9}$$

where t_o is a reference point in time, and the average time Δt is greater than the longest time scales of the turbulent motion.

For non-reacting incompressible turbulent flows, it is justifiable to neglect fluctuations of fluid viscosity and density. After introducing the decomposition in Eq.(2.8) for the dependent variables in Eqs.(2.3-2.5) and time-averaging, the following set of equations

are obtained for a statistically steady flow:

$$\frac{\partial U_i}{\partial x_i} = 0 \tag{2.10}$$

$$\rho \frac{\partial}{\partial x_j}(U_i U_j) = -\frac{\partial p}{\partial x_i} + \frac{\partial}{\partial x_j}\left\{\mu\left(\frac{\partial U_i}{\partial x_j} + \frac{\partial U_j}{\partial x_i}\right) - \rho\overline{u_i u_j}\right\} \tag{2.11}$$

$$\rho \frac{\partial}{\partial x_j}(\Phi U_j) = \frac{\partial}{\partial x_j}\left\{\lambda\left(\frac{\partial \Phi}{\partial x_j}\right) - \rho\overline{\phi u_j}\right\} \tag{2.12}$$

where the overbars for the mean variables have been omitted for clarity.

These equations are similar to their instantaneous counterparts, if the instantaneous quantities are replaced by mean values, with the exception of extra terms $-\rho\overline{u_i u_j}$ and $-\rho\overline{\phi u_j}$ appearing respectively in Eqs.(2.11) and (2.12). These terms, known respectively as Reynolds stresses and turbulent scalar fluxes, consist of mean products of fluctuating components and arise from the averaging of the nonlinear convective terms in Eqs.(2.4-2.5). Physically, these terms represent diffusion of momentum or scalar quantities by turbulent motion.

For the vorticity equation (2.7), the procedure of time-averaging leads to the following equation form given by Sykes et al. (1986):

$$(\mathbf{U} \cdot \nabla)\mathbf{\Omega} = (\mathbf{\Omega} \cdot \nabla)\mathbf{U} + \mathbf{D}(\mathbf{\Omega}) \tag{2.13}$$

where all the variables listed above are the time-averaged quantities. The diffusion term, labelled $\mathbf{D}(\mathbf{\Omega})$, refers to the diffusive action on the vorticity due to the turbulent motion. It can be computed by subtracting the first term on the right hand side of Eq.(2.13) from the convective term on the left hand side.

Turbulence Modelling

To close the system of equations (2.10-2.12), the mean products of fluctuating quantities need to be related either to existing mean quantities or derived by solving additional

equations. A standard model which is widely used in applied research is the '$k - \epsilon$' turbulence model, where k stands for the turbulent kinetic energy, and ϵ denotes the dissipation rate of k.

The $k-\epsilon$ model is based on the eddy viscosity concept and its derivation was given by Launder and Spalding (1974). The model assumes the following relation for the Reynolds stresses:

$$-\rho\overline{u_i u_j} = \mu_t \left(\frac{\partial U_i}{\partial x_j} + \frac{\partial U_j}{\partial x_i} \right) - \frac{2}{3}\rho k \delta_{ij} \tag{2.14}$$

where k is defined as

$$k = \frac{1}{2}(\overline{u_1^2} + \overline{u_2^2} + \overline{u_3^2}) \tag{2.15}$$

The term involving the Kronecker delta on the right hand side of Eq.(2.14) ensures that the sum of the normal stresses is equal to $2k$.

The eddy or turbulent viscosity μ_t is related to definable quantities through the mixing length concept and dimensional reasoning. In this model, the expression for μ_t is

$$\mu_t = C_\mu \, \rho k^2/\epsilon \tag{2.16}$$

where C_μ is an empirical constant of proportionality.

The turbulent stress values can be estimated if values for k and ϵ are known. The equations governing the transport of these quantities are given by Launder and Spalding (1974) and written as

$$\rho U_j \frac{\partial k}{\partial x_j} = \frac{\partial}{\partial x_j}\left(\frac{\mu_{eff}}{\sigma_k} \frac{\partial k}{\partial x_j} \right) + \mu_{eff} \left(\frac{\partial U_i}{\partial x_j} + \frac{\partial U_j}{\partial x_i} \right) \frac{\partial U_i}{\partial x_j} - \rho\epsilon \tag{2.17}$$

and

$$\rho U_j \frac{\partial \epsilon}{\partial x_j} = \frac{\partial}{\partial x_j}\left(\frac{\mu_{eff}}{\sigma_\epsilon} \frac{\partial \epsilon}{\partial x_j} \right) + C_1 \mu_{eff} \frac{\epsilon}{k} \left(\frac{\partial U_i}{\partial x_j} + \frac{\partial U_j}{\partial x_i} \right) \frac{\partial U_i}{\partial x_j} - C_2 \frac{\rho \epsilon^2}{k} \tag{2.18}$$

The effective viscosity μ_{eff} is the sum of the molecular and eddy viscosities:

$$\mu_{eff} = \mu + \mu_t \tag{2.19}$$

The eddy viscosity μ_t also appears in the equation relating the turbulent scalar flux $-\rho\overline{\phi u_j}$ with the mean scalar gradient:

$$-\rho\overline{\phi u_j} = \frac{\mu_t}{\sigma_\phi}\frac{\partial \Phi}{\partial x_j} \tag{2.20}$$

The empiricism of the above model lies in parameters C_μ, C_1, C_2, σ_k, σ_ϵ and σ_ϕ. Launder et al. (1972) made extensive examinations of free turbulent flows to estimate values for these parameters. The values employed in this study are listed below:

C_μ	C_1	C_2	σ_k	σ_ϵ	κ	σ_ϕ
0.09	1.44	1.92	1.0	$\frac{\kappa^2}{(C_2-C_1)C_\mu^{1/2}}$	0.4187	1.0

Table 2.1: Parameters in the $k-\epsilon$ model.

To summarize, with the use of the $k-\epsilon$ turbulence model, the governing equations can be written in the following general form:

$$\frac{\partial}{\partial x_j}(\rho U_j \Psi) = \frac{\partial}{\partial x_j}\left(\Gamma_\Psi \frac{\partial \Psi}{\partial x_j}\right) + S_\Psi \tag{2.21}$$

Equations for continuity, momentum, species concentration, turbulent kinetic energy, and dissipation rate of turbulent kinetic energy are presented in Table 2.2, in terms of a general dependent variable Ψ, a diffusion coefficient Γ_Ψ, and a source term S_Ψ. In Table 2.2 the diffusion coefficient for scalar Φ is written as μ_{eff}/σ_ϕ by assuming that the values of both the laminar Schmidt number representing the ratio μ/λ and its turbulent counterpart, σ_ϕ, have values near unity, and that μ_t is usually much greater than μ in many flow situations.

This turbulence model is attractive because the equations for laminar and turbulent flows have the same form; only the diffusivity coefficients Γ_Ψ are calculated differently. Also, the model has been tested in a variety of flow problems and was found to be robust

Ψ	Γ_Ψ	S_Ψ
1	0	0
U_i, $i = 1,2,3$	μ_{eff}	$-\partial P/\partial x_i + \partial/\partial x_j[(\mu_{eff}(\partial U_j/\partial x_i)]$
Φ	μ_{eff}/σ_ϕ	0
k	μ_{eff}/σ_k	$G - \rho\epsilon$
ϵ	$\mu_{eff}/\sigma_\epsilon$	$(\epsilon/k)(C_1 G - C_2\rho\epsilon)$

$$P = p + \tfrac{2}{3}\rho k$$
$$G = \mu_{eff}[(\partial U_i/\partial x_j) + (\partial U_j/\partial x_i)](\partial U_i/\partial x_j)$$

Table 2.2: Terms representing the time-averaged Navier-Stokes equations with the $k - \epsilon$ turbulence model and a transport equation for an inert scalar.

in many cases. Despite the empiricism, the model gives, at least qualitatively, reasonable results in the majority of cases.

Having discussed a mathematical model for turbulent jets, attention is now turned to the properties of these jets based on experimental observations. The experience with this turbulence model applied to the flow field simulation of these turbulent jets will be described later in this chapter.

2.2 Jets in Quiescent Environments

Jets issuing into a relatively quiescent environment are found in many engineering applications. Some examples are jets used in thrust augmenting ejectors for VTOL aircraft and jets associated with air conditioning devices. Primary air system jets in kraft recovery boilers are free jets because there is little crossflow in the lower part of the furnace. We will first describe the characteristics of an isolated axisymmetric and rectangular jet. This will be followed by a description of multiple-interfering free jets.

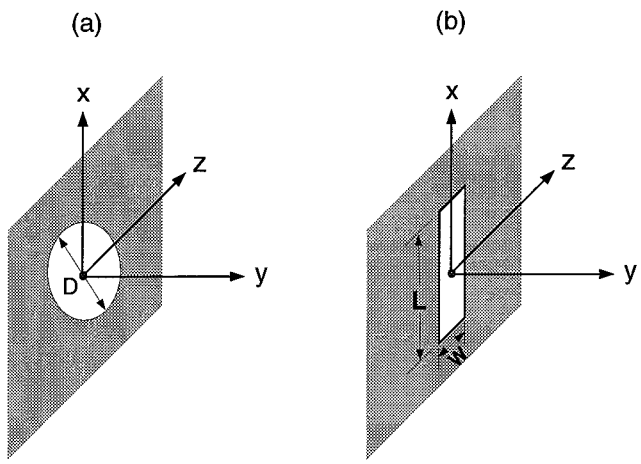

Figure 2.1: Orifices for (a) axisymmetric and (b) rectangular jets.

2.2.1 Axisymmetric Jets

Axisymmetric jets refer to jets issuing from circular orifices. They are the simplest type of free jets and their characteristics have been investigated in detail by Wygnanski and Fiedler (1969). The flow field characteristics depend upon the inlet geometry leading to the jet exit and the magnitude of the turbulence intensity at the jet exit plane. If the Reynolds number of the jet is high enough for fully turbulent flow to exist a short distance downstream from the jet exit, then the flow field is not dependent on the Reynolds number. The orifice for such a jet is shown in Figure 2.1(a).

Near the jet exit is the potential core region where the velocity is uniform since the mixing initiated at the boundaries has not yet permeated into the jet core. Downstream of the potential core, the jet is characterized by the momentum transported per unit time over each cross-section. By applying the principle of conservation of momentum and assuming similarity in the velocity distribution in the fully developed region of the jet flow, dimensional analysis shows that, at zero pressure gradient, the width of the jet is proportional to y and the center-line velocity decays as y^{-1}.

2.2.2 Jets from Rectangular Nozzles

The investigations by Sfeir (1979), Krothapalli et al. (1980), Marsters (1981), and Quinn (1991) reveal a wealth of information about the flow fields associated with rectangular orifices. A diagram of such an orifice is shown in Figure 2.1(b). The flow fields are more complex because of their three-dimensional nature. Nozzle shape and aspect ratio play a major role in the development of rectangular jets. When the decay of the axial mean velocity is used to describe the flow field, the flow is characterized by the presence of three distinct regions. These regions are the potential core region, a characteristic decay region, and an axisymmetric region. The characteristic decay region is influenced directly by the shape and aspect ratio of a slot or nozzle, and originates when the shear layers in the plane containing the short dimension of the nozzle meet. Correspondingly, the axisymmetric region originates approximately where the two shear layers in the plane containing the long dimension of the nozzle meet. A more detailed description of the flow field, together with graphical illustrations, can be found in the works of Sfeir and Krothapalli et al.

A prominent observation for this type of jet is the rapid spreading in the direction of the small dimension of the jet orifice. Sfeir describes this straining of the jet in the $x - z$ plane as due to the presence of vortex rings of elliptical shape surrounding the jet. The velocities induced by these vortex rings have also been suggested as the cause of the 'saddle-back' shape in the streamwise (y) velocity distribution along the spanwise (x) direction.

The effects of orifice aspect ratio on the flow and mixing characteristics for turbulent free jets issuing from sharp-edged rectangular orifices were examined by Quinn (1991). This is of interest to recovery boiler applications because slender orifices of different aspect ratios are often used. Quinn examined jets from sharp edged orifices with aspect

ratios 2, 5, 10 and 20. The results show that the saddle-shaped mean streamwise velocity profiles are present in many cases, especially when the aspect ratio is large. The saddle-shaped profiles are characterized by steep gradients which give rise to a high production of turbulence and thus facilitates effective mixing. The highest shear-layer values of the turbulent kinetic energy are found for the aspect ratio 20 jet. The hypothesis that mixing is more effective for high aspect ratio jets is supported by the far-field mean velocity decay rates, which are observed to increase with increases in slot aspect ratio. It is also supported by observing the lengths of the potential cores in various cases, which become shorter with increases in slot aspect ratio. Furthermore, the spreading rate of the jet, which is determined by the half-velocity widths in both central planes of symmetry, increases with increasing slot aspect ratio. This latter observation implies better far-field mixing and is consistent with the higher velocity decay rates.

2.2.3 Twin Jet Flow

The above description for a single axisymmetric or rectangular turbulent free jet reveals many interesting flow characteristics. However, in many applications, jets are issued in a multiple jet configuration where the interaction between neighboring jets can be significant. A basic unit of this multiple jet configuration is a pair of jets located side-by-side. A study of this flow can lead to some understanding of the nature of multiple jet interactions. A careful experimental investigation of the flow field associated with such twin jet flow was performed by Miller and Comings (1960). They studied subsonic turbulent slot jets at $V_{jet} = 22$ m/s which corresponded to $Re = 17800$ based on slot width. The slot spacing was $S/W = 6$, where W denotes the width of a slot, and S denotes the spacing between the slots. Under these conditions, the experimental results show that the flow is highly symmetrical about the symmetry plane between the pair of jets. This observation suggests that the lateral interaction of the jets does not cause

instability in the flow field. Another observation is that the entrainment in the confined region between the jets produces pronounce negative pressures in this region. Hence, the jet streamlines are deflected inwards as the jets are forced towards one another. Another consequence of the negative pressure in this confined region is that the momentum of the merged flow is less than the combined momentum of the flow emerging from the two slots. Downstream, the merged jets lose their individual identities and behave as a single two-dimensional jet with subsequent conservation of the remaining momentum.

The deflection of jets towards one another is significant only for slot jets. The investigation by Alexander et al. (1953) reveals that for a pair of axisymmetric jets, because the flow around the jets is vented to the surroundings, the jets are only slightly deflected towards one another and the downstream momentum is very nearly equal to the combined momenta of the jets.

2.2.4 Multiple Interfering Jets

Knystautas (1964) performed a comprehensive investigation on the interaction of multiple round jets in a quiescent environment. Figure 2.2 shows the configuration under study. The combination of such a row of jets was labelled a quasi-two-dimensional jet, and three values of jet spacings were examined: $S/D = 1.5$, 2, and 3, where jet diameter $D = 0.0127$ m (0.5 inches). Based on D, the Reynolds number tested range from 6090 to 52800. These values are large enough so that the flow field was insensitive to variation in the Reynolds number.

An important objective of the investigation was to determine the downstream distance from the jet exit plane where the amplitude of the undulating mean velocity profile had first decreased to the point where it could be considered, effectively, two-dimensional. Let this distance be denoted as y_{2d}, and as the following data from the investigation indicate, y_{2d} was found to increase with increasing jet separation.

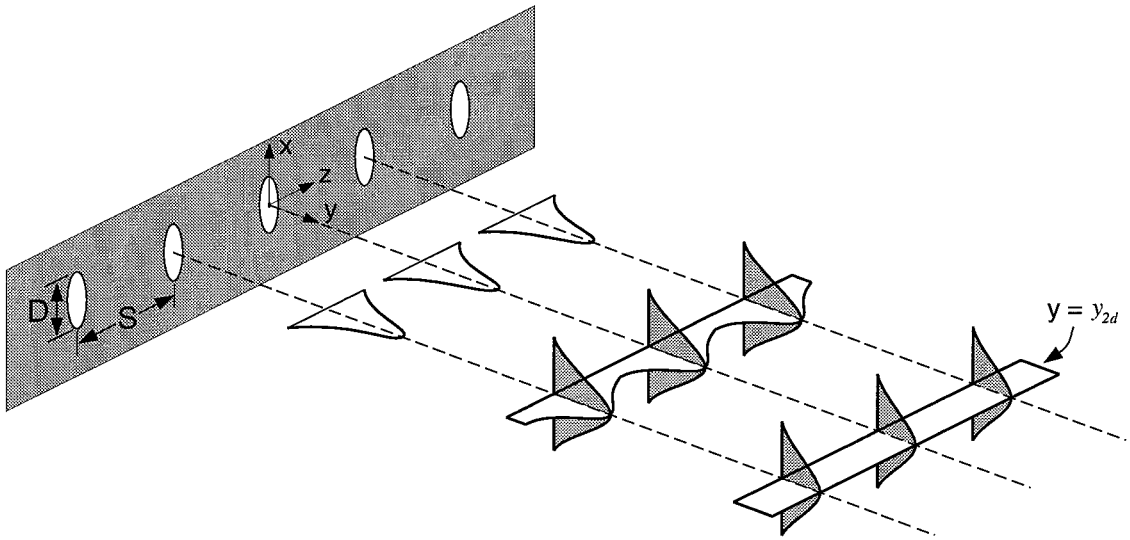

Figure 2.2: Development of a row of circular jets.

$$y_{2d}/D = 20 \quad \text{when} \quad S/D = 1.5$$

$$y_{2d}/D = 28 \quad \text{when} \quad S/D = 2.0$$

$$y_{2d}/D = 37 \quad \text{when} \quad S/D = 3.0$$

In the two-dimensional region of the quasi-two-dimensional jet, the streamwise velocity profiles are self-similar. In addition, the inverse square of the mean center-line velocity decays in proportion to the downstream distance, in accordance with the properties of a plane jet.

The turbulence characteristics of jets from an array of rectangular lobes were investigated by Krothapalli et al. (1980). The aspect ratio L/W of each lobe was 16.7 and the spacing $S/W = 8$, where $W = 3$ mm was the small dimension of a lobe. The mean jet velocity was 60 m/s corresponding to $Re = 12000$ based on W. For such a configuration, neighboring jets do not attract one another, each jet mixes with ambient air quite independently, and the jets merge completely for $y/W \approx 60$. In the downstream region

where the jets are merging, the interaction between the jets results in a lower turbulence level compared to a single jet at corresponding locations.

2.2.5 Primary Jets in Recovery Boilers

There are differences between primary jets in recovery boilers and the conditions studied in the above mentioned investigations. For instance, the primary jets are located on all four walls in a boiler so jets from adjacent walls may interact. Also, the presence of the char bed could affect the flow field by limiting jet penetration.

A study of multiple rectangular free jets was carried out by Sutinen and Karvinen (1992) with applications to kraft recovery boilers in mind. A non-isothermal calculation was performed to simulate the flow field for a row of jets in situations similar to those found for the primary level jets. The goal was to estimate where the two-dimensional assumption for the primary jet flow would be valid for their char bed simulation program. The jet velocity was 40 m/s at 400 K and the furnace temperature was 1200 K, while the bed surface temperature was 1500 K. The distance between adjacent nozzles was set at 0.5 m and the nozzle dimension was 0.10 m by 0.25 m. It was found that the primary jets merge almost completely at about 1.5 m from the injection plane. Sutinen and Karvinen then concluded that the gas flow above the char bed is effectively two-dimensional.

All the studies discussed have illustrated the fact that closely spaced jets will merge quickly not far from the exit plane. Therefore, it is feasible to numerically model primary jets by using suitable slot equivalences. The study of primary jet simulation using slots will be the subject of Chapter 4.

2.3 Single Jet in a Crossflow

Unlike primary jets, the higher level secondary and tertiary jets operate in an environment where there is a crossflow about the jets. This situation also occurs in many other types of engineering applications that include effluent dispersement, jets in combustion chambers, and jets for turbine blade film cooling. In this study, the crossflow is also labelled the cross-stream, mainstream, or main flow. The degree of crossflow uniformity and the importance of confinement varies for different cases. As well, the flow Reynolds number is different for different applications, and for subsonic flows this can range from slow laminar jets to higher speed turbulent jets. The Reynolds numbers of secondary and tertiary jets in a recovery boiler are high so that they are in the turbulent regime.

The basic features of a single jet discharged into a crossflow have been thoroughly studied and form the basis for the interpretation of multiple jets dynamics. Detailed review work can be found in Simitović (1977), Sherif (1985), and Blackwell (1990). In this section, we describe the phenomena associated with a single jet in a crossflow. Numerous experimental, analytical, and theoretical investigations have been performed by researchers to study the dependence of gross characteristics such as jet trajectory, penetration, and spreading on injection parameters. Detailed investigations have also been carried out on the nature of turbulent entrainment and mixing, as well as the characteristics of vortex structures associated with the jet. These results are outlined in the following subsections.

2.3.1 General Shape of a Single Jet in a Crossflow

The general appearance of a jet discharging into a crossflow is shown in Figure 2.3. As the jet is discharged into a crossflow, the jet path is deflected towards the direction of the main flow. This arises because the jet creates a blockage in the crossflow and

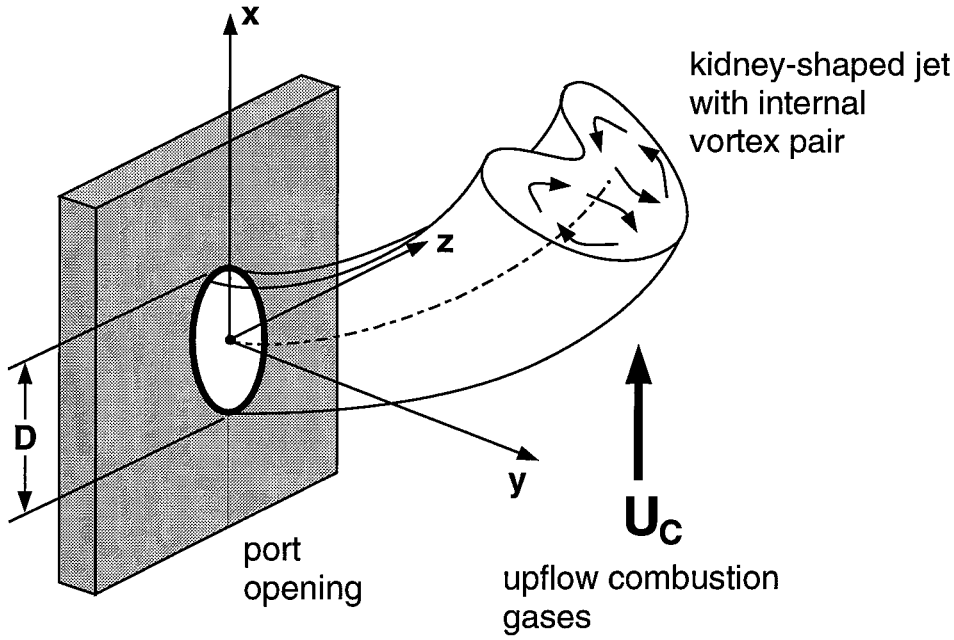

Figure 2.3: A schematic representation of a jet in a crossflow.

consequently, the flow immediately ahead of the jet decelerates, causing an increase in pressure. Downstream, a low pressure wake region occurs and this, combined with the increased upstream pressure, provides a force that deforms and bends the jet. The jet acts like an obstruction to the crossflow but the boundaries of the jet are compliant and entraining. The rapid entrainment of the cross-stream fluid into the jet also helps to push the jet over in the cross-stream direction because of the addition of momentum brought in by the entrained fluid.

It is well known that downstream from the orifice in the x-direction, the cross-section of an isolated jet assumes a kidney shape, as illustrated in Figure 2.3. The development of the kidney shape is a consequence of the intensive mixing between the jet fluid and the cross-stream fluid. The shear experienced by the jet, due to the crossflow, causes the formation of a turbulent shear layer. Peripheral particles of the jet, having less velocity than the particles of the core, are more forcefully bent by the deflecting flow away from

the initial direction and are moved along more curved trajectories. This movement of the peripheral fluid particles leads to the development of a kidney shape in the jet's cross-section.

2.3.2 Jet Trajectory and Penetration

Numerous experiments have been performed by researchers to study the penetration of a jet in a crossflow. The extent of penetration is usually inferred from the jet trajectory. An important parameter that affects the jet penetration is the ratio of the jet momentum to the cross-stream momentum, defined as

$$J = \frac{\rho_{jet} V_{jet}^2}{\rho_C U_C^2} \tag{2.22}$$

The investigation by Andreopoulos and Rodi (1984) reveals that for jets with $J \geq 4$, the jet path is only mildly affected at the exit and penetrates into the crossflow stream before it is bent over. The variation of the trajectory with injection parameters has been the subject of many studies. The details of experimental methods and results are found in Simitović (1977) and Blackwell (1990). A point to note is that the determination of jet trajectory can be different for different experimental methods employed. For experiments that use temperature measurements to locate the jet fluid, the trajectory is usually defined as the locus of the points of maximum jet temperature in the plane of symmetry defined by the jet orifice axis and the direction of the crossflow. When the velocity is measured, the jet trajectory is usually defined as the locus of points of maximum resultant velocity in the same plane as previously defined. With flow visualization experiments, the trajectory may be defined as the median line between the visible boundaries of the jet fluid.

The expression for the jet trajectory is usually correlated with the momentum flux ratio J. These various definitions for the jet trajectory lead to differences in the results

for the trajectory. For circular jets, in the case of normal jet injection into a relatively unconfined crossflow, the trajectories are found to be correlated with the following expression:

$$y = aD^b x^c J^d \tag{2.23}$$

where D is the orifice diameter, $a \approx 1$, $b \approx \frac{2}{3}$, $c \approx \frac{1}{3}$, and $\frac{1}{3} < d < \frac{1}{2}$. Dimensional analysis requires that $b + c = 1$, a constraint on the equation. If the injection angle is not 90°, then additional dependence on the angle has to be expressed.

Effects of Orifice Shape

The effect of orifice shape on jet penetration has been investigated by Hawthorne et al. (1944), Ruggeri et al. (1950), and Reilly (1968). These authors found that as the aspect ratio of the jet orifice increases, with the long side lying in the direction of the main flow, the penetration of the jet increases in many instances. This is due to the fact that as the aspect ratio increases, the rearward part of the jet is deflected less than the forward part. In addition, the area of the jet presented to the crossflow decreases and this can lead to a reduction in the drag force exerted by the crossflow on the jet. However, for a given value of J, there appears to be an optimum orifice aspect ratio which maximizes penetration. Exceeding this optimum value, the increase in shear forces due to the increased jet circumference nullifies the decrease in pressure forces due to the streamlining of the jet and as a result the penetration is reduced.

Effects of Inlet Velocity Profile and Turbulence Intensity

Simitović (1977) reported a study by Kamotani and Greber (1974) on the effects of turbulence intensity and velocity distribution in the incoming jet flow on the temperature and velocity trajectories. They compared two basic types of jet inlet structures,

one with a uniform velocity profile and 0.3% turbulence intensity and the other with a fully-developed pipe flow profile and a level of turbulence of 2.4% on the axis. They found that the penetration of the jets for the two cases differed by about 10%, which may be regarded as insignificant, but no details were given for the nature of the difference. It was not clear whether this effect was caused by the change of turbulence structures, or the inlet velocity profiles, or both.

2.3.3 Jet Width and Thickness

The width and thickness of a jet can be determined from flow visualization measurements, and together these two properties characterize the extent of the mainstream that is affected by the jet. The observations by Rajaratnam and Gangadharaiah (1981,1982) reveal that for the velocity ratio, V_{jet}/U_C, in the range from 2.7 to 23.4, the width and the effective thickness of the jet increase in proportion to the distance along the trajectory from the nozzle. Also, it appears that the kidney shape of the jet becomes less pronounced as the velocity ratio increases and the jet becomes more rounded far downstream. A number of empirical correlations describing the width, thickness, and the profile of the jet are presented in the review work by Blackwell.

2.3.4 Effects of Confinement

Confinement in either the lateral (z direction, Figure 2.3) or transverse (y) direction will limit the jet spreading and affect the characteristics of jets in crossflows. Impingement onto the wall facing the jet occurs if either the jet velocity is too high or the opposing wall is too close to the jet entrance. If there is no impingement, then it has been observed that the jet trajectory has little dependence on the extent of transverse confinement, and the correlation shown in Eq.(2.23) can be used to estimate the trajectory. The lateral confinement will modify the development of the cross-sectional shape of the jet.

2.3.5 Results from Detailed Flow Visualization

Up to this point, the discussion has been on the more easily observed properties concerning jets in crossflows. Attention is now shifted to the more detailed flow structures of a jet to obtain a better understanding of the mixing process.

The detailed flow visualization experiments performed by Fric and Roshko (1989) and Smith et al. (1993) reveal the nature of the intensive mixing between the crossflow and jet fluid. This intensive mixing, in most practical situations, is due to the flow being highly turbulent. Turbulence arises, in part, from the instability of the laminar shear layers at high Reynolds numbers which leads to a rapid formation of a turbulent shear layer around the periphery of the jet. Smith et al. (1993) showed many photographs displaying the intense instantaneous mixing caused by the pronounced large-scale intrusion of mainstream fluid around the jet periphery.

Downstream of the injection plane, the flow field is observed to be dominated by several vorticity structures. These vortex systems are believed to affect the entrainment and mixing characteristics between the jet and the cross-stream. Fric and Roshko (1989) provided detailed visualizations of the near-field and identified four main vorticity structures which comprise the flow. They are as follows:

(a) Distorted shear layer ring vortices at the circumference of the bending jet.

(b) The inception of the counter-rotating pair of vortices which eventually dominates the far field jet structure.

(c) A system of horse-shoe or collar vortices at the crossflow wall.

(d) A system of wake vortices nearly aligned with the initial jet direction.

It is commonly believed that the vorticity structures (a) and (c) have only a small influence on the shape or global behavior of the jet. The shape of the jet is influenced mainly

by the system (b). The mixing of jet fluid and cross-stream fluid can be influenced by both systems (b) and (d).

A key observation made by Fric and Roshko (1989) is that most of the source of the wake vorticity is in the crossflow boundary layer. The crossflow boundary layer separates at the downstream side of the jet to subsequently feed the wake. The fact that the wake vorticity comes from the crossflow boundary layer fluid and not from the jet fluid is of significance when considering the mixing in this flow. This observation suggests that, although the wake region is highly turbulent, it does not add substantially to the mixing of crossflow fluid with jet fluid; the wake contains essentially no jet fluid. This was quite contrary to some long held hypotheses about the wake vortices being shed from the jet, and this observation had been subsequently confirmed by Smith et al. (1993). The latter investigators applied a planar laser-induced fluorescence visualization technique which allowed for a very detailed examination of the instantaneous structure and mixing of a jet in a crossflow. They observed that only a very small amount of jet fluid could enter the wake through wake vortices in the region of the jet that was undergoing curvature.

The above results elevate the importance of the role of the counter-rotating vortex pair in contributing to the mixing between the two fluid streams. In addition, Kulisa et al. (1992) suggest that this vortex pair is responsible for the particular jet cross-sectional shape and the vortex motion serves to transport fluid around the perimeter of the jet and hence facilitates mixing. The discussion in the next section is focussed on this vortex pair because of the significance of its dynamics.

2.3.6 The Counter-Rotating Vortex Pair

The counter-rotating vortex pair is a remarkable characteristic of a jet in a crossflow and has been examined by many investigators. Its origin was discussed by Andreopoulos and Rodi (1984): the vortex pair evolves from the shear layer vorticity of the jet; that is, its

source is in the vorticity issuing from the nozzle. As most of the vorticity issuing from the pipe is reoriented and stretched by the flow, it bundles up into a pair of vortex tubes bound to the lee side of the jet and accentuates the kidney shape of the jet.

The vorticity generated in the jet is propagated downstream by the jet and intensified by the interfacial shear of the initially orthogonal jet and the crossflow stream. This vorticity is also diffused by the turbulent transport process as shown in the vorticity equation (2.13). The characteristics of this vortex pair have been examined by many researchers. Fearn and Weston (1974) correlated the vortex strength with different injection rates and positions along the jet path. Their empirical model was used to build a description of the velocity field in a cross-sectional plane. The observations by Rathgeber and Becker (1983) reveal that the maximum concentration in the jet is at the centers of the two vortices and can be 30% to 75% higher than the concentration on the jet axis. By assuming that the centers of the two low-pressure cells correspond to the centers of the two vortices of the bound vortex system, Rajaratnam and Gangadharaiah (1983) developed correlations for the maximum pressure defect, the separation distance, and the radial distance of the vortices from the axis of the deflected jet. Recently, the detailed visualization results by Smith et al. (1993) reveal that the transient development of the counter-rotating vortex pair can be non-symmetric with significant undulations in the streamwise direction. The variation in the vortex strengths between the vortex pair is proportional to the velocity ratio. The two ends of the kidney profile oscillate at a wavelength comparable to the local jet diameter.

Results for the vortex pair have also been obtained by numerical methods. Using a version of the Reynolds stress closure model, Sykes et al. (1986) showed that the evolution of the vortex pair is from the original vorticity in the sides of the jet. This result is obtained by noting the Lagrangian distortion of vortex lines through the calculation of their trajectories in the three-dimensional vector vorticity field. For impinging jets in a

crossflow, the numerical results by Catalano et al. (1989) using the $k - \epsilon$ model show the persistence of the vortex structure even after impingement.

2.3.7 Turbulence Characteristics

The turbulence characteristics of a jet in a crossflow have been investigated by many researchers. This type of flow field is an example of a complex free turbulent shear flow. The primary goal of these investigations is to examine the structure and characteristics of velocity fluctuations. The data could also be used to guide the development, improvement, and evaluation of better prediction methods and turbulence models for this type of flows.

In relation to mathematical modelling of turbulence characteristics, the experimental results have provided insight into the applicability of turbulence viscosity models such as the one indicated by Eq.(2.14). The results of Andreopoulos and Rodi (1984) show that not all components of the Reynolds stress tensor can be described realistically by a scalar turbulence viscosity model. Specifically, the component which influences the lateral spreading of the jet may not be described well by the simple effective viscosity concept. More favorable results were reported by Pietrzyk et al. (1988) for jets inclined to the direction of the cross-stream. They found coincident peaks in the mean velocity gradient and the turbulent quantities. This points to the possible use of a turbulence viscosity model for this type of flow field. The turbulence field for an impinging jet in a crossflow has been studied by Catalano et al. (1989), who found that the turbulence field was highly anisotropic in the initial region, although there were tendencies towards isotropy further downstream. This latter result suggests that a turbulence model which takes anisotropy into account is needed for the accurate prediction of the flow field in the initial region.

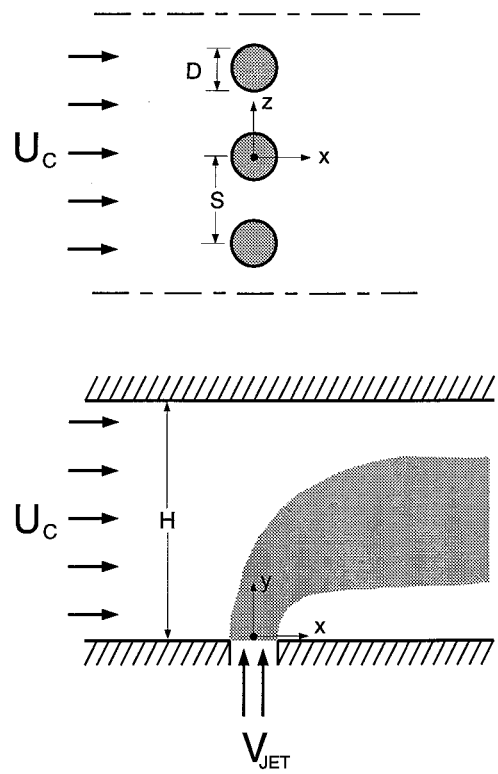

Figure 2.4: A schematic view describing a row of jets discharging into a confined crossflow.

2.4 Multiple Jets in a Crossflow

Experimental evidence shows that for multiple jets in a crossflow, each jet behaves individually until just before merging. The configuration is depicted in Figure 2.4. The understanding acquired for a single jet in a crossflow cannot be applied directly to multiple jet configurations, due to the complexity introduced by jet interaction. Nevertheless, the characteristics of the single jet case may still be useful to interpret some of the observations for multiple jets. This section describes some of the relevant background material in the study of a row of jets discharging into a confined crossflow.

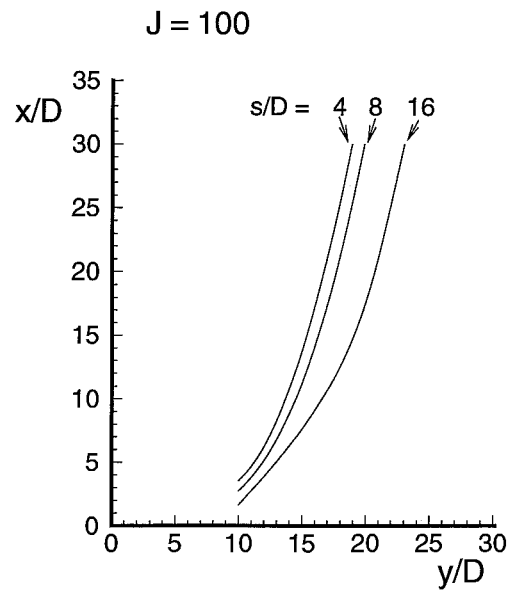

Figure 2.5: Effect of jet spacing on jet trajectory, $J = 100$, Ivanov (1959).

2.4.1 Effects of Varying Jet Spacing and Momentum Ratio

An early investigation into the penetration of a row of jets, when the spacing between jets varies, was made by Ivanov (1959) and his results are quoted by Niessen (1978). The trajectories of jets at $J = 100$ were measured for jet spacings of $S/D = 4$, 8, and 16, and the results are illustrated in Figure 2.5. No details were given for the dimension of confinement H. A notable decrease in the jet trajectory is observed as S/D is reduced from 16 to 8. The interpretation by Niessen suggests that as the jet spacing is reduced, the jets merge into a curtain, like that produced by a plane jet. It appears that the blockage effect of the curtain impedes the flow of the cross-stream around the jets and increases the effective deflecting force due to the crossflow. There is only a minor reduction in the trajectory as the jet spacing is reduced from 8 to 4. This observation is due to the apparent rapid merging of jets close to the injection orifices already occurring at $S/D = 8$.

NASA sponsored a series of systematic investigation into the characteristics of multiple jets in a crossflow. The applications were aimed at the design of air mixing systems for combustion chambers but, because the experimental conditions were turbulent, the results should also be applicable to other systems of turbulent flows having different physical dimensions.

Kamotani and Greber (1974) studied the dynamics of multiple jets in a linear array when the spacing S between jet nozzles and the confinement height H were varied. The arrangement of this jet configuration is shown in Figure 2.4. The values of J ranged from 8 to 72 and jet spacings were 2, 4, 6 and 10 nozzle diameters. In their work, they defined the center-plane jet trajectory as the locus of maximum speed at each cross-stream plane intersecting the jet center-plane. They evaluated the penetration in different cases by comparing those jet trajectories. Results that are relevant to jet penetration are summarized as follows:

(1) At very large jet spacings, $S/D > 10$, each jet behaves independently and the effect of neighboring jets is minimal. Also, the jet penetration is not sensitive to the extent of the confinement.

(2) At moderate jet spacings, $10 > S/D > 2$, the jet penetration is only mildly affected by the presence of a confinement.

(3) At the close jet spacing $S/D = 2$, the jets merge rapidly and the resulting flow field resembles that of a slot jet. The penetration depends strongly on H.

(4) There is a monotonic decrease in penetration as S/D is reduced until a critical value $(S/D)_{cr}$ is reached.

Their results on jet penetration are displayed in Figure 2.6, and they are consistent with those of Ivanov (1959). The results indicate that there is increasing jet deflection

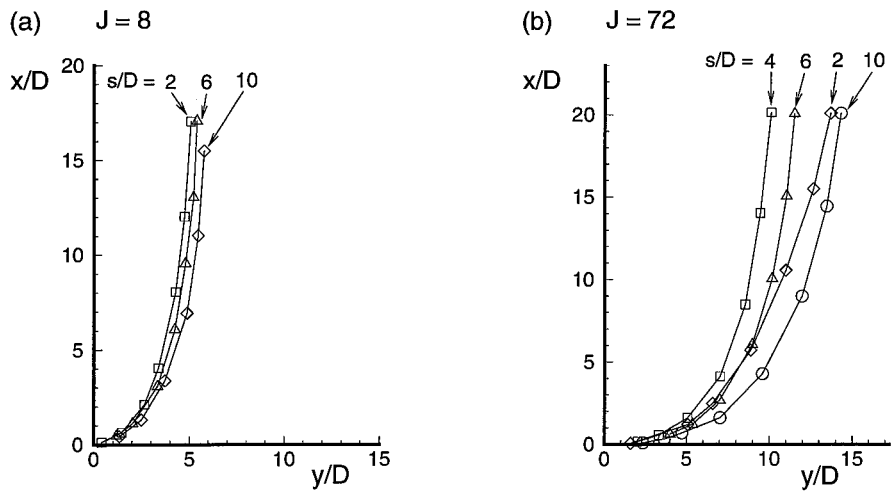

Figure 2.6: Effect of jet spacing on jet trajectory, $H/D = 24$, $J = 8$ and 72, Kamotani and Greber (1974).

by the crossflow as the orifice spacing decreases until a certain critical value is reached. Kamotani and Greber offered an explanation based on the interaction of vorticity of neighboring jets. As discussed earlier, in the far field, a jet in crossflow may be represented by a pair of counter-rotating vortices. The interaction of neighboring vortices from two neighboring jets has two effects. First, the vortex strength of each jet will be reduced due to cross diffusion of vorticity of opposite signs. Secondly, the velocity field induced by each vortex will drive its neighboring vortex down towards the injection wall. This results in less penetration of each jet. Thus, the trajectories of a row of jets will become more deflected as the spacing ratio decreases. This hypothesis was numerically verified by Huang (1989), who took the velocity field induced by the counter-rotating vortex system into account in his calculations.

Kamotani and Greber suggested that when the jet spacing is below the critical value $(S/D)_{cr}$, the jets start to interfere with the entrainment of cross-stream fluid of their neighboring jets. This interference results in a lack of entrainment by each jet and consequently a slower decay of the initial momentum flux in the y direction of the jet.

This slower decay, together with the increase in the momentum flux per length of the array of jets as the spacing becomes smaller, cause the jets to be more resistant to the deflection by the crossflow. The value of the critical spacing ratio $(S/D)_{cr}$ was found to increase with J. They estimated that $(S/D)_{cr} \approx 2$ for $J = 8$ and $(S/D)_{cr} \approx 4$ for $J = 72$.

2.4.2 More Comprehensive Parametric Variations

A comprehensive study of the effects of geometric and operational parameters on the jet penetration and mixing of multiple cold air jets into a ducted subsonic heated mainstream flow was performed by Walker and Kors (1973) and Holdeman and Walker (1977). The application was for air jet mixing in combustion chambers. In their experiments, the momentum flux ratio J ranged from 6 to 60. A variety of jet configurations and flow conditions were tested, which include the variation of orifice size, orifice spacing, extent of transverse confinement (H), and different levels of turbulence in the cross-stream. In their experiments, the spacing ratio S/D ranged from 2 to 6 while the confinement ratio H/D ranged from 4 to 16. The mixing effectiveness for different cases was assessed by examining the uniformity and skewness of temperature distributions at positions downstream of the injection orifices. The main results are summarized below:

(1) Single jet correlations do not adequately describe multiple jet results.

(2) The jet to mainstream momentum ratio is the single most important operating variable influencing jet penetration and mixing.

(3) The absolute momentum flux level does not influence jet penetration or mixing significantly.

(4) The effect of the turbulence level on jet penetration and mixing was insignificant within the range of turbulence levels examined.

(5) The spacing between orifices has a significant effect on lateral spreading of the jets, jet penetration, and jet mixing. Closely spaced orifices ($S/D = 2$) inhibit jet mixing.

(6) For both low and high momentum flux ratios, temperature center-line penetration depth does not increase significantly with increasing x/H beyond a short downstream distance. Instead, a flattening of the temperature profile occurs with increasing x/H for both low and high momentum flux ratios.

(7) The temperature profile does not change shape if S/H and J are held constant and the orifice diameter is varied. Only the magnitude of the temperature distribution changes.

Item (6) is important for the establishment of the following mixing criterion for combustion chamber application: effective mixing between the jet and the mainstream is achieved when the jet penetrates to approximately half way across the chamber as rapidly as possible. This objective serves to establish a symmetrical temperature distribution profile across the width of the chamber. The action of turbulence mixing flattens the temperature profile so that a uniform distribution is found downstream. The observation stated in item (7) is significant. It suggests that for a given momentum flux ratio, there exists a value of S/H such that nearly even temperature distribution across the chamber can be achieved, with the distribution not skewing too much to one side of the chamber or to the other. The hole size may then be chosen based on the desired jet mass-flow-rate.

The fact that a consistent mixing profile can be obtained when S/H and J are held constant suggests that a correlation involving these quantities can be derived to lead to a desirable temperature profile or mixing profile based on the criterion explained in the last paragraph. Such a correlation was developed by Holdeman et al. (1984), by examining the experimental results from various cases. They observed that at a given

jet-to-mainstream mass flow ratio, similarity in the temperature profiles in the $x - y$ plane can be obtained, independent of orifice diameter, when the spacing to confinement ratio S/H is inversely proportional to the square root of the momentum flux ratio. In other words, a consistent extent of jet penetration is obtained when the parameters S, H and J are related by

$$\frac{S}{H} = \frac{C}{\sqrt{J}} \tag{2.24}$$

For their results with cooling jets in a hot crossflow, they found that a value of $C = 2.5$ leads to a jet fluid distribution that is approximately centered across the channel height. A value of $\frac{S}{H} \cdot \sqrt{J}$ that is a factor of two greater or smaller than this optimal value will result in over-penetration or under-penetration, respectively. The observation that the spacing and momentum flux ratio can be coupled in such a simple way for optimal penetration is useful. It allows for a simple estimation of the penetration and mixing performance. Equation (2.24) also illustrates that it is more appropriate to use large widely spaced jets at low momentum flux ratios, while small closely spaced jets are more appropriate at high momentum ratios.

Extension of the above jet mixing study to two-sided injection was carried out by Holdeman et al. (1984). The results of their experiments support the hypothesis that a configuration that mixes well with one-side injection performs even better when every other orifice is moved to the opposite wall. That is, two-sided injection with jets staggered relative to those in the opposing row could give rise to very rapid and effective mixing with the cross-stream.

2.5 Prediction Methods for Turbulent Jets

The complexity of the flow fields associated with turbulent jets causes difficulties with predictions. This complexity increases when multiple jets are involved. Many of the

available prediction methods are summarized and presented in Rajaratnam (1976) and Demuren (1986). These methods may be divided into three broad classes, as empirical, analytical, and numerical, in ascending order of computational complexity. Each of these methods will be briefly discussed.

2.5.1 Empirical Models

The development of empirical models depends largely on the correlation of experimental data for properties such as jet penetration and spreading. The accuracy of the model is valid within the range of the database used for the correlation. Empirical models have been used often for the determination of jet trajectory for a single jet in an unconfined crossflow. The trajectory correlation given in Eq.(2.23) is an example of this type of model. Besides jet trajectory, characteristics such as the jet width, mean velocity profile, and mean concentration profile have all been empirically correlated for a single free jet and a single jet in a crossflow. These models offer simple methods to obtain first-order estimates and a qualitative picture of the evolution of the jet structure as it leaves the orifice.

2.5.2 Analytical Models

Analytical models refer to the group of models where physical phenomena associated with the flow are modelled with mathematical relations which are empirical to varying degrees. These relations are then used to simplify the governing differential equation system such as in Eqs.(2.10-2.12). A loose criterion for a model to be under this classification is that there should not be too much computing effort required to solve the simplified equation system.

An example of analytical models can be found in the theoretical predictions for the shape of the mean velocity profile of an axisymmetric turbulent free jet. The classical

results by Tollmien (1926) and Goertler (1942) were obtained by assuming characteristics of the turbulence. Tollmien applied the mixing-length hypothesis for the determination of the Reynolds stress while Goertler assumed that the eddy viscosity μ_t relating the Reynolds stress to the mean velocity gradient to be proportional to the product of the center-line velocity and the half width of the jet. Their results compare well with experimental data.

Demuren (1986) presented examples of analytical models used in the prediction of jet trajectory for a jet in a crossflow. In these examples, integral equations are derived either by considering a balance of forces acting over an elemental control volume of the jet or by integrating in two spatial directions of the three-dimensional partial differential equations governing the turbulent jet flow. The resulting set of ordinary differential equations can then be solved analytically or numerically. Empirical relations are needed for physical phenomena such as pressure drag, entrainment of cross-stream fluid, and spreading rates. Because of the use of integral equations, these models presented by Demuren are called integral models. With ingenuity and experience, good comparison between predictions and experimental results can be obtained as well as insight into the nature of the flow.

Another variant which may be considered an analytical model is the inviscid three-dimensional vortex sheet model for the problem of a jet in crossflows. This prediction method is favored by some applied mathematicians where certain characteristics of the flow field are assumed to simplify the equation set. In this vortex sheet model, the flows within and without the jet are assumed to be potential and the boundary between them is assumed to be a vortex sheet. The aim is to explain the mechanism responsible for the deflection of the jet and the evolution of vortices. Usually, the perturbation method is used to analyze the equation set where the perturbation parameter is the ratio of crossflow speed to jet speed, and this parameter is assumed to be small. Applications of the technique are found in Needham et al. (1988) and Coelho and Hunt (1989). The

latter group used an empirical formula to include the effects of turbulent entrainment to study the dynamics of the near field of strong jets in a crossflow. Their analytical and experimental results show that turbulent entrainment and the transport of the transverse component of vorticity largely control the dynamics of the jet and its bounding shear layer in the near field of strong jets in a crossflow. In particular, they found that the diffusion of vorticity into the wake is weak and therefore the jet does not act on the crossflow like a bluff body. The dominating mechanism for jet deflection is entrainment rather than the pressure-drag effect. Such insight would be difficult to obtain using other methods.

2.5.3 Numerical Models

A more realistic modelling of a complex three-dimensional jet flow is through the use of numerical models. Prediction methods based on numerical models involve the solution to the partial differential equations governing the turbulent transport of mass or species concentration. Usually, the time-averaged form of the equations is solved using the finite difference technique. Turbulence models are required for closure of the equations and these models usually follow from the eddy-viscosity concept. Other turbulence models are available. Full Reynolds stress modelling and large eddy simulations are frequently employed in turbulence research. The next chapter is devoted to a discussion of a numerical methodology that is used in the present study.

The attractiveness of numerical models stems from the fact that no assumptions are required for the evolution of the jet within the flow domain, but this evolution is obtained as a result of the computations. The complexity of interactions among multiple jets makes numerical models the only suitable means for prediction. The accuracy of the results are dependent upon the quality of the mathematical model employed in the representation of the physical phenomena, the discretization scheme chosen, and the

treatment of boundary conditions. A popular model used in the practical numerical simulation of turbulent jets is the $k - \epsilon$ model described in section 2.1. The following section discusses the applicability of such a model.

2.6 Application of the $k - \epsilon$ Model to Jet Flows

As mentioned earlier in section 2.1, the two-equation $k - \epsilon$ model was derived based on simple turbulent flows such as boundary-layer type shear flows. The model may need modifications before it can be used to analyze free jets or jets in crossflows.

For free jets, McGuirk and Rodi (1977) applied a modified form of the $k - \epsilon$ model in the parametric study of the flow field due to a single rectangular jet emitted from different orifices having the same size but with different aspect ratios. A modification was made to the empirical parameter C_1 (see Table 2.1) in the ϵ-equation to reflect the observation that the velocity decay rate affects the scale of turbulence eddies of the jet. The prediction of the velocity decay rate was good, but some finer flow features such as the saddle-back velocity profile were not captured. Unfortunately, the extension of this modification to the configuration of multiple jets is not simple. Some investigators like Sutinen and Karvinen (1992) used the standard $k - \epsilon$ model for the prediction of the flow field due to multiple jet interactions.

There have been other studies on the applicability of the standard $k - \epsilon$ model to the problem of jets in crossflows. An example is the study by Jones and McGuirk (1979), who computed a round turbulent jet discharging into a confined crossflow. It was found that there was good agreement for the gross features of the flow, such as the area of mixed fluid, the rate of jet dilution, and the jet trajectory. Results from other investigations prior to 1984 were summarized by Demuren (1986) who showed many good qualitative agreements between numerical predictions and experimental data. In addition, specific

verification studies were carried out by Claus (1985), Barata et al. (1988), and Claus and Vanka (1990) to study the errors due to numerical discretization and the $k-\epsilon$ turbulence modelling. The general conclusion is the same, namely that the two-equation model is generally adequate in predicting the gross features of the flow field such as jet penetration.

However, the study by Claus and Vanka also pointed out that the model increases the effective viscosity of the fluid in the region near the jet entrance. This increased viscosity works to damp-out any small scale structures such as horse-shoe vortices that may form. Moreover, the turbulence levels were generally underpredicted in comparisons with data. Nevertheless, as stated by Claus and Vanka, the results of their comparisons for the turbulence intensity levels do not invalidate the use of a two-equation model for this jet-in-crossflow geometry, even though the effect of counter-gradient transport as reported by Andreopoulos and Rodi (1984) was not accounted for by the model.

2.7 Chapter Summary

We have presented a brief description of a number of established results that are relevant to the study of air jet dynamics in a recovery boiler. Concerning the interaction of multiple free jets in an array, the results show that the jets merge relatively quickly and that the lateral attraction caused by a decrease in pressure between each pair of jets is not likely to be significant enough to cause flow instability. These results are valuable in our study of the proper modelling of primary level jets in a boiler.

For the complex problem of multiple jet interactions with a crossflow, numerical techniques appear to be the only viable means for the prediction of the flow field. Numerical solution methods have become more feasible with improvements in algorithms and computer technology. The use of the $k-\epsilon$ model provides reasonable results for phenomena associated with turbulent jets and is adequate for engineering analysis.

Regarding experimental results, the observations made by Holdeman and his co-workers reveal trends that are useful in providing guidance for establishing a scheme where good jet mixing with the crossflow can be achieved. Specifically, they have derived a correlation relating design and operation parameters that are useful in steering the jet trajectory down the middle of a channel. This correlation will be examined in Chapter 6 for jet flows from rectangular orifices in conditions that are typical of those found in a recovery boiler, where the crossflow may exhibit a peaked non-uniformity, and where the momentum ratio J is high.

Chapter 3

Numerical Solution of the Navier-Stokes System

In this chapter, we discuss some numerical solution methods for solving problems with incompressible turbulent jet flow. Solutions are obtained by solving the time-averaged Navier-Stokes equations coupled with the $k-\epsilon$ turbulence model. The multigrid technique is needed to accelerate the convergence of iterative algorithms employed for solving the system of equations. We will discuss the care that is needed with the implementation of the multigrid procedure to solve fluid flow problems. Finally, we will apply this multigrid algorithm to simulate the flow field of a single square jet in a crossflow. The latter study is carried out to validate the implementation of the algorithm and to examine the quality of the mathematical model describing the flow.

3.1 Discretization of Differential Equations

To study the complex phenomena associated with multiple jet interactions, numerical solution technique appears to be the only practical prediction method available. The system of equations to be solved was described in Chapter 2. The form of the equation, as shown in Eq.(2.21), together with Table 2.2 are rewritten here for reference. The mathematical formulae describe the conservation of mass, momentum, species concentration, turbulent kinetic energy, and the dissipation rate of turbulent kinetic energy.

$$\frac{\partial}{\partial x_j}(\rho U_j \Psi) = \frac{\partial}{\partial x_j}\left(\Gamma_\Psi \frac{\partial \Psi}{\partial x_j}\right) + S_\Psi \tag{2.21}$$

Ψ	Γ_Ψ	S_Ψ
1	0	0
U_i, $i = 1,2,3$	μ_{eff}	$-\partial P/\partial x_i + \partial/\partial x_j[(\mu_{eff}(\partial U_j/\partial x_i)]$
Φ	μ_{eff}/σ_ϕ	0
k	μ_{eff}/σ_k	$G - \rho\epsilon$
ϵ	$\mu_{eff}/\sigma_\epsilon$	$(\epsilon/k)(C_1 G - C_2\rho\epsilon)$

$$P = p + \tfrac{2}{3}\rho k$$

$$G = \mu_{eff}[(\partial U_i/\partial x_j) + (\partial U_j/\partial x_i)](\partial U_i/\partial x_j)$$

Table 2.2: Terms representing the time-averaged Navier-Stokes equations with the $k - \epsilon$ turbulence model and a transport equation for an inert scalar.

The above system of differential equations is cast in the strong conservation form, which is convenient for numerical integration. In this form, all terms arising from the divergence operator are under differential operators, and when the differential equations are integrated over a finite number of control volumes and properly discretized, the resulting fluxes from the strong conservation form would cancel in pairs at all interior control volume (cell) faces when summed, so that only boundary fluxes remain. This guarantees overall conservation of the transported quantity.

A large system of difference equations will result upon the discretization of the equations. These difference equations must mirror the properties of the differential equations. That is, they must preserve the properties of conservation, boundedness, and transitivity. In addition, the numerical scheme for differencing should exhibit good accuracy and stability characteristics. Detailed discussions of the above topics can be found in the works of Patankar (1980) and Syed et al. (1985).

The above requirements on the differencing scheme have dictated that much care is needed in the construction of the finite difference equations. The stability requirement,

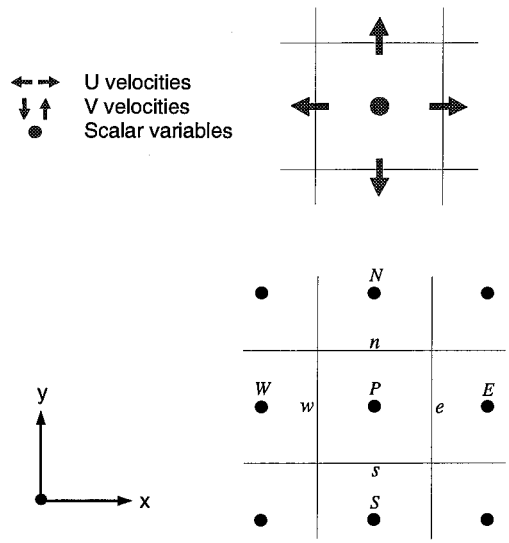

Figure 3.1: Variable arrangements in a staggered grid in two-dimensions.

which will be discussed in section 3.5.1, has led to the use of a staggered grid arrangement for the scalar and velocity variables. A two-dimensional example of the grid arrangement is shown in Figure 3.1. Also shown in the figure are two sets of labels. The labels $\{e,w,n,s\}$ refer respectively to the east, west, north, and south faces of the scalar control volume. The labels $\{E,W,N,S,P\}$ refer respectively to the East, West, North, and South scalar nodes relative to the scalar node P. Velocity variables follow similar labelling schemes. Extension to three-dimensions is straight-forward.

The finite volume integration procedure is the first step in constructing difference equations. Volume integration is performed for Eq.(2.21) around a control volume such as the one shown in Figure 3.1 which represents a two-dimensional projection. The integration is carried out as

$$\iiint\left\{\frac{\partial}{\partial x}(\rho U\Psi)+\frac{\partial}{\partial y}(\rho V\Psi)+\frac{\partial}{\partial z}(\rho W\Psi)\right\}\,dV \;=$$
$$\iiint\left\{\frac{\partial}{\partial x}\left(\Gamma_\Psi\frac{\partial\Psi}{\partial x}\right)+\frac{\partial}{\partial y}\left(\Gamma_\Psi\frac{\partial\Psi}{\partial y}\right)+\frac{\partial}{\partial z}\left(\Gamma_\Psi\frac{\partial\Psi}{\partial z}\right)\right\}\,dV \;+\; \iiint S_\Psi\,dV \quad (3.1)$$

The volume integrals can be transformed to surface integrals using the divergence theorem, yielding the following formula:

$$F_e - F_w + F_n - F_s + F_t - F_b = \iiint S_\Psi \, dV \tag{3.2}$$

where $\{F_e, F_w, F_n, F_s, F_t, F_b\}$ denote the sums of convective and diffusive fluxes through the $\{e, w, n, s, t, b\}$ faces, respectively, of a three-dimensional control volume cell with t and b referring to the top and bottom cell faces. The expression for F_e is

$$F_e = \iint \left(\rho U \Psi - \Gamma_\Psi \frac{\partial \Psi}{\partial x} \right) \bigg|_{x_e} dydz \tag{3.3}$$

$$= C_e + D_e \tag{3.4}$$

with x_e being the location of the cell's east face, and

$$C_e = \iint (\rho U \Psi)|_{x_e} \, dydz \tag{3.5}$$

is the convective flux, while

$$D_e = \iint \left(-\Gamma_\Psi \frac{\partial \Psi}{\partial x} \right) \bigg|_{x_e} dydz \tag{3.6}$$

is the diffusive flux. Similar expressions can also be derived for fluxes through other faces.

In Cartesian coordinates, the diffusive flux is usually approximated by central differencing; in other words,

$$D_e \approx \Gamma_\Psi|_{x_e} \left(\frac{\Psi_P - \Psi_E}{\delta x_i} \right) \Delta y_j \Delta z_k \tag{3.7}$$

where Ψ_P and Ψ_E refer to the values of Ψ at grid points P and E, respectively. The quantity δx_i is the distance between P and E, while Δy_j and Δz_k are the dimensions of the east cell face. The expression for D_e is formally second order accurate in δx.

To approximate the convective flux, Eq.(3.5) is first written as

$$C_e \approx \rho_e U_e \Psi_e \Delta y_j \Delta z_k \tag{3.8}$$

where the subscript e for ρ, U, and Ψ denotes that the values of those quantities are to be taken at the east face of the cell. How Ψ_e is approximated affects the characteristics of the resulting finite difference equations. It is well known that the central difference approximation is numerically unstable if the cell Peclet number $Pe = C_e/D_e$ is greater than 2. The use of upwind differencing will lead to better numerical stability characteristics, but at the expense of accuracy due to numerical diffusion. More accurate differencing schemes are available. For example, the hybrid scheme combines both central differencing and upwind differencing. In addition, upwind weighted schemes such as the power-law scheme and the exponential scheme have been derived to attempt better approximations to the convective and diffusive fluxes. Detailed descriptions of these various schemes can be found in the monograph by Patankar.

Other schemes for the approximation of the convective flux have also been derived aiming to reduce the effect of numerical diffusion in instances when the flow is skewed relative to the grid. Examples include the QUICK scheme and the skew differencing scheme. The application of these schemes requires a larger differencing molecule, and more care is needed to ensure numerical stability. Details of these aspects are presented in the work of Syed et al.

The discretization of the source term starts with its linearization into the following form:

$$\iiint S_\Psi \, dV \approx S_P^\Psi \Psi_P + S_C^\Psi \tag{3.9}$$

The goal is to construct expressions for S_P^Ψ and S_C^Ψ so that the approximation is accurate and the resulting difference equations have good stability characteristics. The numerical stability of difference equations is contingent upon the condition that S_P^Ψ must be non-positive. In addition, for always-positive variables such as turbulent energy and its dissipation rate, the source term must be discretized so that the variable will never

become negative during the iterative solution process. This goal will be achieved if S_C^Ψ is always positive. Patankar (1980) offers a more detailed discussion on the discretization strategy. For the $k-\epsilon$ turbulence model, the discretization of the source terms for various equations is presented in Table 3.1.

Ψ	S_P^Ψ	S_C^Ψ
U	0	$P\|_e^w \Delta y \Delta z + \left(\mu_{eff}\frac{\Delta U}{\delta x}\right)\|_w^e \Delta y \Delta z + \left(\mu_{eff}\frac{\Delta V}{\delta x}\right)\|_s^n \Delta x \Delta z + \left(\mu_{eff}\frac{\Delta W}{\delta x}\right)\|_b^t \Delta x \Delta y$
V	0	$P\|_n^s \Delta x \Delta z + \left(\mu_{eff}\frac{\Delta U}{\delta y}\right)\|_w^e \Delta y \Delta z + \left(\mu_{eff}\frac{\Delta V}{\delta y}\right)\|_s^n \Delta x \Delta z + \left(\mu_{eff}\frac{\Delta W}{\delta y}\right)\|_b^t \Delta x \Delta y$
W	0	$P\|_t^b \Delta x \Delta y + \left(\mu_{eff}\frac{\Delta U}{\delta z}\right)\|_w^e \Delta y \Delta z + \left(\mu_{eff}\frac{\Delta V}{\delta z}\right)\|_s^n \Delta x \Delta z + \left(\mu_{eff}\frac{\Delta W}{\delta z}\right)\|_b^t \Delta x \Delta y$
k	$-\frac{C_\mu \rho^2 k_P}{\mu_t}\Delta x \Delta y \Delta z$	$G\,\Delta x \Delta y \Delta z$
ϵ	$-\frac{C_2 \rho \epsilon_P}{k_P}\Delta x \Delta y \Delta z$	$C_1 \frac{\epsilon_P}{k_P} G\,\Delta x \Delta y \Delta z$

Table 3.1: Discretization of the source terms.

After inserting expressions presented in Eq.(3.2) and Eq.(3.9) into Eq.(3.1), we obtain the following general finite volume equation which is cast into the following quasi-linear form:

$$(a_P - S_P^\Psi)\Psi_P = a_N\Psi_N + a_S\Psi_S + a_E\Psi_E + a_W\Psi_W + a_B\Psi_B + a_T\Psi_T + S_C^\Psi \tag{3.10}$$

with

$$a_P = \sum_i a_i \qquad (i = N, S, E, W, B, T) \tag{3.11}$$

Expressions for the coefficients $\{a_i\}$ for various differencing strategies can be found in the works of Patankar and Syed et al.

3.2 Boundary Conditions

The proper setting of boundary conditions is necessary for the successful simulation of a flow phenomenon. The imposition of boundary conditions reflects either the need to represent a physical boundary for the flow such as a wall, or the need to simplify the representation of the domain. The latter type of boundary conditions includes the symmetry conditions and the inflow and outflow conditions. The introduction of these boundary conditions usually affects the convective or diffusive fluxes entering the flow domain. For example, at a symmetry plane, there is no convective or diffusive flux across the plane. At an outflow boundary, the diffusive flux is neglected since the flow is assumed to exhibit a local parabolic behavior. Because the values of the coefficients $\{a_i\}$ appearing in Eq.(3.10) depend on the convective and diffusive fluxes entering the cell, boundary conditions are usually introduced through modifications to the coefficients for cells adjacent to the boundary.

For simulations of turbulent flows using the $k-\epsilon$ model, additional complications arise at a solid wall boundary. The reason is that the model assumes high Reynolds number flow, a condition that is violated near a wall where the fluid has to be decelerated because of a no-slip condition at the wall surface. To overcome this deficiency in the model, a semi-empirical wall function treatment was introduced by Launder and Spalding (1974) to bridge the gap between the wall and the outer flow. The logarithmic law-of-the-wall is applied to account for the effect of the wall on the shear stress distribution. Consequently, the diffusive fluxes for cells adjacent to the wall boundary are modified. Details of the implementation of this wall function, together with other types of boundary conditions, can be found in the thesis by Djilali (1987).

3.3 Numerical Solution Procedure

For problems with large and complex domains, the discretization procedure described above leads to a large system of algebraic equations. This, coupled with the nonlinear nature of the equations, make it mandatory for the application of iterative or relaxation methods to seek a solution to the system of equations. For the incompressible Navier-Stokes equations, there are primarily two types of iterative methods used by codes based on the primitive-variable formulation: (i) a sequential or decoupled procedure such as the SIMPLE algorithm described by Patankar (1980), and (ii) a coupled method such as the symmetrically coupled Gauss-Seidel (SCGS) scheme described by Vanka (1986). These variations arise due to the fact that for incompressible flows, the pressure field is determined by the entire hydrodynamic equations system and not just by one of the equations. For the determination of the pressure field we need to resolve the coupling between momentum and continuity. Rodi et al. (1989) considered the use of these two solution strategies to represent compromises between memory storage requirements and complexity of programming. These two solution methods are discussed in the next two sections.

3.3.1 Sequential Solution Methods

The algorithm for a sequential or decoupled procedure is usually of the predictor-corrector type. In the predictor step, a new velocity is computed by approximately solving the momentum equations by performing a few standard relaxation sweeps. In the corrector step, both velocity and pressure are updated. The aim is to compute these changes such that the continuity equation is satisfied.

A pressure-correction based scheme such as SIMPLE is one such example. In this algorithm, velocity correction is defined in terms of pressure changes. The use of the

continuity equation leads to an equation for the pressure correction. At each iteration step, the computed pressure and velocity fields are updated through the solution to the pressure correction equation. The solutions to equations for scalar quantities and the turbulence model are carried out by solving those equations sequentially after the hydrodynamic part of the system has been treated. An important advantage of this class of algorithm is the ease with which additional equations can be incorporated into the solution scheme. Another advantage of this procedure is the low memory requirement as the coefficients constructed for an equation can be over-written once the relaxation of that equation is finished.

Besides SIMPLE, there are a number of other sequential type solution schemes. A well known one is the PISO algorithm, which is a two-step procedure of pressure correction type. Other more refined algorithms, derived from SIMPLE, are the SIMPLER and SIMPLE-C schemes. The efficiency of these schemes for laminar and turbulent flow problems have been assessed by Latimer and Pollard (1985), Jang et al. (1986), and Wanik and Schnell (1989). The general observation is that for laminar problems where pressure-velocity coupling is significant, PISO, SIMPLER and SIMPLE-C can all perform better than SIMPLE, but the improvement to a system of equations coupled with a turbulence model is modest.

3.3.2 Coupled Solution Methods

In a coupled solution scheme, the hydrodynamic variables associated with a control volume cell are updated simultaneously. For the staggered grid arrangement, this is carried out by solving the momentum equations and the continuity equation for the velocity components along the edges of the cell and the pressure in the center. A Gauss-Seidel type relaxation method can be used in this process, and the variables can be updated one cell at a time until all cells are considered. This method is known as the symmetrically

coupled Gauss-Seidel (SCGS) relaxation scheme. Alternatively, the equations can be set up in such a way that a line-relaxation technique can be employed to obtain the nodal pressure and the face velocities, simultaneously, along a complete line of grid nodes.

Any additional equations such as the k and ϵ equations are solved in a sequential manner after the flow variables are computed by the coupled method. This part of the solution procedure can be similar to that used in the sequential solution strategy.

An advantage of this type of algorithm is the close coupling of hydrodynamic equations that is maintained by the algorithm since a whole set of unknowns in velocity and pressure is updated simultaneously. This has been shown to be advantageous when a good efficiency is desired in reducing simultaneously the errors present in the results.

3.3.3 Convergence Difficulties

It has been commonly observed that the convergence rate of an iterative solution scheme deteriorates as the grid is made finer. Moreover, most basic schemes suffer convergence stalling problems as the iteration progresses. In the terminology of numerical analysis, the reduction of the residues of a set of equations by an iterative solution procedure is called error smoothing. Thus, the above observation amounts to the fact that most basic iteration schemes exhibit good error smoothing properties only during the initial stage of the solution process.

This observation can be explained by a discrete Fourier analysis on the error or residual functions. Upon decomposing a residual function into its frequency components or modes, it was found that an iterative scheme tended to be effective in reducing the amplitudes of high frequency error components but ineffective in reducing the low frequency components. The realization of this inherent deficiency of most iterative schemes can be used to our advantage with the recognition that on coarser grids, these low frequency modes would appear as having high frequencies and the iterative method would again

be effective. A systematic exploitation of this principle of performing relaxation on a sequence of grids of different coarseness has led to the development of the multigrid technique. This technique can return very rapid smoothing rates by effectively smoothing errors of all wavelengths by working on grids with different coarseness. The basic ideas and implementation of this technique are the focus of the following section.

3.4 Multigrid Procedure

The practical utility of the multigrid technique was developed in the acclaimed work by Brandt (1977). One of its original applications was to accelerate the convergence rate of an iterative procedure when applied to solve a discretized elliptic boundary value problem, such as the Poisson equation with Dirichlet-type boundary conditions. It is well known that any stable discretization of such an elliptic operator will lead to a system of algebraic equations which is in turn elliptic, in the sense defined in Stüben and Trottenberg (1982). This property is critical for the availability of a relaxation process with sufficient error smoothing properties that are independent of the grid size. Because of this, the Poisson equation is an ideal test problem for the multigrid method to showcase its performance. Excellent convergence performance was reported by Brandt (1977).

The multigrid Coarse Grid Correction (CGC) scheme has been developed for linear problems. For non-linear problems such as the Navier-Stokes equation, the Full Approximation Storage (FAS) scheme should be used. Detailed descriptions of this method can be found in Brandt (1977) and Stüben and Trottenberg (1982). The salient features of the multigrid method will be described in the following paragraphs. This description is essential for our later discussion in section 3.6 on the difficulties encountered when the multigrid method is applied to problems describing turbulent flows.

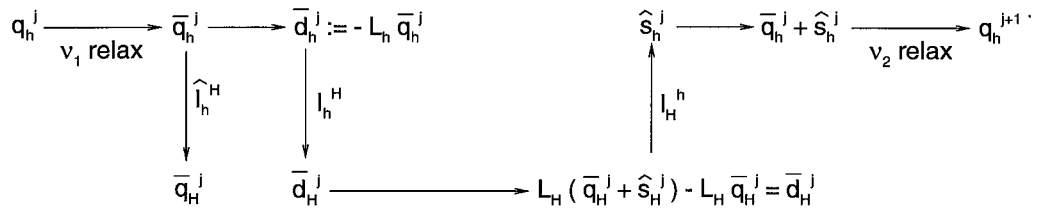

Figure 3.2: FAS (h,H) two-grid method.

Let a system of nonlinear differential equations such as Eq.(2.21) be written as

$$\mathcal{L}Q = 0 \tag{3.12}$$

where $\mathcal{L}$ is some nonlinear differential operator and Q is the solution vector. Let the discretized system on a grid $\tilde{G}_h$ be denoted

$$L_h Q_h = 0 \tag{3.13}$$

where h denotes the characteristic grid size, L_h is a linear difference operator approximation to $\mathcal{L}$ linearized about some values of Q, and Q_h is a discrete approximation to Q.

The Full Approximation Storage (FAS) algorithm can be described on the basis of an FAS (h,H) two-grid method. This is shown in Figure 3.2 illustrating the computation of q_h^{j+1} from q_h^j, where q_h^j is an approximation, to the solution Q_h, with the superscript j denoting the iteration index. The indices h and H denote respectively the fine grid and coarse grid used by the method. The complete FAS algorithm is obtained by applying this two-grid method recursively to the equation in the coarser grid.

In the diagram, $\overline{q}_h^j$ is the result of ν_1 relaxation steps starting with q_h^j as first approximation. The quantity $\overline{d}_h^j$ is the residual or defect quantity in the multigrid terminology. It is smoothed by the relaxation process and is a measure of the accuracy of the computed solution. The quantities $\overline{q}_H^j$ and $\overline{d}_H^j$ are corresponding quantities in the coarser grid $\tilde{G}_H$.

The operators I_h^H, $\hat{I}_h^H$, and I_H^h are intergrid operators for transferring values from $\tilde{G}_h$ to $\tilde{G}_H$, and vice versa. When the transfer is from $\tilde{G}_h$ to $\tilde{G}_H$, it is called restriction; and it is called prolongation when it is from $\tilde{G}_H$ to $\tilde{G}_h$. The reason for having two different restriction operators, $\hat{I}_h^H$ and I_h^H, is that higher accuracy is sometimes sought for the value of the solution $\overline{q}_H^j$ represented in the coarser grid; but very often it is sufficient to use the same restriction operator as for the residue. Finally, the quantity $\hat{s}_H^j$ and its fine grid counterpart $\hat{s}_h^j$ are corrections to be added to the approximate solutions $\overline{q}_H^j$ and $\overline{q}_h^j$, respectively, so that Eq.(3.13) will be approximately satisfied on both grids.

In the algorithm mentioned above, the coarse grid is only visited once from the fine grid. This algorithm is also known as the FAS V-cycle, and is the most basic form of a multigrid algorithm. The following components of the algorithm can be identified:

(i) Pre-Smoothing: Smoothing is carried out ν_1 times to reduce the amplitude of the high frequency error components present in $\overline{d}_h^j$.

(ii) Restriction of defect: By using an appropriate weighting scheme, the smoothed residue from $\tilde{G}_h$ is transferred to a coarser grid $\tilde{G}_H$. There, the low frequency error would appear as a high frequency mode.

(iii) Coarse grid smoothing: The $\tilde{G}_H$ version of the operator $\mathcal{L}$ is constructed and an appropriate smoothing procedure is employed to smooth out the high frequency mode in the correction $\hat{s}_H^j$.

(iv) Prolongation of correction: An appropriate interpolation procedure I_H^h is chosen to transfer the correction $\hat{s}_H^j$ to the finer grid to become $\hat{s}_h^j$.

(v) Post-Smoothing: Smoothing is performed ν_2 times to smooth out any high frequency noise introduced during the interpolation process.

A unique feature of this FAS method is the way in which the coarse grid defect equation is set up and solved. To illustrate, let s_h^j be the *exact* correction to $\overline{q}_h^j$; that is,

$$\overline{q}_h^j + s_h^j = Q_h \tag{3.14}$$

Then Eq.(3.13), together with the definition of $\overline{d}_h^j$ indicated in Figure 3.2, imply the following relationship between s_h^j and $\overline{d}_h^j$ on the grid $\tilde{G}_h$:

$$L_h(\overline{q}_h^j + s_h^j) - L_h\overline{q}_h^j = \overline{d}_h^j \tag{3.15}$$

This equation is then approximated on $\tilde{G}_H$ by

$$L_H(\overline{q}_H^j + \hat{s}_H^j) - L_H\overline{q}_H^j = \overline{d}_H^j \tag{3.16}$$

which is to be solved for the *full approximation* $\overline{q}_H^j + \hat{s}_H^j$, other terms in the equation being known.

It is important to note that it is the correction $\hat{s}_H^j$ that is transferred back to the fine grid and not the full approximation itself. The reason is that it is the correction and defect quantities that are smoothed by relaxation process and can therefore be approximated well on coarser grids.

3.4.1 Full Multigrid Strategy

In the multigrid algorithm described, the calculation is first carried out on the finest grid, while the coarser grids are used to speed up the smoothing of residual quantities. However, the algorithm can be implemented more efficiently through a strategy known as the full multigrid (FMG) algorithm. The procedure is illustrated in Figure 3.3.

In this algorithm, smoothing is first done on the coarsest grid. Upon reaching a reasonable level of convergence, interpolation is carried out to transfer the solution to a finer level where the multigrid cycle will be carried out. This is continued until the finest,

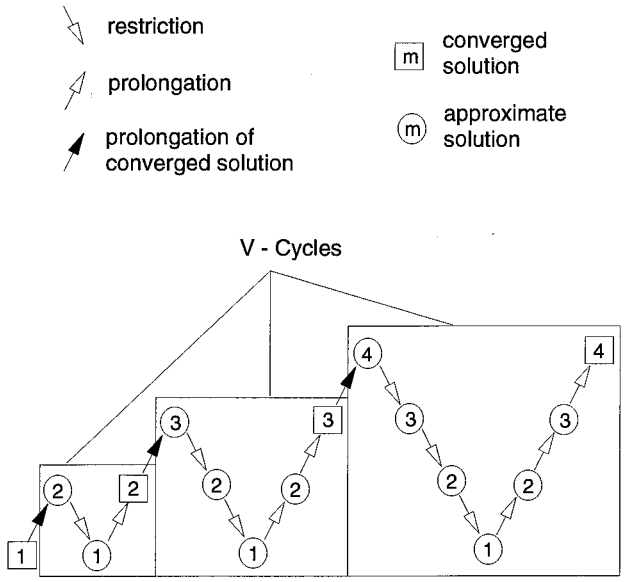

Figure 3.3: The full multigrid (FMG) algorithm.

pre-determined level is reached. This method offers an efficient means to generate an accurate solution field to serve as an initial solution estimate for a finer grid level. Indeed, in many applications of the multigrid method for non-linear boundary value problems, the preferred solution procedure is a combination of this FMG strategy together with the FAS algorithm.

3.4.2 Design of a Multigrid Algorithm

When the multigrid algorithm is implemented correctly, it can return a very fast convergence rate to the iterative procedure. Given a specific problem, unfortunately, there is no general rule for choosing individual components of the algorithm that will lead to an optimal scheme. Nevertheless, some general guidelines can be provided. The knowledge of these guidelines is obtained through experience and local Fourier analysis for test problems, and has been discussed by Brandt (1982). Several essential points are outlined below.

(1) The number of smoothings on a particular grid should not be too large to avoid the re-introduction of high frequency error modes due to interaction with boundary conditions.

(2) The restriction operator should be chosen so that the weighting of residues would not introduce high frequency errors. This concern arises when the equations to be solved are nonlinear or have rapidly varying coefficients. In such cases, nontrivial weighting should be used.

(3) The interpolation procedure for prolongation should be chosen so that the order of interpolation is of the same order as the differential equation. This is done to minimize the generation of spurious frequency modes through the interpolation procedure.

(4) The efficiency of the technique also depends on the choice of the coarse grid operator. The important consideration is that the coarse grid defect equation (3.16) should be a faithful representation of its fine grid counterpart. One way to evaluate the coefficients defining the coarse grid operator is simply to average the corresponding fine grid coefficients. Another way would be to compute new coefficients directly from the restricted variables. The former strategy may save some computations, but for highly nonlinear equations with large source terms it may not lead to convergence since inconsistencies can be magnified during the solution procedure.

It is important to note that the guidelines mentioned above were gained through the application of the multigrid method to relatively simple linear and nonlinear boundary value problems. To extend the method to a system of nonlinear equations such as the Navier-Stokes equations presents many challenges, and the above guidelines may need modifications. It is the objective of the following section to outline some of the attempts

made in extending the procedure to solve fluid flow problems.

3.5 Multigrid Technique as Applied to the Navier-Stokes Equations

The multigrid technique can be applied in many ways to solve the Navier-Stokes equations. For example, the multigrid solver can be implemented to accelerate the convergence of the momentum equations or the pressure correction equation within the SIMPLE algorithm. However, this approach is inefficient because only a time-consuming component in an iterative solution algorithm is replaced by a multigrid solver. The convergence of the global iteration remains slow and any increase in efficiency is very limited.

A more effective approach would be to construct a multigrid procedure for the Navier-Stokes equations as a whole. In this section, we discuss the special attention that is needed in the construction of such a procedure.

3.5.1 Stability of Discretization

Brandt and Dinar (1979), Brandt (1980), and Linden et al. (1988) discussed aspects about stability characteristics when the differential equations are discretized. They emphasized the importance of constructing stable and high order finite-difference approximations to general elliptic partial differential systems. This is important because the construction of a robust and efficient smoother is possible only if the finite difference system itself can be shown to be stable when subjected to an iterative solution procedure. The ellipticity measure of the finite difference equations is one means of showing this condition.

For viscous, incompressible flow problems, there are two sources of numerical instability. First, at high Reynolds numbers, the ellipticity measure of central differencing for the convection-diffusion part of the momentum equations decreases. To counter this, an

additional measure of ellipticity has to be introduced to keep the discrete equations stable. This can be achieved, for example, by using upwind differencing. The second source of instability is due to the fact that pressure appears in the differential equations only in terms of its first derivatives. Consequently, a simple central differencing for the pressure gradient term can lead to a system of difference equations which admits a solution that is periodic in the pressure variation across the grid. Such a system of difference equations is unstable to such periodic perturbations. For flow problems having simple rectilinear domains, the simplest remedy for this instability is to use a staggered grid, as illustrated earlier in Figure 3.1.

3.5.2 Choice of Smoother

To construct an efficient and robust multigrid solution algorithm for Navier-Stokes problems, it is important to use an equation solver that has good error smoothing properties and robustness when the flow Reynolds number changes. Researchers have examined numerous smoothers for their suitability for the above purpose. Examples of solvers tested are the distributive Gauss-Seidel (DGS) scheme and the pressure gradient averaging (PGA) scheme, both belong to the class of coupled solvers, and their descriptions can be found in the works by Brandt (1979) and Fuchs (1984). Brandt made the recommendation that a locally strongly coupled block of unknowns should be relaxed simultaneously; Fuchs observed that the PGA scheme is more robust than the DGS scheme at high Reynolds numbers.

Arakawa et al. (1987) and Linden et al. (1988) compared the use of sequential smoothing versus coupled smoothing for multigrid purposes for laminar flow problems. Both groups of investigators found that coupled smoothing is preferred to sequential smoothing, especially at higher Reynolds numbers, for the following reasons: first, sequential smoothing schemes are conceptually more complicated and, moreover, are sensitive to

the details of implementation. Secondly, the application of the multigrid techniques in connection with the sequential procedure can be problematic because, after smoothing the momentum equations, errors of higher frequencies can be introduced through the velocity corrections. Thirdly, numerical experiments show that coupled smoothers are more robust, particularly at high Reynolds numbers.

The SCGS smoother was used by Vanka (1986), who found that it was very robust for Reynolds number up to 5000 for the driven cavity problem. It was also employed by Thompson and Ferziger (1989), who accounted for its good performance by its attempt to satisfy continuity for each cell at each iteration step. They found that the DGS approach had difficulty when the cell face fluxes did not match well.

3.5.3 Inter-Grid Transfer of Information

It is customary to partition a coarse grid volume into eight fine grid volumes, or, in two dimensions, a course grid cell into four fine cells. The use of the staggered grid, however, makes inter-grid transfer of variables difficult. The reason is that different formulae are needed for velocities, which are stored at scalar cell faces, and for scalar quantities, which are stored at the scalar cell centers. To illustrate a typical grid transfer strategy, it is sufficient to consider the situation shown in Figure 3.4, which depicts a two-dimensional cell with uniform grid spacing. Extension to three dimensions and non-uniform grid spacing is straight-forward.

Restriction

Restriction of grid functions can be made by averaging nearby values. For problems with fluid flows, mass conservation needs to be ensured during grid transfer, and this

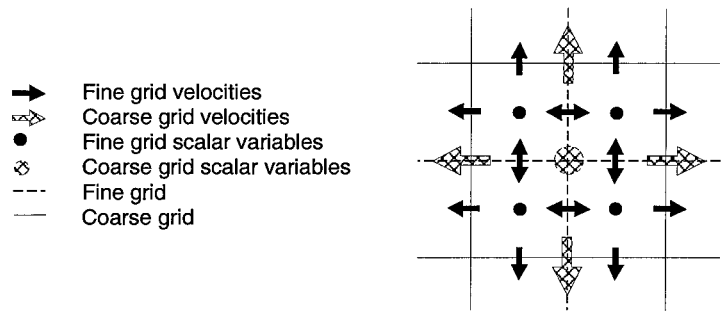

Figure 3.4: Staggered mesh arrangement showing storage of variables in the fine and coarse grids.

requirement leads to the following expression:

$$(\rho U A)_{\text{coarse}} = \sum_{\text{fine}} (\rho U A) \tag{3.17}$$

where the summation is over all fine-grid control volume faces coinciding with the coarse-grid face. Thus, the coarse-grid velocity is given by

$$U_{\text{coarse}} = \frac{\sum_{\text{fine}} (\rho U A)}{(\rho A)_{\text{coarse}}} \tag{3.18}$$

In studies of incompressible flows discretized with a uniform grid, the above requirement leads to the following expressions in two dimensions: let the superscripts c and f denote coarse and fine grid values. Let (ic, jc) and (if, jf) denote coarse and fine mesh indices, respectively. Also, let $U_{i+1/2,j}$ be referred to as $U_{i,j}$ and $U_{i-1/2,j}$ be referred to as $U_{i-1,j}$, and similar expressions for the other velocity component V. Then we have $if = 2(ic) - 1$, $jf = 2(jc) - 1$, and

$$U^c(ic, jc) = \frac{1}{2}[U^f(if, jf) + U^f(if, jf - 1)] \tag{3.19}$$

$$V^c(ic, jc) = \frac{1}{2}[V^f(if, jf) + V^f(if - 1, jf)] \tag{3.20}$$

For scalar variables such as the inert tracer Φ, restriction is achieved by simple linear

interpolation among fine-grid values. The expression is

$$\Phi^c(ic,jc) = \frac{1}{4}[\Phi^f(if,jf) + \Phi^f(if-1,jf) + \Phi^f(if,jf-1) + \Phi^f(if-1,jf-1)] \quad (3.21)$$

This formula is applicable to other solution variables stored at the scalar node, such as the pressure. Similarly, the restriction of solution residues is carried out in an analogous manner.

Prolongation

Prolongation relations are derived by bilinear interpolation. For each coarse grid node, four fine grid values are derived. For the U-velocity, they are

$$U^f(if,jf) = \frac{1}{4}(3U_1^c + U_2^c) \quad (3.22)$$

$$U^f(if,jf+1) = \frac{1}{4}(3U_2^c + U_1^c) \quad (3.23)$$

$$U^f(if+1,jf) = \frac{1}{8}(3U_1^c + U_2^c + 3U_3^c + U_4^c) \quad (3.24)$$

$$U^f(if+1,jf+1) = \frac{1}{8}(3U_2^c + U_1^c + 3U_4^c + U_3^c) \quad (3.25)$$

where

$$\begin{aligned} U_1^c &= U^c(ic,jc) \\ U_2^c &= U^c(ic,jc+1) \\ U_3^c &= U^c(ic+1,jc) \\ U_4^c &= U^c(ic+1,jc+1) \end{aligned}$$

The V-velocity is prolongated by equivalent relations obtained by rotating the coordinates by ninety degrees. The scalar prolongations have different weights because of their cell-centered locations. The relations are

$$\Phi^f(if,jf) = \frac{1}{16}(9\Phi_1^c + 3\Phi_2^c + 3\Phi_3^c + \Phi_4^c) \quad (3.26)$$

$$\Phi^f(if, jf+1) = \frac{1}{16}(9\Phi_3^c + 3\Phi_4^c + 3\Phi_1^c + \Phi_2^c) \tag{3.27}$$

$$\Phi^f(if+1, jf) = \frac{1}{16}(9\Phi_2^c + 3\Phi_1^c + 3\Phi_4^c + \Phi_3^c) \tag{3.28}$$

$$\Phi^f(if+1, jf+1) = \frac{1}{16}(9\Phi_4^c + 3\Phi_2^c + 3\Phi_3^c + \Phi_1^c) \tag{3.29}$$

with

$$\begin{aligned}
\Phi_1^c &= \Phi^c(ic, jc) \\
\Phi_2^c &= \Phi^c(ic+1, jc) \\
\Phi_3^c &= \Phi^c(ic, jc+1) \\
\Phi_4^c &= \Phi^c(ic+1, jc+1)
\end{aligned}$$

The use of a collocated variable arrangement where all variables are stored in the center of a cell simplifies the intergrid transfer algorithm, since the same set of formulae can be used. To deal with the stability problem, a special interpolation practice, called the momentum interpolation by Majumdar (1988), has been introduced. This interpolation procedure is designed for the determination of cell face velocities representing the convective mass fluxes in order to avoid oscillatory solutions which can cause numerical instability.

In examining the effect of altering the order of the interpolation, Thompson and Ferziger (1989) found that the use of more accurate higher order interpolation schemes actually degraded the convergence rate. Their test results show that it is especially bad to use high-order interpolation for prolongation. This may have been caused by the introduction of high-frequency noise which the fine grid iterations need to remove later. Moreover, cubic or higher order polynomial fits can be inconvenient to use in practical flows with complex geometrical shapes and blocked regions. Hence, for most practical problems, the use of simple linear interpolation formulae seems to be adequate.

3.5.4 Construction of Coarse Grid Equation

As shown in Figure 3.2, the construction of the coarse grid equation

$$L_H(\overline{q}_H^j + \hat{s}_H^j) = L_H\overline{q}_H^j + \overline{d}_H^j \tag{3.30}$$

requires the restriction of the defect or residual quantity and the solution vector from the fine grid $\tilde{G}_h$ to the coarse grid $\tilde{G}_H$, together with the setting-up of the coarse grid operator L_H. The restriction of the solution vector can be carried out with formulae similar to those given in the previous section. For the residual quantities, the coarse-cell residues are obtained from an appropriate summation of residues of the fine cells constituting the coarse cell.

A simple approach in constructing the coarse grid operator L_H for the Navier-Stokes system is to restrict the coefficient fields defining the fine grid operator L_h onto the coarse grid directly. As discussed in section 3.4.2, this strategy reduces the computational cost, but is not robust because it does not maintain the consistency between the sources and the associated variable fields. It is preferable to compute the coefficients and the sources by using the coarse grid solution $\overline{q}_H^j$. This preference becomes mandatory when those quantities are dependent on the associated variables.

Thus far, the discussion on applying the multigrid method to fluid flow problems has been based mainly on the laminar Navier-Stokes system. To extend the method to solve turbulent flow problems requires the consideration of a larger set of equations with more complicated source terms. A discussion is presented in the following section on extending the solution procedure to this class of problems.

3.6 Extension of the Multigrid Technique to Turbulent Flow Problems

The extension of the multigrid method to turbulent flow problems faces many additional difficulties, which arise due to the nature of the turbulence model equations. For the

$k - \epsilon$ model, which is the most widely tested model used in multigrid applications, it has been observed that there are a number of difficulties when the implementation of the multigrid method is sought.

3.6.1 Difficulties with Implementation

Several major difficulties with the implementation of the method are listed below:

(1) The best way of incorporating the k and ϵ model equations into the smoothing scheme is not clear when a coupled solver such as SCGS is used.

(2) The use of the wall function to link the flow in the near wall region to the main flow can be problematic for multigrid applications. It is difficult to consistently assign values to grid nodes closest to the wall since those nodes are moved during restriction. Specifically, the fixing of the value of ϵ at the near-wall node implies that every time restriction is carried out, the logarithmic region will extend farther and farther from the wall.

(3) The nonlinearity and the dominance of the source terms in both the k and ϵ equations can adversely affect the performance of the multigrid method because the success of the method relies on the smoothness of the error and correction quantities. Any disturbances introduced into the residues through inaccurate handling of the source terms can lead to serious degradation or complete failure of the algorithm. The ϵ equation has a strong nonlinear $(1/k)$ coupling with the k equation through the production and dissipation terms. This coupling is observed to be much more dominant than the convective and diffusive transport, and unless it is resolved accurately, the solution of these equations can have serious errors. Under-relaxation of these source terms is needed to ensure stability during the solution process.

(4) The constraint of the physical realizability imposed by the turbulence model calls for concerns. Specifically, the values of k and ϵ must always be positive and the turbulent viscosity μ_t defined in Eq.(2.16) should not be unrealistically larger than the molecular viscosity, say 10^5 times larger. Failure to observe these constraints during smoothing or prolongation could lead to numerical instability which could cause the iterative solution procedure to diverge.

Special attention is required to deal with the above concerns.

3.6.2 Experience with Applying Multigrid to the $k - \epsilon$ Model

There have been only a limited number of reports on the application of the multigrid method to equations coupled with the $k - \epsilon$ turbulence model. One of the earliest reports is by Phillips et al. (1985) who applied the FAS multigrid method to simulate a two-dimensional axisymmetric turbulent flow in an expanding duct using the $k - \epsilon$ model with wall function. Both the Stone's method and the Gauss-Seidel method were employed as smoothers. The authors did not discuss any difficulties with their solution process. A comparison of the convergence histories between a single grid calculation and a 4-level multigrid calculation shows that the multigrid procedure requires 76% of the CPU time for the single grid calculation. This inefficiency shows that there might be problems with their implementation of the algorithm.

Vanka (1987) extended his coupled solution multigrid scheme to solve for the turbulent flow problem of an axisymmetric sudden expansion. Again, the $k - \epsilon$ model with wall function was used. The continuity and momentum equations were solved simultaneously by the point SCGS solver. Vanka noted the complexities due to the dominance of the source terms and their nonlinearity in the k and ϵ equations. He also noted the difficulty with the use of the wall function. In his preliminary trials, Vanka had difficulties obtaining

convergence when the k and ϵ equations were solved in a coupled manner with the momentum and continuity equations. He circumvented this problem by solving the k and ϵ equations by a single grid procedure on the finest grid only. He observed that his multigrid solution required 20 times less CPU time than a corresponding SIMPLE solution for the same problem.

Despite the recommendations by Arakawa et al. (1987) and Linden et al. (1988), many investigators prefer to apply SIMPLE-type algorithms as smoothers in their multigrid routines to solve flow problems described by the $k - \epsilon$ model. One reason could be the obvious ease with which the turbulence model equations are to be implemented into the solver. Peric et al. (1989) applied a finite volume multigrid method to compute the turbulent flow over a backward-facing step using the SIMPLE algorithm for error smoothing. They paid special attention to the computation of fluxes on different grids. For instance, the cell-face convective fluxes on the coarse grid were obtained by summing the corresponding fine grid convective fluxes, while the diffusive fluxes were recalculated; the source terms were likewise recalculated for consistency reasons. On a very fine grid, the computational work for multigrid was found to be a hundred times less than that for the standard single-grid procedure. They also found that increasing grid refinement would reduce the range of useful under-relaxation factors.

Lien and Leschziner (1991) also made many interesting observations regarding the use of the multigrid method for calculating complex recirculating turbulent flows. They studied axisymmetric flow in a circular pipe with a sinusoidal constriction. The numerical technique employed was a three-dimensional, non-orthogonal, collocated finite-volume procedure together with the SIMPLE smoothing algorithm. Compared to single grid results, the speedup ratios for the high Reynolds number $k - \epsilon$ model generally ranged from 1.2 to 5.9, with the ratio increasing as the number of control volumes increased. This speedup ratio was significantly less than their laminar results. They observed that

the convergence characteristics were strongly dependent on flow type and geometry, and that the skewness and amount of stretching of the grid affected the performance of the smoother and consequently the multigrid procedure. In addition, the authors presented strategies such as under-relaxing the coarse-grid solutions and conditioning the prolongation process that would help to maintain the realizability constraints $k > 0$ and $\epsilon > 0$.

Rubini et al. (1992) examined the application of the multigrid method to turbulent, variable density flow over a three-dimensional, backward-facing step, using a staggered grid discretization. The standard FMG-FAS technique was used for convergence acceleration while a SIMPLE-type algorithm was used as the smoother. The authors stressed the importance of maintaining mass conservation during restriction and prolongation, and noted that the highly nonlinear nature of the $k - \epsilon$ equations required careful treatment within a multigrid procedure to achieve optimal convergence rates. Additional linearization of the source terms was found necessary to prevent negative values of k or ϵ, which could arise during the prolongation operation in regions of large gradients. The problem was circumvented by simply not updating any locations that would result in a negative value. Their multigrid technique yielded a 25 fold reduction in computer time, but they could not obtain the expected linear increase of computing time with respect to the number of grid nodes. The authors attributed this problem to the use of a low-order prolongation scheme.

Shyy et al. (1993) presented a number of valuable insights into the extension of the multigrid technique to turbulent flows. They discussed three special treatments that were required for the successful implementation of the algorithm. First, the corrections for k and ϵ needed to be checked for negative values after the prolongation procedure. If the requirement was violated, then the same strategy used by Rubini et al. was employed: prolongation would not be carried out for the solution correction at that particular iterative step. Secondly, an upper bound for the turbulent viscosity μ_t was imposed to ensure

that the values of k and ϵ remained realistic during the course of the multigrid procedure. They set the bound to be 10^4 times the laminar value. Thirdly, to alleviate the problem with consistency due to the use of the wall function in different grid levels, the grid line next to the solid boundary was retained during the grid restriction procedure. The convergence rate was found to be improved with this treatment.

So far, several previous studies on applying the multigrid method to turbulent flow problems have been outlined. Our research group has developed a versatile code that can simulate turbulent flows in complicated geometry, with a special focus on applications to problems related to kraft recovery boilers. The problem of a single jet in a crossflow will be used to validate the code and is described in the following section.

3.7 Multigrid Code MGFD for Solving Complex Turbulent Flows

The code developed in our research group is called MGFD and it utilizes the FMG-FAS multigrid algorithm to simulate turbulent flows in complicated geometries. In this section, some salient features of the code are described and the code is validated through the simulation of a single jet in a crossflow. In addition, the efficiencies of several solution methods are examined. A detailed description of the code is given in the report by Nowak (1992).

3.7.1 Features of MGFD

The multigrid scheme used in MGFD is a version of the proven FMG-FAS scheme, which was developed by Nowak (1984). The unique feature of the present version is that the coarse grid solution $\overline{q}_H^j$ is taken from the results obtained in the previous level rather than restricted from the fine grid solution. In some trial runs, this strategy performs as well as the standard FAS scheme, but with less computational cost.

The choice of smoother for the code is based on the need for robustness. The flow patterns in a recovery boiler are very complex. There can be numerous recirculating zones and regions of high velocity gradients due to intense jet interaction. Based on the investigations by Vanka (1986) and Linden et al. (1988), the coupled type smoother line-SCGS scheme was chosen, partly because of its demonstrated reliability and partly because of its conceptual simplicity.

The smoothing of the hydrodynamic equations is carried out as one unit. The relaxation of the k, ϵ, and any other scalar equations is carried out separately, sequentially, and on the finest grid only. The basic Gauess-Seidel scheme is employed with smoothing done along lines traversing in turn to cover all three coordinate directions. In this version, a fixed number of iterations is performed for the equations at each grid level.

The restriction of residual or defect quantities is based on the area-weighted summation of fine grid quantities. Similarly, prolongation of grid variables is carried out using bilinear interpolation. The same prolongation routine is used for both solution transfer and correction transfer. The results have been found to be satisfactory.

Other unique features of the code include its capability to accept a domain subdivided into segments and to perform smoothing sequentially for blocks of cells within a segment. These characteristics are described next.

Segmentation Capability

Even with the multigrid technique, the algorithm may not be optimal for certain types of problems. An important feature of MGFD is that it allows the domain to be subdivided into segments, which are rectangular blocks of cells, for efficient grid distribution. As mentioned earlier in Chapter 1, in a recovery boiler simulation, there is a large variation in dimensions within the domain. The overall dimension of the boiler is much larger than that of an air port. The segmental capability of our code allows the domain to be

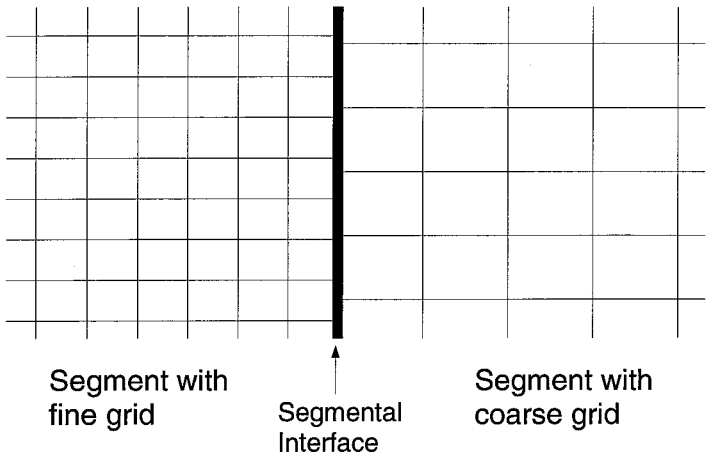

Figure 3.5: Interface of two segments having different grid densities.

covered by a union of segments, each having a different grid density that characterizes the flow phenomena that need to be resolved in different parts of the domain.

For this treatment to be successful in which a domain is divided into segments, it is important to have a conservative scheme to govern the passage of fluxes across segmental boundaries. Working with a similar concept, Thomson and Ferziger (1989) emphasized that the convergence of the method could depend critically on how well this mass conservation is maintained.

The passage of the information of mass fluxes across segmental boundaries is achieved in the following way. Referring to Figure 3.5, at the interface of two segments having different grid densities, the mass flux is computed on the segment that has a finer grid because of the expected higher accuracy in the calculation with this grid. This mass flux is computed through full momentum balance as governed by the Navier-Stokes equations. For each coarse grid cell on the other segment where this mass flux information is to be received, its flux value is obtained by a continuity preserving interpolation process. In this way, global mass conservation is satisfied. The details of the implementation are presented in the report by Nowak (1992).

Smoothing Procedure by Blocks within Each Segment

The iterative relaxation process is performed segment by segment sequentially. Moreover, each segment at each multigrid level is divided into smoothing blocks, each of which consists of a cube of cells. The smoothing within a segment takes place by smoothing within each block sequentially in a 'black-red' manner, thus ensuring efficient coverage of all cells in a minimal number of sweeps. An advantage with this usage of blocks is that the smoothing for cells in different blocks can be carried out with parallel computer processing. Within each block, a line-SCGS process is performed to solve for the variables. The resulting equation is written as a tri-diagonal system, which is solved by the Thomas algorithm. Each coordinate direction is traversed in turn. For most problems, under-relaxation is necessary for velocity, pressure, scalar quantities, turbulent energy, dissipation, and the eddy viscosity. A demonstration of the solution procedure can be found in Salcudean et al. (1992). The validation of the code is the subject of the next section.

3.7.2 Single Jet in a Crossflow : Validation of MGFD

The experimental and numerical results of Simitović (1977) for a single square jet in a confined crossflow is chosen for comparison because of its resemblance to many of our flow situations to be simulated in later chapters. A description of the problem is provided in Figure 3.6. The following values are specified for the problem: $W = 0.0254$ m, $U_C = 6$ m/s, $L_y/W = 2$, and $L_z/W = 4$. These give the following value for the Reynolds number

$$Re = \frac{\rho U_C D_h}{\mu} = 2.7 \times 10^4 \tag{3.31}$$

for properties of air at room temperature, where $D_h = \frac{2L_yL_z}{L_y+L_z}$ is the hydraulic diameter of the tunnel. Different values of jet-to-crossflow velocity ratio V_{jet}/U_C were investigated

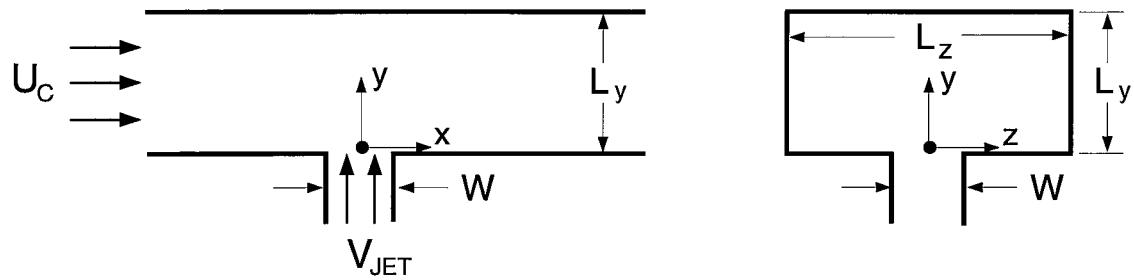

Figure 3.6: A schematic representation of the single square jet in a crossflow studied by Simitović (1977).

by Simitović, but for the validation study to be performed here, we only study the case where $V_{jet} = U_C$.

In the experiment, the mean velocity was measured by a pitot-static pressure probe while the jet fluid concentration was measured by a flame ionization detector, where ethylene was used as the tracer gas. Simitović estimated that the errors in the jet tracer concentration measurements were about $2 - 6\%$.

For the numerical prediction, Simitović applied a 3D-TEACH code to solve the governing equations with the $k - \epsilon$ turbulence model. The domain was extended $9W$ upstream and $10W$ downstream, and the symmetry condition was utilized so that only half of the jet was simulated. The discretization was done on a non-uniform $26 \times 26 \times 26$ grid. Uniform velocity profiles were prescribed at both the main and the jet flows inlet. The zero gradient condition was imposed at the flow outlet. Near the solid boundary, the shear stress was calculated using the wall function.

In our investigation, the TEMA code developed by Lai and Salcudean (1985) is applied to solve the flow problem. The code is similar to the 3D-TEACH. Then multigrid simulations are performed using MGFD. A $36 \times 28 \times 28$ grid is used on the finest grid level. The grid distribution is shown in Figure 3.7.

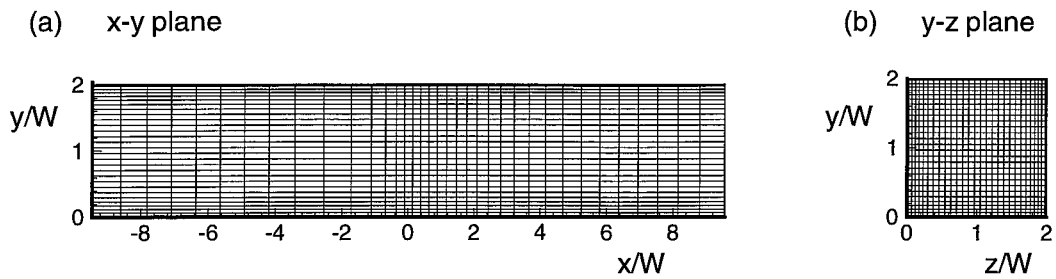

Figure 3.7: Grid distribution for the calculation of a single jet in a crossflow.

Assessment of Multigrid Efficiency

The efficiency of the multigrid procedure is now examined. First, a comparison is made between the basic SCGS relaxation scheme used in MGFD and the sequential SIMPLE-C scheme used in TEMA. Secondly, a comparison is made for the use of different multigrid levels in the calculation. The results of these comparisons validate the correctness, based on performance, of the multigrid implementation.

The convergence of the solution process is monitored by observing the reduction in mass error, which is the residue of the continuity equation. The total mass error is calculated by summing the absolute values of the mass residue of all cells, and is obtained by the following expression:

$$\text{total mass error} = \sum_{\text{all cells}} |r_i| \tag{3.32}$$

where r_i is the mass residue of a typical cell labelled with the subscript i.

The mass error reduction histories are displayed in Figure 3.8 for the following cases: relaxation with SIMPLE-C on a single grid; relaxation with SCGS on a single grid; relaxation with multigrid V-cycle on two grid levels, and relaxation with multigrid V-cycle on three grid levels. The abscissa represents fine grid work units, defined as computer time required for one iteration on the finest grid using the corresponding single-grid scheme. The ordinate represents the total mass error expressed in Eq.(3.32), normalized

by the total mass flow from the mainstream and the jet. In these calculations, the choices for under-relaxation factors are 0.6 for velocity components, 1.0 for pressure, 0.5 for turbulence quantities, and 1.0 for tracer concentration. No particular difficulties in convergence are encountered. The results of the convergence performance are discussed next.

The SIMPLE-C algorithm produces the usual 'ripples' in the residual reduction history that is typical of sequential pressure-correction type algorithms. The overall convergence rate is slow, but it is steady and shows no sign of stalling. The single grid calculation using SCGS shows good reduction of residues during the first 100 iterations. After that, however, the reduction rate slows down significantly. Together these two results illustrate the slowness in attaining convergence by relaxation methods on a single grid. For a smoother to be effective within the multigrid framework, it needs to have good error smoothing properties for high frequency error components. The SCGS scheme shows very rapid reduction of residues in the early stage of the iteration process. This suggests that for the problem considered, it is more effective in reducing high frequency errors than the SIMPLE-type method. This characteristic makes the SCGS scheme more desirable for use with the multigrid algorithm.

Compared to the one-level results, the convergence rate of the two-level calculation is much more rapid. The three-level calculation shows even faster convergence performance. The reason for the better performance is that when using three different grids, a wider range of frequency components of the error function can be smoothed effectively. With proper adjustments made to multigrid parameters such as adjusting the number of iterations to be carried out for the solution correction, it is believed that the 'humps' shown on the error reduction curve for the three-level multigrid calculation (Figure 3.8(d)) can be removed.

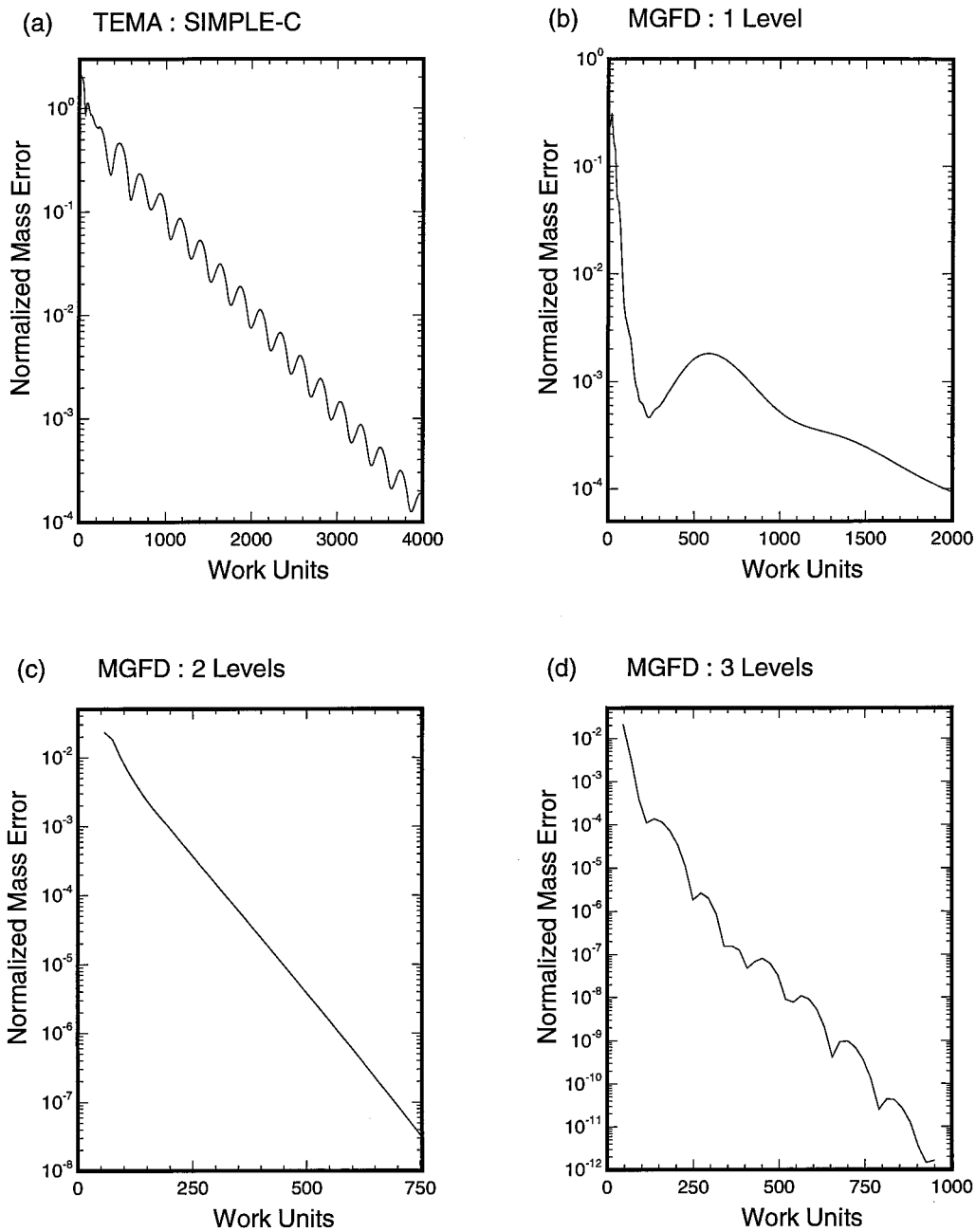

Figure 3.8: Mass error reduction histories for TEMA and MGFD.

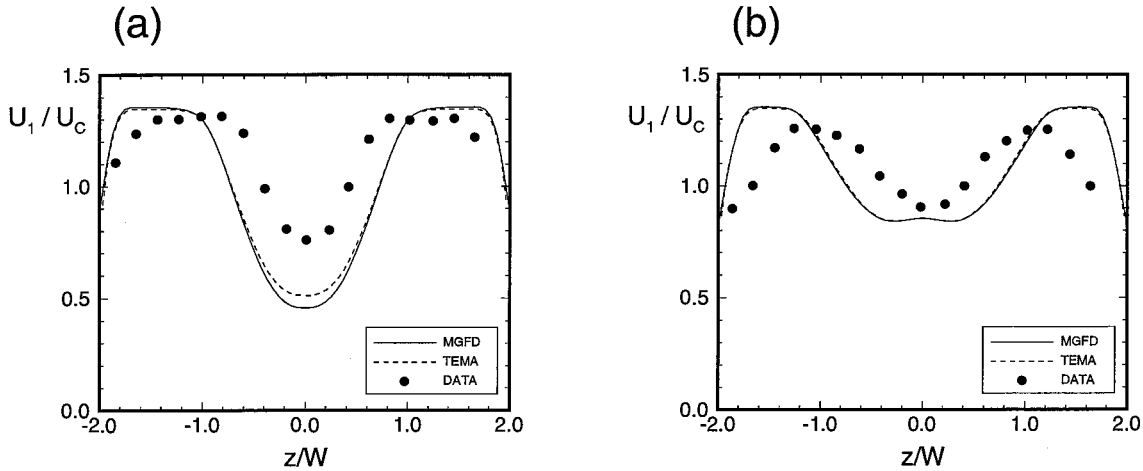

Figure 3.9: Measured and predicted streamwise velocity at $y/W = 1.0$, (a) $x/W = 3.5$, (b) $x/W = 8.25$.

Comparison of Results

The velocity and jet tracer concentration profiles obtained from both the experimental and numerical results are now compared at selected positions. Specifically, the streamwise component of the velocity is compared at the locations $x/W = 3.5$ and 8.25 at $y/W = 1.0$, and $x/W = 3.5$ and 8.25 at $z/W = 0.0$ and 0.5. The tracer concentration is compared at $x/W = 1.75$ and 4.5 at $z/W = 0.0$ and 0.5. These locations are typical of those chosen by Simitović in his study. The results are displayed in Figures 3.9-3.12.

The results show that the agreement between the predictions from the two codes is within a few percents. The results obtained with MGFD exhibit slightly steeper gradients than those obtained with TEMA. This difference is mainly due to the use of different differencing methods in the two codes: hybrid scheme in TEMA and power-law scheme in MGFD. Our predictions using TEMA are visually very similar to those reported by Simitović.

The numerical results exhibit fair agreement with experimental measurements in many regions of the flow field, and is often within $\pm 10\%$, which is probably within

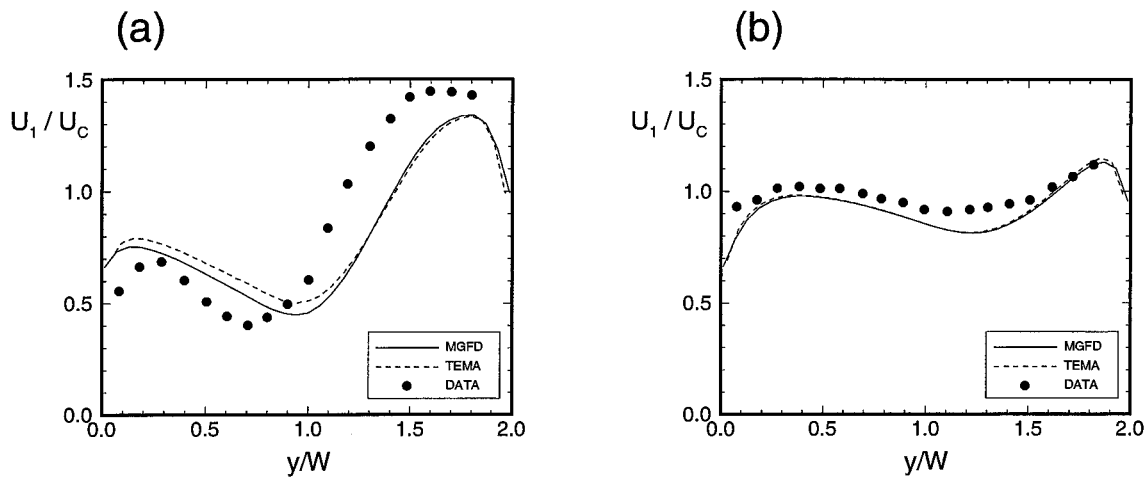

Figure 3.10: Measured and predicted streamwise velocity at $z/W = 0.0$, (a) $x/W = 3.5$, (b) $x/W = 8.25$.

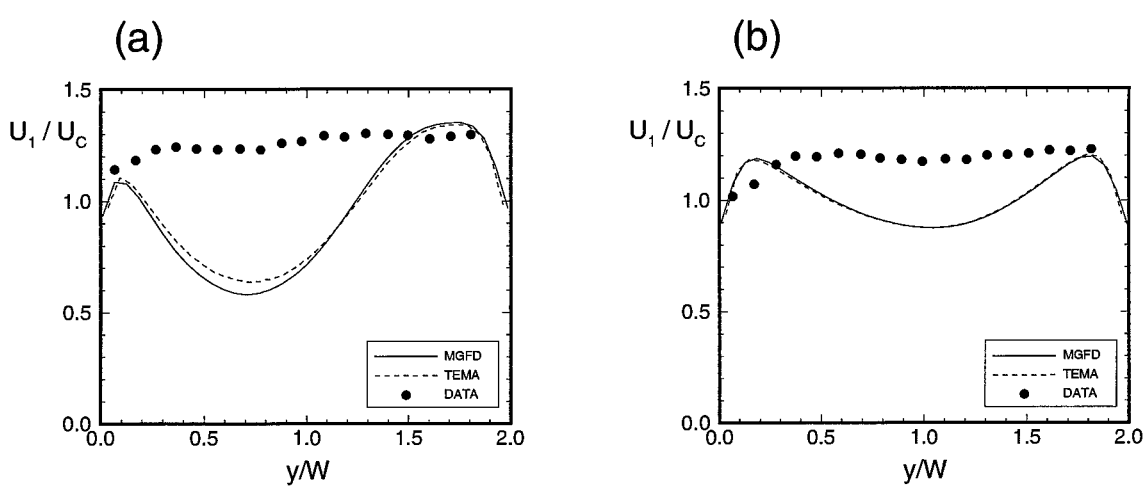

Figure 3.11: Measured and predicted streamwise velocity at $z/W = 0.5$, (a) $x/W = 3.5$, (b) $x/W = 8.25$.

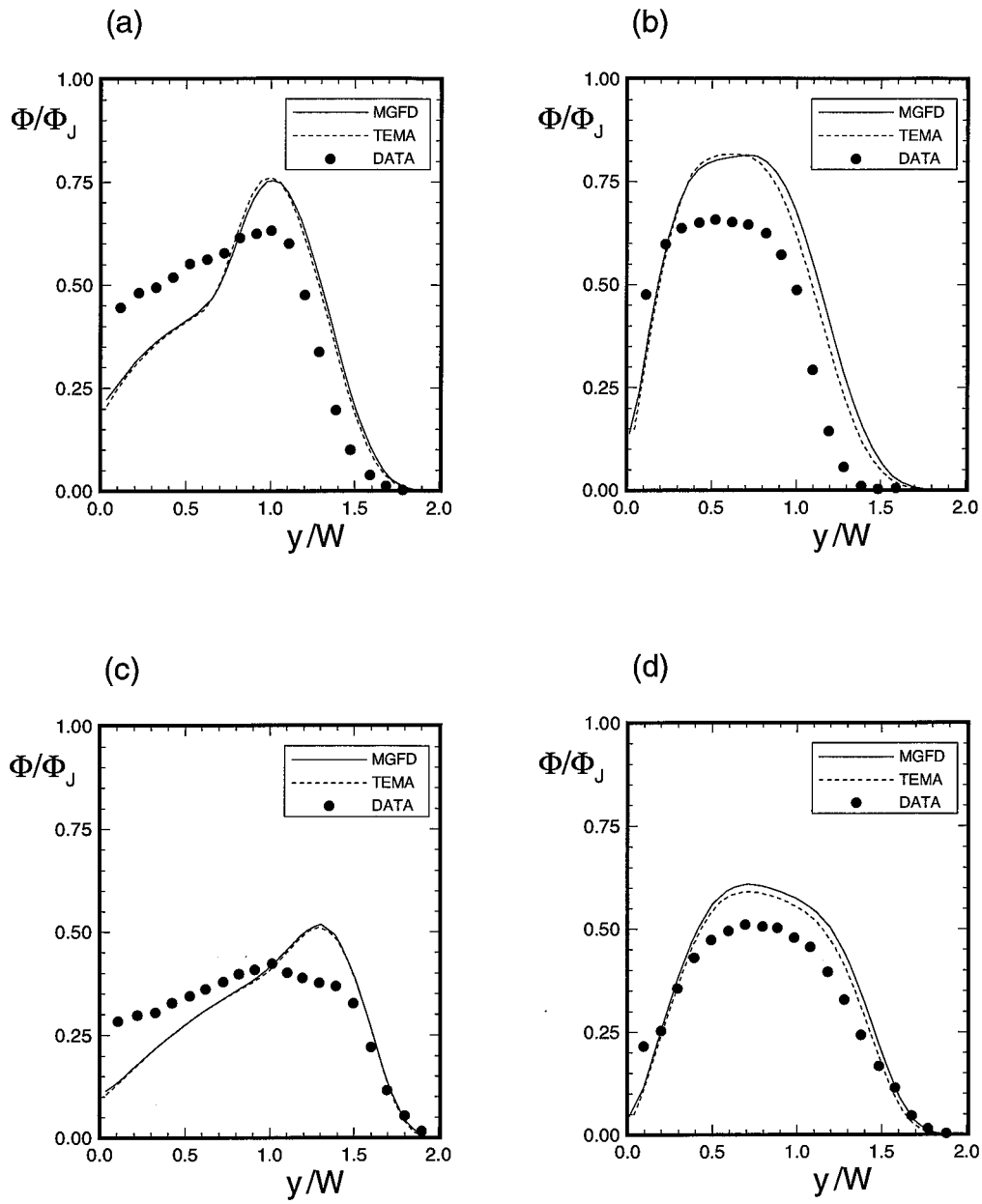

Figure 3.12: Measured and predicted profiles of jet tracer concentration, (a) $z/W = 0.0, x/W = 1.75$, (b) $z/W = 0.5, x/W = 1.75$, (c) $z/W = 0.0, x/W = 4.5$, (d) $z/W = 0.5, x/W = 4.5$.

the range of experimental inaccuracy. The largest discrepancy is found in the velocity distribution in the wake of the jet, which is shown in Figure 3.10(a) and Figure 3.11(a). In the latter figure, the numerical simulation predicts a significant degree of velocity defect; however, this is not supported by the data. Simitović attributed the discrepancy mainly to the measuring problem with the pitot-static pressure probe. The reliability of this type of measurement technique can be affected by strong flow deflection and high turbulence levels. These conditions are very significant in the wake region of a jet in a crossflow. Other causes of discrepancy include the inadequacy of the mathematical model used in the prediction of this type of jet flow. The assumption employed by the $k - \epsilon$ model does not allow for the anisotropy of the turbulent diffusion processes. Moreover, the set of empirical parameters used in the $k - \epsilon$ model has not been tuned for complex flows with recirculation. In addition, the uncertainties about the conditions in the jet as it enters the main duct could cause errors. A more detailed discussion can be found in Simitović (1977).

3.8 Chapter Summary

In this chapter, methods are presented for solving the time-averaged form of the Navier-Stokes equations coupled with the $k - \epsilon$ model and a scalar transport equation. An iterative solution procedure is required, for which the multigrid algorithm can be applied to accelerate the convergence. The feasibility of applying the multigrid technique to the Navier-Stokes system is examined. When applying the technique, careful attention is needed for the multigrid procedure to work as theoretically expected. Important issues are the efficiency and robustness of the equation solver, the conservation of fluxes during grid transfer, and the consistency between the coarse grid problem and the fine grid problem. When the multigrid algorithm is implemented correctly, it can return very fast

convergence rates.

Using the FMG-FAS multigrid algorithm, our research group has developed a code for the prediction of complex turbulent flows. The code is validated through comparison with results obtained with the TEMA code and with experimental data for the problem of a square jet in a crossflow. This problem has relevance for other turbulent jet simulations to be performed later in this study. It is demonstrated that the mathematical model provides a generally good qualitative agreement with the experimental results, and this observation adds confidence to our study of multiple jet interactions to be carried out in the following chapters.

Chapter 4

Simulation of Primary Level Jets

The numerical simulations of primary level jets are presented in this chapter. One of the difficulties with recovery boiler simulation is to represent the large number of small primary air ports that are located around the lower perimeter of the boiler. In a typical design, there can be over a hundred of these primary air ports. A straight-forward modelling effort that includes the representation of every primary air port would require a grid so fine that the modelling effort would become prohibitively expensive and impractical. Moreover, the solution of such a large system of finite difference equations can be very difficult to obtain. Thus, from a numerical modelling perspective, it is necessary to make simplifying assumptions to represent primary jets.

A common practice employed by Jones et al. (1990) in the modelling of these primary ports is to lump several of them together, according to the design of the grid. A simpler approach, used by Salcudean et al. (1992), is to numerically construct a continuous slot spanning across the space that is originally occupied by a row of ports. This practice has been encouraged by the experimental findings in the rapid merging of closely spaced jets by Knystautas (1964), as described in Chapter 2. It is the purpose of this investigation to perform an examination of the quality of continuous slot simulation for primary jets in a kraft recovery boiler.

There are concerns with the turbulent flow simulation of slot jets representing discrete jets. First, flow parameters such as the velocity and mass flow rate need to be selected to reflect similarities between the flows from slots and from discrete ports. Secondly, in

the slot representation the interaction between jets from neighboring ports is neglected, and this can have an effect on the turbulence characteristics of the flow field, and can in turn affect the transport of momentum and scalar quantities. These concerns must be addressed.

This chapter begins with an investigation of the extent of interaction of primary jets. This enables us to judge whether it is appropriate to use the steady state solution algorithm for this application. Then the interaction of primary jets is studied by modelling individual jet openings, and this is referred to as the prototype case. Next, the rows of primary jets are modelled by two types of slot equivalences: open slots and porous slots. Simulations with these slots are performed and the convergence behavior for each simulation is discussed. In each of these simulations, the domain is set up to reflect the bottom portion of the Plymouth water model in the UBC laboratory. Consequently, the char bed is not implemented at this stage in the numerical models. Results of the slot simulations are compared with those of the prototype case. The primary basis of comparison is the distribution of the vertical component of the mean velocity. The distributions of turbulence quantities are investigated to observe any changes in the turbulence characteristics when slot jets are used in place of discrete jets. The effects of different choices of turbulence boundary conditions for the open slot simulation are then addressed. Finally, conclusions and recommendations are made.

4.1 Interaction of Corner Jets

A concern with the prediction of jet flows in a kraft recovery boiler is that the flow field may be unsteady due to the intense interaction of the jets. This has been experimentally observed by Ketler et al. (1992) and numerically simulated by Abdullah et al. (1993). A consequence of this observation is that the prediction of the flow field using an algorithm

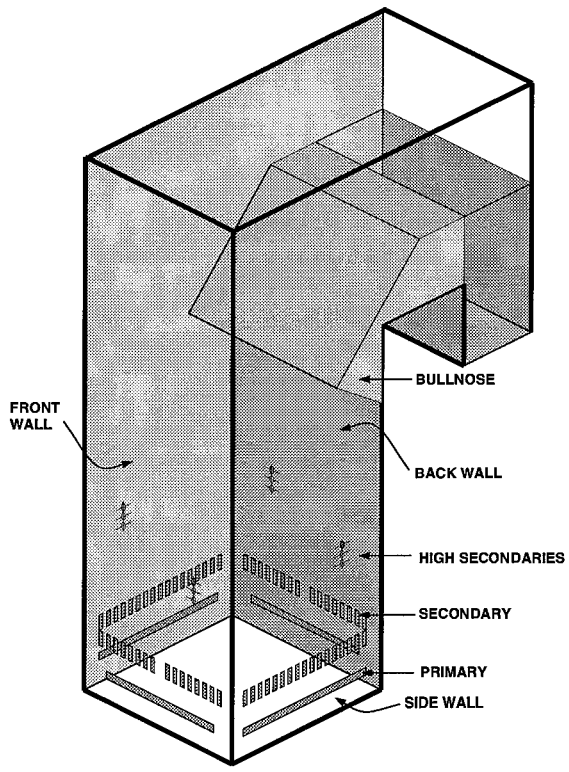

Figure 4.1: A schematic illustration of the Plymouth water model.

for steady flow may not converge. In the simulation of primary jets, even though their velocities are low, there is a possibility that the interaction of jets near the corner of two adjacent walls may lead to flow instability. To examine the suitability of using a solver for steady flow for primary jet simulation, the interaction of several corner jets operating under typical primary jet conditions is studied. A numerical calculation could reveal if unsteadiness exists in the flow field.

The operational characteristics of these corner jets are taken from those of the Plymouth recovery boiler model used in the laboratory at UBC. This is a 1 : 28 scale model constructed primarily of plexiglass. Water is introduced into the model to simulate flow phenomena in a furnace. A schematic drawing of the model is shown in Figure 4.1. A detailed description of the model can be found in Ketler (1993).

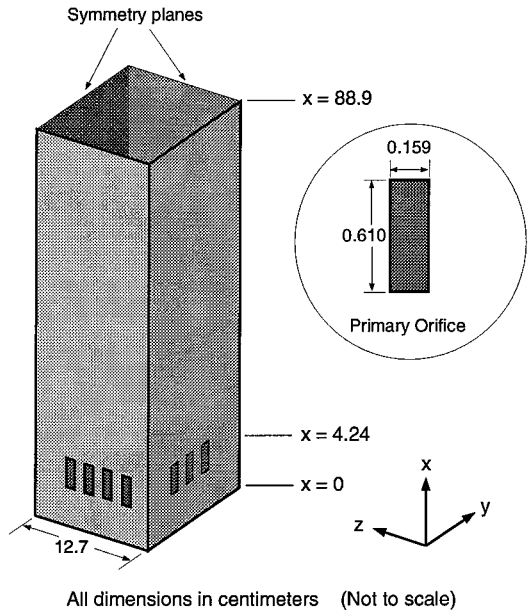

Figure 4.2: Domain for simulating corner jet interaction.

In the simulation, the dimensions of primary ports and the jet velocity are adjusted to reflect the conditions of an actual experiment. The closest seven jets to a corner of the model are simulated: four on one wall and three on the adjacent wall. Each jet orifice has dimensions 0.159 cm (W) by 0.610 cm (L) (0.0625 inches by 0.24 inches). A sketch of the domain is shown in Figure 4.2.

The boundary conditions imposed are as follows: plug-flow condition for the jet velocity; no-slip condition at solid walls; symmetry condition at the two orthogonal planes enclosing the domain, and zero-gradient condition at the top exit plane. The wall function is used to compute the shear stress near the no-slip walls. Symmetry planes are used to limit the size of the domain. These are placed at 0.127 m (5 inches) from the wall corner so they do not affect the interaction of the jets. The top exit plane is located at 0.889 m (35 inches) above the floor. This distance is sufficiently far above the jets such that it is reasonable to assume that the flow is uni-directional at the plane.

At a jet entrance, the magnitude of the jet velocity is set at $V_{jet} = 2$ m/s, with the

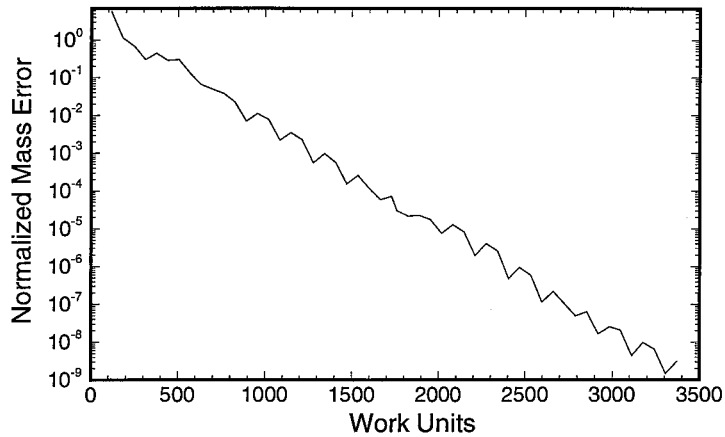

Figure 4.3: Convergence history for the simulation of corner jet interaction.

jet directed slightly downward at an angle of depression of 10°. The turbulent kinetic energy k_{jet} is set at $k_{jet} = 0.005 \times V_{jet}^2$ and the dissipation length scale is chosen to be $L_{diss} = 0.5 \times W$ for the determination of dissipation rate through $\epsilon_{jet} = k_{jet}^{3/2}/L_{diss}$. These choices are made following the usual practice used in jet-in-crossflow calculations.

The domain is segregated into three segments for efficient distribution of grid nodes. A two-level multigrid procedure is carried out to compute the flow field. When the number of iterations performed in each multigrid step is selected properly, convergence is readily obtainable using the steady state algorithm. The convergence history showing the reduction in the total mass error as defined in Chapter 3 is displayed in Figure 4.3. The normalization factor is the total mass inflow from the jets. It is significant to note that the convergence history with the steady state solution algorithm shows no sign of stalling. This observation suggests that a steady state solution does exist and can be obtained by our solution procedure.

This simulation with corner jets provides more challenges for our numerical algorithm than the previous single jet in a crossflow case. Specifically, the number of iterations to be carried out before restriction needs to be increased in order to achieve convergence. For

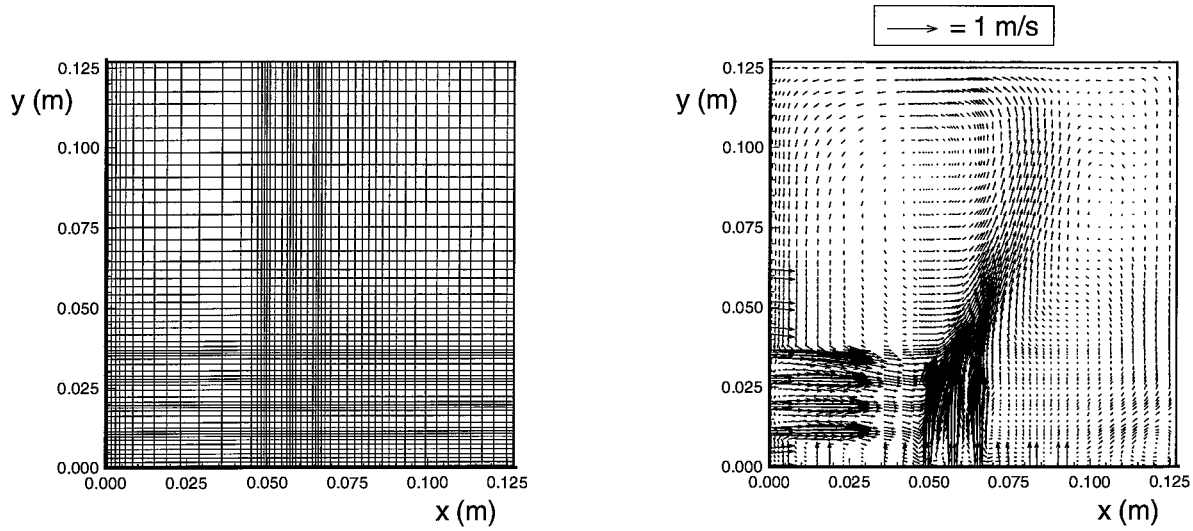

Figure 4.4: Computation mesh and the velocity field at the jet entrance elevation ($x = 4.24$ cm).

the jet-in-crossflow calculation, a good convergence rate is obtained with the number of iterations in this pre-smoothing step set at 10. For calculation of the corner jets, the same number needs to be increased to 50. No attempt is made to optimize the convergence rate by adjusting the number of pre-smoothing iterations.

A velocity vector plot at the elevation of the jet entrances, together with the computational mesh used, is shown in Figure 4.4. The graph shows the collision of the corner jets and the occurrence of recirculating regions in the flow field. The degree of jet interaction is significant, but apparently these primary jets are so weak that their collision is not intense enough to induce any flow unsteadiness. Hence, any flow instability observed in the recovery boiler water model is likely due to the interaction of stronger jets at the two higher levels. This suggestion has been verified by the experimental evidence of Ketler (1993), who observed that the flow field due to primary jets alone was quite steady.

Although the convergence rate is steady, it is slower than the case where a crossflow is present. Physically, the presence of a crossflow can have a stabilizing effect on the flow field by reducing the extent of jet collision. It is apparent that a high degree of

stability in the physical system will manifest itself numerically in improved convergence characteristics.

4.2 Full Discrete Jet Simulation

Having established the suitability of applying the steady state solution algorithm for the computation of primary jet flows, we now apply the algorithm to simulate a more complete set of primary jets. The results will be used as our prototype case, to which the results of the slot simulations will be compared.

In the Plymouth model, there are 156 primary ports arranged almost symmetrically around a square cross-section in close proximity to the floor. Since only the dynamics of primary jet interaction is desired, the representation of the domain is simplified by neglecting the complex physical structures that are presented in the upper portion of the Plymouth model. Due to computer memory limitations, only a quarter of this bottom region can be simulated with all the primary ports included. The domain of calculation is similar to that depicted in Figure 4.2, but there are now 17 jets along the y-direction and 22 jets along the z-direction. A three-dimensional sketch of the domain is presented in Figure 4.5.

The domain is again divided into three segments. The grid used is shown in Figure 4.6. The simulation requires 153984 cells, which is much too numerous to be incorporated into a full scale boiler simulation. Boundary conditions are prescribed in much the same way as in our earlier calculation for corner jets, except that the symmetry planes are now located at 0.194 m (7.65 inches) from the corner, which is the midpoint location on one side of the Plymouth model. A two-level multigrid cycling process is used for the calculation and the convergence history is displayed in Figure 4.7. The results of the flow field will be shown later when compared with the slot representations. The

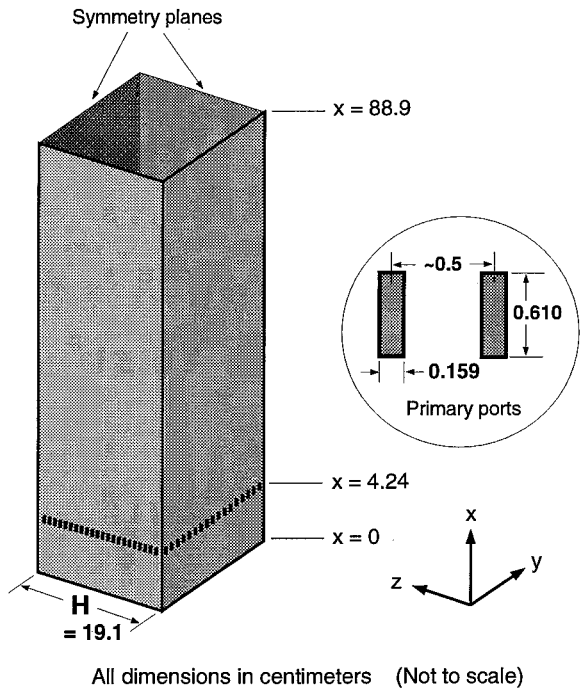

Figure 4.5: A three-dimensional view of the computation domain.

computational requirement for this full discrete jet simulation is about 43 megabytes of RAM.

The convergence rate is similar to the corner jet simulation. However, compared to the previous case, a much longer computational time is required for this calculation since the domain is comprised of many more cells. It is important to remark that in a trial calculation where smoothing is performed only on a single grid level, the convergence stalls after approximately a thousand iterations. This observation illustrates the significance of the multigrid method: not only does it provide faster convergence, in some particularly difficult cases it gives convergence where a standard iterative method fails.

Having established the prototype case for comparison, the two types of slot representations for primary jets are now considered.

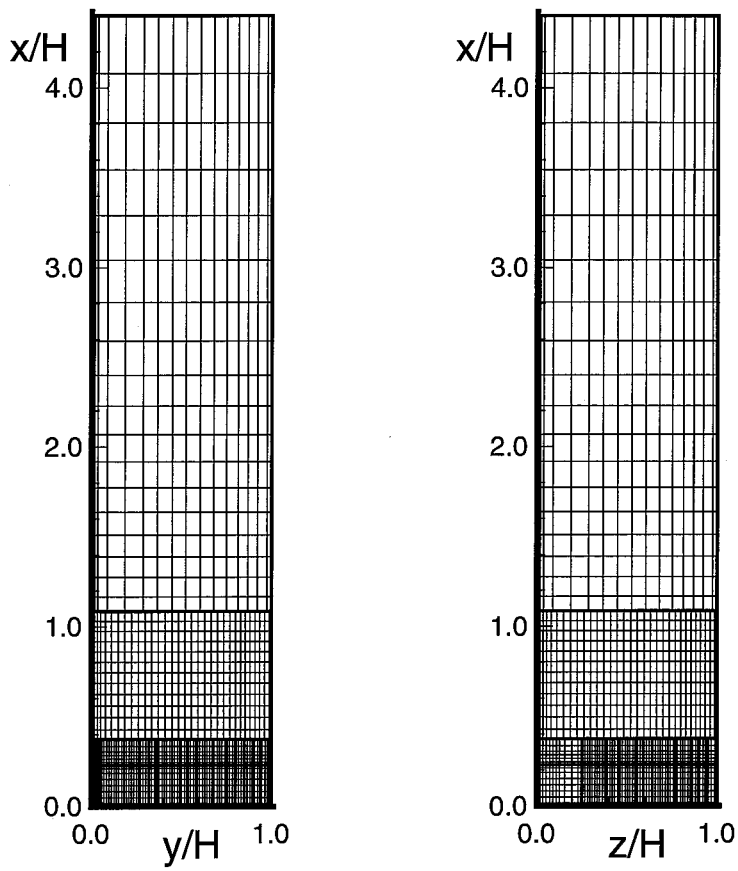

Figure 4.6: Computation mesh used in the primary discrete jet simulation.

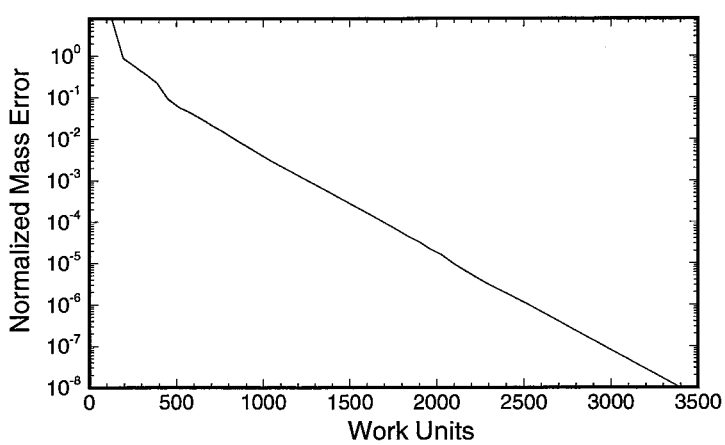

Figure 4.7: Convergence history for the full primary discrete jet simulation.

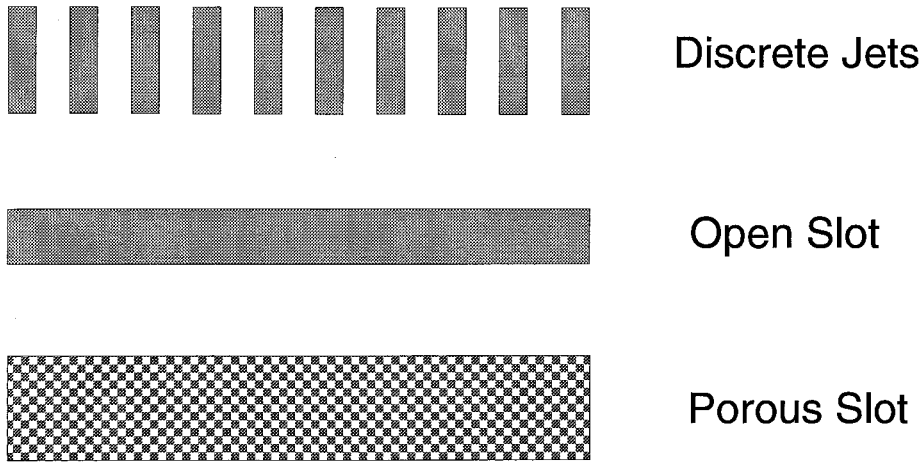

Figure 4.8: Representations of primary level jets: discrete jets, open slot, and porous slot.

4.3 Slot Representations of Primary Jets

The two types of slot representations, open slots and porous slots, are examined. The criteria for the simulation are to maintain the same mass flow rate and the jet velocity. The slots span across the same space that is occupied by the discrete primary ports. A schematic illustration contrasting the three simulations is shown in Figure 4.8. The modelling of these slot jets are discussed next.

4.3.1 Open Slots

An advantage of simulating primary jets with open slots is the simplicity of the representation. These slot jets are simulated simply by allocating cells on the sides of the domain to constitute the opening of the slots. This is done by assigning the velocity values at those cells in accordance with the desired jet velocity, which is chosen to be the same as that of the original primary jets. To maintain the same mass flow rate, the height of each slot must be less than the height of an individual air port so that the total area

is the same. For the simulation, the following dimensions are used: in the y-direction, the slot spans from 4.89 cm to 19.4 cm (1.909 inches to 7.65 inches). In the z-direction, the slot spans from 1.04 cm to 19.4 cm (0.409 inches to 7.65 inches). A height of 0.115 cm (0.0451 inches) is selected to give the slots a combined total area of 3.77 cm^2 (0.585 square inches), the same total area of the discrete jet orifices for which the simulation is intended.

Boundary conditions are treated the same way as in the prototype case: plug-flow condition for velocity; no-slip condition at solid walls; symmetry condition at the two orthogonal planes bounding the domain; zero-gradient condition at the top exit plane, and the wall function for cells near the no-slip walls. The main concern is with the choice of the turbulence parameters. The objective is to choose boundary values for k and ϵ such that the simulated flow field is similar to the prototype case.

The value for k_{jet} is chosen as before, that is, $k_{jet} = 0.005 \times V_{jet}^2$. However, the choice for ϵ_{jet} is not as obvious. There is no clear choice for the dissipation length scale L_{diss}. In the simulation with discrete jets, L_{diss} is chosen to be half of the smaller dimension (width) of an orifice, which is a common practice. For the open slot simulation, the slot is only a mathematical abstraction of the row of jets it represents, and hence the proper value of L_{diss} is not clear. For simplicity reasons, L_{diss} is chosen to be the same as that of the earlier case, $L_{diss} = 0.5 \times W$ where W is the width of an original primary jet orifice. Then ϵ_{jet} is computed through $\epsilon_{jet} = k_{jet}^{3/2}/L_{diss}$, which yields a value the same as that used in the prototype case.

A two-level multigrid scheme is used for the calculation. This grid is much coarser in the y and z directions than in the prototype case. Figure 4.9 shows the mesh used in this simulation. This simulation requires 36432 cells, about 24% of that used in the full discrete jet simulation. The convergence history is displayed in Figure 4.10. The convergence rate is similar to that of the previous cases, but the computational time is

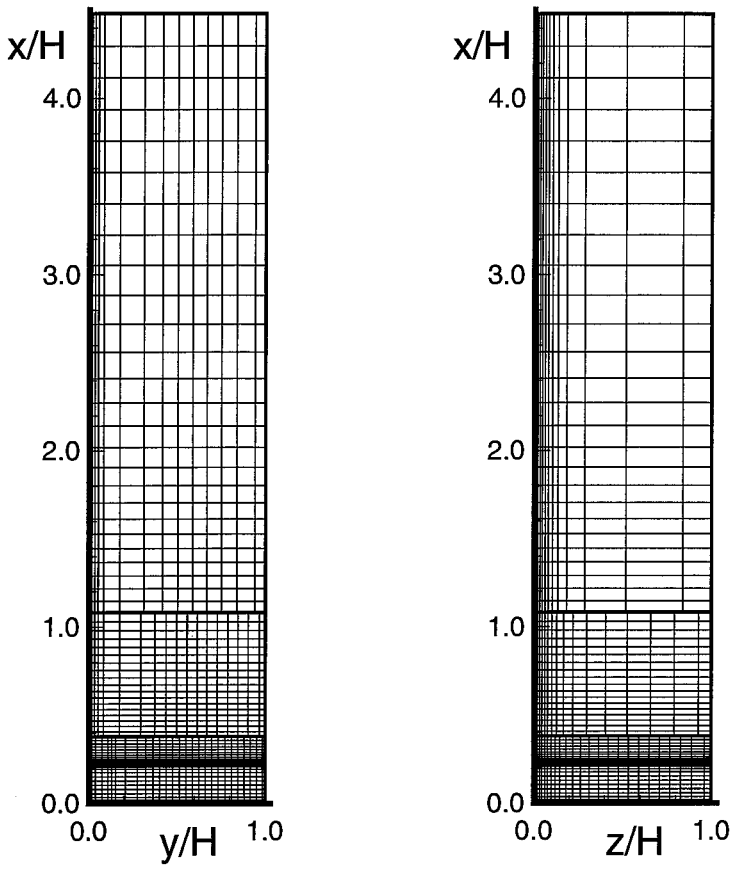

Figure 4.9: Computation mesh used in the slot jet simulation.

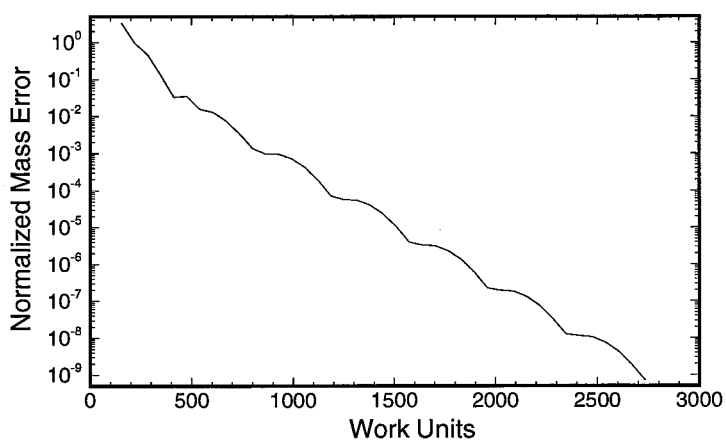

Figure 4.10: Convergence history for the open slot simulation.

much shorter due to the coarser grid. The results are shown later in section 4.4 where comparisons are made.

4.3.2 Porous Slots

In the simulation with porous slots, slots of the same span are again introduced to represent the rows of primary jets, but this time the height of each slot is set to be the same as that of an individual primary port. This physical parameter is preserved because it is thought that the resulting prediction for the velocity field may be more like the prototype case, particularly in regions near the slots.

The velocity of the fluid entering through these enlarged slots is set to be the same as that used for open slots. To keep the same amount of mass flux entering through the slots, the increase in the entrance area must be countered by the introduction of a porosity factor. For incompressible flow, because the density is constant, this porosity factor ζ can be defined simply as the ratio of the total area of the original ports to the area of the porous slot representing those ports. That is,

$$\zeta = \frac{\sum \text{ Area of Discrete Jets}}{\text{Area of Slot}} \tag{4.1}$$

This parameter is introduced into the code to adjust the mass flux entering through boundary cell faces where a porous slot is located. Specifically, at a boundary cell face denoted as $(\Delta x)(\Delta y)$, The mass flux entering the face is set to be

$$\text{Mass Flux} = \zeta \times [\rho_{jet} V_{jet} (\Delta x)(\Delta y)]_{\text{enlarged porous slot}} \tag{4.2}$$

This value of the mass flux is used in the computation of the coefficients in the finite difference equations. To summarize, the product of this effort is to have jets entering the domain at the same magnitude of velocity but through larger slots; the total amount of the mass flux entering is maintained as in the previous cases with the use of this porosity

factor. This strategy is sometimes used in computer simulations by researchers in the boiler industry.

Before the set-up in our simulation is discussed, it is necessary to point out a concern for numerical difficulties with this porosity approach. In this approach, the *effective* area is different from the *total* area on the side of the cell where the slot is located. From continuity of mass there will be changes of velocity or inflow/outflow in the first cell, leading to possible changes in momentum flux on the opposite side. The pressure change necessary to effect this change in momentum flux is an artifact of the porosity assumption and is not physically correct. The momentum flux leaving the cell determines in part the characteristics of the jet and this causes a new and physically incorrect boundary condition for the jet entry. The effect of this change of boundary conditions and the degree to which grid refinement may affect the overall result are problem specific and need to be examined further. Present comparisons are interesting but must be treated with some reservation.

In our simulation, the following values of the porosity factor are used: $\zeta = 0.185$ for the slot spanning along the y-direction and $\zeta = 0.190$ for the slot spanning along the z-direction. The mesh used for this simulation is identical to that used in the previous open slot case. The boundary conditions are also the same. Specifically, the same choices of k_{jet} and ϵ_{jet} are made. The convergence rate is similar to the open slot simulation. The quality of this simulation will be considered in the next section, where comparisons will be made for all three simulations discussed.

4.4 Comparison of Mean Up-flow Velocity

A criterion for assessing the quality of each slot representation is the distribution of the vertical component of the mean velocity at various elevations. This criterion is chosen

because the regions of up-flow and down-flow are represented by the distribution of this velocity component. The extent of these regions of up-flow and down-flow affect the nature of flow interactions in the upper region of the boiler. Results of the distribution of the mean velocity component at the elevations $x = 4.24$ cm (1.67 inches), 7.62 cm (3 inches), and 17.78 cm (7 inches) are shown in Figures 4.11-4.13 for the three simulations. The lowest elevation corresponds to the jet entrance level.

An examination of Figures 4.11-4.13 reveals that the use of either open slots or porous slots gives results that are in reasonably good agreement with the prototype results. This is already evident at the jet entrance level, and more so at higher elevations. At the jet entrance level, shown in Figure 4.11, the extent of up-flow and down-flow is similar among the three cases, with the exception of the region near the lower right corner at $y/H = 1.0$ and $z/H = 0.0$. This discrepancy is caused by the use of continuous slots across $y/H = 1.0$ in both the open slot and porous slot simulations. By examining the magnitude of the velocity peaks located at the center of each graph in Figure 4.11, it is seen that the porous slot simulation gives results that show slightly more resemblance to the prototype case than do the results of the open slot simulation. The porous slots preserve the height of the jet opening, and give a better representation of the flow field at elevations close to the jet entrances. However, further up at $x = 7.62$ cm and 17.78 cm, the results shown in Figures 4.12-4.13 reveal that both slot representations give similar velocity distribution to the prototype case, and that the advantage of the porous slot simulation diminishes.

To summarize, our results verify that it is reasonable to represent rows of closely spaced jets such as the primary level jets with slots. In the simulation of slot jets using the $k - \epsilon$ model, we obtain results of the velocity field that resemble the prototype case when we choose values for the turbulent energy and its dissipation rate at the jet entrances to be the same as those used in the prototype case. The results with porous

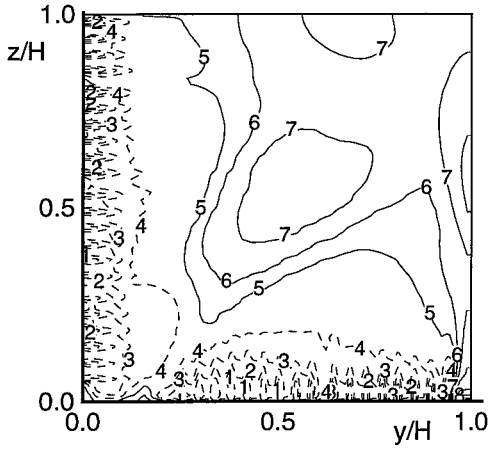

Discrete Jets

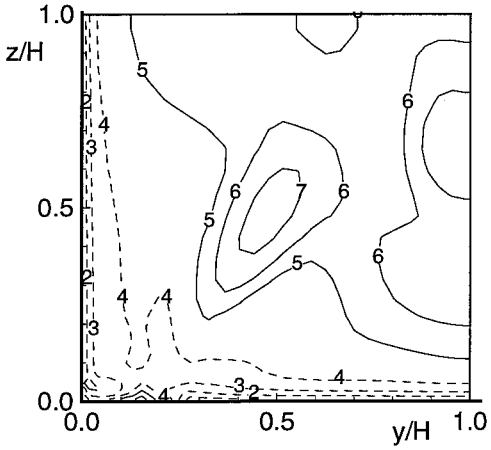

Open Slots

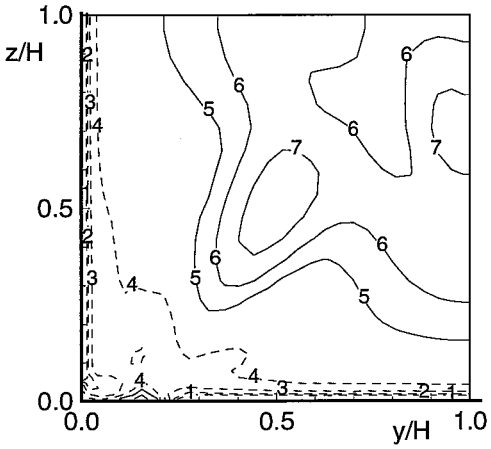

Porous Slots

Levels	U/V_{jet}
9	0.16
8	0.12
7	0.08
6	0.04
5	0.00
4	-0.04
3	-0.08
2	-0.12
1	-0.16

Figure 4.11: Distribution of the vertical velocity component at $x = 4.24$ cm.

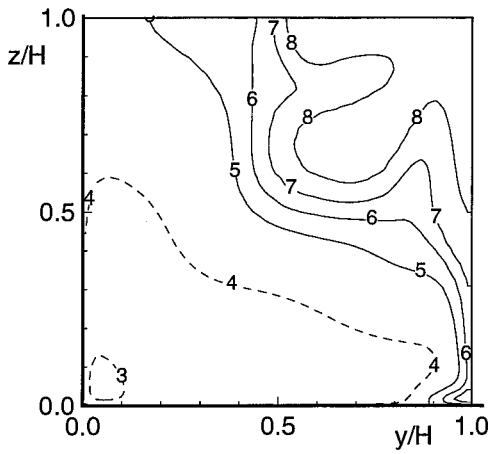

Discrete Jets

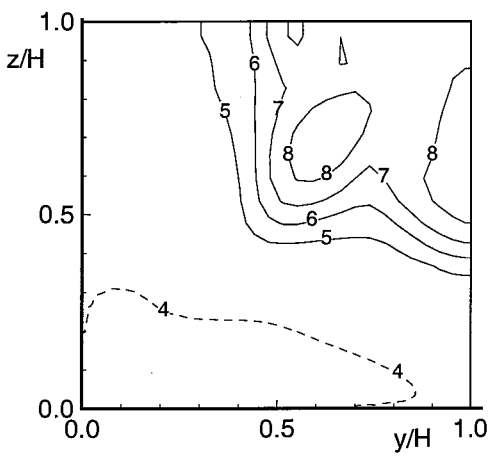

Open Slots

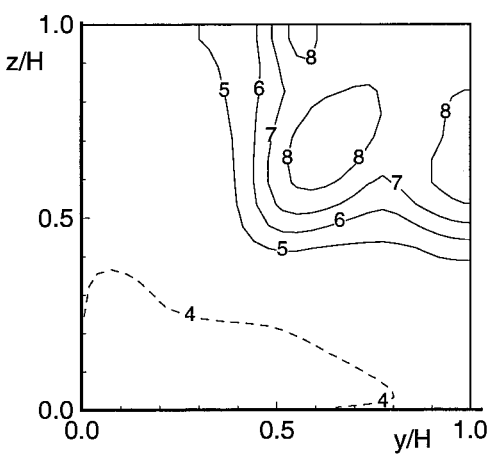

Porous Slots

Levels	U/V_{jet}
9	0.16
8	0.12
7	0.08
6	0.04
5	0.00
4	-0.04
3	-0.08
2	-0.12
1	-0.16

Figure 4.12: Distribution of the vertical velocity component at $x = 7.62$ cm.

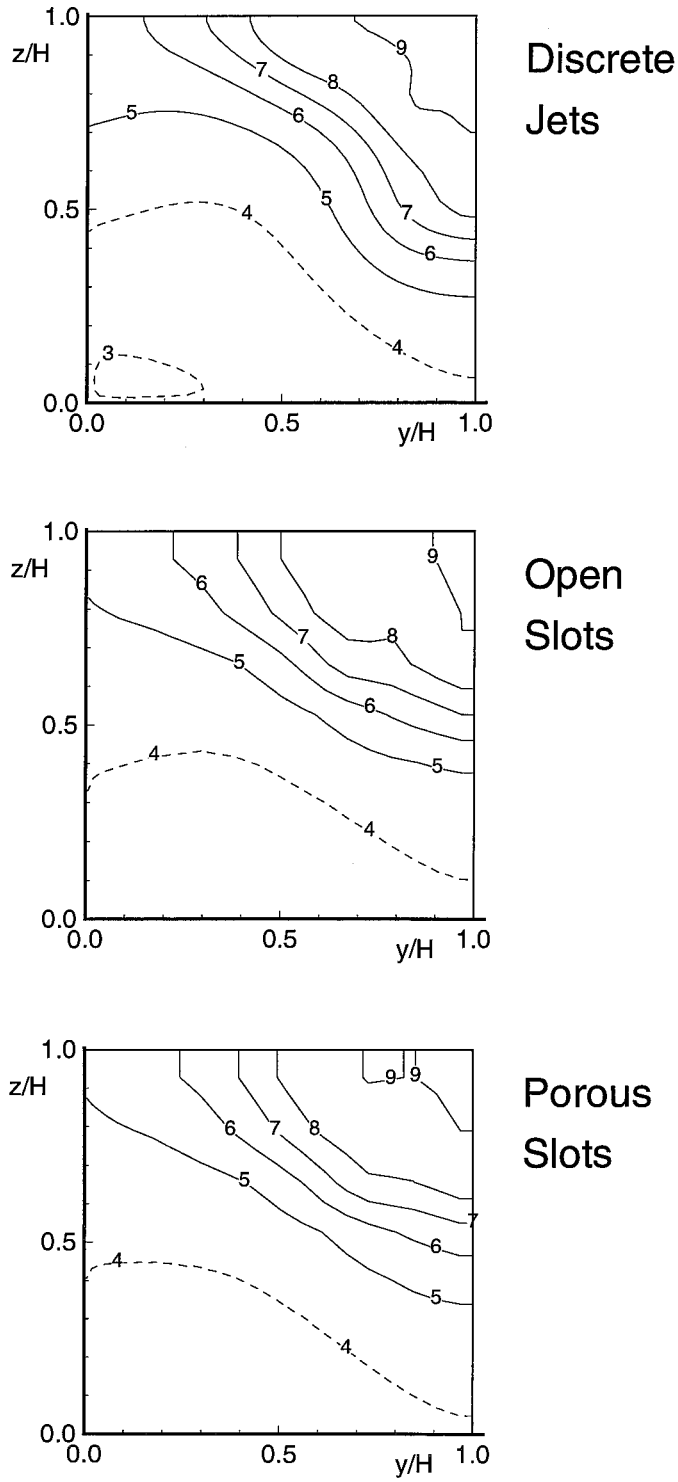

Levels	U/V_{jet}
9	0.16
8	0.12
7	0.08
6	0.04
5	0.00
4	-0.04
3	-0.08
2	-0.12
1	-0.16

Figure 4.13: Distribution of the vertical velocity component at $x = 17.78$ cm.

slots are only marginally better than those with open slots, and the benefit is limited to elevations close to the jet entrances.

4.5 Comparison of Turbulence Quantities

A concern with these slot representations is that a lower level of turbulent energy may be predicted compared to the prototype results due to the neglect of turbulence generated by shear in regions between neighboring jet orifices. A series of jets in-line will develop intense turbulence intensity near the jet outlets due to the shear layers surrounding each jet. A slot will lack this intensity in the near field and it is therefore important to check the turbulence characteristics in the simulation of closely spaced jets by slots.

The distributions of the turbulent kinetic energy and its dissipation rate are examined at the jet entrance elevation for the three simulations. The results are shown in Figures 4.14-4.15, which illustrate the steep gradients in both k and ϵ near the jet outlets. Magnified views for the turbulent energy and its dissipation rate for the prototype simulation with discrete jets are shown in Figure 4.16 for clarity.

The results shown in Figure 4.16 reveal that there is substantial generation of turbulent energy in regions between each pair of neighboring jets, but the regions of high levels of k also correspond to those of high levels of ϵ. Thus, the turbulent energy generated is dissipated rapidly over a short distance, and the distinction in the turbulence characteristics due to the simulation of discrete jets is very localized, as can be seen in Figures 4.14 and 4.15.

Results of turbulent energy distribution at higher elevations are shown in Figures 4.17-4.18. The results illustrate that the prototype (discrete jets) case gives values of k that are larger than the slot representations give. The corresponding results of the dissipation rate ϵ are shown in Figures 4.19-4.20. A comparison of these latter graphs to

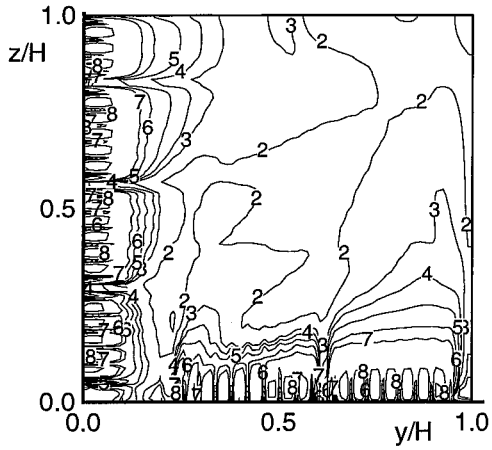

Discrete Jets

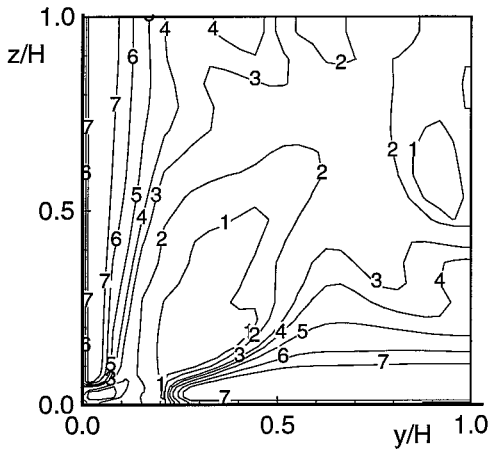

Open Slots

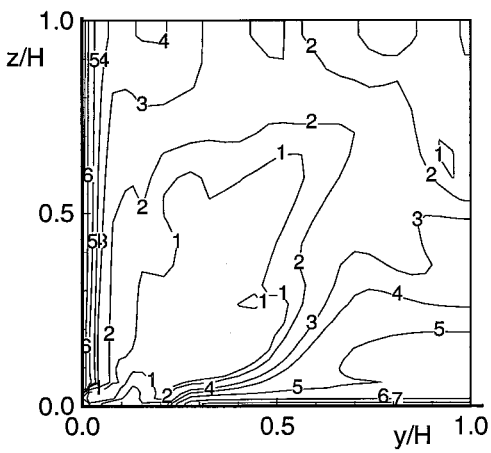

Porous Slots

Levels	k / V_{jet}^2
9	0.100
8	0.050
7	0.020
6	0.015
5	0.010
4	0.007
3	0.005
2	0.002
1	0.001

Figure 4.14: Distribution of turbulent kinetic energy at $x = 4.24$ cm.

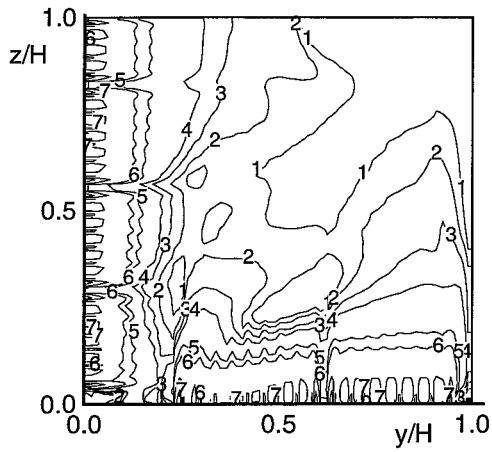

Discrete Jets

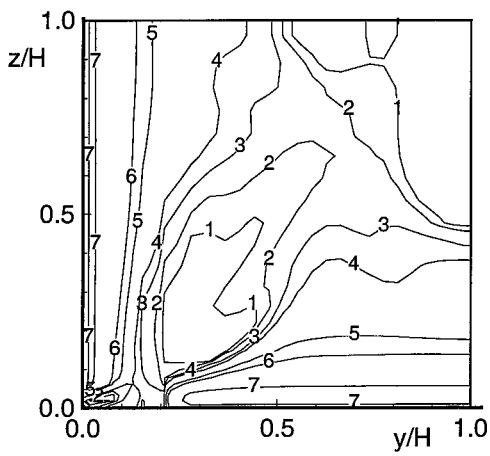

Open Slots

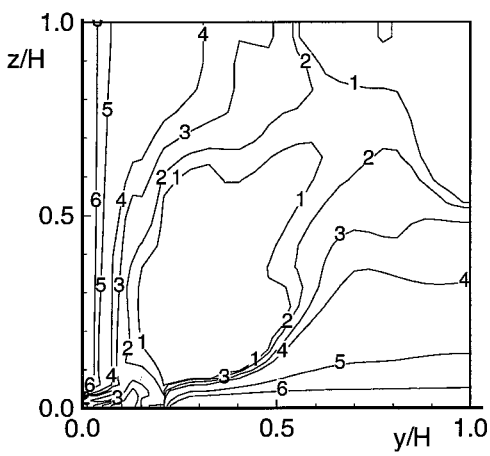

Porous Slots

Levels	ε / (V_{jet}^3/H)
9	5.000
8	1.500
7	0.500
6	0.100
5	0.050
4	0.010
3	0.005
2	0.002
1	0.001

Figure 4.15: Distribution of dissipation rate of turbulent kinetic energy at $x = 4.24$ cm.

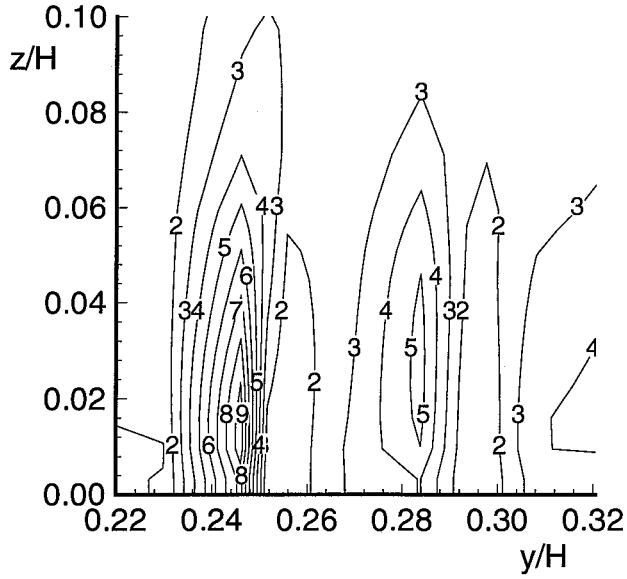

Turbulence Energy

Levels	k / V_{jet}^2
9	0.098
8	0.086
7	0.074
6	0.062
5	0.050
4	0.038
3	0.026
2	0.014
1	0.002

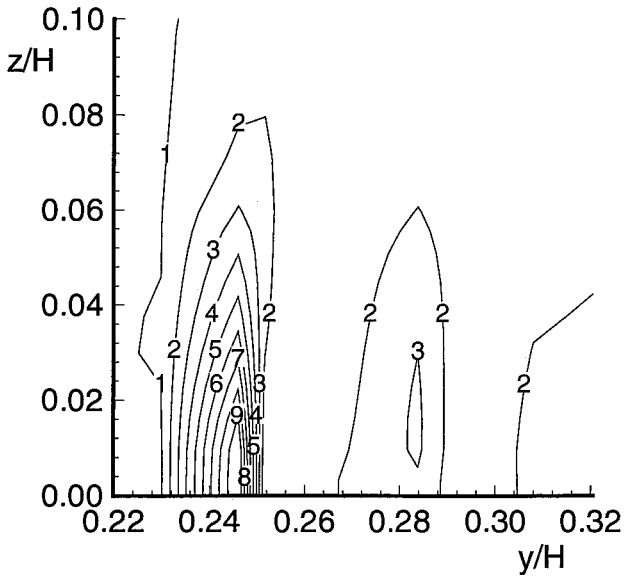

Energy Dissipation

Levels	$\varepsilon / (V_{jet}^3/H)$
9	2.45
8	2.15
7	1.85
6	1.55
5	1.25
4	0.95
3	0.65
2	0.35
1	0.05

Figure 4.16: Magnified views of the distributions of turbulent energy and its dissipation rate for discrete jets.

Figures 4.12 and 4.13 yields the observation that the regions of low values of ϵ correspond to the regions of down-flow. The steep gradients of ϵ near the wall are the result of the adoption of the wall function formulation in the simulations.

Of more interest to the phenomenon of fluid mixing is the distribution of the turbulent viscosity $\mu_t = C_\mu \rho k^2/\epsilon$. This quantity affects the extent of diffusive transport of scalar tracer and momentum. An examination of the turbulent viscosity distribution at the jet entrance level, displayed in Figure 4.21, shows that the detailed distribution of the turbulent viscosity resulting from the various simulations are not alike, particularly near the jet entrances. In the prototype case, much higher values of μ_t are predicted near the jet entrances compared to the slot cases.

The distribution of μ_t at higher elevations is shown in Figures 4.22-4.23. The shapes of the distribution obtained from various simulations attain similarity in overall shapes as the elevation increases. However, the prototype case gives values of μ_t that are consistently around one and a half times greater than those produced by slot representations.

The fact that higher values of μ_t are simulated in the prototype case is of interest. Because of the role of μ_t in the diffusive transport of scalar tracer and momentum, a lower value predicted by slot jets may imply that the transport of fluid can be appreciably affected. This observation points to the precaution one must take when attempting to represent a row of discrete jets by their slot equivalences in boiler simulations. The seemingly good agreement in the velocity distribution shown in the last section through the use of either open slots or porous slots may not be a sufficient assurance for the validity of slot representations.

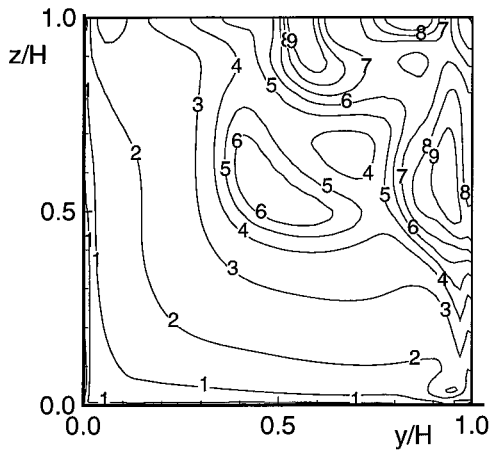

Discrete Jets

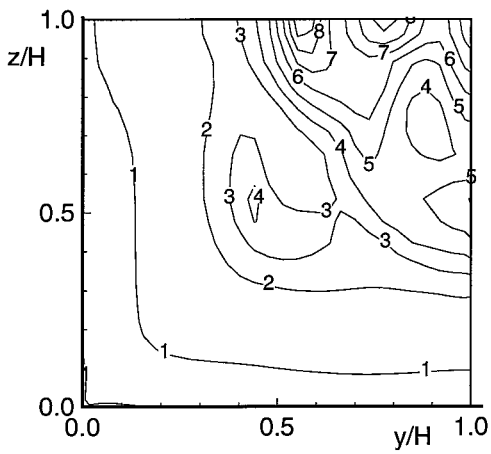

Open Slots

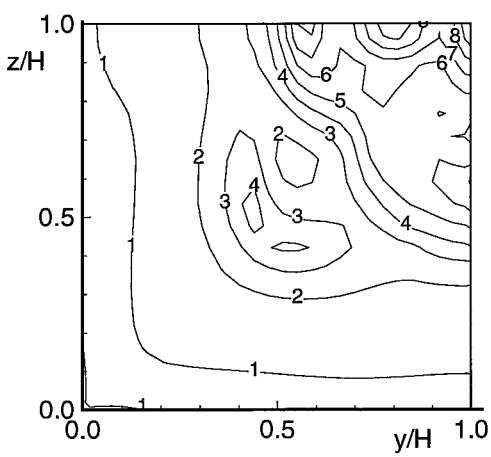

Porous Slots

Levels	k / V_{jet}^2
9	0.0027
8	0.0024
7	0.0021
6	0.0018
5	0.0015
4	0.0012
3	0.0009
2	0.0006
1	0.0003

Figure 4.17: Distribution of turbulent kinetic energy at $x = 7.62$ cm.

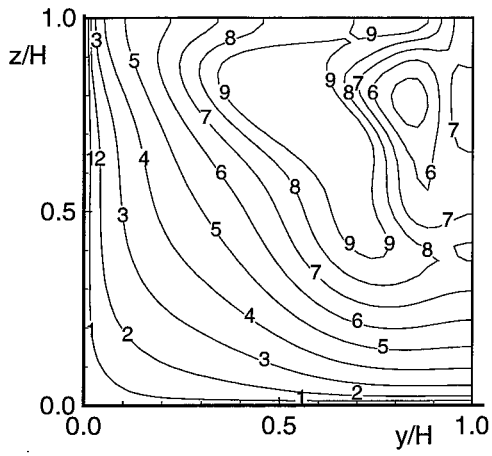

Discrete Jets

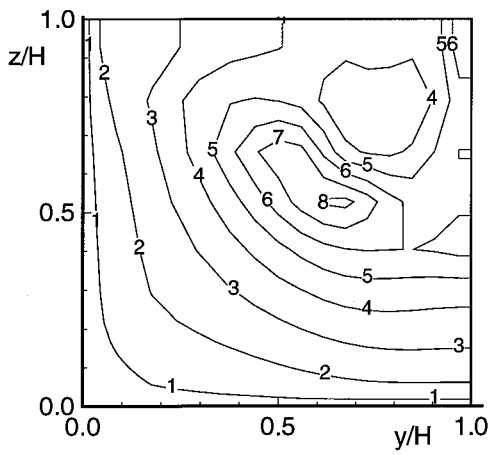

Open Slots

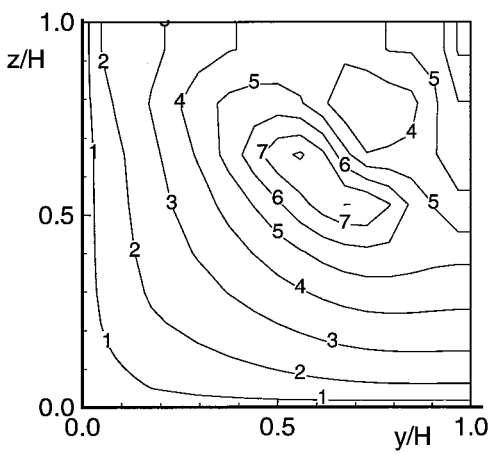

Porous Slots

Levels	k / V_{jet}^2
9	0.0018
8	0.0016
7	0.0014
6	0.0012
5	0.0010
4	0.0008
3	0.0006
2	0.0004
1	0.0002

Figure 4.18: Distribution of turbulent kinetic energy at $x = 17.78$ cm.

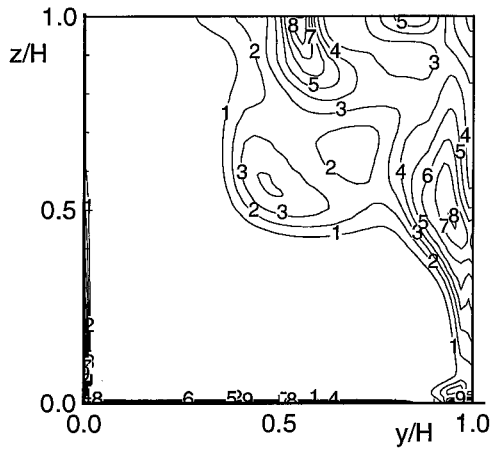

Discrete Jets

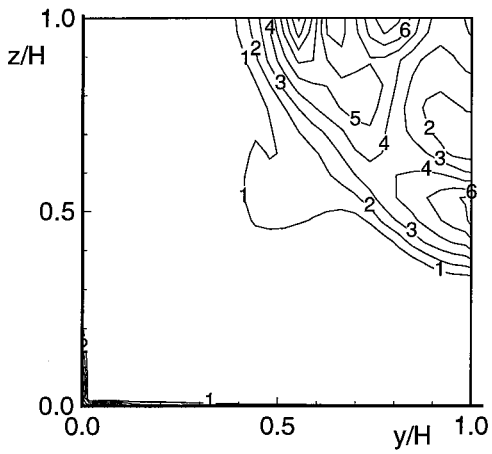

Open Slots

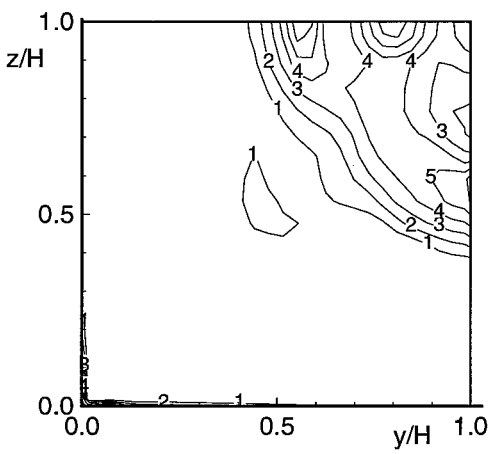

Porous Slots

Levels	$\varepsilon / (V_{jet}^3/H)$
9	0.00145
8	0.00130
7	0.00115
6	0.00100
5	0.00085
4	0.00070
3	0.00055
2	0.00040
1	0.00025

Figure 4.19: Distribution of dissipation rate of turbulent kinetic energy at $x = 7.62$ cm.

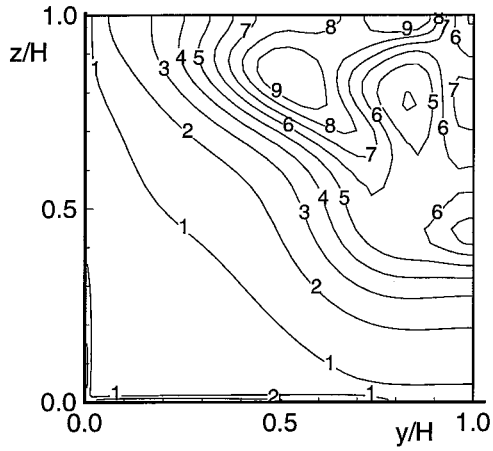

Discrete Jets

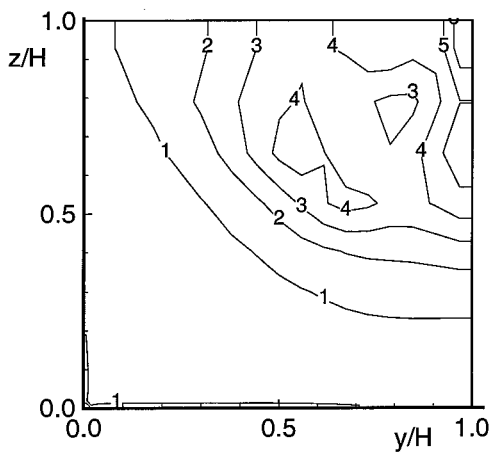

Open Slots

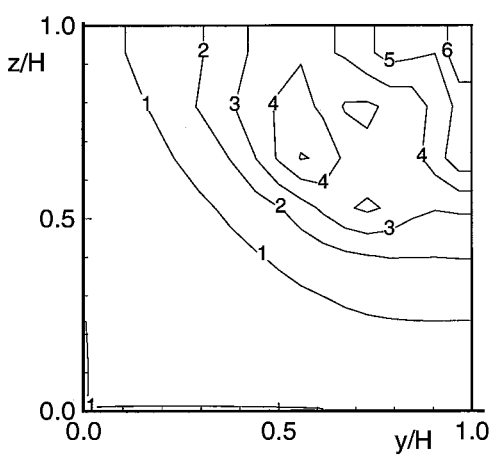

Porous Slots

Levels	ε / (V_{jet}^3/H)
9	0.00036
8	0.00032
7	0.00028
6	0.00024
5	0.00020
4	0.00016
3	0.00012
2	0.00008
1	0.00004

Figure 4.20: Distribution of dissipation rate of turbulent kinetic energy at $x = 17.78$ cm.

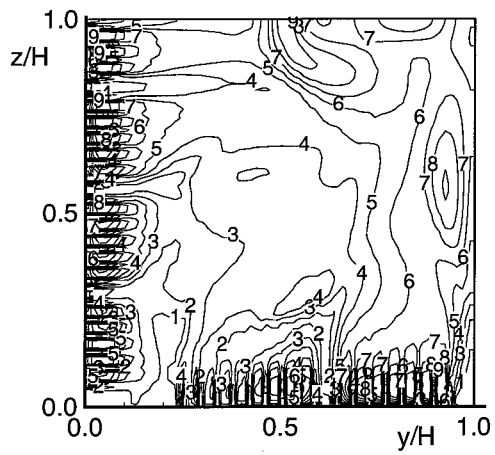

Discrete Jets

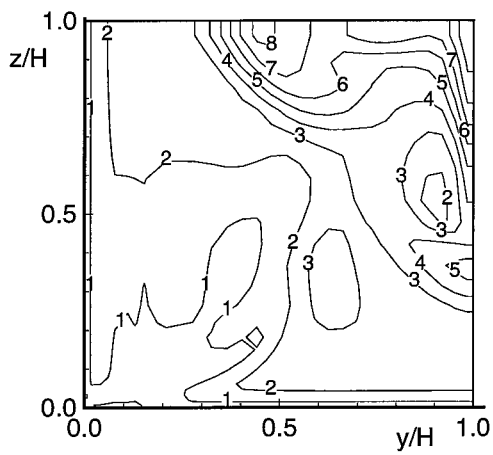

Open Slots

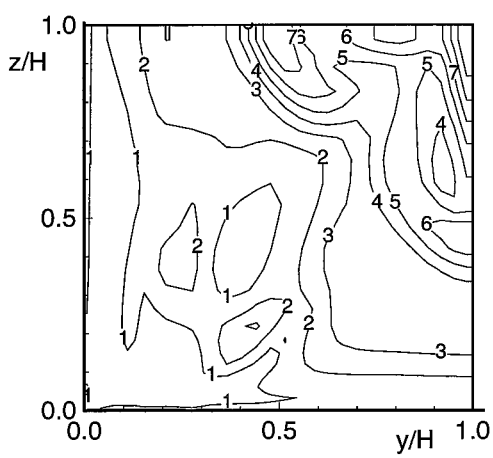

Porous Slots

Levels	μ_t / μ
9	270.0
8	240.0
7	210.0
6	180.0
5	150.0
4	120.0
3	90.0
2	60.0
1	30.0

Figure 4.21: Distribution of turbulent viscosity at $x = 4.24$ cm.

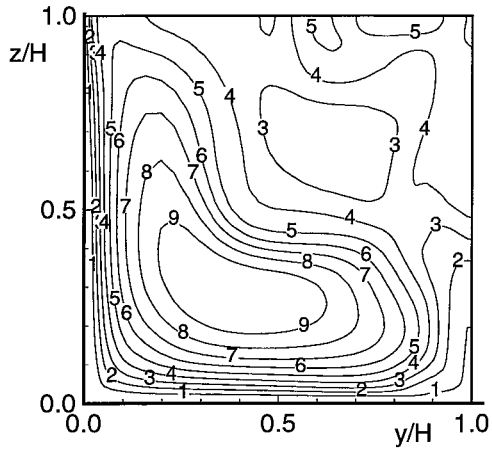

Discrete Jets

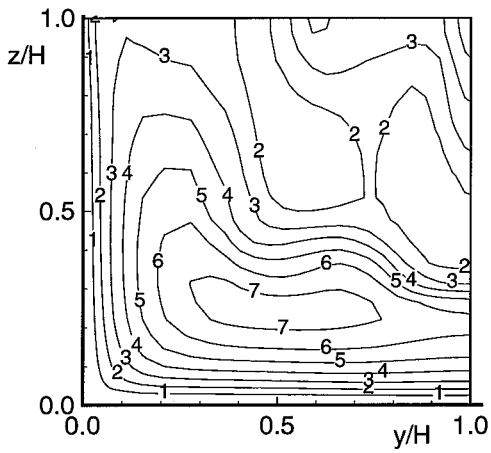

Open Slots

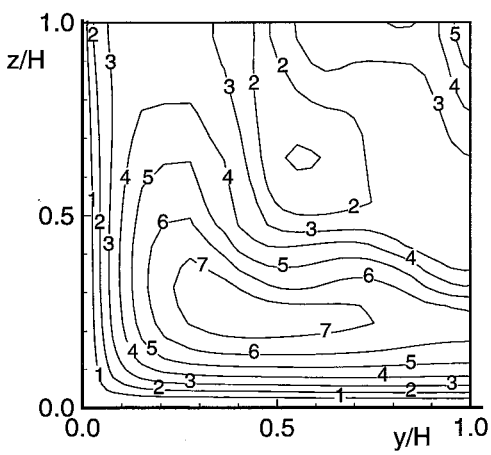

Porous Slots

Levels	μ_t / μ
9	530.0
8	470.0
7	410.0
6	350.0
5	290.0
4	230.0
3	170.0
2	110.0
1	50.0

Figure 4.22: Distribution of turbulent viscosity at $x = 7.62$ cm.

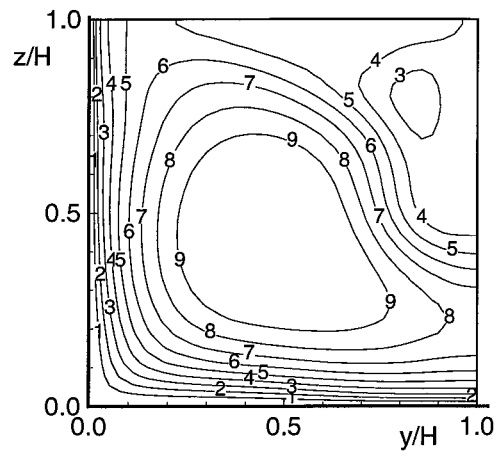

Discrete Jets

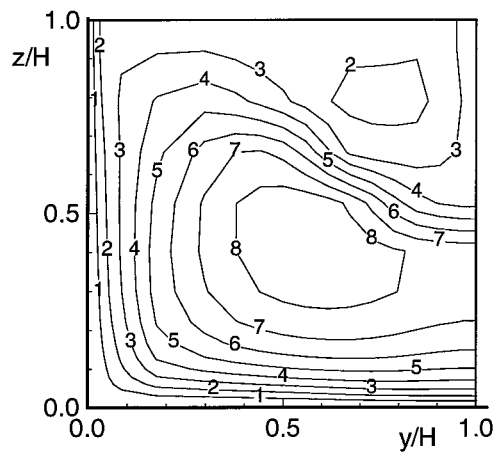

Open Slots

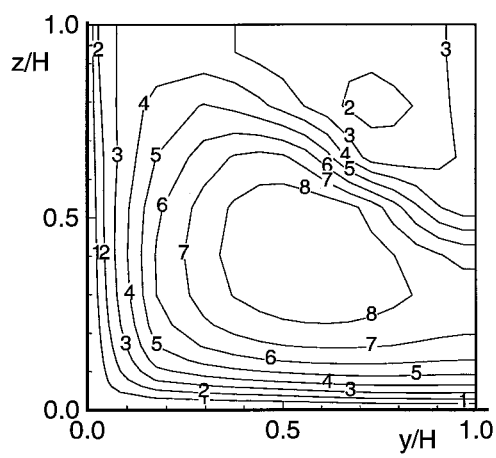

Porous Slots

Levels	μ_t / μ
9	630.0
8	560.0
7	490.0
6	420.0
5	350.0
4	280.0
3	210.0
2	140.0
1	70.0

Figure 4.23: Distribution of turbulent viscosity at $x = 17.78$ cm.

4.6 Varying the Turbulence Input Parameters in Slot Simulations

In the simulations using slots, lower values of μ_t are produced in the flow field as a consequence of the omission of the extra turbulence intensity near the outlets of discrete jets. Thus, it is important to examine the effects of increasing the turbulence intensity used in slot simulations. Because of similarities in the results produced by open slots and porous slots, the attention here will be focussed only on simulations with open slots.

Our aim is to observe if there are any changes to the flow field when the value of the jet turbulent energy k_{jet} is varied. The choice for $L_{diss} = 0.5 \times W$ is maintained such that the value of ϵ_{jet} increases as k_{jet} increases. The following two cases are considered: $k_{jet} = 0.05 \times V_{jet}^2$ and $k_{jet} = 0.5 \times V_{jet}^2$, which correspond to an increase in the jet turbulent energy by factors of 10 and 100, respectively.

Calculations are carried out with the same multigrid procedure as before. The convergence rates of these latter simulations are similar to the previous open slot simulation. The distributions of turbulent energy and its dissipation rate are examined at the jet entrance elevation and are shown in Figure 4.24. The graphs there illustrate the results that there are steep gradients in k and ϵ near the jet entrances. A comparison of Figure 4.24(a) with 4.24(b) and with the open slot case in Figure 4.14 shows that there is an increase in the turbulent energy near the jet entrances as the value of k_{jet} increases. However, the corresponding energy dissipation rate ϵ also attains higher values near the jet entrances.

In order to examine how the mean velocity may be affected, the distributions of the turbulent viscosity and the vertical component of the mean velocity are compared at the same jet entrance elevation, and the results are shown in Figure 4.25. A comparison of the graphs in this figure to those in Figures 4.11 and 4.21 shows that similar distributions are obtained for both the turbulent viscosity and velocity fields for the different choices

of k_{jet}.

The results of our simulations reveal the following characteristic in the calculation of primary jet flows with the $k - \epsilon$ turbulence model: when the input turbulent energy is increased while the dissipation length scale is maintained the same, the model will be self-adjusting so that the extra turbulent energy will be consumed. Consequently, similar levels of turbulent viscosity are predicted. Moreover, within the bulk of the flow field, the turbulence intensity appears to be governed primarily by the shearing action within the flow field and is not very sensitive to the incoming turbulence intensity level.

Additional graphs displaying the distributions of k, ϵ, μ_t, and the vertical component of velocity at higher elevations are shown in Figures 4.26-4.29. These results are compared with the corresponding earlier results of open slots shown in Figures 4.12-4.13, 4.17-4.20, and 4.22-4.23. The point to note is that for the cases examined, there is a high degree of similarity in the results. It is apparent that the extra turbulent viscosity simulated in the prototype case cannot be reproduced easily by increasing the turbulence intensity prescribed for the slot jets.

In passing, we mention that we have also tried varying the dissipation length scale L_{diss} by increasing it first to $L_{diss} = 5 \times W$, and then to $50 \times W$, while maintaining $k_{jet} = 0.005 \times V_{jet}^2$. These two cases correspond to decreasing ϵ_{jet} by factors of 10 and 100, respectively. The convergence characteristics of these simulations are similar to the original open slot simulation and the results of the mean vertical velocity component and turbulence quantities are also similar. This observation further confirms that in the simulations with slots, the turbulence and mean flow characteristics are influenced more strongly by the intense jet interactions than by the prescribed boundary data of the turbulence quantities.

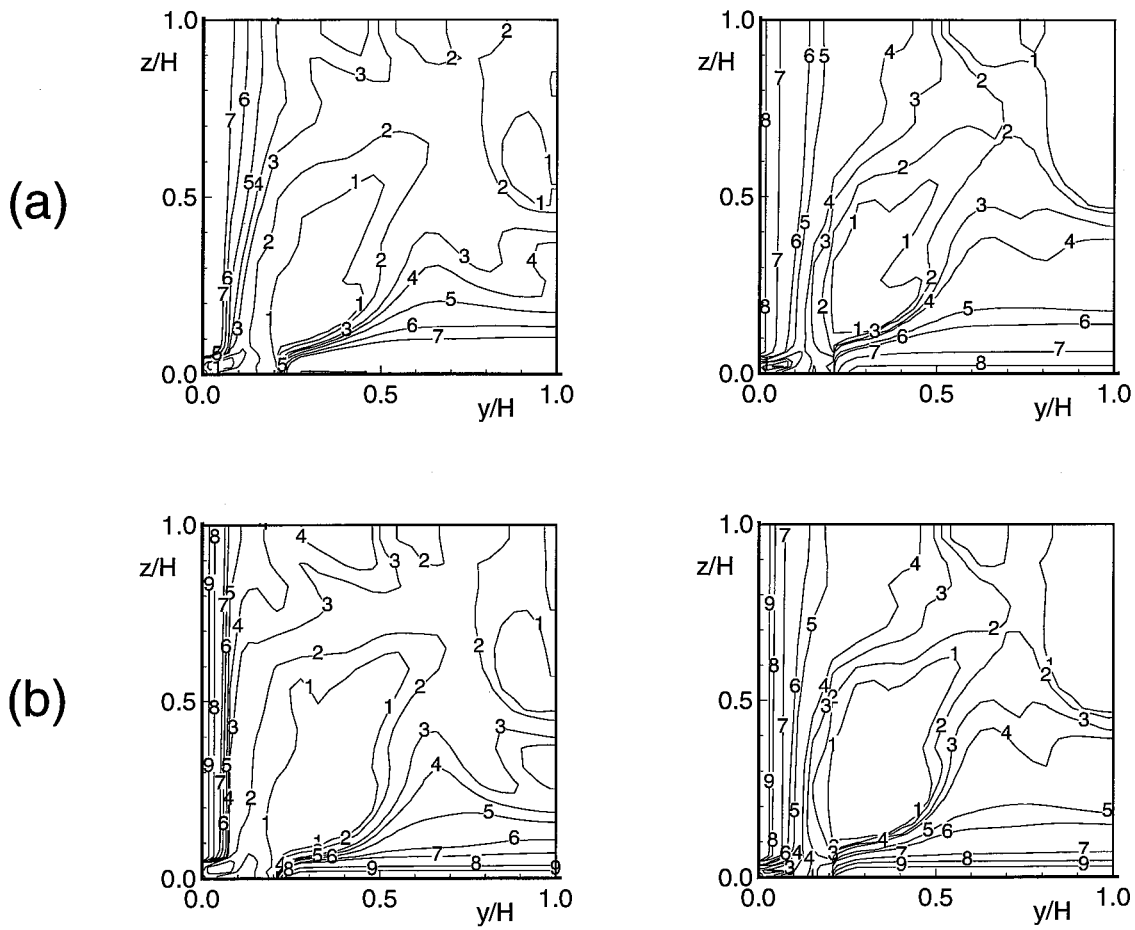

Turbulent Energy

Levels	k / V_{jet}^2
9	0.100
8	0.050
7	0.020
6	0.015
5	0.010
4	0.007
3	0.005
2	0.002
1	0.001

Energy Dissipation

Levels	$\varepsilon / (V_{jet}^3/H)$
9	5.000
8	1.500
7	0.500
6	0.100
5	0.050
4	0.010
3	0.005
2	0.002
1	0.001

Figure 4.24: Distributions of turbulent energy and dissipation at $x = 4.24$ cm for (a) $k_{jet} = 0.05 \times V_{jet}^2$ and (b) $k_{jet} = 0.5 \times V_{jet}^2$.

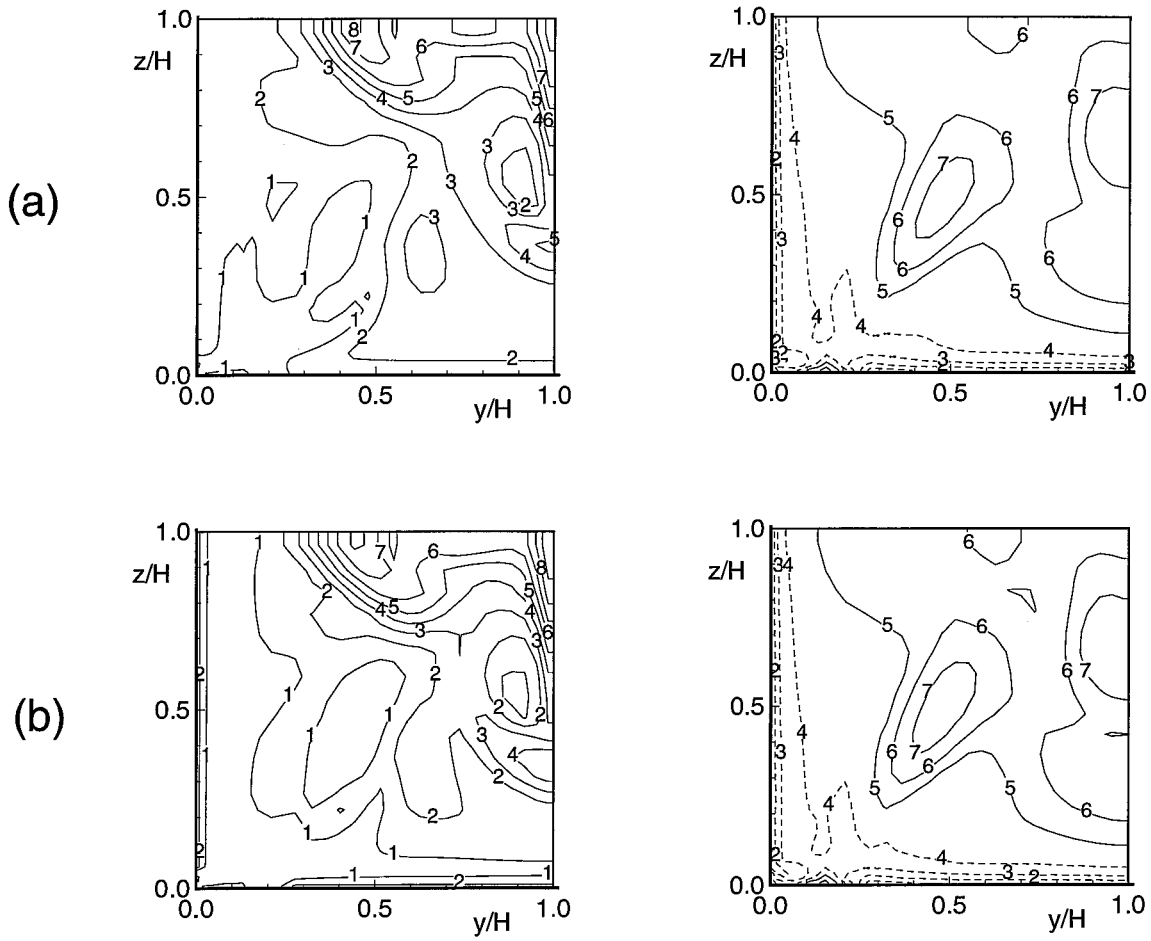

Turbulent Viscosity

Levels	μ_t / μ
9	270.0
8	240.0
7	210.0
6	180.0
5	150.0
4	120.0
3	90.0
2	60.0
1	30.0

Upflow and Downflow

Levels	U / V_{jet}
9	0.16
8	0.12
7	0.08
6	0.04
5	0.00
4	-0.04
3	-0.08
2	-0.12
1	-0.16

Figure 4.25: Distributions of turbulent viscosity and mean vertical velocity at $x = 4.24$ cm for (a) $k_{jet} = 0.05 \times V_{jet}^2$ and (b) $k_{jet} = 0.5 \times V_{jet}^2$.

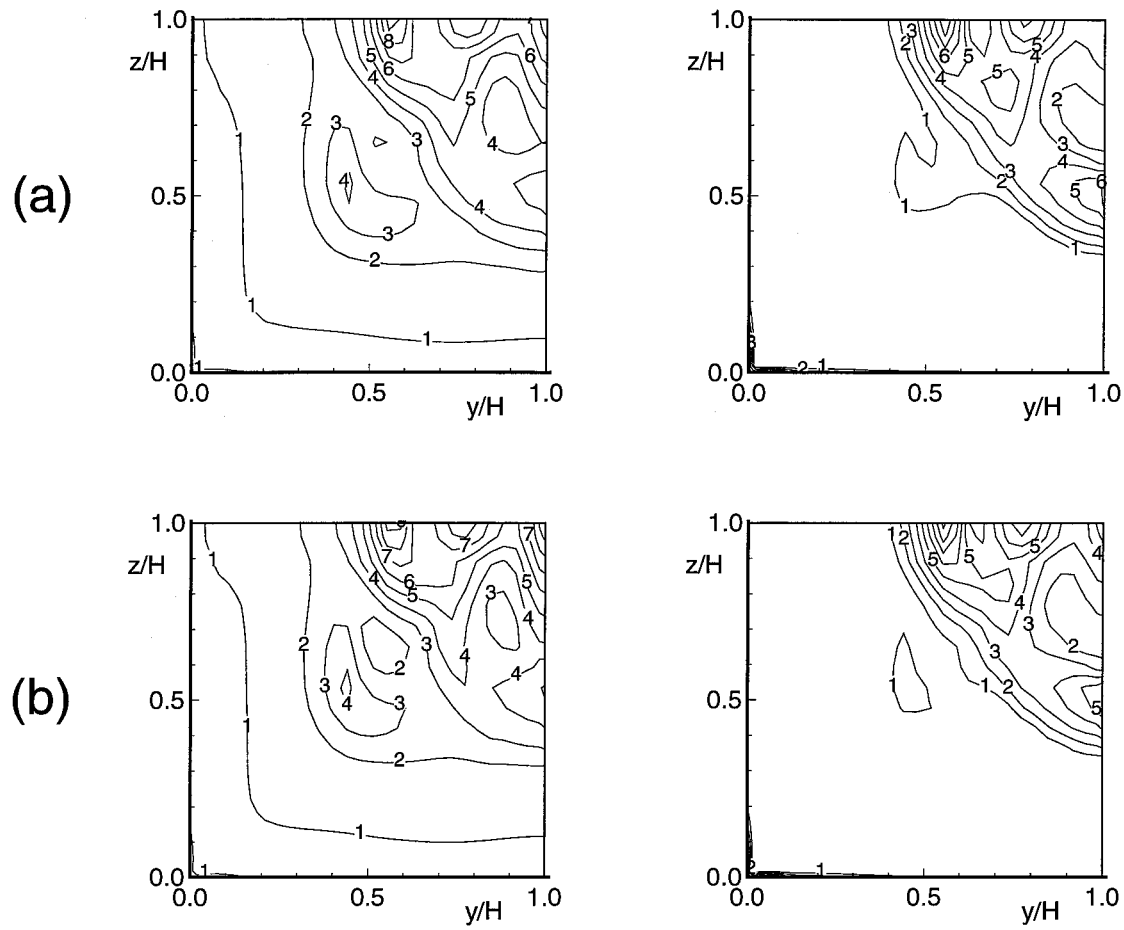

Turbulent Energy

Levels	k / V_{jet}^2
9	0.0027
8	0.0024
7	0.0021
6	0.0018
5	0.0015
4	0.0012
3	0.0009
2	0.0006
1	0.0003

Energy Dissipation

Levels	$\varepsilon / (V_{jet}^3/H)$
9	0.00145
8	0.00130
7	0.00115
6	0.00100
5	0.00085
4	0.00070
3	0.00055
2	0.00040
1	0.00025

Figure 4.26: Distributions of turbulent energy and dissipation at $x = 7.62$ cm for (a) $k_{jet} = 0.05 \times V_{jet}^2$ and (b) $k_{jet} = 0.5 \times V_{jet}^2$.

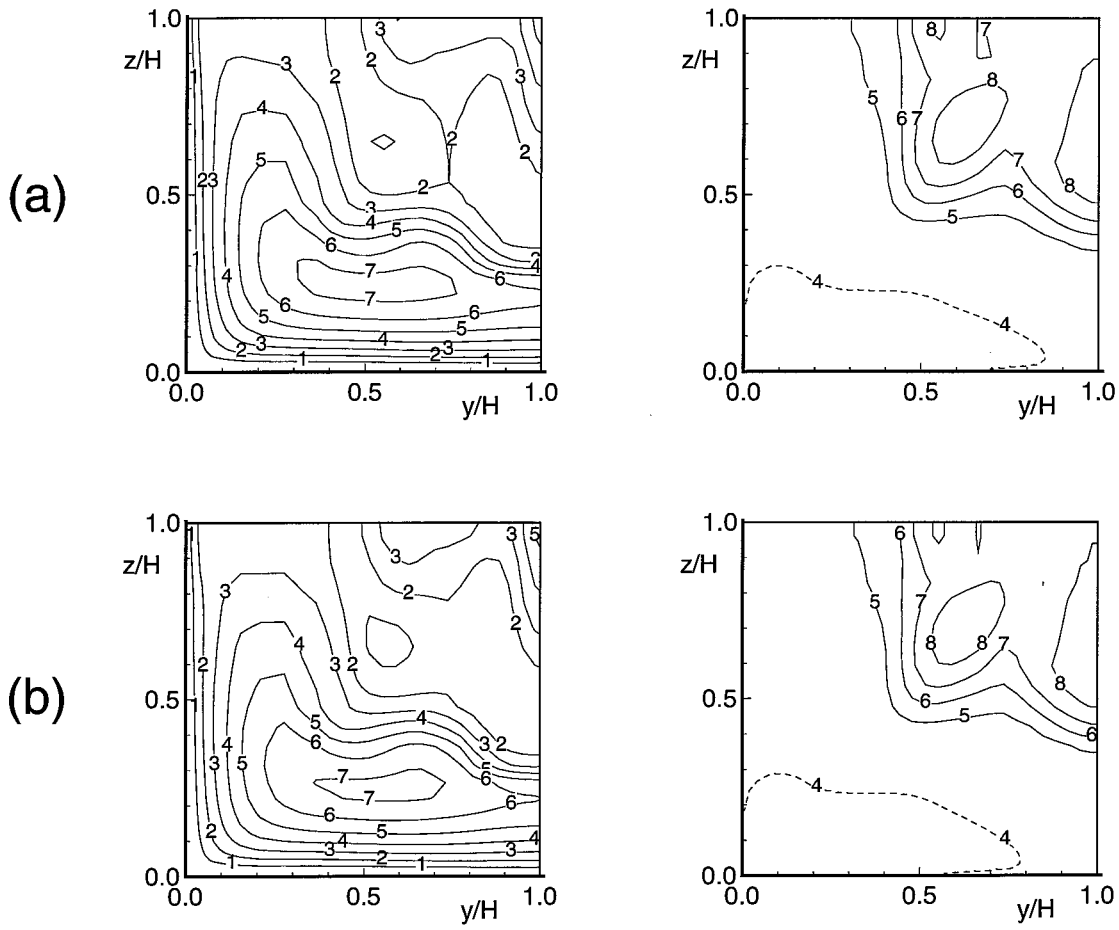

Turbulent Viscosity

Levels	μ_t / μ
9	530.0
8	470.0
7	410.0
6	350.0
5	290.0
4	230.0
3	170.0
2	110.0
1	50.0

Upflow and Downflow

Levels	U / V_{jet}
9	0.16
8	0.12
7	0.08
6	0.04
5	0.00
4	-0.04
3	-0.08
2	-0.12
1	-0.16

Figure 4.27: Distributions of turbulent viscosity and mean vertical velocity at $x = 7.62$ cm for (a) $k_{jet} = 0.05 \times V_{jet}^2$ and (b) $k_{jet} = 0.5 \times V_{jet}^2$.

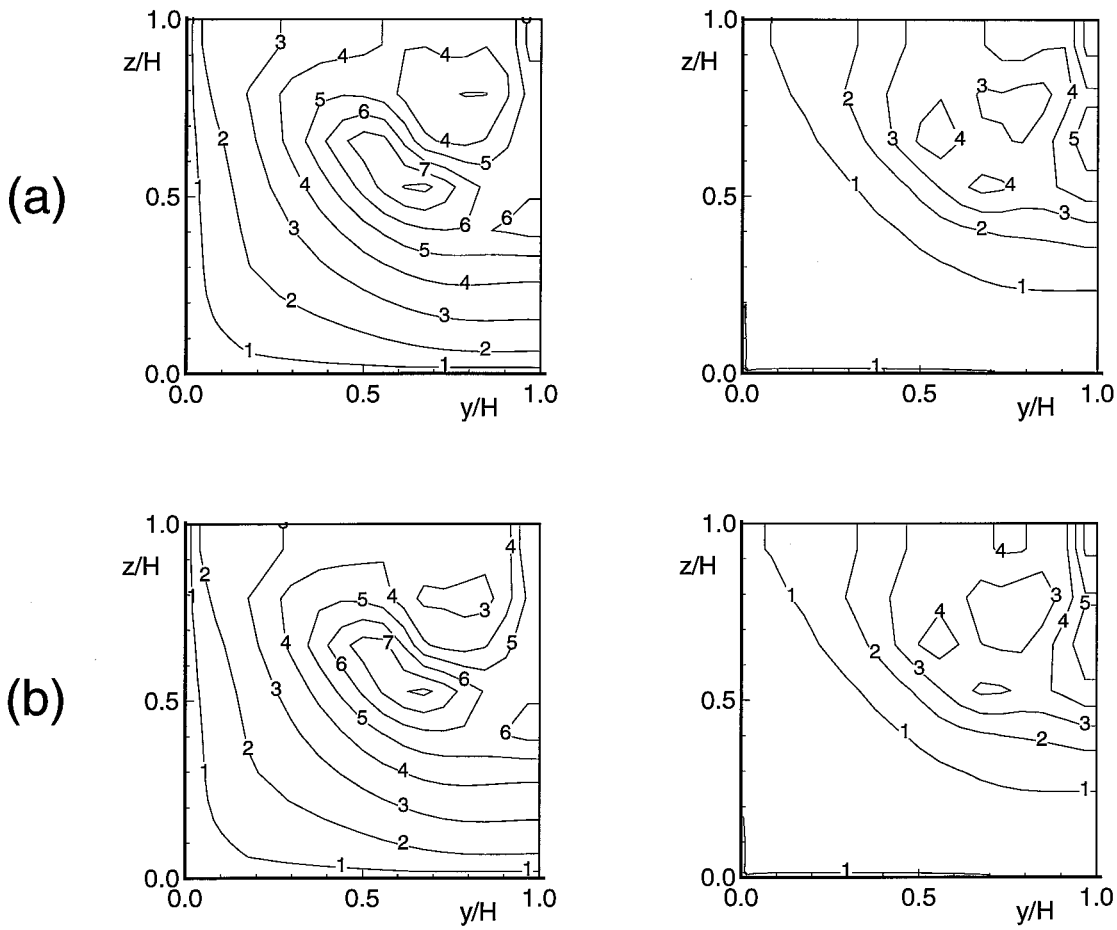

Turbulent Energy

Levels	k / V_{jet}^2
9	0.0018
8	0.0016
7	0.0014
6	0.0012
5	0.0010
4	0.0008
3	0.0006
2	0.0004
1	0.0002

Energy Dissipation

Levels	$\varepsilon / (V_{jet}^3/H)$
9	0.00036
8	0.00032
7	0.00028
6	0.00024
5	0.00020
4	0.00016
3	0.00012
2	0.00008
1	0.00004

Figure 4.28: Distributions of turbulent energy and dissipation at $x = 17.78$ cm for (a) $k_{jet} = 0.05 \times V_{jet}^2$ and (b) $k_{jet} = 0.5 \times V_{jet}^2$.

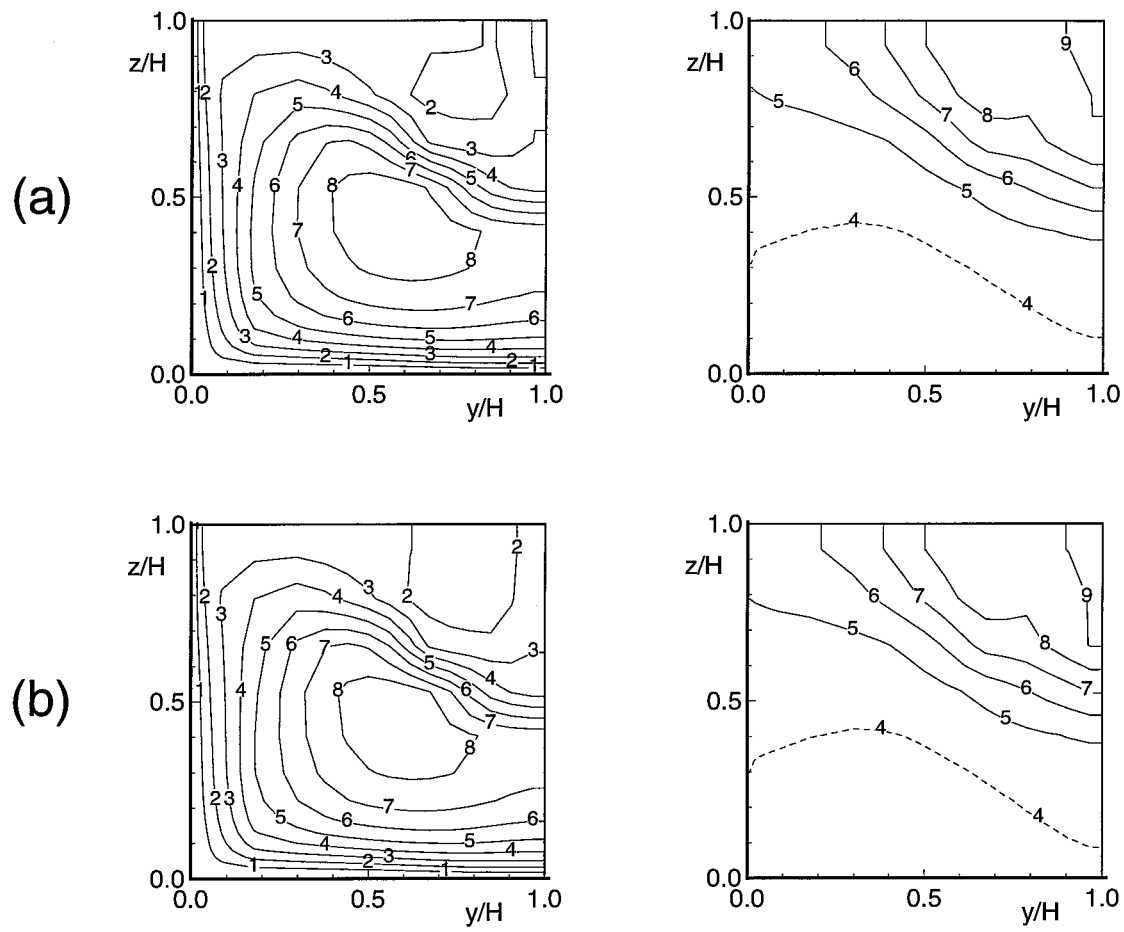

Turbulent Viscosity

Levels	μ_t / μ
9	630.0
8	560.0
7	490.0
6	420.0
5	350.0
4	280.0
3	210.0
2	140.0
1	70.0

Upflow and Downflow

Levels	U / V_{jet}
9	0.16
8	0.12
7	0.08
6	0.04
5	0.00
4	-0.04
3	-0.08
2	-0.12
1	-0.16

Figure 4.29: Distributions of turbulent viscosity and mean vertical velocity at $x = 17.78$ cm for (a) $k_{jet} = 0.05 \times V_{jet}^2$ and (b) $k_{jet} = 0.5 \times V_{jet}^2$.

4.7 Concluding Remarks

When jets are closely spaced in a row, they may be represented numerically by slots. Our computational experience shows that the use of slot representation for primary jets is essential for numerical modelling. If individual primary jets were to be modelled, the system of equations could become so large that convergence would be difficult to achieve. In such a case, the multigrid method may be difficult to apply unless the computer system has sufficient memory capability.

In the simulations with slot jets, the important flow parameters that need to be maintained are the jet speed and the total mass flow rate. Our results show that the velocity profiles are captured fairly well by the use of either open slots or porous slots. In comparison to open slot simulations, modelling with porous slots yields a slightly better agreement with the prototype case in the regions near the jet entrances. However, at higher elevations, there is no advantage in adopting porous slots.

It is important to note that the values of turbulent viscosity are under-predicted by slot simulations. This raises the concern that properties such as the extent of fluid mixing may not be reproduced well by slot simulations without further refinement to the modelling methodology. Moreover, note that only a single level of jets is simulated. In an actual boiler simulation with several levels of jets, one may encounter surprising results not illustrated with the present simple configuration.

Chapter 5

Characteristics of a Row of Jets in a Confined Crossflow

A study is carried out on the characteristics due to a row of jets injecting into a confined crossflow. Such a configuration will also be called a row-jet injection scheme. This study is relevant to improving the understanding of the dynamics of jet interaction in a kraft recovery boiler because the secondary and tertiary level jets operate in an environment where a crossflow is present. The results of our investigation provide information that can be used to interpret the observations arising from more comprehensive modelling studies, such as the effects on jet penetration when both orifice spacing and dimensions are varied.

In this chapter, attention is restricted to the interaction of a single row of jets with a confined uniform crossflow. This simple geometric configuration provides a suitable basis for the study of jet dynamics that should precede the consideration of more complex configurations. However, even with this simplification, there are still many geometric and operational parameters that make a systematic study difficult. Examples of geometric parameters are the shape and size of jet orifices, their separation, and the extent of confinement. Examples of operational parameters are the jet velocity, the mainstream velocity, and the ratio of jet momentum to mainstream momentum.

Among the many possible parametric variations, two studies which deserve attention are the effects of varying jet spacing while maintaining jet momentum constant, and the effects of varying jet momentum while holding spacing constant. One purpose of the present investigation is to verify the observations by Kamotani and Greber (1974)

concerning the changes in jet penetration when the jet spacing is varied. Another purpose is to reveal detailed features such as the vorticity dynamics of the flow field due to the interaction between a row of jets and a crossflow. This study provides results which contrast the flow characteristics of a row of jets with those of an isolated jet in a crossflow.

First, a description is presented for the jet-in-crossflow problem under consideration. Then the solution method and the convergence characteristics are discussed. Next, the jet penetration and the development of the cross-section of a jet is examined for different values of jet spacing and momentum ratio. Finally, the vorticity dynamics is investigated.

5.1 Problem Description and Boundary Conditions

The geometry of the injection scheme is displayed in Figure 5.1. The following geometric conditions are selected: jet width $W = 0.00635$ m (0.25 inches), dimension of channel $H = 24 \times W$, and spacing between a pair of jets $S/W = 2$, 4, 8, and 16.

Two values of the jet-to-crossflow momentum ratio are considered: $J = 8$ and 72. The speed of the crossflow is set at $U_C = 6$ m/s. Consequently, the speeds of the jets are $V_{jet} = 17$ and 51 m/s, respectively. These conditions are chosen to emulate the experimental work by Kamotani and Greber (1974), where round jets having a diameter of 0.00635 m were used.

In the numerical model, the domain of the flow field is represented as a rectangular box, much like that in the previous computation for a single jet. Due to flow symmetry, only half of a jet needs to be computed. Symmetry conditions are imposed on the two lateral planes bounding the space between the jet center-line and the distance mid-way between two adjacent jets. The separation between these two symmetry planes is varied to permit simulation of different values of S/W.

The wall function is used to evaluate the shear stress near solid boundaries. The choice

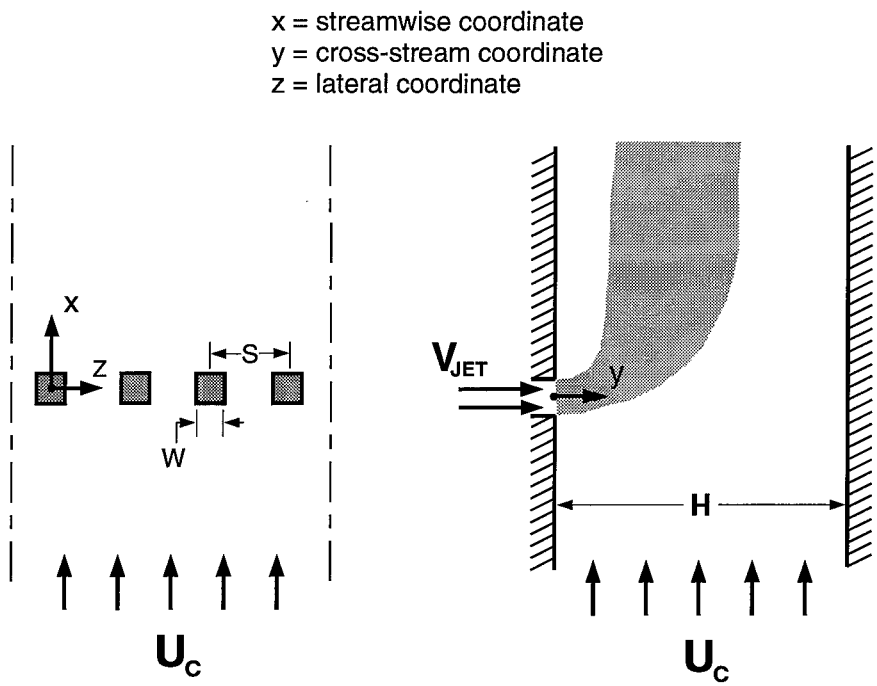

Figure 5.1: Schematic representation of jet injection from a row of square orifices.

for the location of the inlet plane for the crossflow is influenced by two considerations: first, the location needs to be sufficiently far from the jet so that the presence of the jet will not lead to an unrealistic velocity distribution near the plane. Secondly, the plane should not be too far upstream to avoid unnecessarily thick boundary layer at the jet entrance. Based on these two considerations, it is decided that the inlet plane to be located at about 10 jet widths upstream of the jet, where a uniform velocity U_C is assigned in the plane. The inlet turbulent energy is specified by $k_C = 0.005 \times U_C^2$, while the dissipation length scale is chosen to be $L_{diss} = 0.1 \times H$ and the dissipation rate at the inlet is set at $\epsilon_C = k_C^{3/2}/L_{diss}$. At the jet entrance, due to the strength of the jet, uniform values for the jet velocity, turbulence quantities, and the jet tracer are specified. The turbulent kinetic energy is set at $k_{jet} = 0.005 \times V_{jet}^2$, and the dissipation length scale is set at $L_{diss} = 0.5 \times W$ so that the dissipation rate is $\epsilon_{jet} = k_{jet}^{3/2}/(0.5 \times W)$. Based on past experience with the calculation of a single jet in a crossflow, the turbulence

characteristics for this type of flow field should be governed mainly by the shearing action of the flow and not by the prescribed boundary data for k and ϵ. A unit value of an inert tracer is prescribed at the jet entrance to mark the dispersion of the jet fluid. For the exit condition, the exit plane is placed at up to 100 jet widths downstream of the jet entrance. The zero-gradient condition for the dependent variables is imposed.

5.2 Convergence Performance

For the type of flow field considered in this chapter, our multigrid method generally provides very fast convergence. However, the convergence rate deteriorates as the jet momentum is increased and as the jet spacing is reduced. To illustrate this, the convergence histories for the cases $S/W = 4$ at $J = 8$ and $S/W = 2$ and 4 at $J = 72$ are presented in Figure 5.2. The mass residues have been normalized by the total incoming mass flow from the cross-stream and the jet.

The deterioration of the performance of the multigrid solver is apparent from the above results. Moreover, it needs to be noted that for the difficult case $S/W = 2$ at $J = 72$, the number of iterations carried out before the restriction cannot be too small; otherwise, stalling or divergence can occur. This observation is similar to that for the primary jet simulations carried out in the previous chapter. This is a little surprising because in past experience with applying the multigrid method to nonlinear equations as outlined in section 3.4.2, if too many smoothing iterations are carried out, high frequency errors may be re-introduced into the solution due to interactions with boundary conditions. However, our results suggest that for difficult turbulent flow simulations caused by close jet spacing and high jet-to-crossflow momentum ratio, a significant amount of smoothing is needed to eliminate the high frequency error components. If this is not done before the solution is transferred to the coarser grid, there can be too much 'noise'

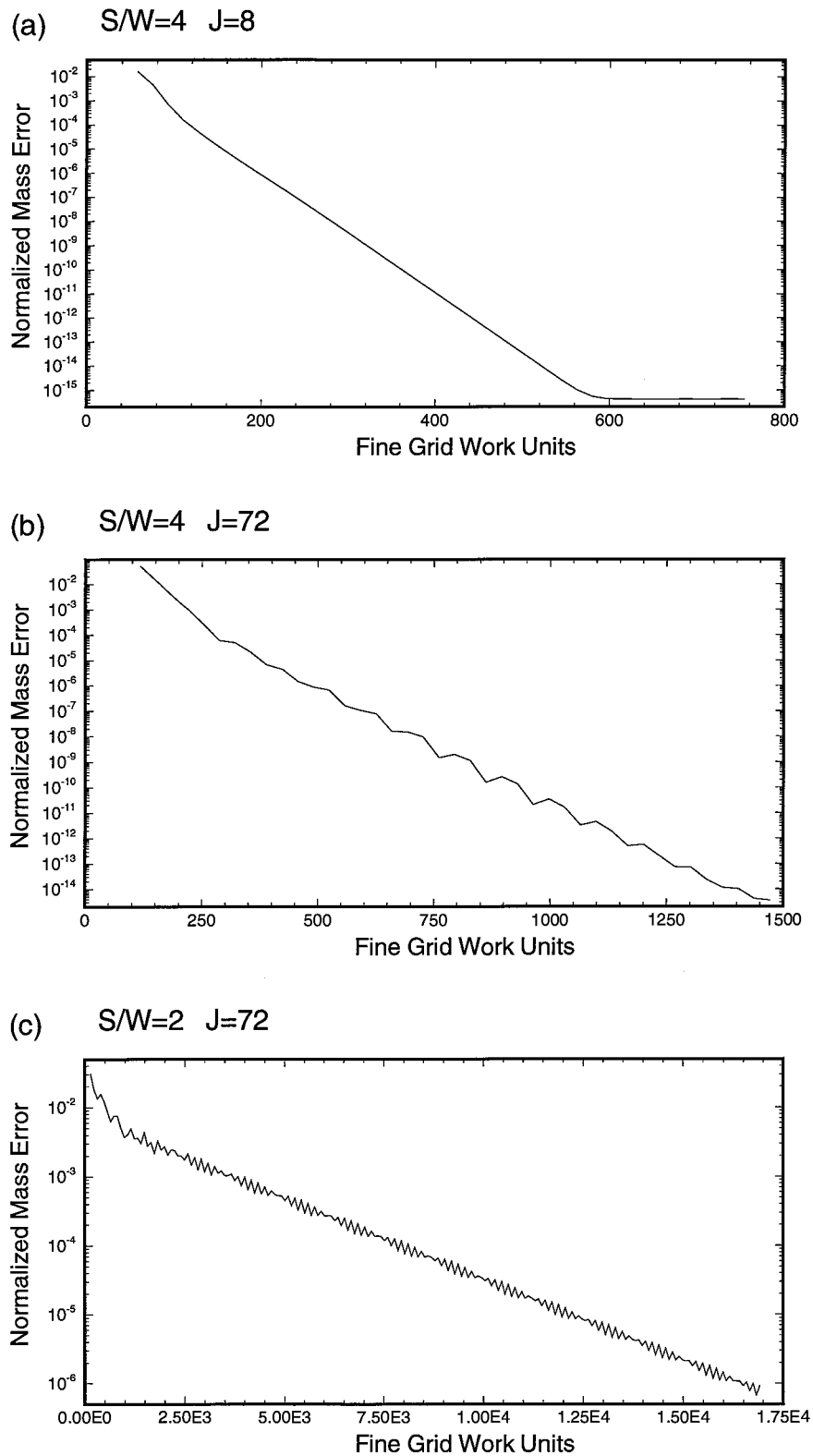

Figure 5.2: Convergence histories for different cases of S/W and J.

in the auxiliary problem in the coarse grid and convergence becomes difficult to achieve.

It has been commonly observed in many flow situations that convergence becomes difficult when the flow Reynolds number is increased. Examples include the laminar driven cavity problem and the flow over a backward-facing step. Vanka (1986) suggested that the problem is due to an increase in the nonlinearity measure of the equations as the Reynolds number is increased. Thomson and Ferziger (1989) also remarked that as the Reynolds number is increased, the flow may develop more fine-scale structures. If the grid is too coarse to resolve these structures, the solution may be slightly 'wiggly' and convergence may be hindered.

One reason for the deterioration in the convergence performance is that when the jets are closely spaced, they merge to form a curtain that impedes the crossflow from passing between them. As a result, a recirculating bubble is formed behind each jet, and consequently a much longer domain is needed to place the exit plane. Thus, certain grid cells may be highly stretched, which can cause numerical anisotropy and may adversely affect the rate of convergence. This latter effect is caused by the slowness in the transfer of information along the direction parallel to the long side of the grid cells. The use of a line solver is inefficient for problems with a long domain since the solver updates information in a relatively local manner. In this regard, the use of a global iterative solver may improve convergence. An example of such a global solver is the lower-upper (LU) factorization algorithm discussed in many standard textbooks such as Maron (1987).

The convergence rate for this case of high momentum value and close jet spacing can be improved if the system of equations possesses additional numerical stability characteristics. These characteristics may be introduced by treating the problem as a transient one, and the steady state solution, if it exists, can be obtained by stepping through time. The transient equations of motion are obtained by including the time rate of change

terms into Eqs.(2.11-2.12). The equations become

$$\rho\frac{\partial U_i}{\partial t} + \rho\frac{\partial}{\partial x_j}(U_iU_j) = -\frac{\partial p}{\partial x_i} + \frac{\partial}{\partial x_j}\left\{\mu\left(\frac{\partial U_i}{\partial x_j} + \frac{\partial U_j}{\partial x_i}\right) - \rho\overline{u_iu_j}\right\} \tag{5.1}$$

$$\rho\frac{\partial \Phi}{\partial t} + \rho\frac{\partial}{\partial x_j}(\Phi U_j) = \frac{\partial}{\partial x_j}\left\{\lambda\left(\frac{\partial \Phi}{\partial x_j}\right) - \rho\overline{\phi u_j}\right\} \tag{5.2}$$

These modified equations describe the gross unsteadiness in the mean flow field, if such an unsteadiness exists. For Eqs.(5.1-5.2) to be physically meaningful, the time scale of the unsteadiness has to be much larger than the longest time scales of the turbulent motion.

The inclusion of the time dependent terms improves the numerical stability characteristics because it increases the diagonal dominance of the resulting system of finite difference equations. In the calculation, a time step value of 0.5 seconds is chosen. Starting at time $t = 0$, we march forward in time. The convergence history is displayed in Figure 5.3, which is to be compared to that presented in Figure 5.2c. The results of the flow field obtained here are visually indistinguishable to those obtained earlier using the steady state solver. It is evident that a faster convergence has been achieved and that the overall residue reduction rate is rather constant, even though it is still significantly slower than in the cases where the jet spacings are larger.

5.3 Jet Penetration

Our study on jet penetration complements the experimental investigations by Ivanov (1959) and by Kamotani and Greber (1974) discussed earlier in Chapter 2. The focus of this section is on the effect of jet spacing on the penetration for moderately spaced jets.

The results of the numerical simulations are depicted in Figures 5.4-5.7. In Figure 5.4, the center-plane velocity profiles are displayed for $S/W = 2$, 4, 8, and 16 at $J = 8$. It is apparent that at this low momentum ratio, the blockage effect caused by the jet

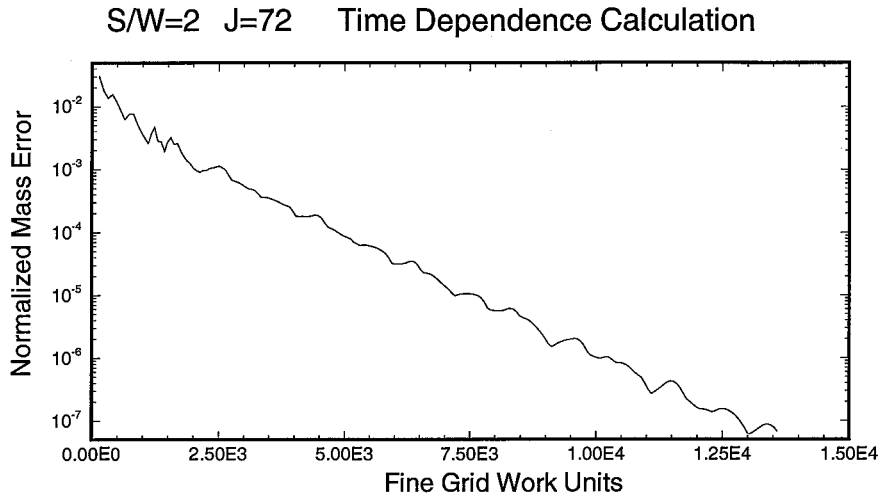

Figure 5.3: Convergence history for $S/W = 2$ at $J = 72$; time dependence calculation.

on the crossflow at low values of S/W is not significant, and this is revealed by the absence of a recirculating bubble behind the jet root for the case $S/W = 2$. The jet tracer concentration profiles along the same longitudinal plane are shown in Figure 5.5 for the same cases. These profiles are used to estimate the jet penetration in each case. Also shown in the graphs in Figure 5.5 are streamlines representing paths of fluid particles leaving the center of the jet orifice. These streamlines are representative of the jet trajectories in this center-plane. In passing, we note and recall that the definitions of jet trajectories are varied in different investigations. Kamotani and Greber defined the center-plane jet trajectory to be the locus of maximum speed at each cross-stream plane intersecting the jet center-plane.

Similar results of the velocity profiles and jet tracer concentration for the high momentum case $J = 72$ are presented in Figures 5.6 and 5.7, respectively. At this higher momentum, each jet spreads farther and the blockage effect on the crossflow is more prominent. When $S/W = 2$, a large reverse flow region is formed behind each jet. Consequently, the exit plane has to be placed very far downstream at $x = 100 \times W$, a condition that may adversely affect solution convergence as discussed in section 5.2.

Our numerical results also indicate that for both $J = 8$ and 72, there is a monotonic reduction in jet penetration as S/W is reduced. The reduction is more significant when S/W decreases from 16 to 8 and less so from 8 to 4. Comparing the results in Figures 5.5 and 5.7 to those shown in Figures 2.5-2.6, our results are similar to those reported by Ivanov and slightly different from those by Kamotani and Greber. At $J = 72$, our results predict a rise in jet penetration as reported by Kamotani and Greber when S/W is reduced from 4 to 2, but only in the region close to the jet entrance ($0 < x/W < 30$). The discrepancy may be attributed to factors such as different definitions used for the jet trajectory, experimental uncertainties, and deficiencies in the mathematical model used for the flow prediction.

The observed decrease in jet penetration with reduction in orifice spacing is useful in providing a physical basis to explain Holdeman's correlation. Equation (2.24) is used for obtaining consistent jet penetration, and will be discussed in the next chapter. Besides penetration, other characteristics that are of interest for the problem of jet mixing include the spreading and vorticity dynamics associated with each jet in this row-jet configuration. In addition to its role on jet mixing, the dynamics of the pair of counter-rotating vortices has been suggested by Kamotani and Greber (1974) to be instrumental in reducing the penetration of the jet as the jet spacing decreases. These characteristics are examined in the next section.

5.4 Development of the Cross-section of a Jet

The effects of jet spacing or lateral confinement on the development of the cross-sectional shape of a jet are now discussed. The development of the cross-section as the jet is propagating downstream is described in Figures 5.8-5.11. The figures show the evolution

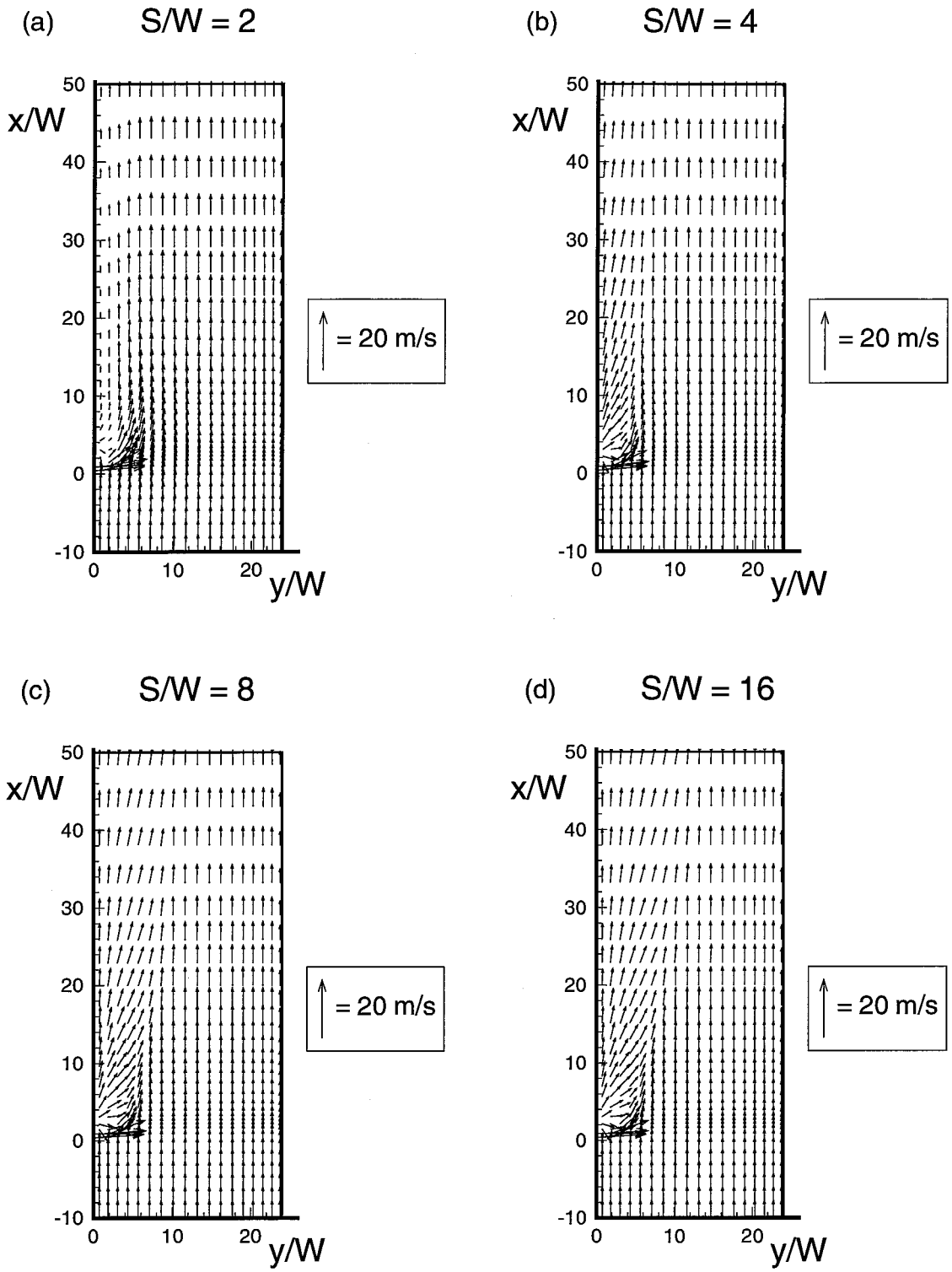

Figure 5.4: Velocity profiles for $S/W = 2$, 4, 8, and 16 at $J = 8$ along the jet center-plane.

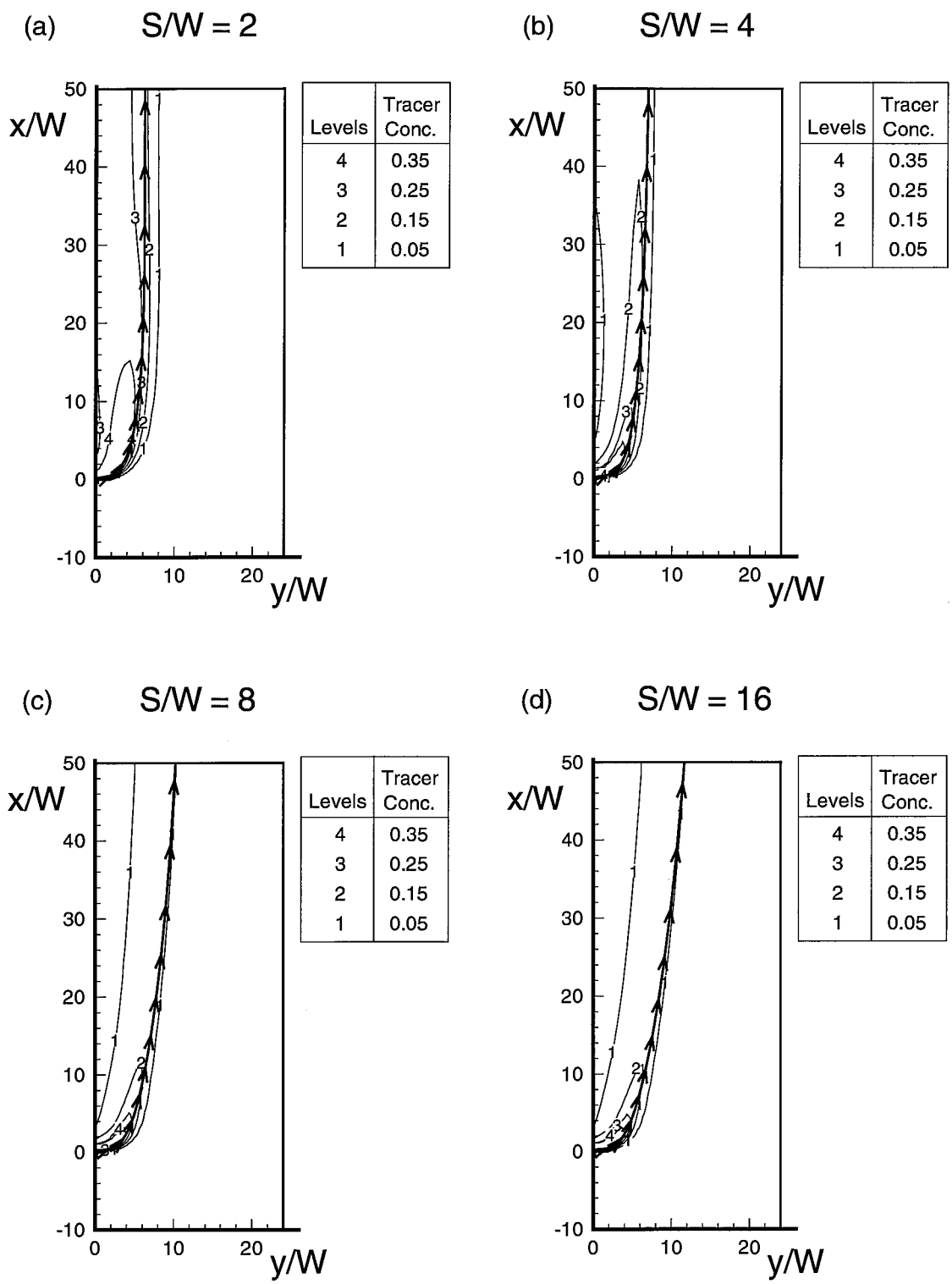

Figure 5.5: Jet tracer concentration profiles for $S/W = 2$, 4, 8, and 16 at $J = 8$ along the jet center-plane.

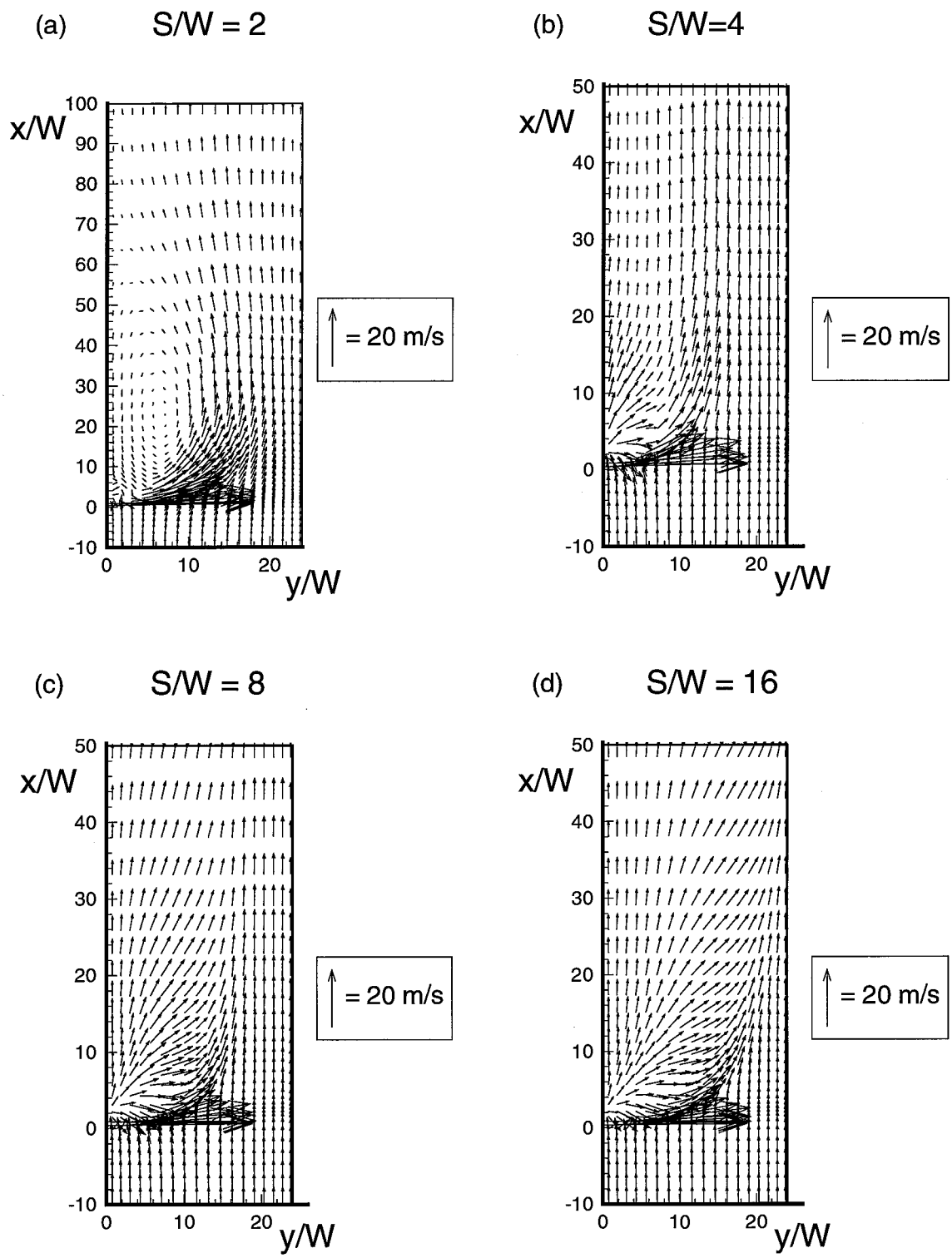

Figure 5.6: Velocity profiles for $S/W = 2$, 4, 8, and 16 at $J = 72$ along the jet center-plane.

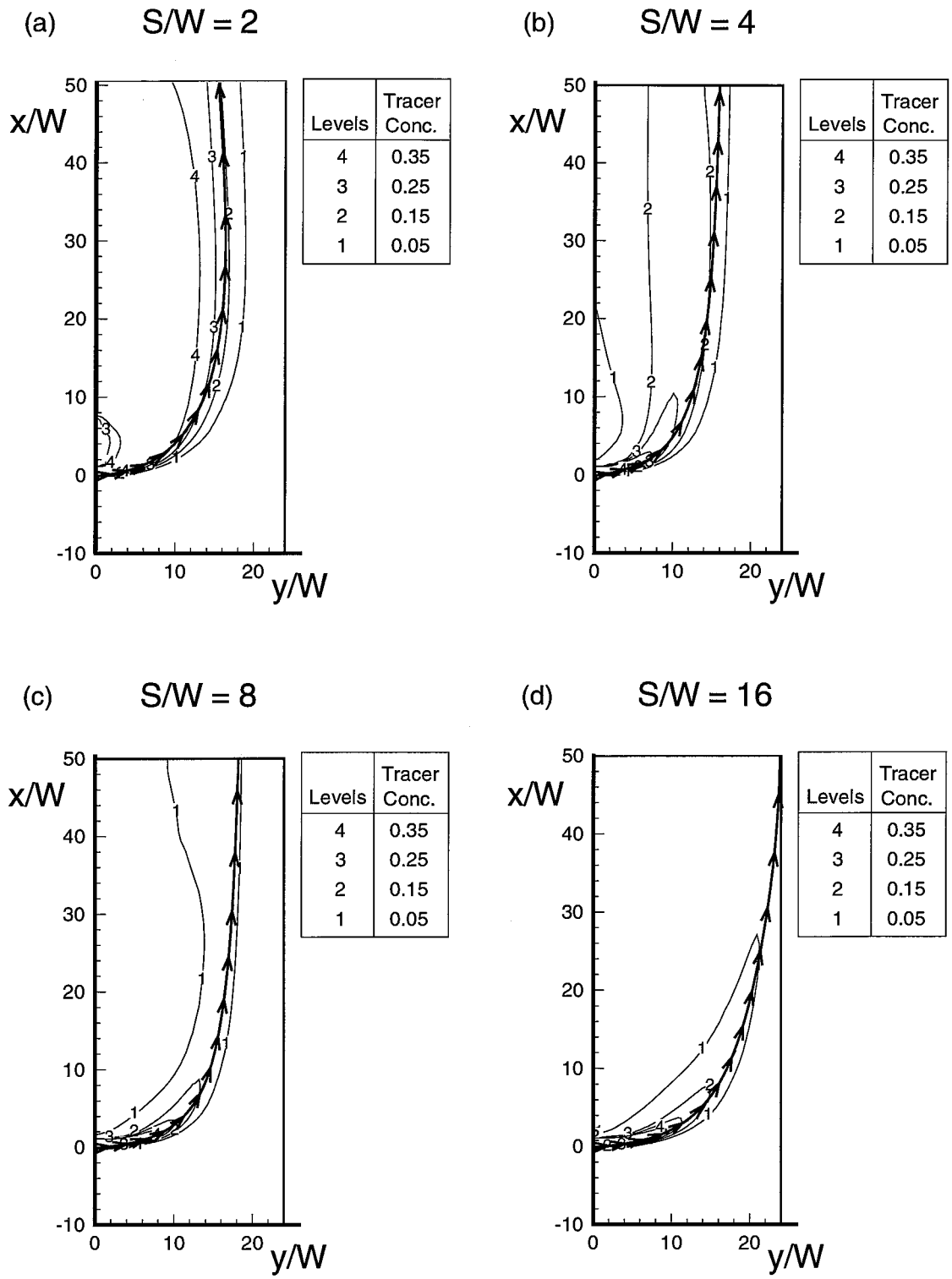

Figure 5.7: Jet tracer concentration profiles for $S/W = 2$, 4, 8, and 16 at $J = 72$ along the jet center-plane.

in the jet fluid distribution from $x/W = 5$ to 10 and for the cases $S/W = 2$, 4, and 8 at $J = 8$ and 72. The following observations are made: first, the jets spread out faster laterally as J increases, and as the jet spacing is reduced the jets merge rapidly. Secondly, the jet fluid distribution bifurcates into two cores about the symmetry plane $z = 0$ only when the jet spacing is sufficiently large ($S/W \geq 4$); otherwise, the maximum concentration of the jet fluid lies along the symmetry plane. The latter phenomenon is caused by the severe lateral confinement which prevents the jet fluid from bifurcating into two plumes.

As mentioned in Chapter 2, the pair of counter-rotating vortices associated with each jet has a significant role in the following areas: the mixing of the jet fluid; the cross-sectional shape of the jet, and the velocity distribution in the cross-sectional plane. A quantitative study of the vortices is difficult because a large amount of velocity data is required to construct the vorticity field. Thus, numerical simulations offer a viable alternative for the study provided the mathematical model can yield correct information about the flow field. Some results concerning the vorticity dynamics of a single jet in a crossflow have already been discussed in Chapter 2. The vorticity dynamics for multiple jets, however, has rarely been discussed. A study of this vorticity dynamics is the focus of the following section.

5.5 Vorticity Dynamics for a Row of Square Jets in a Crossflow

In the setting of multiple jets, the mutual interaction between neighboring jets brings additional complications to the vorticity phenomena. There are two conflicting and competing mechanisms that affect the vorticity characteristics of multiple jets. First, any blockage caused by a row of jets can lead to an acceleration of the crossflow around each jet. Thus, the streamwise vorticity is intensified by this extensional strain rate.

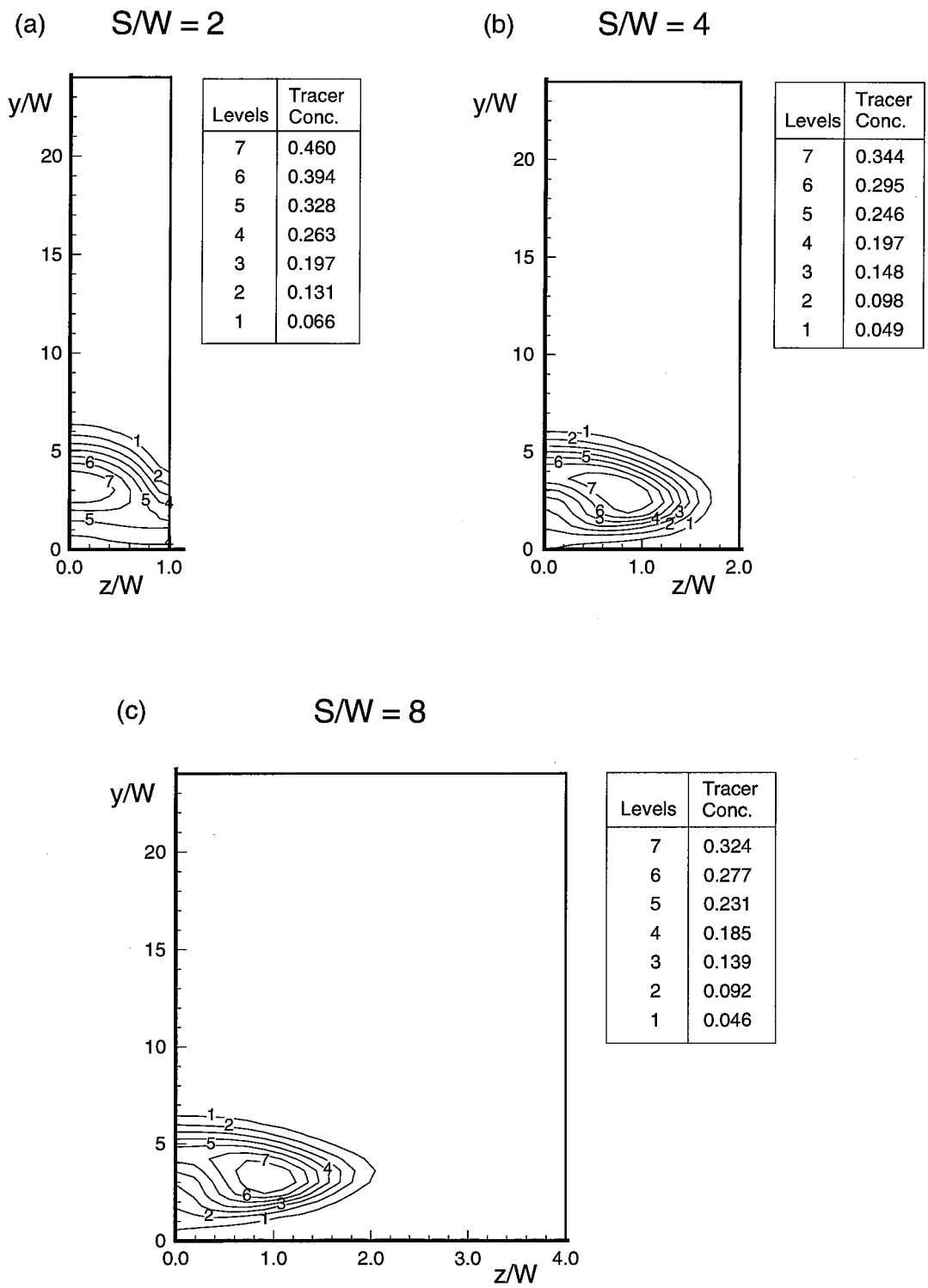

Figure 5.8: Jet tracer concentration profiles for $S/W = 2$, 4, and 8 in the cross-stream plane $x/W = 5$ at $J = 8$.

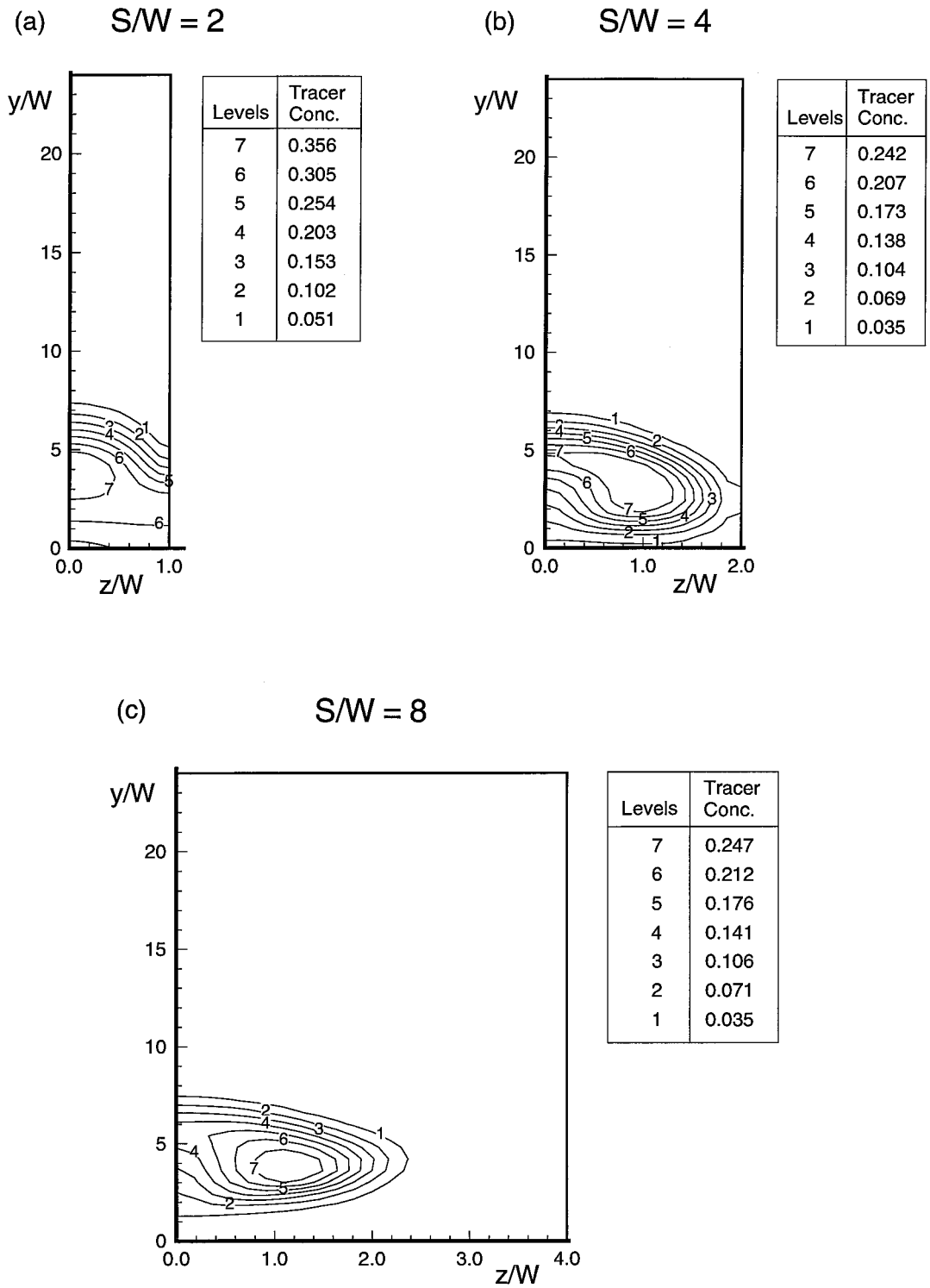

Figure 5.9: Jet tracer concentration profiles for $S/W = 2$, 4, and 8 in the cross-stream plane $x/W = 10$ at $J = 8$.

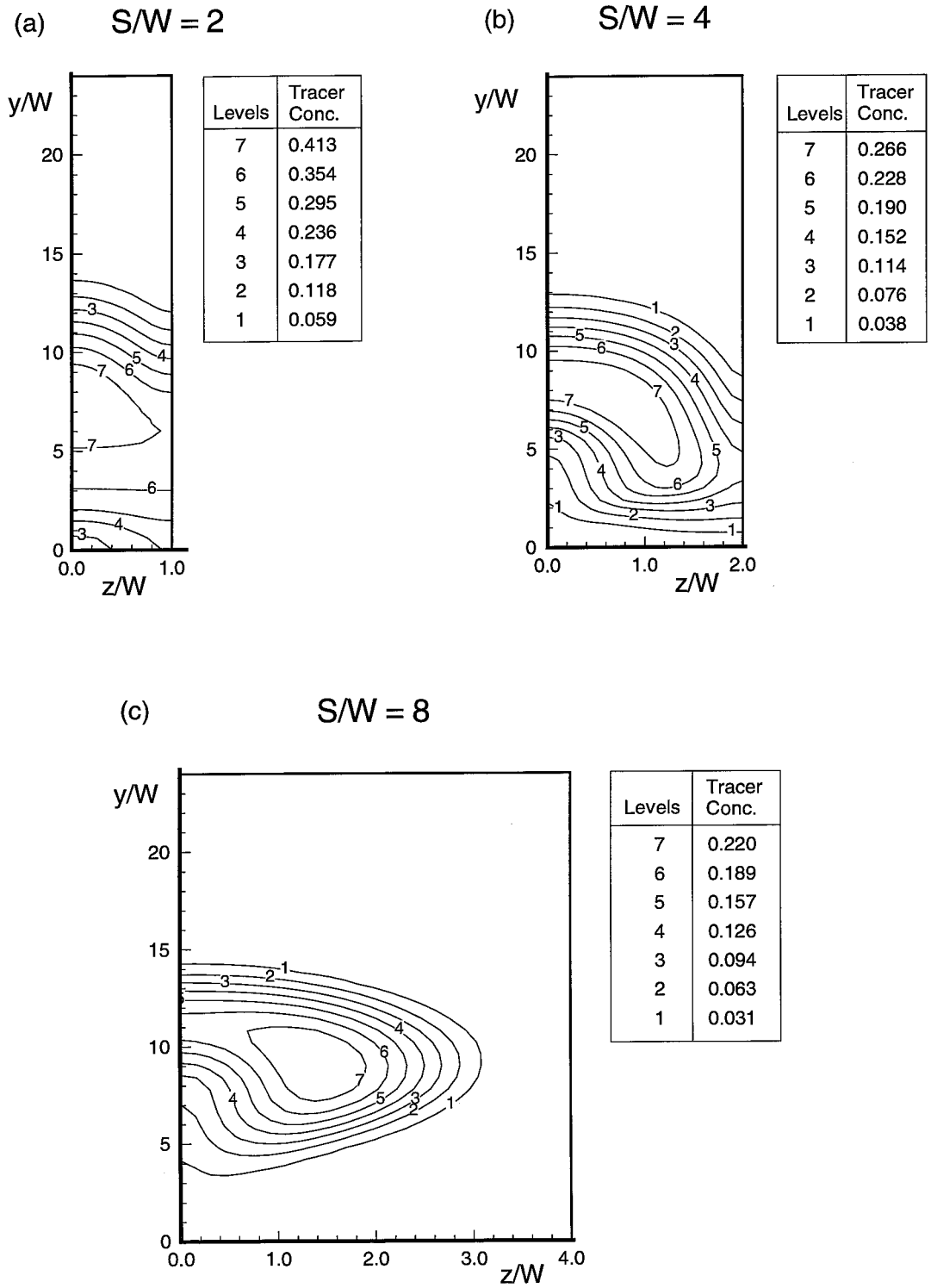

Figure 5.10: Jet tracer concentration profiles for $S/W = 2$, 4, and 8 in the cross-stream plane $x/W = 5$ at $J = 72$.

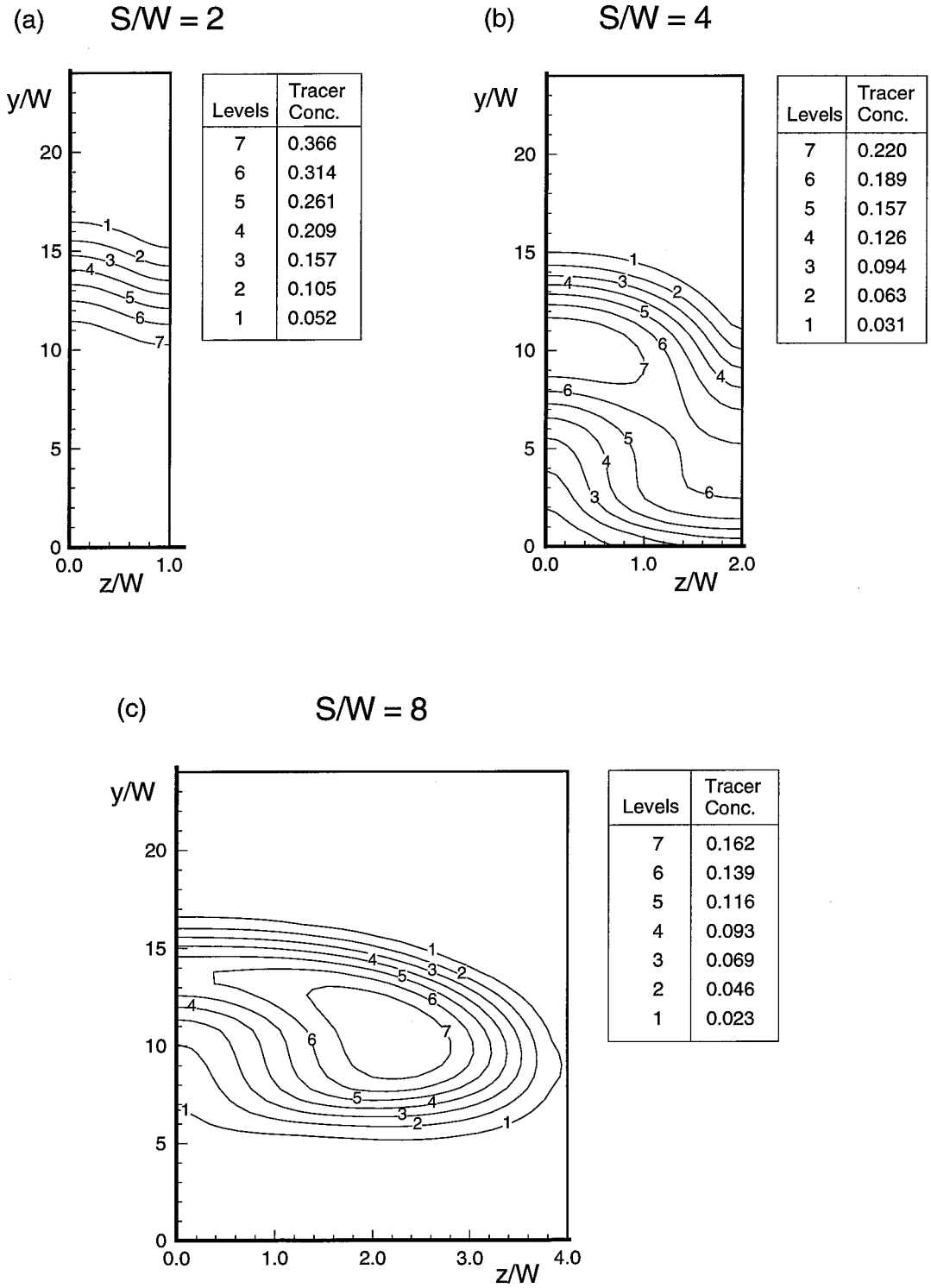

Figure 5.11: Jet tracer concentration profiles for $S/W = 2$, 4, and 8 in the cross-stream plane $x/W = 10$ at $J = 72$.

Secondly, the adjacent vortices from two neighboring jets have opposite signs, and their interaction leads to a reduction in their strength. Hence, in a multiple jet configuration, it is of interest to note the distributions of the jet fluid and vorticity as they could be quite different from those of a single jet. It has been suggested by Stevens and Carrotte (1988) that the decay rates of the vorticity present in the counter-rotating vortex pair affect the jet mixing with the main flow, but the interpretation of the effect of jet spacing on vorticity is not trivial. The following study is aimed at elucidating some characteristics of the vorticity dynamics in this multiple jet context.

5.5.1 Magnitudes of the Streamwise Vorticity

It was suggested by Stevens and Carrotte that the blockage caused by confined, laterally spaced jets would result in a significant increase in the magnitude of the vorticity. Our results show that the suggestion needs to be stated more carefully.

At a cross-sectional plane sufficiently far downstream of the jet, where most of the vorticity is in the streamwise (x) direction, we compute the maximum value of the streamwise component Ω_x of the vorticity of half of the jet that is being simulated. This streamwise vorticity is defined as

$$\Omega_x = \frac{\partial U_3}{\partial y} - \frac{\partial U_2}{\partial z} \tag{5.3}$$

The variation of the maximum streamwise vorticity with the downstream position is plotted in Figure 5.12 for various values of S/W and for $J = 8$ and 72. The values of the vorticity are made non-dimensional through multiplication by W/U_C.

When the jets are very closely spaced at $S/W = 2$, the maximum vorticity is at the lowest compared to other spacings for both $J = 8$ and 72. For $J = 72$, the maximum vorticity is still lower for $S/W = 4$ than for $S/W = 8$. This result is due to the rapid merging of jets at close spacings, especially when the momentum ratio is high. When the

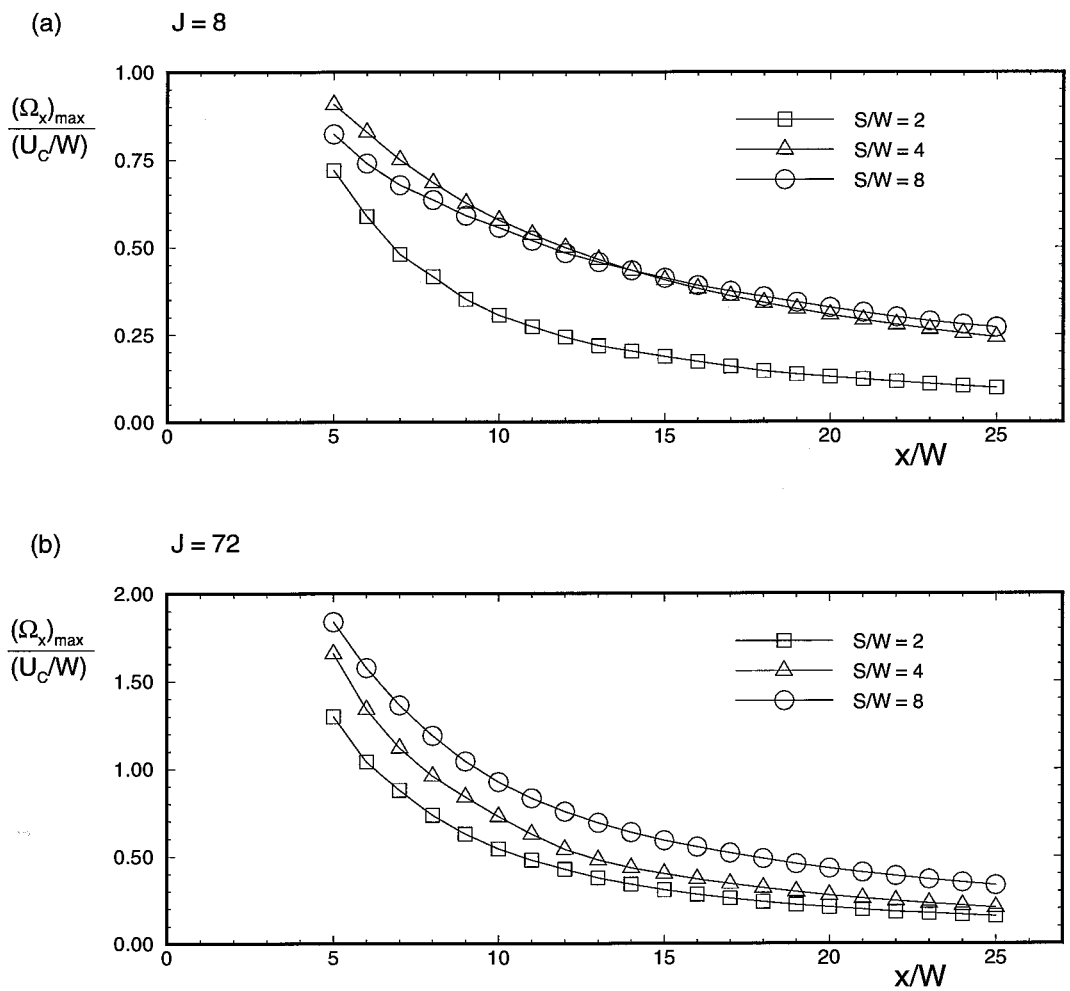

Figure 5.12: Variations in the maximum streamwise vorticity with downstream distance for $S/W = 2$, 4, and 8.

jets merge, the crossflow is prevented from passing through the space between neighboring jets. The decrease in the lateral shear, together with an increase in the vorticity diffusion across jets, contribute to a reduction in the vorticity. Hence, for $J = 72$, there is a decrease in the vorticity as the jet spacing is reduced for the cases shown. For the lower momentum case $J = 8$, the results displayed in Figure 5.12(a) show that there is an increase in the vorticity when the spacing is reduced from $S/W = 8$ to 4. Nevertheless, the increase is slight and the trend reverses a short distance downstream.

To summarize, the results of our simulations show that the increase in blockage caused by a reduction in the spacing between neighboring jets does not always lead to an increase in the maximum vorticity of each jet. The competing effects of vorticity production due to lateral shear and vorticity diffusion need to be considered in the estimation of the vorticity maximum.

5.5.2 Distribution of the Streamwise Vorticity

An examination of the streamwise vorticity distribution reveals the vorticity development for various cases. At the location $x/W = 10$, the cross-sectional distribution of the streamwise component of vorticity, together with the secondary flow vectors, are plotted in Figures 5.13-5.16 for the cases $S/W = 2$, 4, and 8 at $J = 8$ and 72. In each graph, the distribution of the streamwise vorticity is shown for half of the jet between the two longitudinal symmetry planes. The vorticity distribution of the other half of the jet is the mirror image of the distribution shown but with the opposite sign.

A number of observations are noted. First, by comparing the vorticity distribution with the corresponding vector field of the secondary flow in the same cross-sectional plane, it is seen that in many cases, the vorticity cores correspond to the centers of fluid rotation. However, for the case $S/W = 2$ at $J = 72$ shown in Figure 5.15(a) and Figure 5.16(a), the vorticity core is well defined even though there is no apparent recirculating

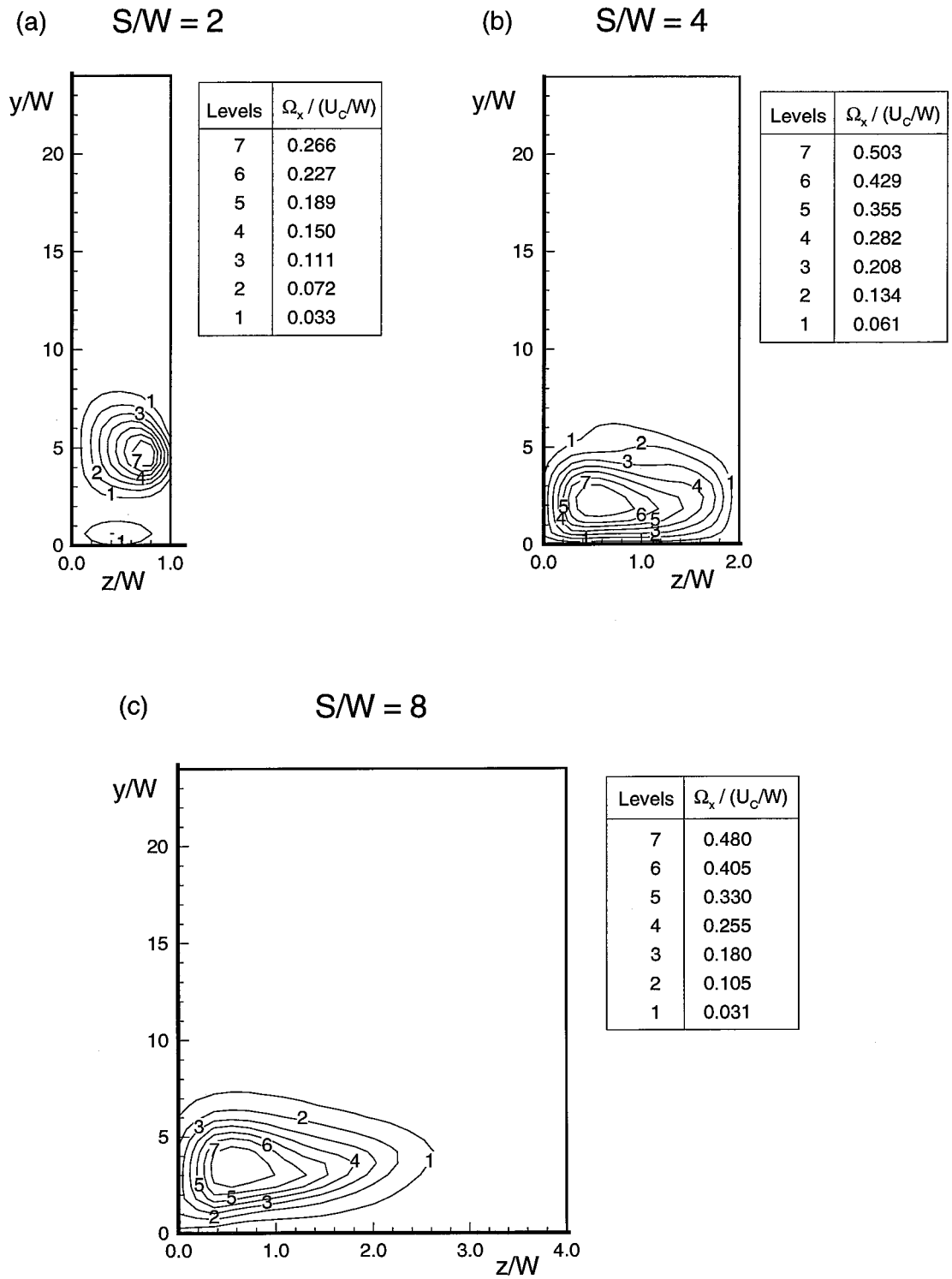

Figure 5.13: Distribution of the streamwise vorticity in the cross-stream plane $x/W = 10$ for $S/W = 2$, 4, and 8 at $J = 8$.

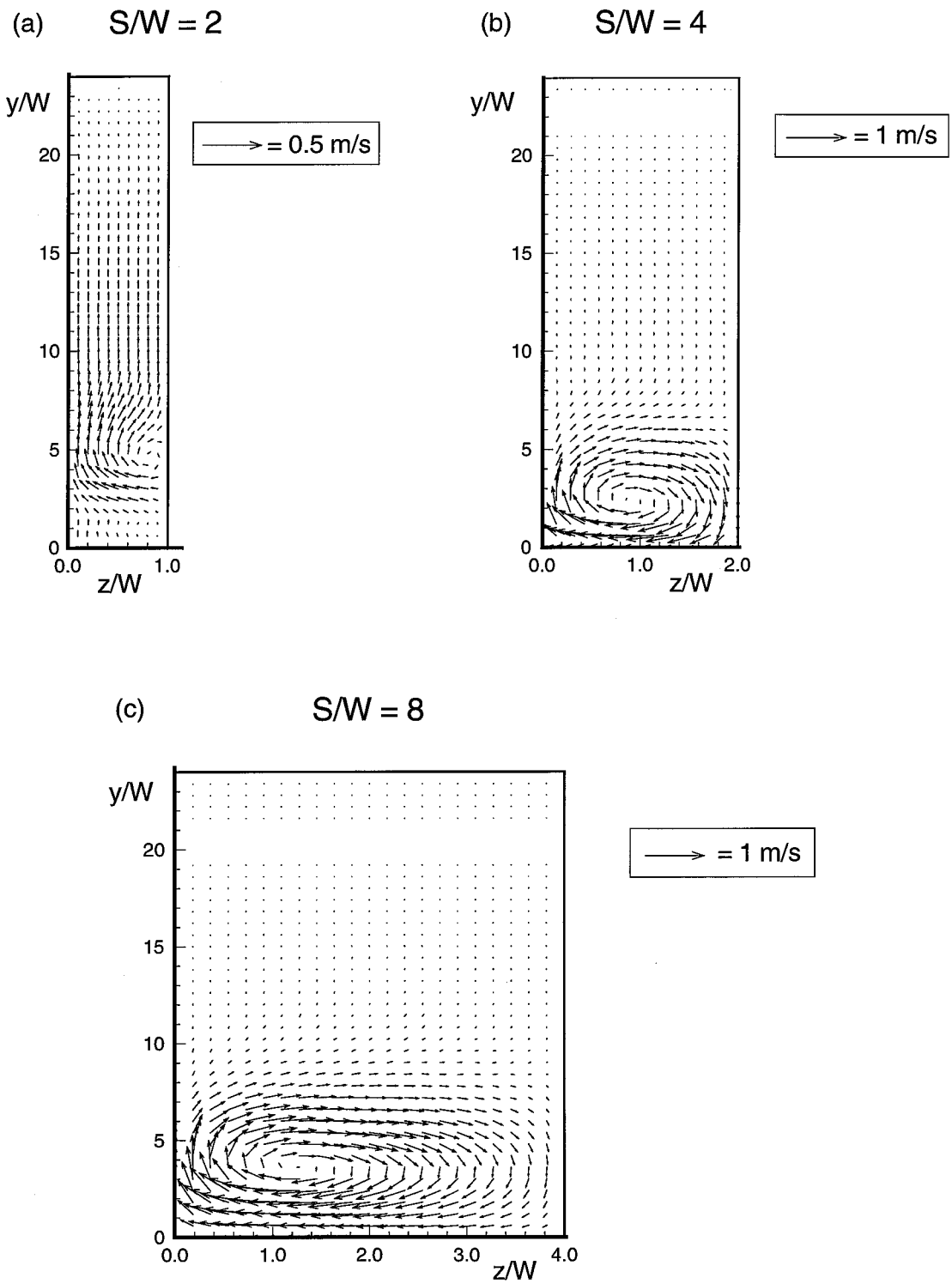

Figure 5.14: Secondary flow vectors in the cross-stream plane $x/W = 10$ for $S/W = 2$, 4, and 8 at $J = 8$.

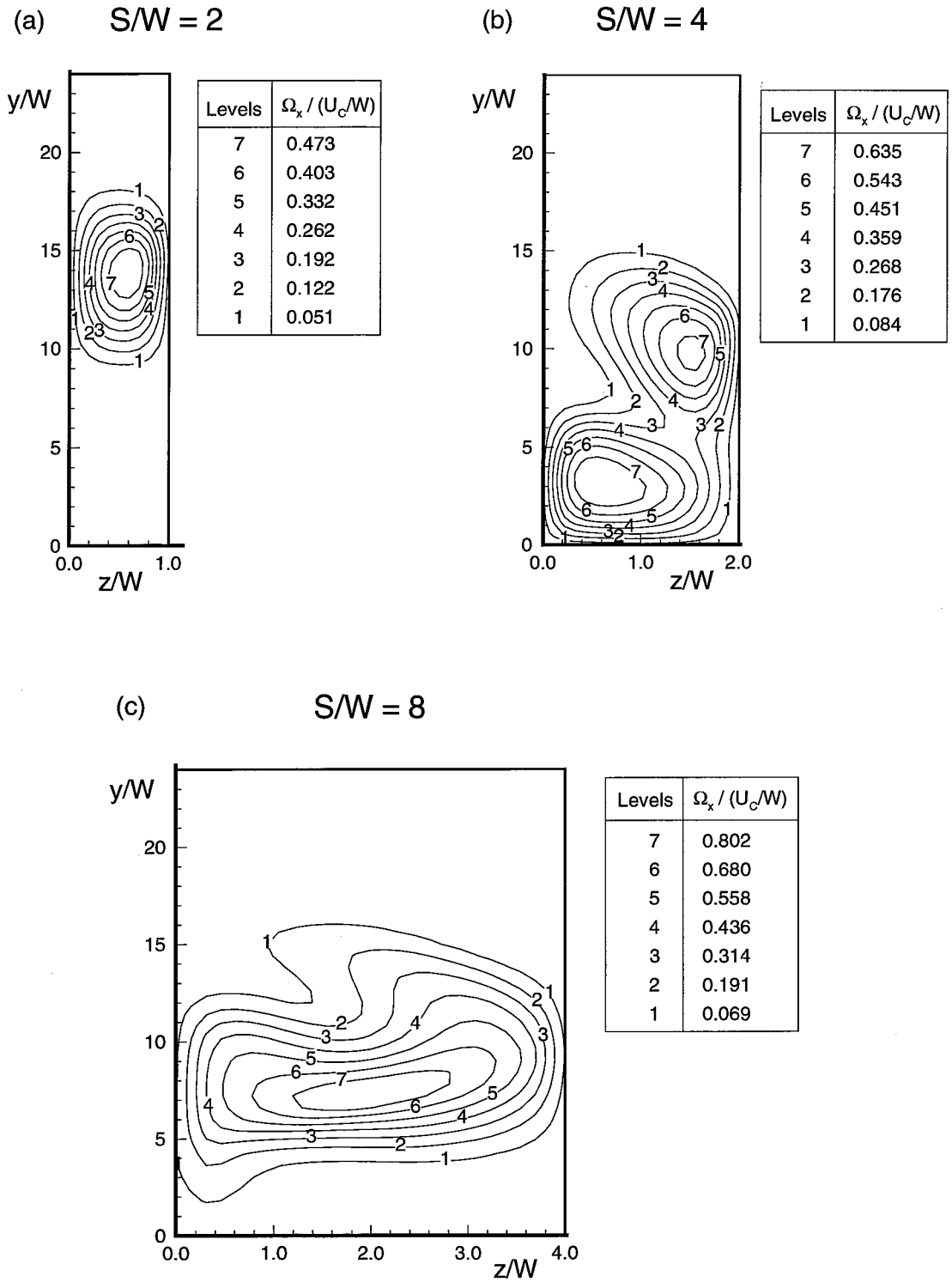

Figure 5.15: Distribution of the streamwise vorticity in the cross-stream plane $x/W = 10$ for $S/W = 2$, 4, and 8 at $J = 72$.

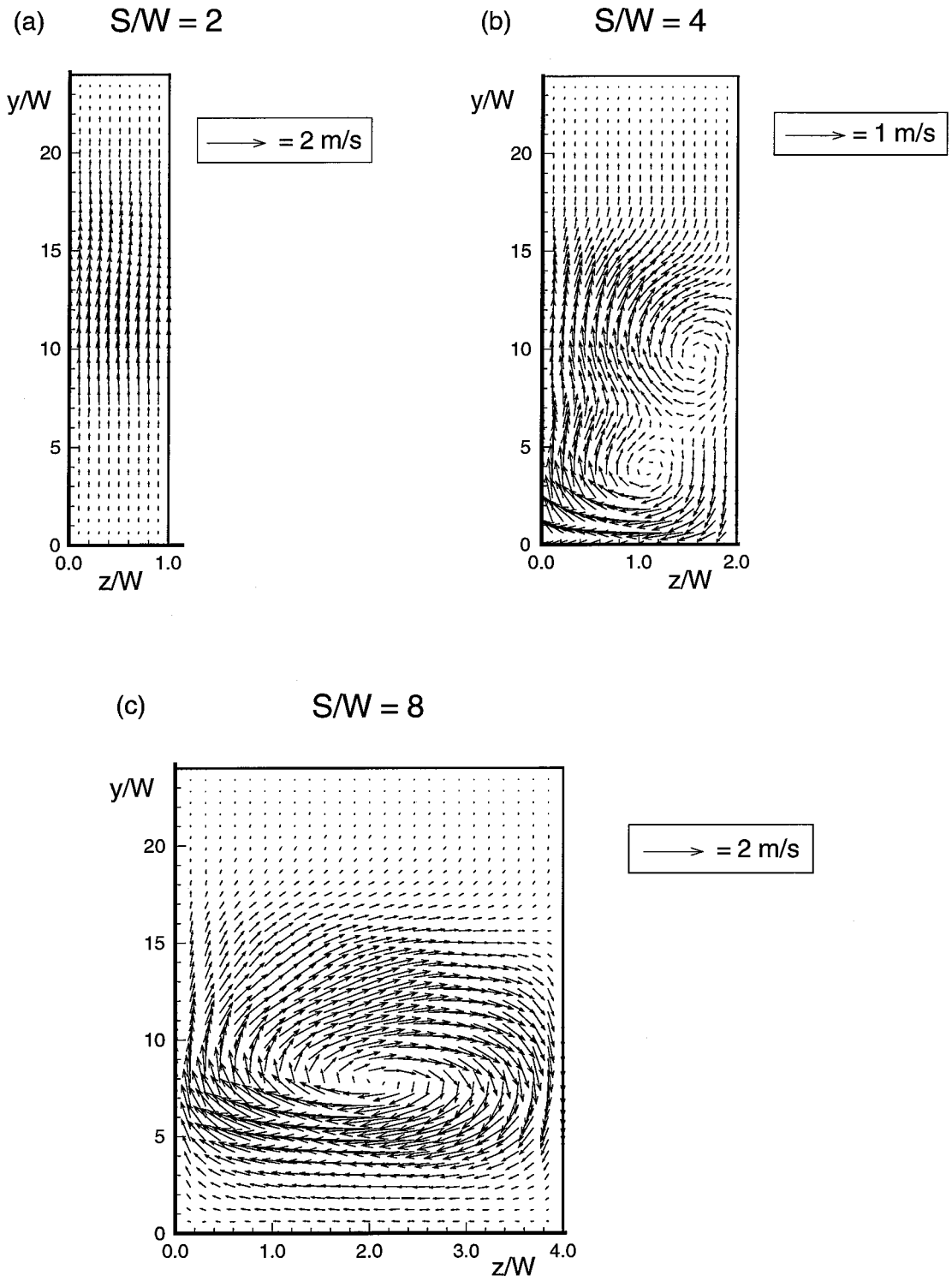

Figure 5.16: Secondary flow vectors in the cross-stream plane $x/W = 10$ for $S/W = 2$, 4, and 8 at $J = 72$.

pattern in the vector field. For this case, at the downstream position $x/W = 10$, the jet is still moving primarily upward as shown earlier in Figure 5.6(a). Thus, the secondary flow field lacks any recirculating appearance. Nevertheless, the vortex core has already been developed at that downstream position.

Secondly, in this multiple jet configuration, the distribution of vorticity and the scalar tracer may not be alike in certain cases. An example is seen at the close jet spacing $S/W = 2$ at $J = 8$ shown in Figures 5.9(a) and 5.13(a), displaying the jet tracer concentration and vorticity distribution at $x/W = 10$. As discussed in Chapter 2, for a single jet, it has been well accepted that the maximum concentration of the jet fluid is in the vortex cores, with a concentration that is 30-70% higher than that on the jet axis. For row-jet injection where the jets are closely spaced, the lateral confinement forces the jet fluid concentration profile to stop bifurcating into two plumes. The streamwise component of the vorticity, however, must be identically equal to zero in the symmetry plane. Therefore, the development of individual vortex cores in the two halves of the cross-section of the jet is guaranteed. The contrast between Figure 5.9(a) and Figure 5.13(a) illustrates the above discussion.

At larger jet spacings, however, the vorticity distribution is similar to the jet fluid distribution. For $S/W = 4$ and 8 at $J = 8$, the regions of high jet fluid concentration lie close to the maximum vorticity locations. This observation is similar to that for a single jet made by Rathgeber and Becker (1983) and by Sykes et al. (1986) at high values of jet-to-crossflow velocity ratio.

The most intriguing observation, however, occurs at $J = 72$. In Figure 5.15(b), it is seen that at the spacing $S/W = 4$, instead of one vortex core in the half-plane for each jet, two cores are observed. Contrasting Figure 5.15(b) with Figure 5.11(b), the cross-sectional profile of the jet fluid distribution displays the usual 'kidney' shape, while the locations of the twin vortex cores do not correspond to the position of maximum jet

fluid concentration. Farther downstream, the streamwise vorticity is dominated by the upper vortex core, which will be demonstrated later. These twin vortex cores are not found for other integral values of S/W at the same momentum ratio.

The formation and intensification of the upper vortex core can be understood by examining the individual terms in the vorticity equation (2.13) in the form proposed by Sykes et al. (1986), which is recast below:

$$(\mathbf{U} \cdot \nabla)\mathbf{\Omega} = (\mathbf{\Omega} \cdot \nabla)\mathbf{U} + \mathbf{D}(\mathbf{\Omega})$$

The terms representing vorticity production and diffusion are examined. The streamwise components of the production and diffusion terms are $\hat{P} = (\mathbf{\Omega} \cdot \nabla)U_1$ and $\hat{D} = \mathbf{D}_x(\mathbf{\Omega})$, respectively. As mentioned in Chapter 2, the production term represents vortex stretching while the diffusion term is due to the turbulence transport process. Their distributions in the plane $x/W = 10$ are shown in Figure 5.17. The values are made non-dimensional through multiplication by $(W/U_C)^2$. Note that the distribution of the diffusion term exhibits two negative 'peaks' while the production term has two positive peaks. These peaks are located near the vortex cores. The upper peak of the production term represents the shearing action of the crossflow passing over the upper edge of the merging jet. This shearing action is more significant at this spacing than at larger spacings since a smaller area is available for the crossflow to pass between neighboring jets. The shearing causes fluid elements to be stretched and thus intensifies the upper vortex core, while farther downstream, the lower vortex core has its significance reduced due to the less intense shear experienced on the lower side of the jet. This dominance of the upper vortex core over the lower one is supported by comparing Figure 5.15(b) with Figure 5.18, which displays the vorticity distribution at a later downstream position at $x/W = 20$.

Finally, the results in Figure 5.17 show that the magnitude of the lowest negative

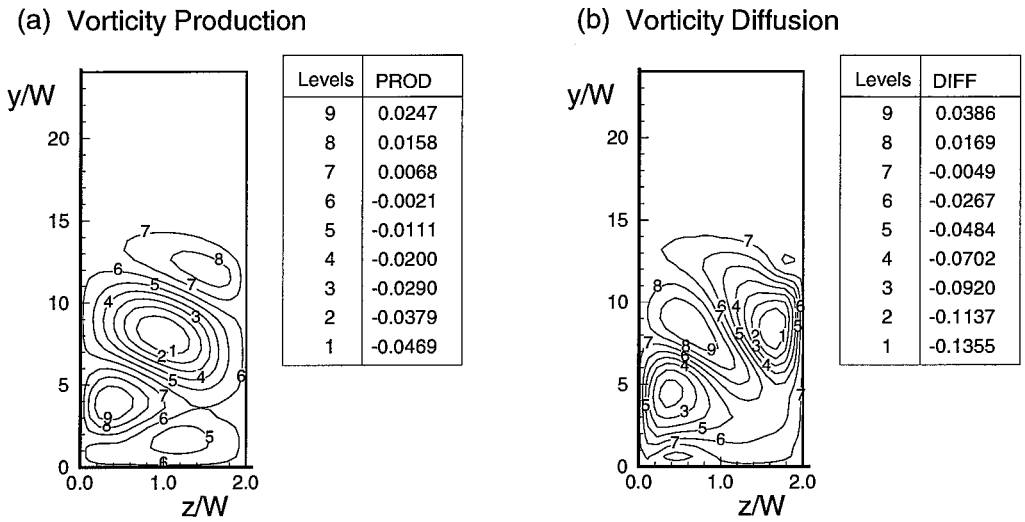

Levels	PROD
9	0.0247
8	0.0158
7	0.0068
6	-0.0021
5	-0.0111
4	-0.0200
3	-0.0290
2	-0.0379
1	-0.0469

Levels	DIFF
9	0.0386
8	0.0169
7	-0.0049
6	-0.0267
5	-0.0484
4	-0.0702
3	-0.0920
2	-0.1137
1	-0.1355

Figure 5.17: Distributions of the production and diffusion terms in the cross-stream plane $x/W = 10$ for $S/W = 4$ at $J = 72$.

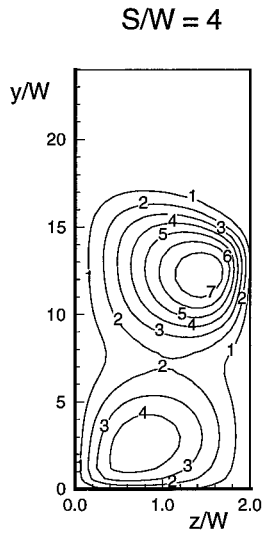

Levels	$\Omega_x / (U_C/W)$
7	0.241
6	0.206
5	0.171
4	0.136
3	0.101
2	0.066
1	0.031

Figure 5.18: Distribution of the streamwise vorticity in the cross-stream plane $x/W = 20$ for $S/W = 4$ at $J = 72$.

vorticity diffusion is several times the highest positive vorticity production. Thus, turbulence diffusion is actively reducing the vorticity whereas the effect of production is less significant. The same trend is observed for other values of jet spacing ratio S/W at both $J = 8$ and 72. This observation illustrates the dominance of diffusion over stretching on the magnitude of maximum vorticity for this type of flow in the far field.

5.6 Concluding Remarks

The numerical simulation for row-jet injection into a crossflow can be difficult to perform. Indeed, our attempt to compute the flow field for the case of high jet-to-crossflow momentum ratio at small lateral jet spacing reveals the slowness in convergence. Many iteration steps are needed in the pre-smoothing stage of the multigrid algorithm to achieve convergence. In addition, our results show that the use of a transient solution method has a positive stabilizing effect on the overall iterative procedure and improves the convergence rate. These observations are useful in understanding and improving the robustness of our present numerical procedure, which in turn is valuable for the prediction of more complex flows such as those found in full recovery boiler simulations.

In this study, a number of characteristics concerning the flow fields of multiple jets in a confined crossflow are identified. First, using the jet fluid distribution as the criterion, the jet penetration is observed to decrease as the jet spacing is reduced. This observation agrees in principle with the experimental observations of Ivanov (1959) and Kamotani and Greber (1974). The result is also useful in understanding the Holdeman correlation formula for jet penetration which will be studied in the next chapter.

The results of the vorticity dynamics in this row-jet configuration serve to quantify some basic characteristics regarding this type of flow field. When the spacing between a pair of jets is small, the jets merge rapidly and the diffusion of vorticity across the

jets weakens the vorticity of each individual jet. It is observed that an increase in lateral shear on the jet due to a reduction in jet spacing does not increase the maximum vorticity significantly. In fact, at the high value of $J = 72$, diffusion dominates production at close jet spacing and the maximum value of vorticity is reduced.

The results of the jet fluid distribution in the cross-stream planes and the corresponding streamwise vorticity distribution reveal that the usual understanding of the dynamics for a single jet in a crossflow needs to be modified substantially when applied to multiple jets. This is demonstrated in the observation that the locations of the maximum jet fluid concentration do not always correspond to the centers of streamwise vortices. Indeed, at $J = 72$ and $S/W = 4$, multiple cores of the streamwise vorticity are numerically simulated.

Chapter 6

Multiple Jet Interactions with a Crossflow

In the previous chapter, the characteristics of a row of square jets in a confined crossflow were investigated. These characteristics are useful in providing a basis for the understanding and interpretation of the phenomena observed in situations where multiple jets are used, such as changes in jet penetration when an array of jets are under various geometric and operating conditions.

For applications to air systems in kraft recovery boilers, it is essential to study the dynamics of jets issuing from rectangular orifices. The aim of this chapter is to study the penetration and mixing of multiple rectangular jets in a confined crossflow.

6.1 Jet Penetration Study : Effects of Parametric Variations

As discussed in the last chapter, the major difficulty in the study of a row of jets interacting with a crossflow is the presence of many geometric and operational parameters that are associated with the description of the flow problem. Fortunately, the results of Walker and Kors (1973) indicate conditions on geometric and operational parameters that influence jet penetration. These conditions were discussed in Chapter 2 and the results of Walker and Kors were correlated by Holdeman and his co-workers. The extension of Holdeman's relationship to rectangular jets of different aspect ratios is the focus of the following sections.

6.1.1 A Non-dimensional Relationship

The investigations by Holdeman and Walker (1977) and Holdeman et al. (1984) identified the jet-to-mainstream momentum flux ratio J as the most important parameter in governing jet penetration. Also, their results were grouped to define 'desirable' mixing in which the jet trajectory was bent by the crossflow so that it travelled down the center of the confining chamber. This strategy seems to be reasonable for applications related to combustion, where it is desirable to have air jets penetrating into the interior of the chamber without significant over-penetration or under-penetration. In any specific application of course the desirable mixing is problem dependent, but similar non-dimensional relationships are likely to exist in most cases.

Upon examining their results, Holdeman and his co-workers identified that when the geometric and operational parameters are related through the formula

$$\frac{S}{H} = \frac{C}{\sqrt{J}} \tag{6.1}$$

then the jet penetration will be desirable, in the sense that it becomes central in the confining chamber. In the above expression, which was also displayed as Eq.(2.24), S is the center-line spacing of the jets in a long array, H is the cross dimension of the confining chamber (see Figure 6.1), and C is a dimensionless parameter whose value for round cold jets entering a hot crossflow was found to be 2.5. The above expression implies that more widely spaced jets (S/H large) require a lower momentum to penetrate to the center-line of the chamber, or conversely that closely spaced jets (S/H small) require more momentum to penetrate to the chamber center-line. It can also be viewed as a correlation of jet penetration: for $\frac{S}{H} \cdot \sqrt{J} = 2.5$, the jets penetrate to the center of the chamber; for $\frac{S}{H} \cdot \sqrt{J} > 2.5$, the jets penetrate more deeply than the center; for $\frac{S}{H} \cdot \sqrt{J} < 2.5$, the jets do not penetrate as far as the center-line. In the present study, we consider penetration from one side to the chamber center-line, following Holdeman et al.

(1984) in considering this a 'good' mixing arrangement.

The derivation of Eq.(6.1) by Holdeman and his co-workers was based entirely on experimental observations. However, it can be put on a firmer basis by showing that it also reflects the results of Kamotani and Greber (1974). First, the latter experimental results reveal that at a certain jet spacing that is not too small ($S/W > 3$), increasing the confinement dimension H does not affect the jet trajectory too much. This is reflected in Eq.(6.1) through the recognition that if S is kept constant, then to maintain the same extent of penetration when H is increased, $\sqrt{J}$ needs to be increased proportionally. In other words, the jet velocity V_{jet} needs to be increased in proportional to any increase in H to maintain suitable penetration. Another observation by Kamotani and Greber concerns the decrease in jet penetration as spacing S is reduced for moderately spaced jets ($3 < S/W < 10$) examined in the last chapter. If H is held fixed in Eq.(6.1), then for the same extent of penetration, $1/\sqrt{J}$ needs to be changed in proportion to S. In other words, a reduction of S requires an increase of V_{jet} to maintain the penetration for fixed H. Hence, once again there is consistency between the physical trend observed and the empirical correlation.

The results by Kamotani and Greber also reveal the limitation of the applicability of Eq.(6.1). The correlation is useful only when the spacing S divided by jet width W is neither too small (very closely spaced jets) nor too large (essentially isolated jets). Closely spaced jets coalesce and the resulting lack of three dimensional entrainment increases the penetration so that Eq.(6.1) is no longer appropriate. The validity of the correlation for a range of jet sizes and shapes is investigated here using numerical simulations. The possible implications of the correlation for recovery furnaces will then be considered.

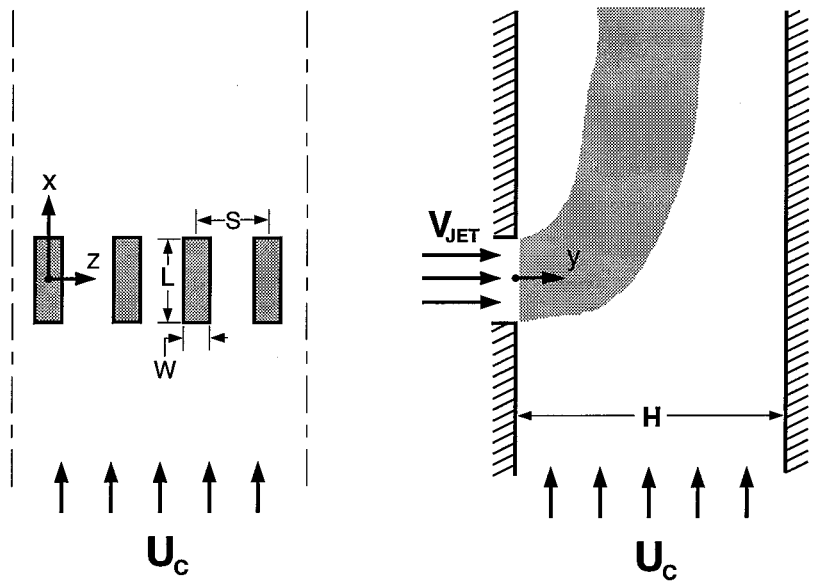

Figure 6.1: A schematic description of the domain for one-side injection.

6.1.2 A Row of Rectangular Jets in a Crossflow

The configuration for one-sided injection is illustrated in Figure 6.1. Again, the flow field is obtained by solving the time-averaged form of the Navier-Stokes equations coupled with the $k - \epsilon$ turbulence model. Boundary conditions are handled the same way as in the last chapter. Symmetry conditions are applied on lateral sides of a jet to minimize the size of the domain. Hence, in the study, only half of a jet is simulated. Other boundary conditions applied include imposed values for the velocity and scalar at the flow inlet and jet entrance, the zero-gradient exit condition, and the wall function formulation at no-slip walls. A unit of a passive tracer is injected with the jet to indicate the dispersion of the jet fluid. Multigrid calculations are performed for square jets and rectangular jets of various aspect ratios. With proper attention to the placement of the exit plane and the choice of the number of iterations carried out within the multigrid procedure, convergence is achieved readily for the problems studied in this chapter.

To extend Holdeman's well-mixing criterion to the case of rectangular jets of different

aspect ratios, numerous simulations are performed with different values of S/H and J to examine the appropriate choice of C for each case. The control parameter is the jet-to-mainstream mass flow ratio M, which for constant density flow is evaluated from the formula

$$M = \frac{LW}{HS} \cdot \frac{V_{jet}}{U_C} = \frac{AR\, W^2}{HS} \cdot \sqrt{J} \tag{6.2}$$

This quantity is significant in combustion applications, where its value is fixed by the stoichiometric requirement of air. In our simulations, at a given value of J, M is held fixed when the extent of jet penetration is examined in various cases.

6.1.3 Results for Uniform Crossflow

Square Jets

Turbulent flow simulations are carried out to emulate the experiments of Holdeman and Walker (1977). The results should not be affected significantly by changes in actual size or Reynolds number, provided other dimensionless ratios are kept constant. Thus, the non-dimensional correlations derived are useful in describing flows in larger devices.

$H = 0.1016$ m (4 inches) $U_C = 15$ m/s			
J	M	S/H	W/H
6	0.15	0.25	0.1250
		0.50	0.1768
		0.75	0.2165
25	0.31	0.10	0.0394
		0.20	0.0557
		0.30	0.0682

Table 6.1: Parameters chosen for simulations of square jets.

The values of the geometric and operational parameters considered are listed in Table 6.1. Two values of J are chosen to represent the cases where the jets have momentum that is low or moderate. For each value of J, three values of S/H are chosen to study the effects of varying the jet spacing. A value of M is then chosen and the jet width W can be determined from Eq.(6.2). A larger value of M is chosen for $J = 25$ so that the corresponding value of W will not be too small for each choice of S/H.

Following Holdeman and Walker, the jet fluid distribution in the symmetry plane $z = 0$ is examined and the results are shown in Figures 6.2-6.3. By examining these profiles, and applying the requirement that jet penetration be such as to bring the concentration maxima to the approximate center of the chamber, we deduce that for $J = 6$, the jet penetration is optimal when S/H is between 0.5 and 0.75, and for $J = 25$, it is $S/H = 0.3$. Based on these observations, a value of $C \approx 1.5$ correlates the results for optimal jet penetration for square jets in constant density flow. This value is about one half that recommended by Holdeman and his co-workers. Our lower value for C may be due to the use of isothermal flow in the present study.

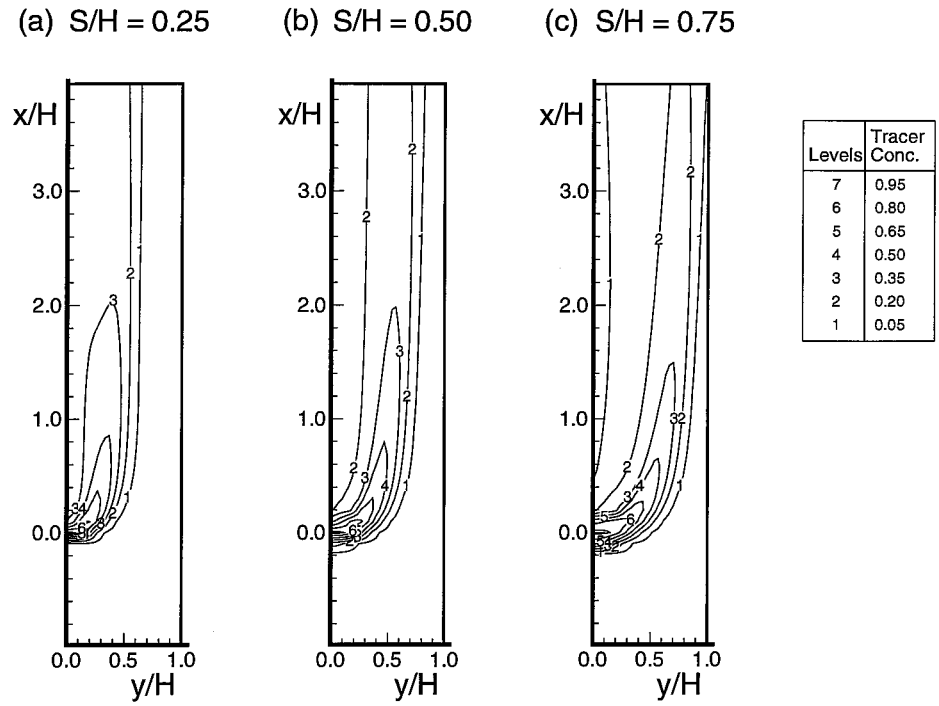

Figure 6.2: Distribution of jet tracer concentration in the center-plane ($z = 0$) for square jets at $J = 6$ and $M = 0.15$.

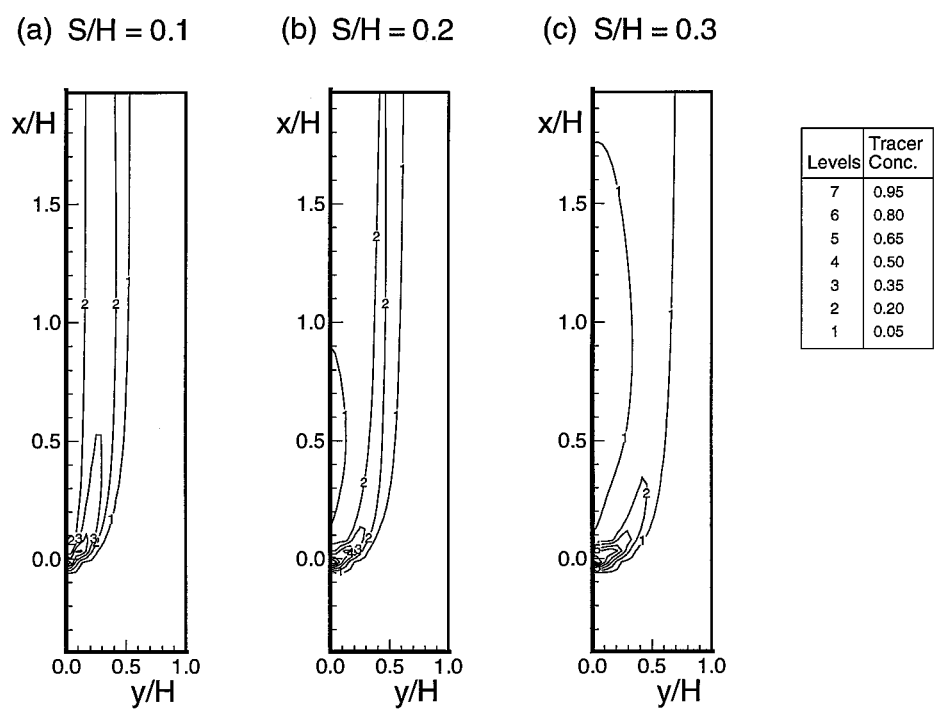

Figure 6.3: Distribution of jet tracer concentration in the center-plane ($z = 0$) for square jets at $J = 25$ and $M = 0.31$.

Rectangular Jets of Aspect Ratio 3 and 6

Similar calculations are carried out for orifices having aspect ratio $AR = L/W$ of 3 and 6. Values of $J = 6$ and $M = 0.15$ are used as before. These cases are listed in Table 6.2.

$H = 0.1016$ m (4 inches) $U_C = 15$ m/s $J = 6$, $M = 0.15$		
AR	S/H	W/H
3	0.25	0.0720
	0.50	0.1021
	0.75	0.1250
6	0.25	0.0510
	0.50	0.0722
	0.75	0.0884

Table 6.2: Parameters chosen for simulations of rectangular jets with $AR = 3$ and 6.

Again the jet tracer concentration contours are plotted in the center-plane $z = 0$. The results are shown in Figures 6.4-6.5 for $AR = 3$ and 6, respectively. In addition, the cross-sectional profiles of the jet tracer concentration for jets at $S/H = 0.5$ but with different values of AR are shown in Figures 6.6-6.7 for comparison. The results show the differences in jet characteristics caused by changes in the shape of the jet orifice.

The following results are revealed. First, higher aspect ratio jets penetrate deeper into the crossflow when conditions such as the orifice area, jet spacing, and jet momentum are equal. Secondly, the regions of high jet fluid concentration in the jet's cross-section split about the center-plane $z = 0$ for jets with $AR = 3$ and 6. In these cases, the locations of high jet fluid concentration lie below the jet concentration trajectory in the center-plane. These observations influence the choice of optimal penetration depth.

For jets with $AR = 3$, optimal penetration occurs at a spacing close to $S/H = 0.5$, which is less than that for square jets. For jets with $AR = 6$, the optimal spacing should

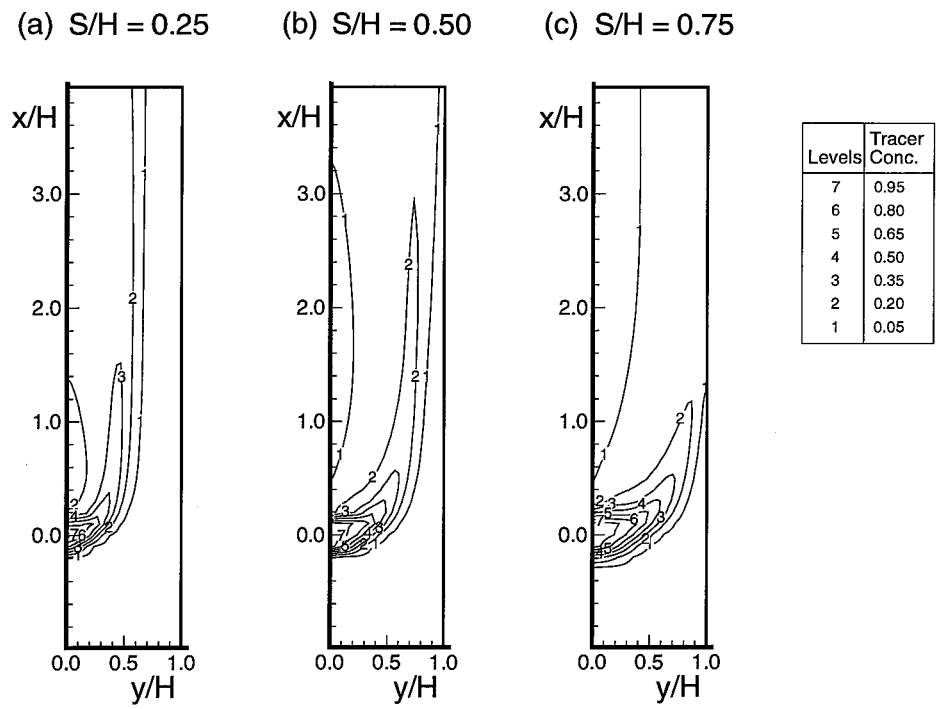

Figure 6.4: Distribution of jet tracer concentration in the center-plane ($z = 0$) for $AR = 3$ jets at $J = 6$ and $M = 0.15$.

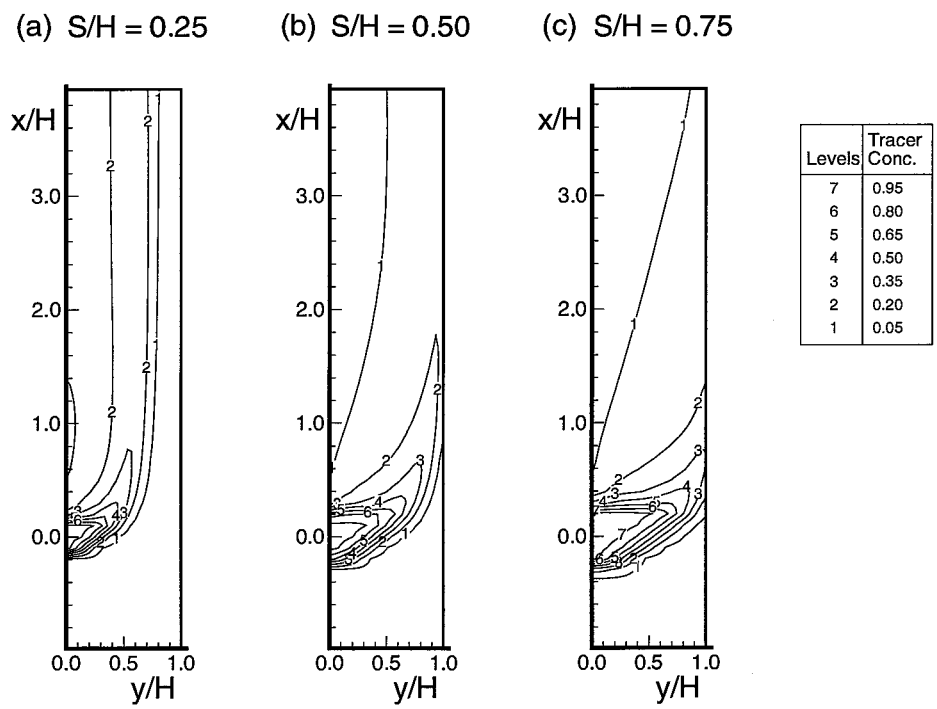

Figure 6.5: Distribution of jet tracer concentration in the center-plane ($z = 0$) for $AR = 6$ jets at $J = 6$ and $M = 0.15$.

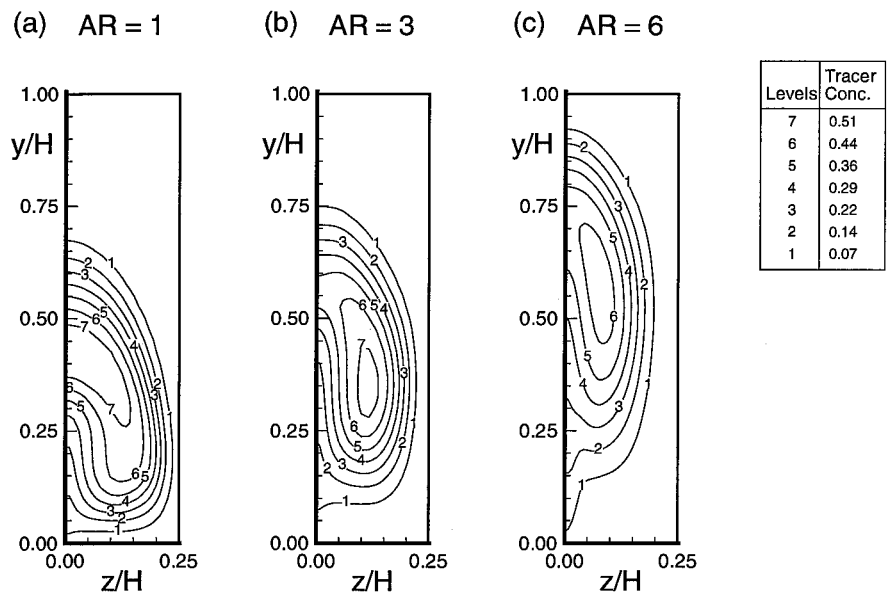

Figure 6.6: Jet tracer concentration in the cross-sectional plane $x/H = 0.5$ at the spacing $S/H = 0.5$.

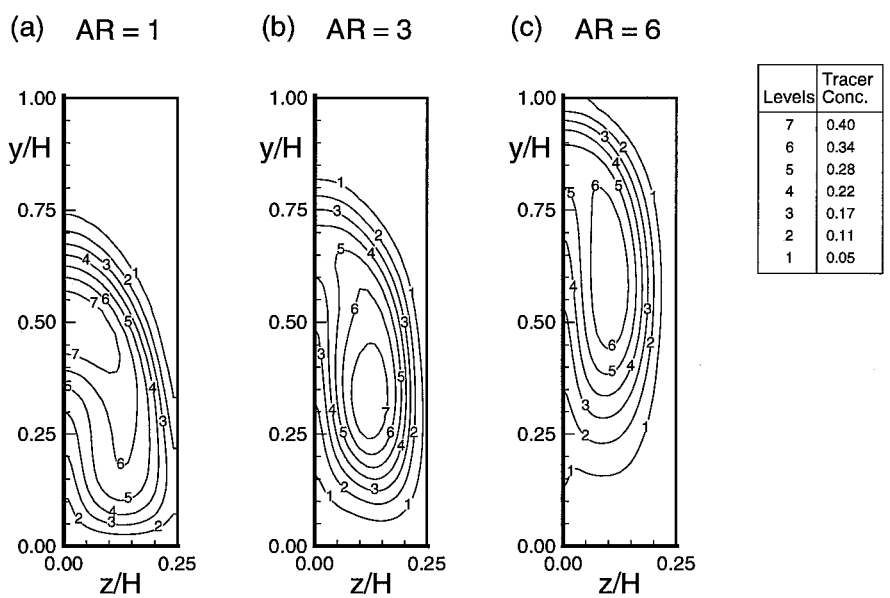

Figure 6.7: Jet tracer concentration in the cross-sectional plane $x/H = 1.0$ at the spacing $S/H = 0.5$.

be slightly greater than $S/H = 0.25$. In making these choices for rectangular jets, the jet trajectory in the center-plane is preferred to be slightly beyond the middle of the chamber, so that the jet fluid will not be too close to the injection wall. Thus, the following values for C are estimated for proper jet penetration: $C \approx 1.0$ for $\mathcal{AR} = 3$ and $C \approx 0.65$ for $\mathcal{AR} = 6$. These estimates are listed in Table 6.3. For jets whose aspect ratio is between 1 and 6, the optimal value of C may be obtained by interpolation.

$\mathcal{AR}$	Optimal C
1	1.5
3	1.0
6	0.65

Table 6.3: Optimal values of C for orifices having different aspect ratios.

6.1.4 Experimental Investigation on Jet Penetration

An experimental investigation is carried out to verify the difference in jet penetration between wide jets and slender jets that is observed in the numerical simulation. The experiment is performed in the 1 : 30 scaled Kamloops boiler model shown in Figure 6.8 in which the flow of water is used to simulate the fluid motion within a recovery boiler unit. There are three levels of jets in the model, and in the experiment the lowest primary level jets are all turned on to let in water to generate a cross-flow for the jets located at higher elevations. The total water flow rate entering these primary orifices is 7.7×10^{-3} m^3/s (122 US gal/min). A flow visualization experiment is carried out to observe the jet penetration. The details of the experimental set-up are provided in Appendix A.

An important reason for performing the experiment in the Kamloops model rather than in a wind tunnel or water tunnel is to observe the behavior of jet penetration when the conditions of the cross-stream deviate from the ideal. In the numerical simulation,

jet penetration is examined when the incoming conditions for the crossflow are perfectly uniform. However, in many practical situations as in a recovery boiler, the cross-stream can exhibit great non-uniformity. Thus, the objectives of the experiment are to compare jet penetration when the shape of the jet orifice changes and to observe the effect of cross-stream non-uniformity on jet penetration.

In the experiment, the jets at the secondary level are turned off and only one side of the tertiary injection system is used. The two templates shown in Figure 6.9 act as the jet inlet holes. The area of each orifice opening is 4 cm^2 and the rectangular orifices have aspect ratio $AR = 4$. The flow rate for each jet is set constant at 2.5×10^{-4} m^3/s (4 US gal/min), which corresponds to an average jet velocity of 0.63 m/s. The focus of the flow visualization study is on the middle jet, where the cross-stream is moving upward most prominently in the vicinity of the jet entrance. A sheet of laser light is used to shine along the center-plane cutting longitudinally across the jet orifice. An S-VHS camera is used to record approximately five minutes of the flow field in each case of square jet injection and rectangular jet injection. Typical results are shown in Figure 6.10, which are photographs taken from a video display. The exposure time is 0.125 seconds to allow for the showing of streak lines on the photographs. These streak lines indicate the movement of small polystyrene particles carried by the flow and the lines are good indicators of the flow pattern appearing in the boiler model.

The flow structures displayed in the photographs in Figure 6.10 show that the penetration of rectangular jets is deeper than square jets. This observation is consistent with our numerical predictions. During the time of filming, it is observed that there are moments of flow unsteadiness where there are changes to the crossflow pattern. Such changes involve fluid flowing laterally instead of upwards, and this can affect jet penetration by allowing it to be deeper or not as deep. Nevertheless, it is generally observed that, in the situation considered, rectangular jets penetrate deeper than square jets.

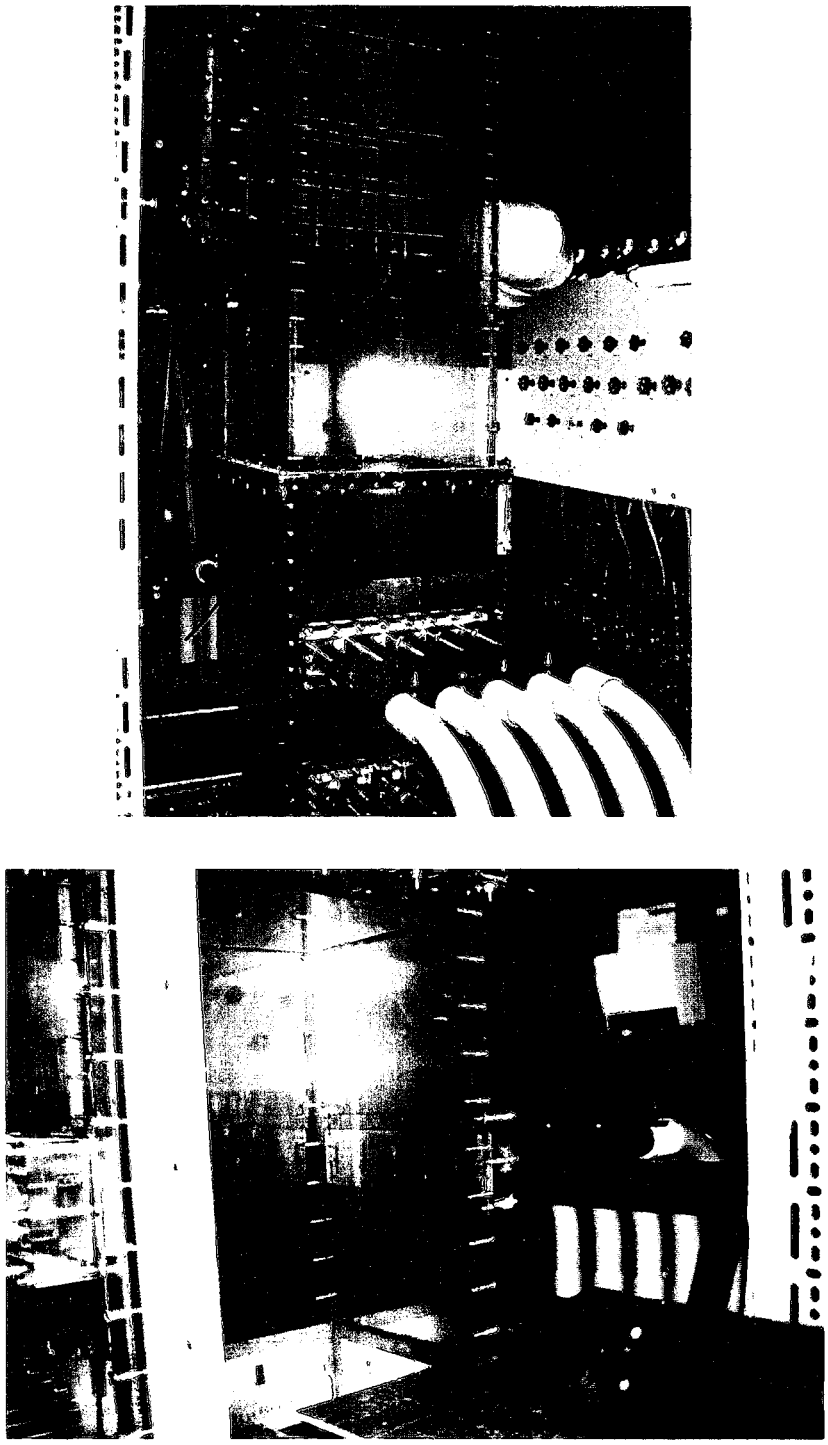

Figure 6.8: Photographs of the Kamloops water model showing the overall model and the orifices for tertiary jets.

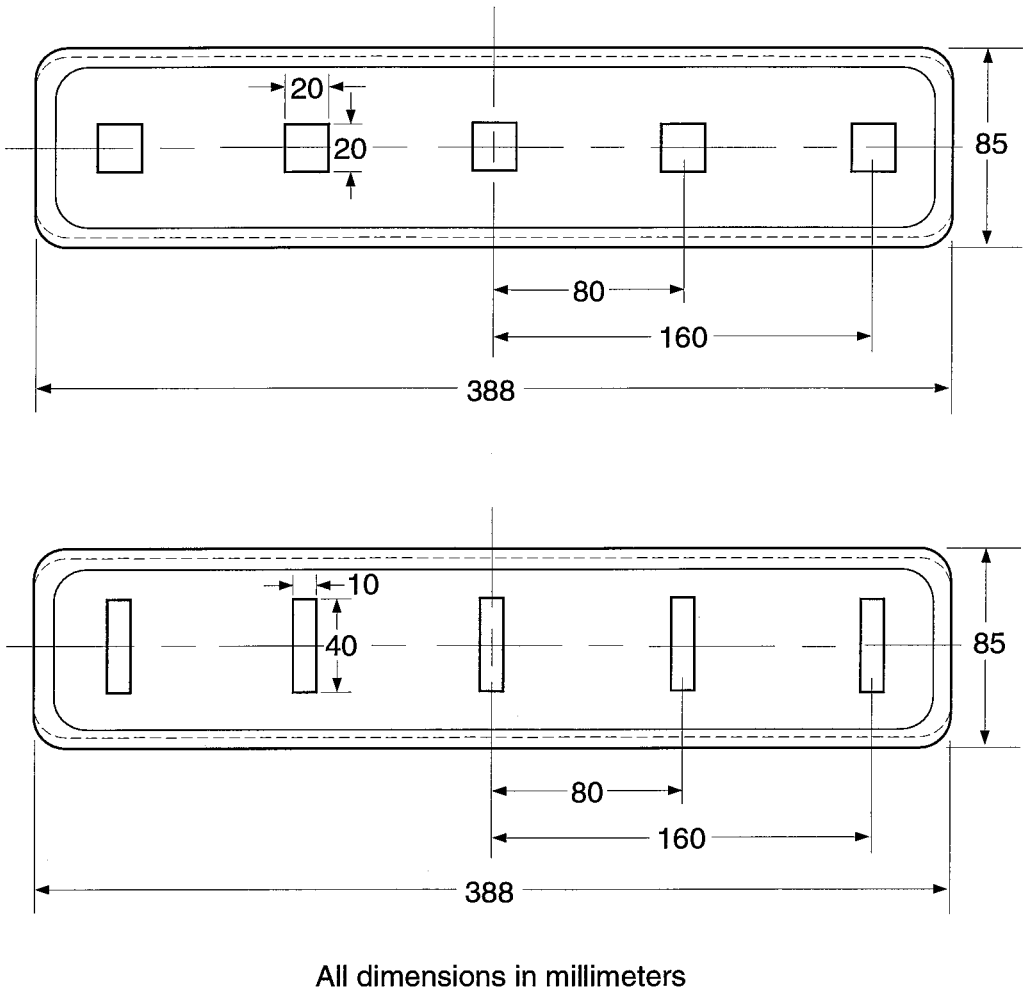

Figure 6.9: The two templates used in the experiment: square orifices and rectangular $\mathcal{AR} = 4$ orifices.

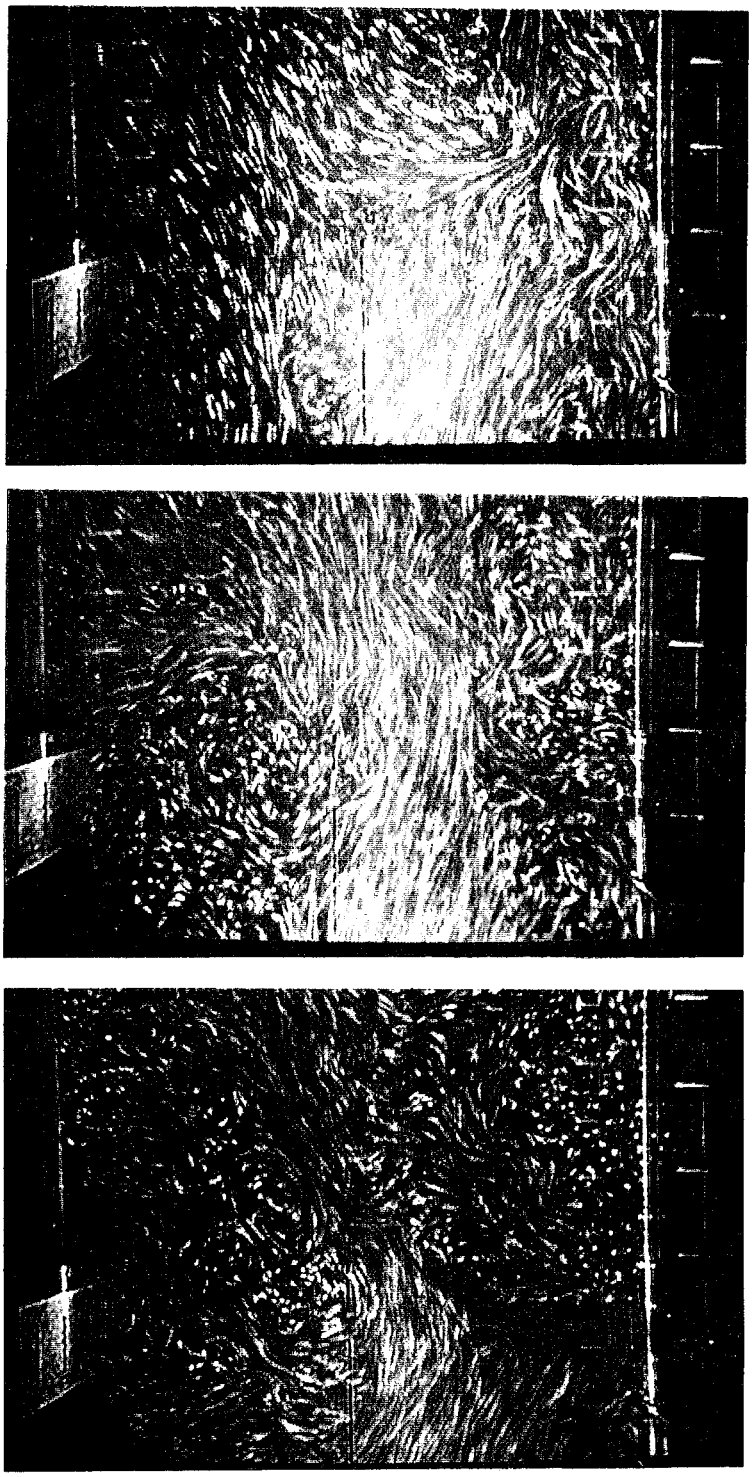

Figure 6.10: Photographs displaying jet penetration. Top: crossflow. Middle: square jet injection. Bottom: rectangular jet injection. Jets enter from the right side only.

6.2 Mixing and Vorticity Characteristics

The previous discussion on optimal jet penetration is based on visual inspection of the jet trajectory in the center-plane. The goal is to have the jet penetrating to the center of the chamber. A quantitative study is now carried out to examine the degree of mixing in various cases to verify whether jets penetrating to the center of a chamber is indeed an optimal strategy. In addition, the characteristics of the streamwise vorticity are studied for jets that have different aspect ratios and at different jet spacings. An objective of this study is to investigate the relationship between the extent of jet mixing and vorticity reduction for various cases.

6.2.1 Quantitative Study of Jet Mixing

The methodology employed here has application to combustion in furnaces. Specifically, attention is focussed on the volume of fluid per unit time passing through a cross-sectional plane having concentration of a scalar tracer in a certain range. The implication for combustion is that it is important to know the concentration of combustibles within certain critical ranges where burning occurs.

The above objective is met by considering the probability density function $f(\xi)$ derived in Appendix B. At a cross-sectional plane with elemental area $d\mathbf{S}$ located at streamwise coordinate x, this density function is denoted as

$$f_x(\xi) \equiv \frac{1}{\Delta\xi}\left\{\frac{(\mathbf{U}\cdot d\mathbf{S})_x \textit{ having concentration in range } \xi\pm\frac{\Delta\xi}{2}}{Q_1+Q_2}\right\} \tag{6.3}$$

where $\xi = \Phi - \Phi_{av}$, with Φ_{av} being the average or fully mixed concentration value, and $\Delta\xi$ being some small increment of ξ. In addition, Q_1 and Q_2 are the volume flow rates of the cross-stream and the jet, respectively. It is shown in Appendix B that the mean of $f_x(\xi)$ is zero and that for perfectly mixed fluid, the variance of $f_x(\xi)$ is also zero.

At the same cross-sectional plane, the variance σ_x^2 of $f_x(\xi)$ can be computed as

$$\sigma_x^2 = \int_{-\infty}^{\infty} \xi^2 f_x(\xi)\, d\xi \tag{6.4}$$

It is defined in Appendix B that the quantity, δ_x, is a normalized measure for mixing. It is defined as

$$\delta_x = \frac{\sigma_x}{\sigma_o} \tag{6.5}$$

where σ_o is the maximum variance computed before any mixing has occurred. The values of δ_x vary from 1 (no mixing) to 0 (fully mixed), and is a good quantitative measure of jet-crossflow mixing.

The values of $f_x(\xi)$ and subsequently δ_x are computed for the cases with $J = 6$ listed in Tables 6.1 and 6.2. The evaluation is carried out in cross-stream planes in the range $0.5 \leq x/H \leq 3.0$. The graphs of $f_x(\xi)$ for $\mathcal{AR} = 6$ and $S/H = 0.25$ at $x/H = 1.0$, 2.0, and 3.0 are shown in Figure 6.11 to demonstrate the change in the shape of the profile as the downstream position is varied. It is seen that the spread of the distribution reduces as the downstream position increases, indicating that more mixing has taken place, resulting in a more uniform distribution of the tracer flux.

The graphs for the variation of δ_x are shown in Figure 6.12. Comparison is first carried out for jets that have the same aspect ratio but at different spacings. For square jets ($\mathcal{AR} = 1$) at the spacings $S/H = 0.5$ and 0.75, the values of δ_x experience sharper decays past $x/H = 1$ than at $S/H = 0.25$. This sharper reduction in δ_x occurring at $S/H = 0.5$ and 0.75 is consistent with our earlier objective to have the jets penetrate into the middle of the chamber, as discussed in section 6.1.3. Figure 6.2 illustrates that the jet penetrates into the middle of the chamber at $S/H = 0.5$ and slightly over-penetrates at $S/H = 0.75$. Thus, the results have quantified the observation by Walker and Kors (1973) that over-penetration (at $S/H = 0.75$) is preferred to under-penetration (at $S/H = 0.25$) for the purpose of jet-crossflow mixing. Similar observations are also apparent for rectangular

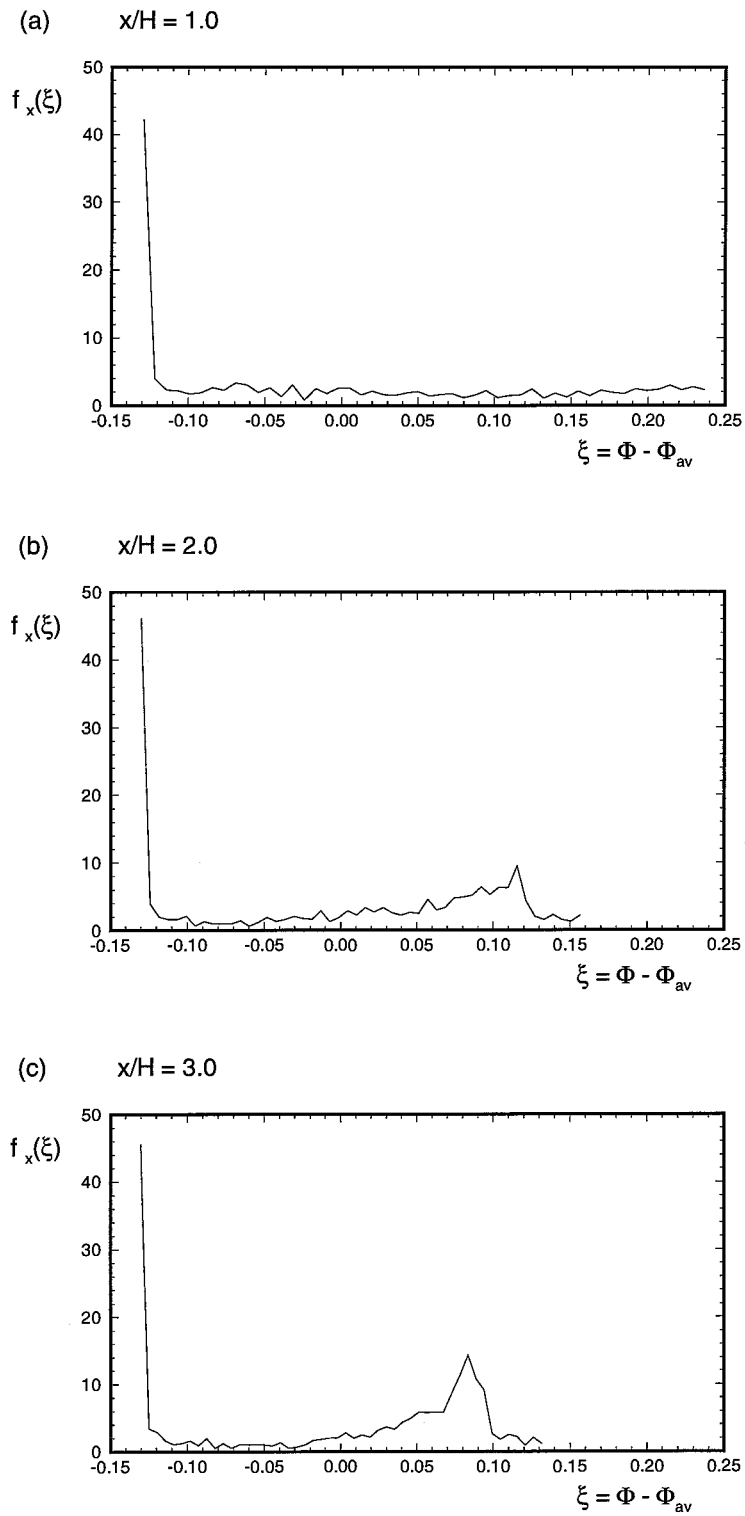

Figure 6.11: Profiles of $f_x(\xi)$ for $AR = 6$ and $S/H = 0.25$ at various downstream locations.

jets. For jets with $AR = 3$, the fact that δ_x assumes lower values at $S/H = 0.5$ than at the other two spacings ($S/H = 0.25$ and 0.75) is again consistent with the penetration profiles in the center-plane shown in Figure 6.4. The figure shows that the jet propagates down the chamber too close to the injection wall at $S/H = 0.25$ and too close to the opposing wall at $S/H = 0.75$. Finally, for jets with $AR = 6$, the values of δ_x are the highest at $S/H = 0.75$. These high values correspond to the results shown in Figure 6.5 that the jet over-penetrates significantly at this spacing. The near-impingement of the jet with the opposing wall reduces the amount of jet volume available for mixing with the mainstream. To conclude, the above observations confirm that the strategy to have the jet propagates down the middle of a chamber is indeed desirable for good mixing.

Another observation from Figure 6.12 is that at the close jet spacings of $S/H = 0.25$ and 0.5, better mixing is achieved with higher aspect ratio jets. This is related to the observation of the cross-sectional shapes of the jets displayed in Figures 6.6-6.7, which show that jets from slender orifices have more elongated cross-sectional shapes. These jets propagate downstream for a longer time before they merge with the neighboring jets. Since the merging of jets reduces the amount of mainstream volume that will be affected by each jet, the postponement in merging results in better mixing by high aspect ratio jets at close lateral spacings. On the other hand, when the spacing is large ($S/H = 0.75$), jets with $AR = 1$ and 3 both have ample amount of time to develop independently before any merging will occur. Consequently, the degree of mixing is similar for the two kinds of jets, as shown in Figure 6.12(c). Jets with $AR = 6$, however, mix less effectively at large downstream locations because of the significant over-penetration as discussed in the last paragraph.

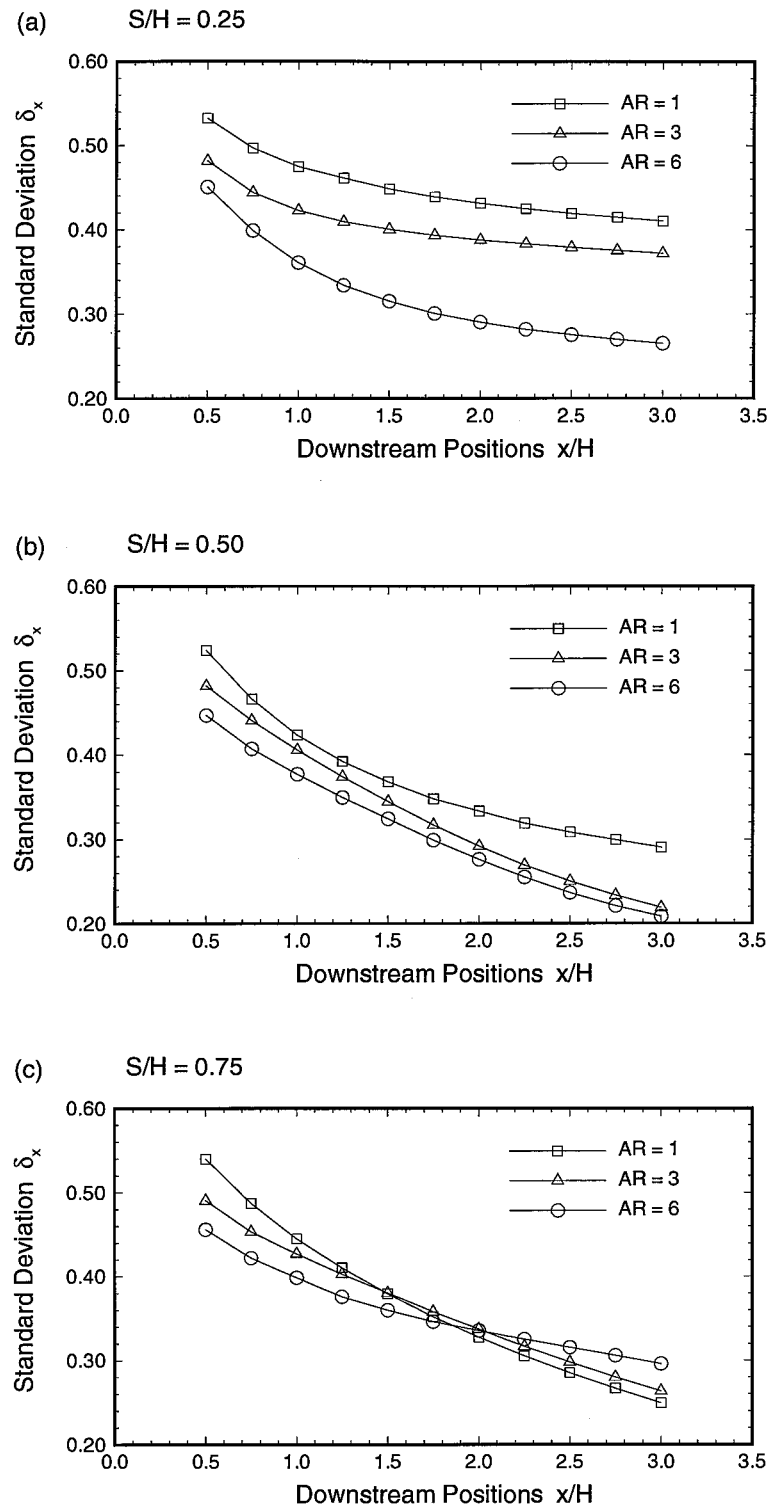

Figure 6.12: Variation of δ_x with x/H for jet-crossflow mixing for various cases of AR and S/H.

6.2.2 Vorticity Considerations

As shown in the last chapter, the counter-rotating vortex cores of each jet dominate the far field jet structure. These vortices provide a mechanism for mixing between the cross-stream fluid and the deflected jet. As in the previous study, the streamwise component of the vorticity, defined by Eq.(5.3), is computed for the cases of $J = 6$ listed in Tables 6.1 and 6.2 at various downstream positions x/H. Far enough downstream, this streamwise component of vorticity represents almost all of the vorticity the jet possesses.

The variations of the maximum values of the streamwise component of vorticity are plotted in Figure 6.13 for the three jet spacings. The values of these vorticity maxima are affected by vortex stretching and turbulence diffusion. To evaluate the relative importance of these two effects, the vorticity production and diffusion terms in the vorticity equation are examined following the practice in section 5.5.2. In almost every case the location of maximum vorticity also corresponds to the locations of lowest negative vorticity diffusion and highest positive vorticity production. These results are similar to those stated in section 5.5.2. Typical results are displayed in Figure 6.14. The figure shows the distributions of the streamwise vorticity, its production, and its diffusion for the case $AR = 3$ and $S/H = 0.5$ at $x/H = 1$. The values in Figure 6.14 are non-dimensionalized by V_{jet}/H for the vorticity and V_{jet}^2/H^2 for the vorticity production and diffusion.

The results shown in Figure 6.14 reveal the general trend that the vorticity core is strengthened by vorticity stretching while weakened by turbulence diffusion, a phenomenon also observed for the cases studied in the previous chapter. Moreover, the magnitude of the lowest negative diffusion is generally several times greater than the highest positive production. This is an indication that diffusion due to turbulence is the major controlling factor for the reduction in the vorticity values shown in Figure 6.13.

Returning to Figure 6.13, a comparison of the graphs there with those in Figure

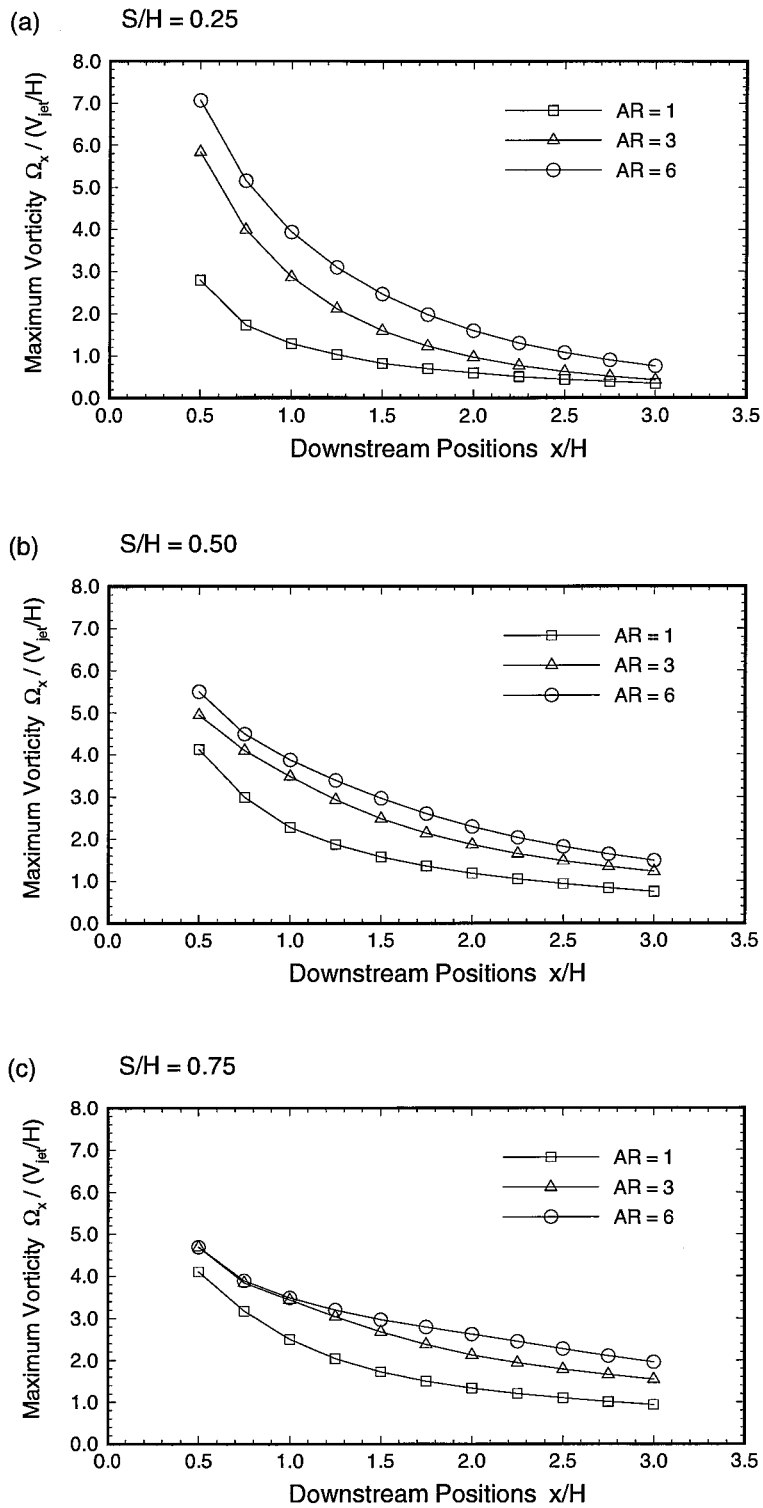

Figure 6.13: Variation of the maximum streamwise vorticity with x/H for jets from orifices that have different aspect ratios and at various lateral spacings.

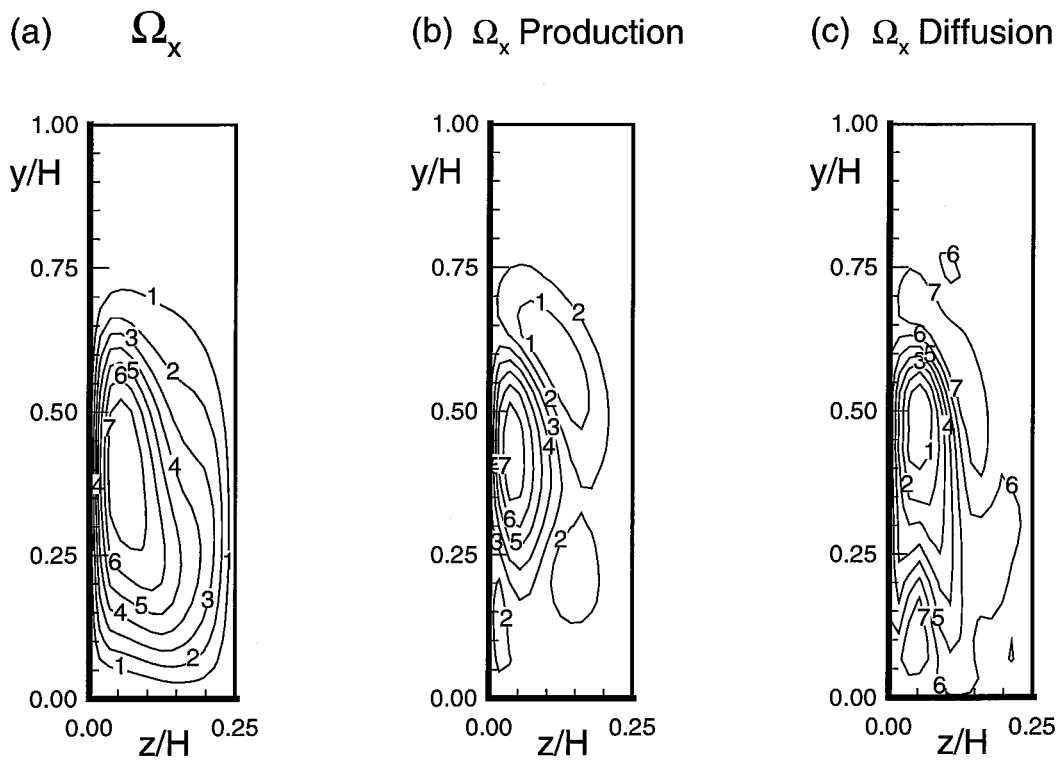

Levels	Ω_x
7	3.02
6	2.58
5	2.15
4	1.72
3	1.29
2	0.86
1	0.43

Levels	PROD
7	0.51
6	0.40
5	0.29
4	0.18
3	0.07
2	-0.04
1	-0.15

Levels	DIFF
7	0.23
6	-0.03
5	-0.28
4	-0.54
3	-0.80
2	-1.05
1	-1.31

Figure 6.14: Distributions of streamwise vorticity, production, and diffusion for the case $AR = 3$ and $S/H = 0.5$ in the cross-stream plane $x/H = 1.0$.

6.12 reveals the following observation: at the same jet spacing, a larger reduction in the vorticity value corresponds to more mixing has taken place. This is particularly evident for jets with $\mathcal{AR} = 6$ at $S/H = 0.25$, where the reduction in vorticity is most rapid (from Figure 6.13(a)) and the corresponding value of δ_x is least (from Figure 6.12(a)) so that the fluid is most well mixed. At $S/H = 0.5$, the rates of vorticity reduction are similar for the three types of jets, and correspondingly the reduction rates of δ_x are approximately the same. Similarities also hold for the case $S/H = 0.75$. This observation lends support to the role of the streamwise vorticity on jet mixing in the far field.

It is also interesting to note that at the same lateral spacing, jets from high aspect ratio orifices possess higher absolute values of streamwise vorticity than those from square orifices. This is due to the fact that slender jets have larger lateral surface areas to be acted upon by the crossflow than blunt jets of the same area. The shearing action of the crossflow stretches the fluid elements within the jet and consequently a higher value of the streamwise vorticity results.

6.3 Consequences of Holdeman's Relationship

To further check the consistency in the extent of jet penetration for which Eq.(6.1) is expected to apply, we observe that at a given value of M, a rearrangement of Eqs.(6.1) and (6.2) leads to the following relationships for J and S/W:

$$J = \frac{CM}{\mathcal{AR}} \frac{H^2}{W^2} \tag{6.6}$$

$$\frac{S}{W} = \sqrt{\frac{C\mathcal{AR}}{M}} \tag{6.7}$$

That is, for a given choice of M, $\mathcal{AR}$, and C, the momentum flux ratio J is proportional to H^2/W^2 and the spacing ratio S/W has a unique value. Therefore, it is possible to choose different values for the jet width W such that desirable jet penetration and mixing

are achieved in each case. The values of the momentum ratio J and the jet spacing S are subjected to the choice of W. This observation is used to check the consistency of Holdeman's correlation by examining the jet penetration due to different choices of W. The following study is carried out with parametric values that are typical for tertiary jets in a recovery boiler.

6.4 Implications for Tertiary Level Jets in a Recovery Boiler

In an idealization of the tertiary air system of a recovery boiler, we consider an array of jets coming from orifices of aspect ratio 4, which is common in recovery boilers. The mass flow input is chosen to be 20% of the crossflow mass, so that $M = 0.20$.

Now, Eq.(6.6) implies that small jets, for which $W = 0.10$ m (say) require much higher velocity to achieve good penetration than do larger jets of $W = 0.20$ m. Choosing typical recovery boiler values of $U_C = 3$ m/s and $H = 10$ m, corresponding jet velocity values may be calculated easily if $C = 0.8$ is chosen as a value appropriate for jets of aspect ratio 4. This value of C is obtained by interpolating the values listed in Table 6.3.

Since the attention now is on the tertiary air system, the values of the jet width chosen are $W = 0.10$, 0.15 and 0.20 m. The corresponding values of J and hence V_{jet} are obtained from Eq.(6.6) and listed in Table 6.4. The penetration in the center-plane for the three cases are shown in Figure 6.15. It is observed that the penetration for each case is slightly beyond the center, and this is caused by the high momenta of the jets under consideration. At such high momenta, the jets merge more rapidly and this causes the trajectory to be lifted up, as mentioned in the last chapter. The remarkable observation is that the penetration is nearly the same for the three cases. This verifies the validity of using Eq.(6.1) to predict jet penetration.

It is further remarked that the trends shown in Eqs.(6.6) and (6.7) provide insight

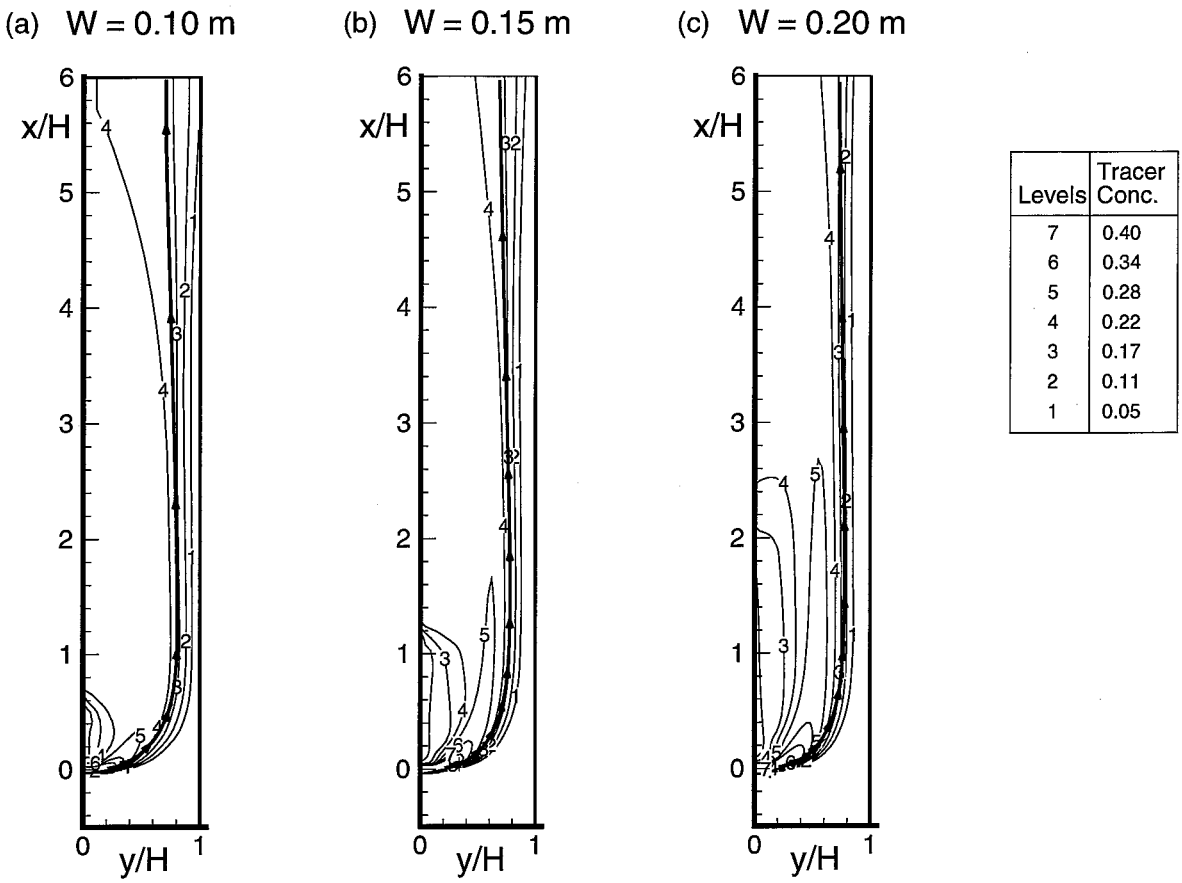

Figure 6.15: Jet tracer concentration in the center-plane for uniform crossflow.

W (m)	J	V_{jet} (m/s)
0.10	400	60
0.15	178	40
0.20	100	30

Table 6.4: Values of W, J and V_{jet} employed in the simulation of tertiary-type jets.

that is useful for the design of air injection systems. The relation that J varies as $(H/W)^2$ for a given shape of jet orifice and required mass input, is of interest, suggesting that large, low speed jets can penetrate as deeply and have similar mixing effects as small, high speed jets. The fact that S/W is a constant for given $\mathcal{AR}$ and M as indicated in Eq.(6.7) is also of interest. For the values chosen here ($M = 0.20$, $\mathcal{AR} = 4$, $C = 0.8$), S/W becomes equal to 4, so that small jets must be more closely spaced (i.e. S is small) than large jets (for which S is larger), the ratio of S/W remaining constant.

Considerations for Opposing Jets

The results given above are a great simplification of actual tertiary jets; isothermal jets from one side of a chamber (of size H) have been correlated, and jet penetration to the center of the chamber has been identified. For actual furnace tertiary jets which are interlaced or opposed, other effects may appear, such as oscillation or other forms of instability. For instance, it has been observed by Quick et al. (1991) that when plane jets are discharged strongly at each other, bifurcation may occur and the flow field may exhibit steady states that are asymmetric, or may not reach steady state at all. To avoid this instability, the penetration of the jets must be reduced, as shown in Figure 6.16. Then Eq.(6.1) is useful in finding conditions that establish the required trajectories if $H/2$ is used as the confinement dimension.

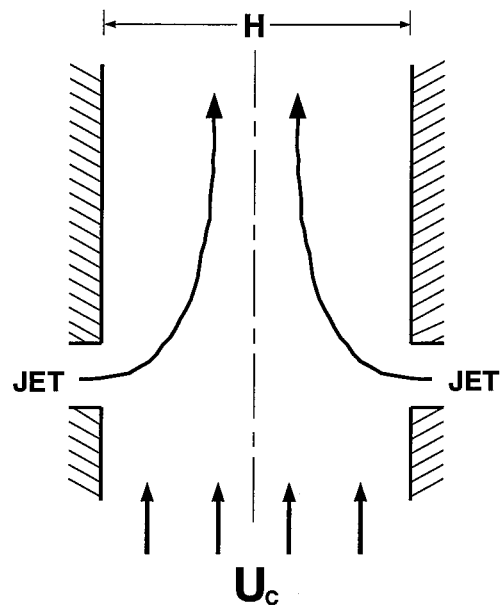

Figure 6.16: Schematic representation of opposing jets in a crossflow with penetration reduced to avoid collision between jets.

6.5 Non-uniform Crossflow

In practice, the up-flow approaching actual tertiary jets is not likely to be uniform. Thus, the effects due to crossflow non-uniformity need to be examined. To accomplish this, a peaked crossflow profile with a flat top, shown in Figure 6.17, is chosen for this study. The profile is mathematically described by

$$U_C\left(\frac{y}{H}\right) = \frac{A \cdot U_o}{A + \left[2\left(\frac{y}{H} - \frac{1}{2}\right)\right]^4} \tag{6.8}$$

where $U_C = U_o$ when $\frac{y}{H} = \frac{1}{2}$ so that U_o is the peak velocity and $U_C(y/H)$ is symmetrical about $\frac{y}{H} = \frac{1}{2}$. The values of U_o and A are chosen so that the integrated mean velocity U_{mean} for the profile has the value of 3 m/s, and that the minimum velocity, found at $y/H = 0$ or 1 at the inlet, is 10% of the peak velocity U_o. With these two criteria, the peak velocity U_o is $1.65 \times U_{mean}$, or 4.95 m/s, and $A = \frac{1}{9}$. This non-uniform velocity profile has a value of standard deviation of 1.68 m/s.

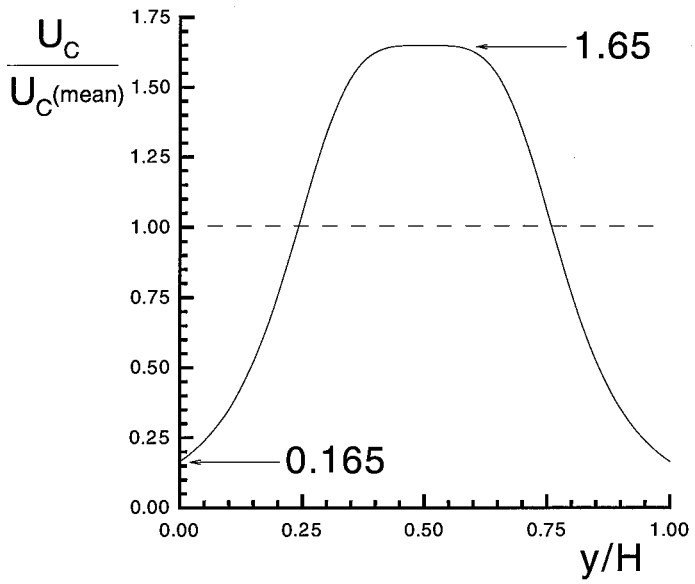

Figure 6.17: Velocity profile of the peaked crossflow.

The calculation is performed with the same choices of jet parameters and chamber width as in the previous section. The resulting jet fluid concentration profiles in the center-plane, obtained with this non-uniform crossflow, are shown in Figure 6.18. It is observed that the jet fluid distribution, and hence the jet penetration, for the three cases are similar to those obtained when the crossflow was uniform. This provides the assurance that the non-uniformity of the type examined does not affect the applicability of the relationships Eqs.(6.1), (6.6) and (6.7) describing the penetration when geometric and operational parameters are varied. This observation will have to be validated for a more complex flow generated by the interaction among primary, secondary, and tertiary jets in a boiler.

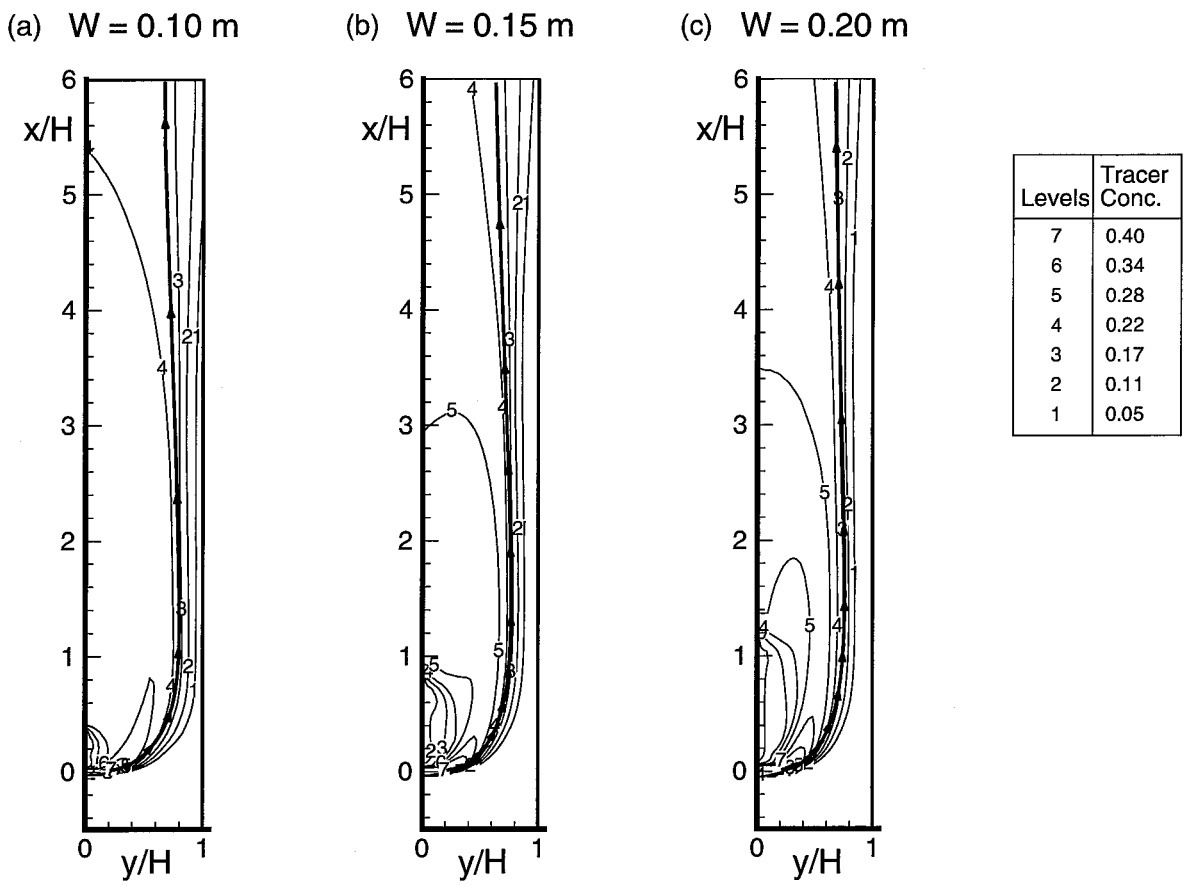

Figure 6.18: Jet tracer concentration in the center-plane for non-uniform crossflow.

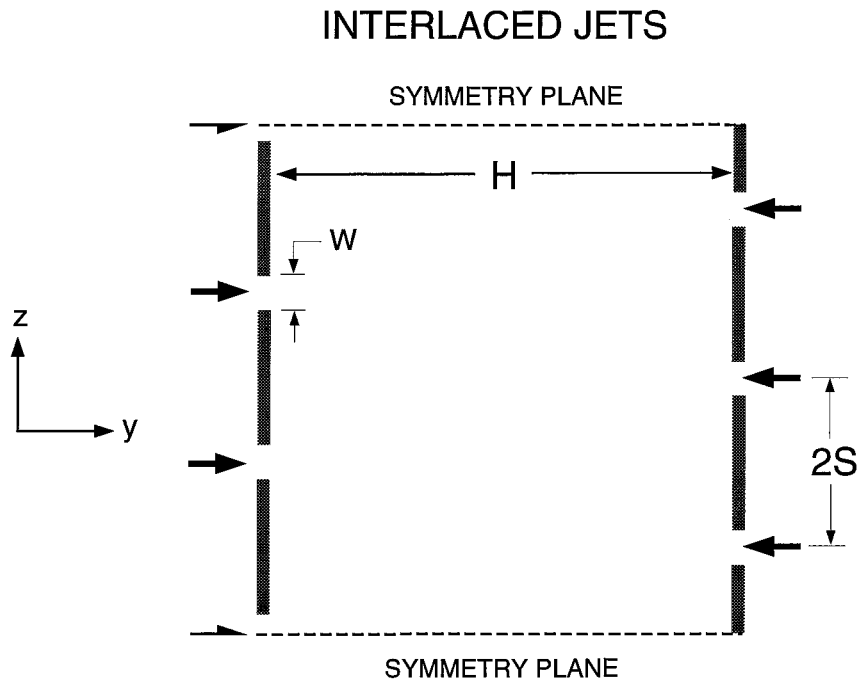

Figure 6.19: Plan view of the interlaced jet injection scheme.

6.6 Interlaced Jets on Both Sides of the Chamber

The experimental results of Holdeman et al. (1984) suggest that interlaced jets provide very effective mixing. The interlaced arrangement is introduced by placing every second jet on the opposite wall, so that in our previous simulations where the jet spacing was $S/W = 4$, the interlaced arrangement would lead to $S/W = 8$ on either wall. Figure 6.19 shows the arrangement.

Simulations are carried out with the same three jet sizes and velocities listed in Table 6.4. The jets act on the same non-uniform crossflow profile given in Eq.(6.8). The cross-sectional profiles of the jet fluid distribution at the downstream location $x/H = 1.0$ are shown in Figure 6.20. The profiles indicate that, in each case, the maximum concentration of the jet fluid is located at the center of the chamber. This observation verifies that the application of Eq.(6.1) results in adequate jet penetration even for interlaced arrangements.

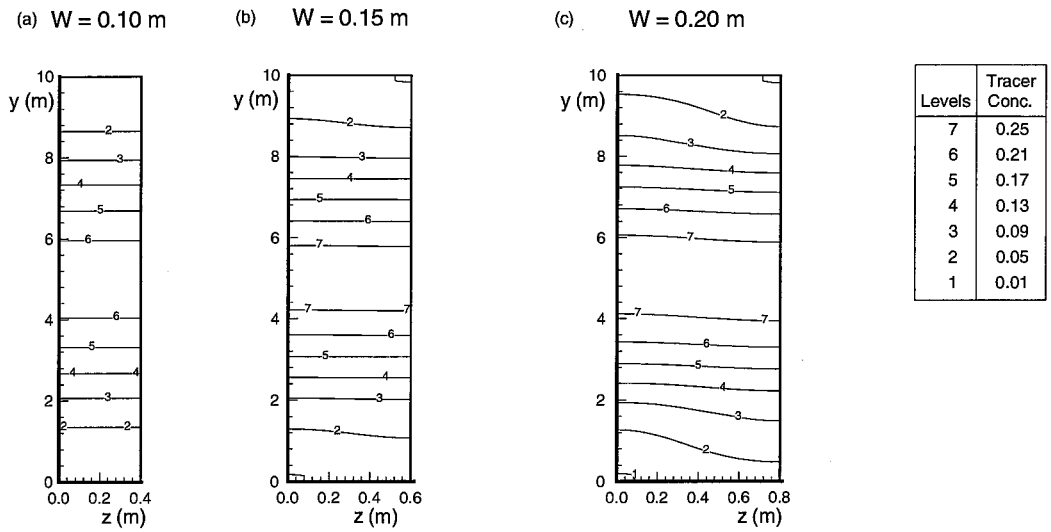

Figure 6.20: Jet tracer concentration in the cross-stream plane $x/H = 1.0$ due to mixing with interlaced jets.

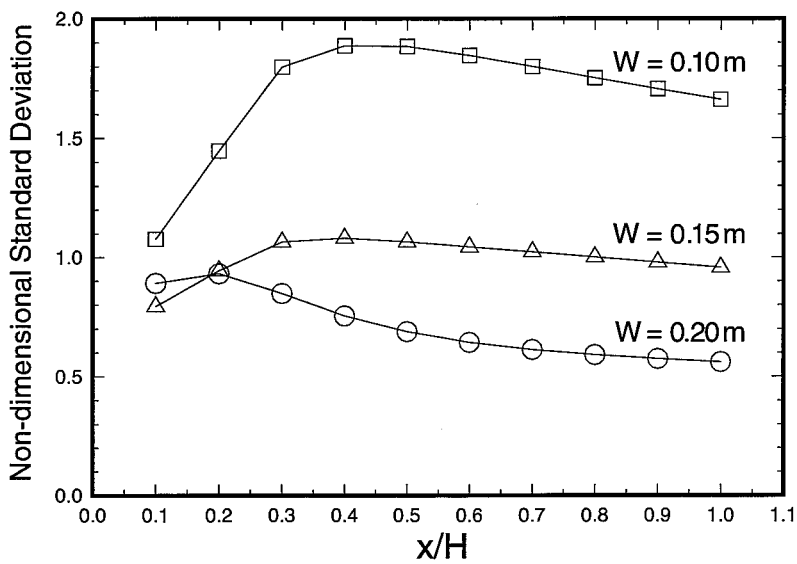

Figure 6.21: Standard deviation of the streamwise velocity component at various downstream positions for the three sizes of interlaced jets.

Although the jet fluid distribution is similar, the velocity distribution shows differences for the different choices of orifice width W. Thus, the uniformity in the velocity distribution is investigated. The standard deviation of the streamwise velocity component from its average value is computed for each of the three cases. A low value of the standard deviation indicates a more uniform flow profile than a high value. For applications to recovery boilers, it is often desirable to have a velocity distribution as uniform as possible in the main flow downstream of the tertiary jets.

The results are shown in Figure 6.21 for the variation of the standard deviation of the streamwise velocity component with the downstream position x/H for the three types of jets. The standard deviation is non-dimensionalized by the value of the standard deviation of the original non-uniform profile (1.68 m/s). The largest jets that are operated at the lowest momentum provide the most uniform flow farther downstream – smallest standard deviation at large x/H. Hence, the following conclusion is made: for interlaced jets interacting with the type of non-uniform crossflow prescribed, large jets at a low momentum satisfy the mass flow requirement and create less flow non-uniformity far downstream.

In passing, note that with this interlaced jet injection scheme, the highest momentum ratio case ($J = 400$, Table 6.4) corresponds to the following parametric values: $H = 10$ m, $W = 0.10$ m, $AR = 4$, $S/W = 8$, and $V_{jet} = 60$ m/s. For the 1000 tons-per-day boiler owned by the Weyerhaeuser company in Kamloops, B.C., the conditions for tertiary jets are as follows: $H = 11$ m, $W = 0.15$ m, $AR = 4.3$, $S/W = 9$, and $V_{jet} = 69$ m/s. The Kamloops boiler's tertiary jets are therefore operating under conditions that are similar to those studied here. Hence, the jets should penetrate to the middle of the boiler adequately. It is worthwhile to note that according to our results, similar penetration could be achieved with bigger jets operating at a lower speed. The use of lower speed jets is more power efficient since at the same mass flow requirement, they need less power to

operate than higher speed jets.

6.7 Concluding Remarks

Our results indicate that Holdeman's correlation Eq.(6.1) is useful in correlating conditions upon which the jet trajectory in the center-plane is similar. A certain choice of the value of C leads to conditions that will give rise to effective transport of jet fluid into the chamber. The value is chosen based on the desire to have the jets to penetrate into the middle of the chamber without significant over-penetration or under-penetration. The optimality of this strategy is verified by our quantitative study on jet mixing. Suitable choice for the value of C depends on the aspect ratio of the jet orifice, and decreases as aspect ratio increases. From the data listed in Table 6.3, the following empirical formula relating C and $\mathcal{AR}$ is obtained:

$$C = 1.83 - 0.36\ \mathcal{AR} + 0.027\ \mathcal{AR}^2 \tag{6.9}$$

The formula is valid for values of $\mathcal{AR}$ in the range of 1 and 6.

A value of $C = \sqrt{J} \cdot \frac{S}{H}$ that is a factor of two larger than the optimal value predicted by Eq.(6.9) would mean over-penetration, and vice versa. Also, for two-sided interlaced jets, the effective orifice spacing would be half the spacing between neighboring jets on the same wall. Keeping these items in mind, Eq.(6.1) can be used as a quick reference to estimate how jets will penetrate into a confined crossflow. To be cautious, it should be remembered that the formula only applies in situations where lateral jet interaction is significant and where the jet spacing is not too small. Also, for cold jets entering a hot crossflow, the Thring-Newby scaling criterion, discussed in Perchanok et al. (1989), should be applied first to determine the effective size of the orifice opening to account for the effects of jet expansion. After this is done, the above strategy can be used to estimate the jet penetration for such a case.

Our quantitative study of jet mixing reveals that the extent of the dispersion of jet fluid is related to the decay rate of the vorticity possessed by the counter-rotating vortices constituting the cross-section of each jet. This demonstrates the important role of vorticity dynamics for jet entrainment. In addition, our results show that slender rectangular jets can have a higher mixing capability than square jets with equivalent areas, especially when the jet spacing is small. This observation should be considered in the design of combustion chambers or boilers where rapid mixing of air with fuel is desired.

In the study of mixing with interlaced jets, the following trend is revealed: at a given mass flow ratio, higher velocity uniformity in the flow downstream of the jets is observed with the use of bigger jets operating at a lower momentum ratio. When applying our results, however, we need to realize that the actual flow in a recovery boiler is significantly more complex than our idealized conditions. Moreover, our focus has been on the jet penetration, which is only one criterion and does not necessarily reflect the many parameters which need to be accounted for in the optimization of the design of a boiler. Nevertheless, the present study provides an estimate of the trends with different parametric variations, and these trends can be used as guidelines for air system development.

Chapter 7

Conclusions and Recommendations

Our studies of turbulent jets reveal valuable information on the characteristics of the flow fields. The information is useful for gaining basic understanding about the nature of turbulent jet interactions, and for simulations and designs of kraft recovery boilers. The contributions of the thesis are summarized in the following section.

7.1 Results of the Present Study

In our simulations of closely spaced jets issuing into a quiescent surrounding, our numerical results agree with the experimental observations that the jets merge rapidly and the merging is complete not far from the jet entrance. These results suggest the possibility of simulating primary level jets in a kraft recovery boiler using slot equivalences. Two types of slot jets are considered: open slots and porous slots. They both give results that adequately reflect the structures in the velocity field due to the interaction of discrete primary jets, and this is done with a significant saving in computational costs. However, in our simulations, slot jets produce lower values of turbulent viscosity in the flow field. This may have implications on the diffusive transport of scalar tracer and momentum. Thus, we need to exercise caution in the representation of discrete primary jets by slots.

Our parametric studies on a row of square jets in a confined crossflow clarify certain basic characteristics of multiple jet interactions. In the investigation on the characteristics of streamwise vorticity associated with each jet, it is found that an increase in lateral confinement due to a reduction in orifice spacing does not increase the maximum vorticity

very much. This result is due to the competing effects of vorticity diffusion across from the neighboring jet, which weakens the vorticity, and the shearing flow around the jet, which strengthens the vorticity. In addition, our mathematical model produces the result that at a high momentum ratio between the jet and the crossflow and at an intermediate value of jet spacing, the usual vortex core seen in half of the cross-section of a jet modifies into two cores. This unexpected result is a consequence of the increase in shear experienced near the top surface of the jet. It serves to illustrate how the jet structures can modify in such a row-jet configuration when compared to the structures of an isolated jet.

Our parametric studies on row-jet injection into a crossflow verify that, with a minor modification, the semi-empirical relationship (Eq.(2.24) or Eq.(6.1)) due to Holdeman and his co-workers can be applied to jets from rectangular orifices. The relationship gives conditions on the geometric and operational parameters to yield consistent jet penetration. The modification is needed because a slender jet with the long side aligned in the direction of the crossflow penetrates deeper than a wider jet that has the same orifice area. This fact is verified by our flow visualization experiment.

In addition to penetrating deeper into the crossflow, slender jets are observed to possess higher absolute values of the streamwise vorticity. This is a consequence of the larger lateral surface of the jet available to experience the shear by the crossflow, which stretches the fluid elements within the jet. The decay of the streamwise vorticity is observed to follow trends that are consistent with the degree of mixing between the jet and the cross-stream. This observation is made in our examination of jets from orifices having different aspect ratios. It is found that in the cases where the spacing between each pair of jets is the same, a larger reduction in the vorticity possessed by each jet indicates a higher degree of mixing. This observation points to the significance of the counter-rotating vortex cores within each jet on jet mixing. Furthermore, our quantitative study on jet mixing demonstrates that the strategy to have the jet to penetrate mid-way into

the cross-stream indeed leads to most uniformly mixed fluid.

For jets interacting with the non-uniform crossflow defined in Eq.(6.8), the results show that Holdeman's semi-empirical relationship remains valid in estimating the jet penetration. The non-uniformity is prescribed as a peaked velocity profile with a flattened top, the type of profile that may be found in a kraft recovery boiler having a chimney-type up-flowing core.

An examination of Holdeman's relationship reveals that at a given jet-to-crossflow mass flow rate, larger jets operating at a lower momentum can penetrate into the crossflow as effectively as smaller jets at a higher momentum. In addition, when jets are placed in an interlaced arrangement, the use of Holdeman's correlation also yields satisfactory jet penetration. When these interlaced jets interact with the non-uniform crossflow described in the last paragraph, our results show that, at a given mass flow requirement, the use of larger jets leads to a higher degree of flow uniformity in the mainstream. This observation is a consequence of the lower momentum requirement for the larger jets compared to smaller jets.

The numerous calculations required in this study are performed successfully and efficiently with the use of the multigrid solution technique. Our relatively simple problems of jets in crossflows have provided many useful cases to test the correctness in the implementation and the robustness of the multigrid algorithm. The results are useful in validating the simulation strategy for kraft recovery boilers and in providing guidelines for air system design for the boilers.

7.2 Recommendations for Further Studies

The modelling strategy for primary level jets using slots may need further refinement to account for the lower values in turbulent viscosity produced in slot simulations. Our

results show that a simple increase in the input turbulence intensity does not raise the turbulent viscosity levels. Thus, more studies are needed to examine how a better reproduction of the turbulent viscosity field can be achieved, and to examine the significance of the turbulent viscosity on the flow field.

When this study was commenced, the mathematical model used in the code could only allow for the simulations of isothermal flows. Consequently, the use of Thring-Newby scaling criterion is necessary to study the jet behavior when there are differences in temperature between the jet and the crossflow. The use of Holdeman's correlation Eq.(6.1) to estimate jet penetration should now be examined further through non-isothermal calculations. The value of the parameter C appearing in the correlation may need to be adjusted when the differences in temperature between the jet and the crossflow are taken into account.

The observation regarding the existence of multiple vortex cores in half of a jet reveals that there are fundamental differences in the jet structure between an isolated jet and a jet within an array in a crossflow. These differences should be examined more carefully with the use of more sophisticated turbulence models. Indeed, better models that take into account the anisotropy in the turbulence characteristics are needed for more accurate simulations of jet flows both in quiescent environments and in crossflows. The $k-\epsilon$ model may be adequate in simulating gross flow features such as the penetration and spreading rates of jets; however, more refined models, such as the multiple-time-scale model discussed by Kim and Benson (1993) or the Reynolds-stress closure models described by Leschziner (1989), are needed in the detailed examination of the flow field. The implementation of these more sophisticated models will enable more accurate simulations for both jet flows and complicated recirculatory flows found in a recovery boiler.

The use of a more sophisticated turbulence model will also test the computational efficiency of our multigrid algorithm. At the current stage of development, the algorithm

used in our multigrid code MGFD is termed geometric multigrid; that is, the algorithm operates on multiple levels of grids constrainted by the physical characteristics of the domain. Although much improvement in the convergence rate has been achieved through the present algorithm, this method has the drawback that the coarsest grid used still has to be rather fine relative to the size of the domain. This is the case because the coarsest grid has to resolve fine geometric features such as jet orifices. Even though the use of domain segmentation has helped to improve the efficiency, a better approach is to use the algebraic multigrid method discussed in Ruge and Stüben (1987).

The algebraic multigrid method does not consider the geometric constraints of the domain when coarse grid levels are defined and hence very coarse grid can be reached within the multigrid algorithm. Convergence rate can thus be improved since a large error range can now be acted upon by the solution smoother. The extension of this algebraic multigrid technique to the Navier-Stokes equations is not trivial, but this method, when coupled with an adaptation strategy such as the one presented in Thompson and Ferziger (1989) for selective local grid refinement, appears to be a very promising solution algorithm.

Another subject matter that deserves attention is the problem with close jet spacing at a high jet-to-crossflow momentum ratio. In Chapter 5, it is found that for the case $S/W = 2$ at $J = 72$, the convergence performance of our solution algorithm deteriorates drastically. In particular, it is observed that large residues for the momentum and turbulence model equations are found at cells adjacent to the jet entrance. These findings suggest that complex flow structures may be present near the root of the jet and these structures may influence the performance of our solver.

These complex structures may be caused by the unsteadiness in the phenomena of flow separation and reattachment around the root of the jet. The occurrence of such unsteadiness at a high Reynolds number at locations where flow separates from and

reattaches to a physical body is common in many problems of engineering interest. An example is the flow over a blunt plate discussed by Djilali (1987) and Tafti and Vanka (1991). A similar kind of unsteadiness can occur around the circumference of the jet entrance where the jet meets the mainstream and consequently the structures of the system of collar or horse-shoe vortices around the jet root can be affected. It is possible that the severity of the unsteadiness increases as the jet spacing is reduced, which may explain the difficulty in obtaining convergence for the case $S/W = 2$ at $J = 72$.

For this case, if our interest is only in the gross characteristics of the time-averaged flow field, then the results presented in Chapter 5 may be adequate. However, a more refined time-dependent numerical study is needed in order to understand the detailed physical characteristics of the flow field, especially around the jet entrance. At present, the large eddy simulations (LES) used by Tafti and Vanka appear to be indispensable to yield information on the detailed structures of flow separation and reattachment. However, such a simulation requires a large amount of computing resources. The algebraic multigrid method described previously may offer substantial saving in computing costs. A detailed experimental investigation of the flow field for this case of close jet spacing at a high value of J will also be needed to validate the numerical results.

Appendix A

Flow Visualization Experiment

The flow visualization experiment is performed in the Kamloops water model shown in Figure 6.8. A detailed description of the experimental facility and the instrumentation can be found in the thesis by Ketler (1993). The model is constructed primarily of transparent plexiglass with numerous orifices located around the sides to serve as jet inlets. Water is led into the model through many pipes, with each pipe feeding about 7-8 orifices at the primary level and a single orifice at the secondary level. For the tertiary jets, each orifice is also fed by a single pipe located directly behind the orifice to maximize flow uniformity. The flow rate entering each pipe is adjustable and is monitored by an analog flow meter.

There are 174 primary orifices distributed almost uniformly on all four sides of the model near the base. A total amount of 122 US gal/min or 7.7×10^{-3} m^3/s of water is fed into the model through these orifices to generate an up-flowing stream within the model. At this flow rate, the overall flow pattern generated by the primary jets is observed to be quite steady. Jets on the secondary level are not used since it has been observed that the interaction caused by flow from this level would cause gross unsteadiness in the flow pattern.

The tertiary orifices are located on two opposing walls, with five orifices drilled into a removable aluminum template on each wall. Only one set of orifices is used since the interest here is on jet penetration due to single-sided injection. Two templates, shown in Figure 6.9, are made for the experiment, one for square orifices and the other for

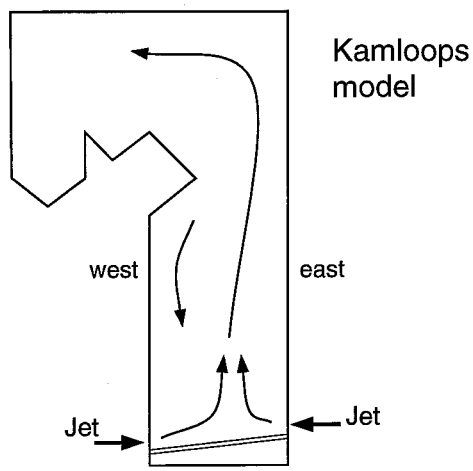

Figure A.1: Schematic of the flow pattern in the east-west plane within the model generated by primary jets.

rectangular orifices of $\mathcal{AR} = 4$.

Preliminary visualization study has shown that the flow pattern generated by the primary jets is quite steady but non-uniform. A main reason for the lack of uniformity is that the base of the model is sloped to one side. As a result, a gross recirculating pattern is formed as shown in Figure A.1.

Because the objective here is to study jet penetration into a cross-flowing stream, the existence of such a pattern causes the choice of the east wall to be used as the location of the jets as indicated in Figure A.1. It is observed that the extent of the up-flowing region at the tertiary jet level is slightly larger than half of the width of the model, and within the region the flow is quite steady and unidirectional. Thus, this region is to be used as the crossflow on which the tertiary jets act. The flow rate chosen for the tertiary jets is 4 US gal/min or 2.5×10^{-4} m^3/s for each jet.

The flow visualization experiment is carried out by the use of a sheet of laser light shining through the transparent base of the model. The sheet is generated by a prism optic set-up located below the base. The laser light is generated by a powerful 7 Watts

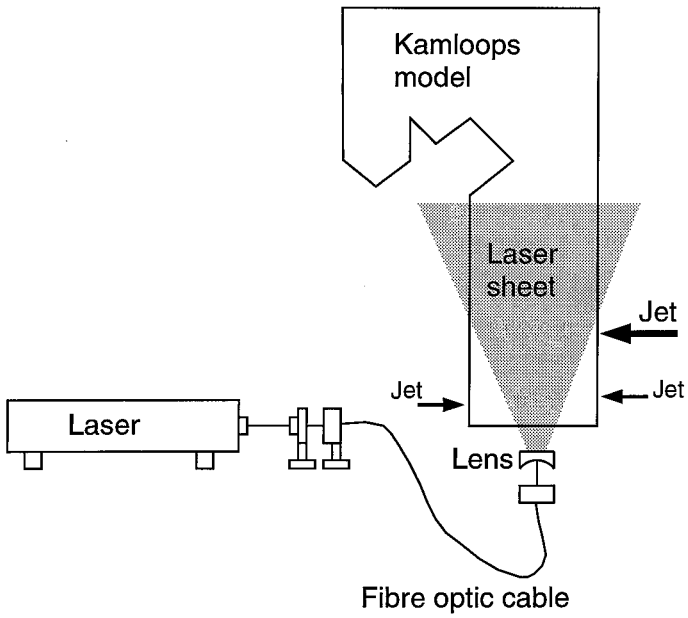

Figure A.2: Schematic of the experimental set-up for flow visualization.

argon laser and is transmitted to the prism optic via a fiber optic cable. The set-up of the visualization experiment is shown in Figure A.2.

The flow pattern is marked by the displacement of tiny polystyrene balls added to the flow. The diameter of those balls are about 200 μm and they have density very close to that of water, which makes them very suitable for flow visualization. Light will be reflected from these balls when they are illuminated by the laser sheet. The image of the flow pattern within the sheet of illumination is captured by a S-VHS camera, which records at 30 frames per second. The recorded images can be processed by image discretization for particle image velocimetry analysis. A crude estimate on the velocity at a particular location within the flow may also be obtained simply by studying successive video frames on a monitor display, with the knowledge that the time lapse between any two frames is $\frac{1}{30}$ seconds.

Appendix B

A Quantitative Description of Jet Mixing

Consider mixing between a single jet and a mainstream shown in Figure B.1, where the flow is assumed to be incompressible and steady. Let the volume flow rate of the mainstream and the jet be Q_1 and Q_2, respectively, and let Φ_1 and Φ_2 be the respective concentration of tracer per unit volume of each flow. The average concentration of the mixture can then be defined as

$$\Phi_{av} = \frac{\Phi_1 Q_1 + \Phi_2 Q_2}{Q_1 + Q_2} \tag{B.1}$$

If the mixing were perfect, then every fluid element will have this Φ_{av} amount of tracer concentration.

By continuity of fluid volume and tracer concentration, the following expressions are derived for a cross-section A downstream of the jet:

$$\int_A \mathbf{U} \cdot d\mathbf{A} = Q_1 + Q_2 \tag{B.2}$$

and

$$\int_A \Phi \mathbf{U} \cdot d\mathbf{A} = \Phi_1 Q_1 + \Phi_2 Q_2 \tag{B.3}$$

Combining Eqs.(B.1-B.3), we obtain

$$\begin{aligned} \int_A \Phi \mathbf{U} \cdot d\mathbf{A} &= \Phi_{av}(Q_1 + Q_2) \\ &= \Phi_{av} \int_A \mathbf{U} \cdot d\mathbf{A} \end{aligned} \tag{B.4}$$

Therefore,

$$\int_A (\Phi - \Phi_{av}) \mathbf{U} \cdot d\mathbf{A} = 0 \tag{B.5}$$

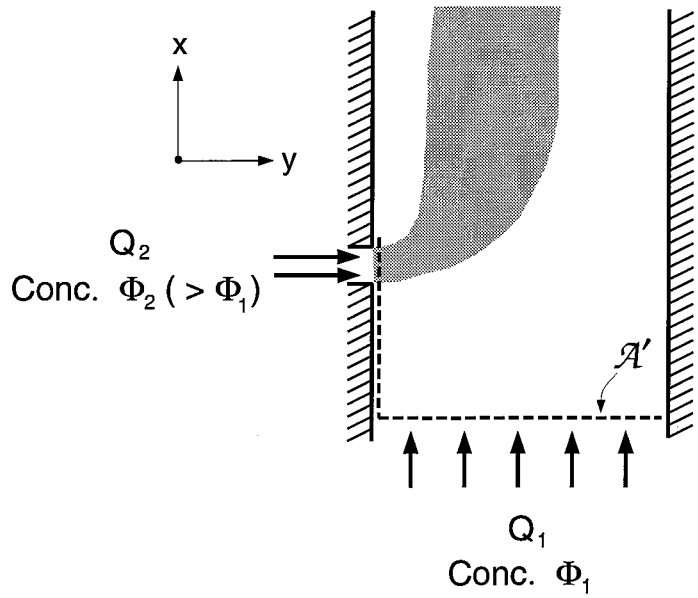

Figure B.1: A schematic drawing representing the mixing between a jet and a crossflow.

The evaluation of $\mathbf{U} \cdot d\mathbf{A}$ and $(\Phi - \Phi_{av})$ at every point in the cross-section A will give the volume per unit time passing each point and the defect from perfect mixing of that volume, respectively. The graph of the volume flow rate $\mathbf{U} \cdot d\mathbf{A}$ versus the concentration defect $(\Phi - \Phi_{av})$ gives a distribution at the cross-section in which Eq.(B.5) dictates that when integrated over A, the distribution has a mean value of zero. Such a distribution is useful in noting the volume flow rate across the section having tracer concentration lying within a certain range.

Instead of working directly with such a distribution, it is more convenient to work with its normalized form written as a probability density function $f(\xi)$, defined as

$$f(\xi) \equiv \frac{1}{\Delta\xi} \left\{ \frac{(\mathbf{U} \cdot d\mathbf{A})_{\textit{having concentration in range } \xi \pm \frac{\Delta\xi}{2}}}{Q_1 + Q_2} \right\} \tag{B.6}$$

where $\xi = \Phi - \Phi_{av}$.

To show that the normalization is correct, note that

$$\begin{aligned}\int_{-\infty}^{\infty} f(\xi)\, d\xi &= \sum_{\xi_i} f(\xi_i)\, \Delta\xi_i \\ &= \sum_{\xi_i} \frac{(\mathbf{U}\cdot d\mathbf{A})_{\xi_i}}{Q_1+Q_2} \\ &= 1 \end{aligned} \tag{B.7}$$

because taking all values of $(\mathbf{U}\cdot d\mathbf{A})_{\xi_i}$ over all possible values of $\xi_i \in (-\infty, \infty)$ gives the total volume flow rate $Q_1 + Q_2$. Here, the notation $(\mathbf{U}\cdot d\mathbf{A})_{\xi_i}$ refers to the flow rate of fluid elements having concentration in the range of $(\xi_i - \frac{\Delta\xi_i}{2}, \xi_i + \frac{\Delta\xi_i}{2})$ where $\Delta\xi_i$ is a small increment in ξ_i. The mean of $f(\xi)$ is zero since

$$\begin{aligned}\int_{-\infty}^{\infty} \xi\, f(\xi)\, d\xi &= \sum_{\xi_i} \xi_i\, f(\xi_i)\, \Delta\xi_i \\ &= \sum_{\xi_i} \frac{\xi_i\, (\mathbf{U}\cdot d\mathbf{A})_{\xi_i}}{Q_1+Q_2} \\ &= 0 \end{aligned} \tag{B.8}$$

by virtue of Eq.(B.5).

A measure of how well the tracer has been mixed is provided by the variance of $f(\xi)$, defined as

$$\sigma_x^2 = \int_{-\infty}^{\infty} \xi^2 f(\xi)\, d\xi \tag{B.9}$$

where the subscript x denotes that the integral is evaluated with the values of ξ and $f(\xi)$ to be computed in the cross-stream plane located at the streamwise coordinate x. Clearly, $\sigma_x^2 = 0$ for perfect mixing since then $\xi \equiv 0$ in the cross-stream plane. When $f(\xi)$ is specified to be evaluated in the plane at x, it may be denoted as $f_x(\xi)$, as shown in Eq.(6.3). This quantity σ_x^2 measures the spread of the tracer defect $\Phi - \Phi_{av}$ from the value of perfect mixing, which is zero. This variance can be normalized by σ_o^2, which is defined as the largest possible value of the variance corresponded to the situation before

any mixing has started. Its value is obtained by considering the distributions of ξ and $\mathbf{U} \cdot d\mathbf{A}$ in the surface $\mathcal{A}'$ shown in Figure B.1. The surface $\mathcal{A}'$ is defined to extend from the jet exit to a cross-sectional plane far upstream from the jet, where the effects of the jet are not felt.

To evaluate σ_o^2, recall that at any section A,

$$f(\xi_i) = \frac{1}{Q_1 + Q_2} \cdot \frac{1}{\Delta\xi_i}(\mathbf{U} \cdot d\mathbf{A})_{\xi_i} \tag{B.10}$$

Define $\xi_1 = \Phi_1 - \Phi_{av}$ and $\xi_2 = \Phi_2 - \Phi_{av}$, then at the section $\mathcal{A}'$, $f(\xi_i)$ is equal to zero except at $\xi = \xi_1$ and $\xi = \xi_2$, where it takes on the values

$$f(\xi_1) = \frac{1}{Q_1 + Q_2} \cdot \frac{Q_1}{\Delta\xi_1} \quad \text{and} \quad f(\xi_2) = \frac{1}{Q_1 + Q_2} \cdot \frac{Q_2}{\Delta\xi_2} \tag{B.11}$$

Therefore, the value of σ_o^2 is obtained as

$$\sigma_o^2 = \int_{-\infty}^{\infty} \xi^2 f(\xi)\, d\xi \Big|_{\mathcal{A}'} \tag{B.12}$$

$$= \sum_{\xi=\xi_1,\xi_2} \xi^2 f(\xi)\, \Delta\xi \tag{B.13}$$

$$= \xi_1^2 \frac{Q_1}{Q_1 + Q_2} + \xi_2^2 \frac{Q_2}{Q_1 + Q_2} \tag{B.14}$$

Finally, to have a normalized measure for mixing, a standard deviation δ_x may be defined as

$$\delta_x = \sqrt{\sigma_x^2/\sigma_o^2} \tag{B.15}$$

It has value ranges from 1 (no mixing) to 0 (fully mixed) and should be a good quantitative measure of jet-crossflow mixing.

In passing, we remark that with simple modifications such as to take into account the possible density difference between the jet stream and the cross-stream, the methodology presented here can be extended to variable density flows. Extension to mixing with multiple levels of jets is equally simple by taking more fluid streams into account than just the two presented here.

Bibliography

Abdullah, Z., Salcudean, M., Nowak, P., Xiao, Z., Savage, M., Markovic, C., Uloth, V., and Thorn, P., "An Initial Validation of a Cold Flow Mathematical Model of a Recovery Boiler", TAPPI Proceedings, 1993 Engineering Conference, Orlando, August, 1993.

Adams, T.N. and Frederick, W.J., Kraft Recovery Boiler Physical and Chemical Processes, The American Paper Institute, Inc., New York, 1988.

Alexander, L.G., Baron, T., and Comings, E.W., "Transport of Momentum, Mass, and Heat in Turbulent Jets", Engineering Experiment Station Bulletin No. 413, University of Illinois, 1953.

Andreopoulos J. and Rodi, W., "Experimental investigation of jets in a crossflow", *Journal of Fluid Mechanics*, vol.138, pp.93-127, 1984.

Arakawa, Ch., Demuren, A.O., Rodi, W., and Schönung, B., "Application of Multigrid Methods for the Coupled and Decoupled Solution of the Incompressible Navier-Stokes Equations", *Notes on Numerical Fluid Mechanics*, vol.20, pp.1-8, 1987.

Barata, J.M.M., Durao, D.F.G., Heitor, M.V., and McGuirk, J.J., "On the Validation of 3-D Numerical Simulations of Turbulent Impinging Jets through a Crossflow", AGARD – Validation of Computational Fluid Dynamics, Panel in Lisbon, Portugal, May 2-5, 1988.

Barsin, J.A., "Recovery Boiler Design Considerations", TAPPI Seminar Notes, Kraft Recovery Operations, Orlando, Florida, pp.223-238, 1989.

Blackwell, B., "Improved Gas Mixing in Kraft Recovery Boilers – Air Jet Theory", Report V7582, Sandwell Inc., Vancouver, B.C., November, 1990.

Brandt, A., "Multi-Level Adaptive Solutions to Boundary-Value Problems", *Mathematics of Computation*, vol.31, no.138, pp.333-390, 1977.

Brandt, A., "Multilevel Adaptive Computations in Fluid Dynamics", *AIAA Journal*, vol.18, no.10, pp.1165-1172, 1980.

Brandt, A., "Guide to Multigrid Development", in Multigrid Methods, Lecture Notes in Mathematics, vol.960, W. Hackbusch and U. Trottenberg (eds.), Springer-Verlag, Berlin, pp.220-312, 1982.

Brandt, A. and Dinar, N., "Multigrid Solutions to Elliptic Flow Problems", in Numerical Methods for Partial Differential Equations, S.V.Parter (ed.), Academic Press, New York, pp.53-147, 1979.

Catalano, G.D., Chang, K.S., and Mathis, J.A., "Investigation of Turbulent Jet Impingement in a Confined Crossflow", *AIAA Journal*, vol.27, no.11, pp.1530-1535, 1989.

Chapman, P.J. and Jones, A.K., "Recovery Boiler Secondary Air System Development using Experimental and Computational Fluid Dynamics", TAPPI Proceedings, Engineering Conference, pp.193-203, 1990.

Claus, R.W., "Numerical Calculation of Subsonic Jets in Crossflow with Reduced Numerical Diffusion", NASA Technical Memorandum 87003, 1985.

Claus, R.W. and Vanka, S.P., "Multigrid Calculations of a Jet in Crossflow", AIAA 28th Aerospace Sciences Meeting, AIAA-90-0444, January, 1990.

Coelho, S.L.V. and Hunt, J.C.R., "The dynamics of the near field of strong jets in crossflows", *Journal of Fluid Mechanics*, vol.200, pp.95-120, 1989.

Demuren, A.O., "Modeling Turbulent Jets in Crossflow", in Encyclopedia of Fluid Mechanics, Vol.2, Chapter 17, pp.430-465, Gulf Pub. Co., Houston, 1986.

Djilali, N., "An Investigation of Two-Dimensional Flow Separation with Reattachment", Ph.D. Thesis, Department of Mechanical Engineering, The University of British Columbia, 1987.

Fearn, R. and Weston, R.P., "Vorticity Associated with a Jet in a Cross Flow", *AIAA Journal*, vol.12, no.12, pp.1666-1671, 1974.

Foss, J., "Interaction Region Phenomena for the Jet in a Cross-flow Problem", Rep. SFB 80/E/161, Universität Karlsruhe, Germany, 1980.

Fric, T.F. and Roshko, A., "Structure in the Near Field of the Transverse Jet", Seventh Symposium on Turbulent Shear Flows, Stanford University, pp.6.4.1-6.4.6, August, 1989.

Fuchs, L., "Multi-Grid Schemes for Incompressible Flows", *Notes on Numerical Fluid Mechanics*, vol.10, pp.38-51, 1984.

Goertler, H., "Berechnung von Aufgaben der freien Turbulenz auf Grund eines neuen Naherungsansatzes", ZAMM, vol.22, pp.244-254, 1942.

Grace, T., Walsh, A., Jones, A., Sumnicht, D., and Farrington, T., "A Three-Dimensional Mathematical Model of the Kraft Recovery Furnace", TAPPI Short Course Notes, 1990 Kraft Recovery Operations, pp.173-180, 1990.

Hawthorne, W.R., Rogers, G.F.C., and Zaczek, B.Y., "Mixing of Gas Streams – The Penetration of a Jet of Cold Air into a Hot Stream", Tech. Note No. Eng. 271, British R.A.E., March, 1944.

Holdeman, J.D. and Walker, R.E., "Mixing of a Row of Jets with a Confined Crossflow", *AIAA Journal*, vol.15, pp.243-249, 1977.

Holdeman, J.D., Srinivasan, R., and Berenfeld, A., "Experiments in Dilution Jet Mixing", *AIAA Journal*, vol.22, no.10, pp.1436-1443, 1984.

Huang, P., "Modelisation et Calcul de Jets tridimensionnels en présence d'un Ecoulement Transversal", Thèse de Doctorat, Ecole Centrale Lyon, E.C.L. 89-007, France, 1989.

Ivanov, Y.V., "Effective Combustion of Overfire Fuel Gases in Furnaces", (quoted by Niessen, 1978), Estonian State Pub. House, Tallin, USSR, 1959.

Jang, D.S., Jetli, R., and Acharya, S., "Comparison of the PISO, SIMPLER, and SIMPLEC Algorithms for the Treatment of the Pressure-Velocity Coupling in Steady Flow Problems", *Numerical Heat Transfer*, vol.10, pp.209-228, 1986.

Jones, W.P. and McGuirk, J.J., "Computation of a Round Turbulent Jet Discharging into a Confined Cross-Flow", Turbulent Shear Flows II, Springer-Verlag, New York, pp.233-245, 1979.

Kamotani, Y. and Greber, I., "Experiments on Confined Turbulent Jets in Cross Flow", NASA CR-2392, 1974.

Ketler, S.P., "Physical Modelling of a Kraft Recovery Boiler", M.A.Sc. Thesis, Department of Mechanical Engineering, University of British Columbia, Vancouver, Canada, 1993.

Ketler, S.P., Savage, M.C., and Gartshore, I.S., "Physical Modeling of Flows in Black Liquor Recovery Boilers", TAPPI Proceedings, Engineering Conference, pp.581-599, 1992.

Ketler, S.P., Savage, M.C., and Gartshore, I.S., "Recovery Boiler Sensitivity to Secondary Level Flows", TAPPI Proceedings, Engineering Conference, pp.271-285, 1993.

Kim, S.-W. and Benson, T.J., "Fluid Flow of a Row of Jets in Crossflow – A Numerical Study", *AIAA Journal*, vol.31, no.5, pp.806-811, 1993.

Knystautas, R., "The Turbulent Jet from a Series of Holes in Line", *The Aeronautical Quarterly*, vol.XV, pp.1-28, 1964.

Krothapalli, A., Baganoff, D., and Karamcheti, K., "Development and Structure of a Rectangular Jet in a Multiple Jet Configuration", *AIAA Journal*, vol.18, no.8, pp.945-950, 1980.

Kulisa, P., Leboeuf, F., and Perrin, G., "Computation of a Wall Boundary Layer with Discrete Jet Injections", ASME *Journal of Turbomachinery*, vol.114, pp.756-764, 1992.

Lai, K.Y.M. and Salcudean, M., "TEMA : A computer program for two-phase, multidimensional, turbulent recirculating flows", Internal Report, Department of Mechanical Engineering, University of Ottawa, Canada.

Latimer, B.R. and Pollard, A., "Comparison of Pressure-Velocity Coupling Solution Algorithms", *Numerical Heat Transfer*, vol.8, pp.635-652, 1985.

Launder, B.E., Morse, A., Rodi, W., and Spalding, D.B., "The prediction of free shear flows – A comparison of the performance of six turbulence models", Proceedings of NASA Conference on Free Shear Flows, Langley, 1972.

Launder, B.E. and Spalding, D.B., "The Numerical Computation of Turbulent Flows", *Computer Methods in Applied Mechanics and Engineering*, vol.3, pp.269-289, 1974.

Lefebvre, B.E. and Burelle, R., "The Chemical Recovery Boiler Optimized Ait System", TAPPI Seminar Notes, pp.239-246, 1989 Kraft Recovery Operations, 1989.

Leschziner, M.A., "Modeling turbulent recirculating flows by finite-volume methods – current status and future directions", *Int. J. Heat and Fluid Flow*, vol.10, no.3, pp.186-202, 1989.

Lien, F.-S. and Leschziner, M.A., "Multigrid Convergence Acceleration for Complex Flow Including Turbulence", *International Series of Numerical Mathematics*, vol.98, pp.277-288, 1991.

Linden, J., Lonsdale, G., Steckel, B., and Stüben K., "Multigrid for the Steady-State Incompressible Navier-Stokes Equations : a Survey", *Arbeitspapiere der GMD*, Gesellschaft fur Mathematik und Datenverarbeitung mbH, pp.1-16, July, 1988.

Majumdar, S., "Role of Underrelaxation in Momentum Interpolation for Calculation of Flow with Nonstaggered Grids", *Numerical Heat Transfer*, vol.13, pp.125-132, 1988.

Maron, M.J., Numerical Analysis: A Practical Approach, Second Edition, Macmillan Publishing Company, New York, 1987.

Marsters, G.F., "Spanwise Velocity Distributions in Jets from Rectangular Slots", *AIAA Journal*, vol.19, no.2, pp.148-152, 1981.

McGuirk, J.J. and Rodi, W., "The Calculation of Three-Dimensional Turbulent Free Jets", Symposium on Turbulent Shear Flows, Pennsylvania State University, pp.1.29-1.36, April, 1977.

Miller, D.R. and Comings, E.W., "Force-momentum fields in a dual-jet flow", *Journal of Fluid Mechanics*, vol.7, no.2, pp.237-255, 1960.

Moussa, Z.M., Trischka, J.W., and Eskinazi, S., "The near field in the mixing of a round jet with a cross-stream", *Journal of Fluid Mechanics*, vol.80, pp.49-80, 1977.

Needham, D.J., Riley, N., and Smith, J.H.B., "A jet in crossflow", *Journal of Fluid Mechanics*, vol.188, pp.159-184, 1988.

Niessen, W.R., Combustion and Incineration Processes : Applications in Environmental Engineering, Marcel Dekker, Inc., New York, 1978.

Nowak, P.Z., "Calculations of transonic flows around single and multi-element airfoils on a small computer", Reports of the Department of Mathematics and Informatics no. 84-48, Delft University of Technology, Delft, the Netherlands, 1984.

Nowak, P.Z., "Multigrid Methods", Internal Report, Department of Mechanical Engineering, University of British Columbia, 1992.

Patankar, S.V., Numerical Heat Transfer and Fluid Flow, Hemisphere Publishing Corporation, McGraw-Hill Book Company, New York, 1980.

Perchanok, M.S., Bruce, D.M., and Gartshore, I.S., "Velocity Measurements in an Isothermal Scale Model of a Hog Fuel Boiler Furnace," *Journal of Pulp and Paper Science*, vol.15, No.6, pp.J212-J219, Nov. 1989.

Peric, M., Ruger, M., and Scheuerer, G., "A finite volume multigrid method for calculating turbulent flows", Seventh Symposium on Turbulent Shear Flows, Stanford University, pp.7.3.1-7.3.6, August, 1989.

Phillips, R.E., Miller, T.F., and Schmidt, F.W., "A Multilevel-Multigrid Algorithm for Axisymmetric Recirculating Flows", Fifth Symposium on Turbulent Shear Flows, Cornell University, pp.20.21-20.25, 1985.

Pietrzyk, J.R., Bogard, D.G., and Crawford, M.E., "Hydrodynamic Measurements of Jets in Crossflow for Gas Turbine Film Cooling Application", ASME *Journal of Turbomachinery*, vol.111, pp.139-145, 1989.

Quick, J.W., Gartshore, I.S., and Salcudean, M., "The Bifurcation of Steady States for Opposing Jets in Cross Flow; Application to Recovery Boilers," Proceedings of the Thirteenth Canadian Congress of Applied Mechanics, CANCAM 91, June 2-June 6, 1991.

Quinn, W.R., "Effects of slot aspect ratio on turbulent free jet flows issuing from sharp-edged rectangular slots", Proceedings of the Second World Conference on Experimental Heat Transfer, Fluid Mechanics, and Thermodynamics, J.F. Keffer, R.K. Shah, and E.N. Ganic (eds.), pp.170-177, 1991.

Rajaratnum, N., Turbulent Jets, Elsevier Scientific Pub. Co., New York, 1976.

Rajaratnum, N. and Gangadharaiah, T., "Scales for Circular Jets in Cross-Flow", *Journal of the Hydraulics Division*, Proceedings of the American Society of Civil Engineers, vol.107, pp.497-500, 1981.

Rajaratnum, N. and Gangadharaiah, T., "Entrainment by Circular Jets in Cross-Flow", *Journal of Wind Engineering and Industrial Aerodynamics*, vol.9, pp.251-255, 1982.

Rajaratnum, N. and Gangadharaiah, T., "Vortex Structure of Circular Jets in Cross-flow", *Journal of Wind Engineering and Industrial Aerodynamics*, vol.12, pp.155-164, 1983.

Rathgeber, D.E. and Becker, H.A., "Mixing Between a Round Jet and a Transverse Turbulent Pipe Flow", *The Canadian Journal of Chemical Engineering*, vol.61, pp.148-157, 1983.

Reilly, R.S., "Investigation of the deformation and penetration of a turbulent subsonic jet issuing transversely into a uniform, subsonic main stream", Ph.D. Thesis, University of Maryland, USA, 1968.

Rodi, W., Majumdar, S., and Schönung, B., "Finite Volume Methods for Two-Dimensional Incompressible Flows with Complex Boundaries", *Computer Methods in Applied Mechanics and Engineering*, vol.75, pp.369-392, 1989.

Rubini, P.A., Becker, H.A., Grandmaison, E.W., Pollard, A., Sobiesiak, A., and Thurgood, C., "Multigrid Acceleration of Three-Dimensional Turbulent, Variable-Density Flows", *Numerical Heat Transfer, Part B*, vol.22, pp.163-177, 1992.

Ruge, J.W. and Stüben, K., "Algebraic Multigrid", in Multigrid Methods, Chapter 4, Frontiers in Applied Mathematics, S.F. McCormick (ed.), SIAM, 1987.

Ruggeri, R.S., Callaghan, E.E., and Bowden, D.T., "Penetration of Air Jets Issuing from Circular, Square, and Elliptical Orifices Directed Perpendicularly to an Air Stream", NACA Technical Note 2019, February, 1950.

Salcudean, M., Nowak, P., and Abdullah, Z., "Mathematical Modelling of Recovery Furnaces", TAPPI Proceedings, International Chemical Recovery Conference, Seattle, pp.197-208, June, 1992.

Schetz, J.A., Injection and Mixing in Turbulent Flow, American Institute of Aeronautics and Astronautics, New York, 1980.

Sfeir, A.A., "Investigation of Three-Dimensional Turbulent Rectangular Jets", *AIAA Journal*, vol.17, no.10, pp.1055-1060, 1979.

Sherif, S.A., "Measurements of the Flow and Thermal Characteristics of Turbulent Jets in Cross Flow", Ph.D. Dissertation, Iowa State University, Ames, Iowa, 1985.

Shyy, W., Sun, C.-S., Chen, M.-H., and Chang, K.C., "Multigrid Computation for Turbulent Recirculating Flows in Complex Geometries", *Numerical Heat Transfer, Part A*, vol.23, pp.79-98, 1993.

Simitović, R., "Turbulent Flow in a Rectangular Duct with an Obliquely - Introduced Secondary Jet", Ph.D. Thesis, Department of Mechanical Engineering, University of London, March, 1977.

Smith, S.H., Lozano, A., Mungal, M.G., and Hanson, R.K., "Scalar Mixing in the Subsonic Jet in Crossflow", 72nd AGARD Fluid Dynamics Panel Meeting and Symposium on Computational and Experimental Assessment of Jets in Cross Flow, Winchester, U.K., 19-22 April, 1993.

Stevens, S.J. and Carrotte, J.F., "Experimental Studies of Combustor Dilution Zone Aerodynamics", AIAA Paper No. 88-3274, 1988.

Stüben, K. and Trottenberg, U., "Multigrid Methods : Fundamental Algorithms, Model Problem Analysis, and Applications", *Multigrid Methods*, Lecture Notes in Mathematics, vol.960, W. Hackbusch and U. Trottenberg (eds.), Springer-Verlag, Berlin, 1982.

Sutinen, J.E. and Karvinen, R., "Numerical Modeling of Char Bed Phenomena", TAPPI Proceedings, International Chemical Recovery Conference, Seattle, Washington, pp.79-83, 1992.

Syed, S.A., Chiappetta, L.M., and Gosman, A.D., "Error Reduction Program – Final Report", NASA CR-174776, April, 1985.

Sykes, R.I., Lewellen, W.S., and Parker, S.F., "On the vorticity dynamics of a turbulent jet in a crossflow", *Journal of Fluid Mechanics*, vol.168, pp.393-413, 1986.

Tafti, D.K. and Vanka, S.P., "A numerical study of flow separation and reattachment on a blunt plate", *Phys. Fluids A*, vol.3, no.7, pp.1749-1759, 1991.

Thompson, M.C. and Ferziger, J.H., "An Adaptive Multigrid Technique for the Incompressible Navier-Stokes Equation", *Journal of Computational Physics*, vol.82, pp.94-121, 1989.

Tollmien, W., "Berechnung turbulenter Ausbreitungsvorgänge", *Z.A.M.M.*, vol.6, pp.468-478, 1926. (English translation, N.A.C.A. TM 1085, 1945.)

Uppstu, E., Hyoty, P., Karvinen, R., and Siiskonen, P., "Alternative Air Supply System for Recovery Boilers", TAPPI Proceedings, International Chemical Recovery Conference, Ottawa, Ontario, pp.9-13, April, 1989.

Vanka, S.P., "Block-Implicit Multigrid Solution of Navier-Stokes Equations in Primitive Variables", *Journal of Computational Physics"*, vol.65, pp.138-158, 1986.

Vanka, S.P., "Block - Implicit Computation of Viscous Internal Flows – Recent Results", AIAA 25th Aerospace Sciences Meeting, January 12-15, 1987.

Walker, R.E. and Kors, D.L., "Multiple Jet Study – Final Report", NASA CR-121217, 1973.

Wanik, A. and Schnell, U., "Some Remarks on the PISO and SIMPLE Algorithms for Steady Turbulent Flow Problems", *Computers & Fluids*, vol.17, no.4, pp.555-570, 1989.

Wygnanski, L. and Fiedler, H., "Some measurements in the self-preserving jet", *Journal of Fluid Mechanics*, vol.38, pp.577-612, 1969.